THE UNIVERSITY OF CHICAGO

SILICON NANOWIRES AS INTRACELLULAR DEVICES

A DISSERTATION SUBMITTED TO

THE FACULTY OF THE DIVISION OF THE PHYSICAL SCIENCES

IN CANDIDACY FOR THE DEGREE OF

DOCTOR OF PHILOSOPHY

DEPARTMENT OF CHEMISTRY

BY

JOHN F. ZIMMERMAN

CHICAGO, ILLINOIS

AUGUST 2016

Table of Contents

List of Figures

List of Supplemental Videos

List of Tables

Acknowledgements

While this work represents the culmination of my efforts at the University of Chicago, there are a greatly many people without whom this document might not have ever been completed. I want to express my most sincere thanks to all of those that have been there for me throughout my journey.

First, I would like to thank my advisor Bozhi Tian for his constant and continued support. It has been such a privilege to see his lab grow from the ground up. For me, it has been an amazing environment to work in, and has really given me the chance to explore my creativity in a way that I don't believe I would have had in any other lab. For this I am so incredibly grateful!

In this vein, I also want to take the opportunity to thank my fellow lab members, past and present, all of whom have had to survive my endless inane prattle, and have had the good social graces to at least pretend to find it interesting: Ramya Parameswaran, Graeme Murray, Kelliann Koehler, Yuanwen Jiang, Andrew Phillips, Youjin Lee, Hector Acaron Ledesma, Dr. Zhiqiang Luo, Dr. Yucai Wang and Dr. Jaeseok Yi.

I would also like to express my thank to the numerous other educators and instructors that I have had the good fortune of knowing. More specifically, the staff and faculty of both the University of Chicago and Whitman College, who were invaluable in cultivating my interest in science. In this regard, I would like to thank Dr. Tim Machonkin and Dr. Marion Götz, both of whom encouraged me to pursue a career as a graduate student.

To my family, I also owe a great deal of gratitude, as I certainly would not have made it this far without their continued love and support. To my mother, Karen Gutowsky-Zimmerman, and my father John R. Zimmerman, I want to thank you for being the best parents a person could ever ask for, and to my sister Jonelle Zimmerman, for always bringing a ray of sunshine and a flair of style into my day.

Finally, I want to thank my friends for all of the enjoyable memories. Here's to the fellowship of physical chemists who spent too many sleepless nights in Kent basement: Chad Heaps, John Jumper, Grant Langlois (and of course Traci Beilharz), Alex Lincoln, Edward Malachosky, Ben McKown, Nick Rubin and Mark Whitfield. And to those others in my life willing to engage in less than educational opportunities: Nicole James, Stephen Gray, Dan O'Hanlon, Julian Freed Brown, Landon Durak, Chris D'Autremont, Ryan Lum, Jackson Cahn, Michael Logan, Nathan Kessler, Henry Star Tuttle, Jordan Lucke, Alex Landicho, Thomas Kimmel, and Ross Henderson.

Thank you all so much!

Preface

When we first began exploring the topic of substrate free incorporation of silicon nanowires, relatively few papers had been published on the subject. Reports from the Yang group in Purdue had shown that SiNWs surface functionalized with amine groups could be internalized and that such wires could be imaged in-vivo. Additionally, a brief study using focused ion beam scanning electron microscopy (FIB-SEM) out of the Mølhave group in Denmark, was able to show that unlabelled SiNWs could be detached from a growth substrate and incorporated into vesicles, however in both cases little was done to understand the mechanism of uptake. Since then, in addition to our own work, a few reports of interest have emerged, including the incorporation of surface modified SiNWs into neuronal cells out of the Lieber group at Harvard and the characterization of the uptake mechanism of the related material silicon carbide nanowires by F. Ravanetti out of the University of Parma. Despite these efforts, little was previously known about how these devices enter cells, especially in a time-dependent manner. Yet, such knowledge is critical in informing future device design, and in implementing cell specific targeting.

To expand on this outlook, we wanted to achieved several goals. First, over the past decade, there has been a growing debate as to how substrate bound nanowires interact with cellular system. Specifically, how nanowires access intracellular regions, and whether or not this process is driven by gravity/adhesion assisted puncturing of cell membranes, or if it is driven by endogenous cellular processes. By removing the nanowires from the substrate, we were poised to be able to address this question in a

reasonable manner, as such a setup would minimize the effects of gravity and adhesion forces, and would hopefully be able demonstrate that nanowire endocytosis is a protein dependent process. Through this work, we hoped to show that endogenous processes play a critical role in nanowire-cell interactions, and as a result could be of significant interest to those working within this field.

Second, we strongly believe that the field needs a better method of quantitating nanowire-cell interactions, and in particular the mechanism of nanowire uptake. In the past, nanomaterial internalization for high-aspect ratio particles has been primarily achieved through studying cell morphology during internalization. While we have also included similar details, in general this marks a poor state of affairs, as internalization morphologies can vary across cell lines and are highly subjective, depending upon the researcher. To help remedy this situation, we wanted to introduce new quantitative metrics for monitoring SiNW internalization on both the single nanowire level and ensemble scales.

Finally, we this felt that this was a singular moment in active therapeutics and that our work represents a unique opportunity. Namely, that SiNWs have the chance to be used as a platform technology for designing a wide variety of intracellular devices and that by investigating the mechanism of internalization we could place these devices into a broader biological context. From here, we hoped to demonstrate not only that wires could be internalized, but that they could be used as nanoscale therapeutics and diagnostics; showing that independent intracellular devices are not just a possibility of the future, but that they can be realized in the here and now.

In all three regards, I feel that we have been highly successful. In this work we explore the silicon nanowire cell interface, showing that silicon nanowire internalization is an endogenous, protein driven process, and that it can occur in the absence of gravity/adhesion driven abrasion. To achieve this, we have introduced a simple single-capture Dark-field/Phase Contrast optical imaging modality, scatter enhanced phase contrast (SEPC), which enables the simultaneous visualization of both cellular components and inorganic nanostructures. Additionally, we have developed a robust set of quantitative metrics for examining nanowire internalization on both the single and ensemble nanowire levels. Finally, we will discuss how this approach can be used to make rationally designed devices capable of substrate independent operation, providing a simple and scalable method for continuous inter- and intracellular force dynamics studies.

Abstract

Semiconductor nanowire devices are an exciting class of materials for biomedical and electrophysiology applications, with current studies primarily delivering substrate bound devices through mechanical abrasion or electroporation. However, the ability to distribute these devices in a drug-like fashion is an important step in developing next-generation active therapeutic devices. In this work, we will discuss the interaction of label free Silicon nanowires (SiNWs) with cellular systems, showing that they can be internalized in multiple cell lines, and undergo an active 'burst-like' transport process.

The first portion of this work will be primarily focused on examining the interface between SiNWs and biological systems and on exploring the cellular mechanism of nanowire internalization. In specific, this work will start with a general introduction into working with nanomaterials at the interface with biology, and into cellular endocytosis processes. From here, we will demonstrate that SiNWs can be internalized, discussing a new microscopy technique, Scatter Enhanced Phase Contrast (SEPC) for visualizing SiNW/cell interactions, before showing how this technique can be used for tracking individual nanowire dynamics. Next, we will discuss SiNW internalization on the ensemble level, and show how this information can be used to explore the specific mechanism of endocytosis; concluding that SiNWs are primarily internalized through a phagocytosis process. This will be followed by a brief dialogue on how the route of endocytosis can be used to inform future device design.

In the second portion of this manuscript, we will explore the use of SiNWs as independent diagnostic devices, showing that SiNWs with a kinked morphology can be used as inter- and intracellular force for extended continuous monitoring. This section

will include a brief interlude into Euler-Bernoulli beam theory, describing the governing principle behind these force probes, before demonstrating their use in cellular systems. From here, we investigate force transduction dynamics, showing that the cell's cytoskeleton plays an important role in imparting force to the internalized devices. During the course of this investigation, it became clear that nanowire diameter plays a critical role in analyzing force probe device performance. To address this problem, we will conclude with a method for precisely calibrating intracellular nanowire diameter, using an optical to electron microscopy (EM) mapping function. In this process, we will study the interaction of light with silicon nanomaterials using Lorentz-Mie theory, to describe the range over which the optical transform is possible. Collectively, this work represents one of the first dynamic studies of semiconductor nanowire internalization and offers valuable insight into designing devices for bio-molecule delivery, intracellular sensing and photoresponsive therapies.

(Additional supplementary video files detailing nanowire-cell interactions are available online.)

Chapter 1. Introduction•

1.1 Semiconductor Nanomaterials in Biology

1.1.1 'Nano' as a length scale for interfacing with cellular biology

Biological systems are organized hierarchically, with unique characteristics and functionalities spanning multiple length scales; with some examples including collagen fibers[1], metabolic networks[2], and even chromosome organization[3]. When interfacing inorganic materials with biological systems, selecting an organizational length scale plays a key role in determining device design and functionality. In the case of cellular biology, this domain is designated by the size of individual cells and their sub-cellular components, with length scales spanning between the micron range for whole cells, down to tens of nanometeres for protein complexes[4]. This provides a 'natural length scale' at which a device must be able to operate, in order to be able to distinguish between distinct cellular features. This minimal length scale has traditionally made cellular systems particularly difficult to probe or interact with in a rational and controllable manner, as implementing devices at this length scale presents a significant engineering challenge. In recent years however, inorganic nanomaterials have emerged as a new class of material for interfacing with biological systems, offering excellent synthetic control and a broad range of material properties. Such devices have the opportunity to present biologists with new tools for probing cellular systems[5,6], while nanotechnology benefits from gaining access to unprecedented biological functionalities.

•A portion of this text has been adapted from Zimmerman J. F. et. al. , Biomater. Sci. 2, 619 (2014), with permission from the Centre National de la Recherche Scientifique (CNRS) and The Royal Society of Chemistry.

The size of these nanoscale semiconductor devices make them well suited for addressing the natural length scale of cellular biology[4]. As "intermediate' sized materials, nanoscale devices are small compared to cellular features making them minimally invasive while providing high-spatial resolution, however they are also large compared to other molecular systems, allowing for the potential incorporation of multiple functionalities into a single device, such as photoelectric, photothermal, and mechanical responses. This ability to include multiple domains and features is difficult to achieve on the molecular scale and is permitted by the union of top-down fabrication and bottom up synthetic strategies being used to create a single device. This allows nanoscale materials to merge bulk engineering principles with traditional synthetic chemistry to enable distinct physical properties not achievable at any other scale. As a result, semiconductor devices have a rich set of properties that makes them a desirable target for designing next generation biomedical devices, such as extreme chemical and electrical sensitivity[7], bio-marker selectivity[8], multiplexed signal detection[9], and flexible device configuration[10].

1.1.2 Creating a library of bio-orthogonal tools

One of the most promising aspect of introducing semiconducting nanomaterials into biology is the ability to generate a diverse set of device configurations and designs, with nanoconstructs providing an expanded library of tools for use in synthetic cellular biology. Semiconductor materials are well suited for this, as during the past several decades, many such materials have been designed and realized, including colloidal nanoparticles[11,12], semiconductor nanowires (NWs)[13–15] and carbon nanotubes[16,17]. This diverse set of materials provides a wide range of nanoscopic "building blocks" that can

be applied in a biological context leading to a host of possible applications, with some examples including nanoscale biosensors[7,18], drug delivery systems[19,20], intracellular pressure sensors[21] and engineered tissue scaffolds[22].

This library of NW-based devices can be primarily used for two different modes in biomedical science. The first is the use SiNWs as a basic platform for designing detectors and sensors which can be readily adapted to address existing biomedical applications, providing robust alternative techniques for replacing and reinforcing currently existing medical diagnostics and assays**.** The second is the use of NWs as an advanced platform for modulating and understanding cell behavior in unique and exciting ways which cannot be achieved using traditional macroscopic approaches. This entails designing novel systems which can operate at the cellular length scale, providing never-before available experimental opportunities.

Basic NW applications make use of traditional NW materials and devices, with well defined chemical and physical properties, and have already seen use in a wide-range of applications, with some examples including 2D NW field effect transistors (NWFETs)[23–25] and vertical NW arrays[26–28]. In a biological context, these platforms have been used as biomolecular sensors[29,30], extracellular recording devices[29,30], drug delivery platforms[31,32,33], and probes for localized cellular imaging[34]. While recapitulating existing diagnostics, these basic applications offer the promise of being more robust, reusable, and sensitive than traditional methods. Advanced NW devices however can designed to address current limitations in a variety of fields, including synthetic biology and electrophysiology. By making devices which naturally operate at the nanoscale, NW are able to address cellular systems at their natural length scale, allowing unique

interactions and measurements that have not previously been available[22,35,36]. In this manuscript, it is primarily this second mode of operation that we are interested in, which uses NWs as an independent platform for exploring the interface between semiconductor nanomaterials and biology.

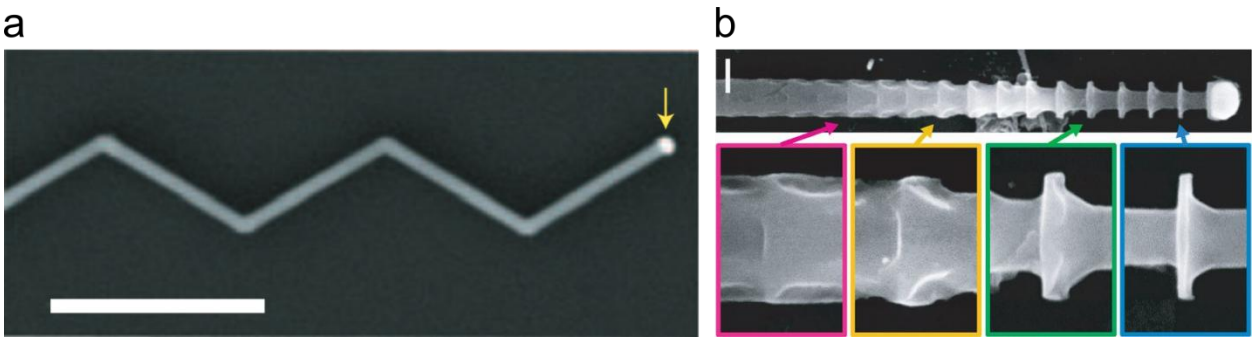

Figure 1.1 SiNWs with Complex Morphologies.
(**a**) SEM micrograph of a controllably kinked two-dimensional SiNW with multiple arm segments of equal lengths. (1 µm scale bar). (**b**) SEM micrograph of an etched SiNW showing controlled modulation of structural morphology using atomically deposited gold lithography (200 nm scale bar). **a** adapted with permission from Tian et al., 2009[37]. **b** adapted with permission from Luo et al., 2015[38].

With regards to flexibility in device configuration, silicon nanowires (SiNWs) have been one of the most successful nanoscopic platforms, as SiNW structures can be designed and synthetically realized with complex, yet controlled, modulations in composition[15,39–41], doping[42–44] , defects[45,46], and even topography[38,47,48] (**Figure 1.1**). This high degree of synthetic control enables the creation of building blocks with predictable physical properties and the assembly of hybrid or multicomponent functional materials in novel layouts and configurations[23–25,49–55]. This in turn allows for the rational exploration of the silicon/biology interface, as nanowires can be tuned to test specific device parameters. In this way, SiNW are a promising platform for creating a library of bio-orthogonal tools for use in cellular biology.

1.2 Introduction To Nanomaterials Growth

1.2.1 VLS and CVD Assisted Nanowire Growth

To understand how a diverse set a functional devices can be designed using SiNWs, we turn to synthetic strategies, examining how nanowires are produced. First proposed in the mid 1960's by Wagner and Ellis[56], the vapor-liquid solid (VLS) mechanism is one of the primary growth methods for synthesizing semiconducting nanowires[57]. This process works by using a small metal catalyst, often gold, as a sink for gaseous silicon precursors, typically silane (SiH_4) or silicon tetrachloride ($SiCL_4$) (**Figure 1.2**). Upon contacting the metal particle, gaseous precursors decompose and are incorporated into the metal, forming an eutectic alloy. In the case of gold/silicon alloys, a common growth system, this eutectic point occurs at a mixture of ~19% atomic silicon and 81% atomic gold, allowing the particle to melt and form a liquid droplet at ~363 °C[58]. This decreases the melting point by approximately 700 K and 1000 K in the case of pure bulk gold and silicon respectively[59], allowing nanowire growth to occur at a greatly decreased temperatures. As more precursor gas is introduced into the system, it will be incorporated into the liquid droplet resulting in the formation of a super saturated solution. The excess silicon then deposits out as a solid, preferentially nucleating at the substrate surface. As even more precursor gas is introduced into the system this nucleation process will continue, however, as the droplet remains a liquid, it will stay on top of the resulting nanostructure, allowing for a continues growth process. This will then cause the formation of a nanowire, which will take on radial dimensions similar in

scale to the starting metal catalyst[60]. The name 'Vapor-liquid-solid' reflects the nanowire growth process, and refers to vaporous precursor gas, the liquid alloy droplet, and the deposited solid substrate.

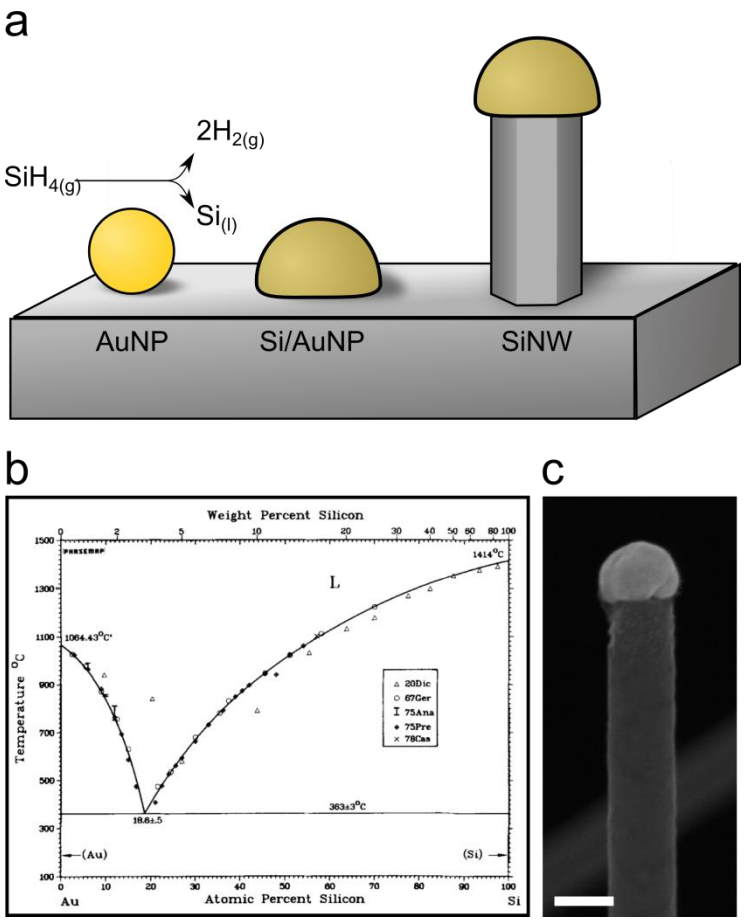

Figure 1.2 Vapor Liquid Solid Growth Mechanism.
(**a**) Schematic diagram showing the VLS growth mechanism for silicon nanowires. AuNPs act as a catalyst for silane gas decomposition, forming a liquid eutectic alloy and releasing hydrogen as a side product. As more silane is fed over the system, the droplet becomes saturated, depositing out a solid silicon phase with a diameter similar to that of the droplet. (**b**) Gold-Silicon phase diagram, showing the solid crystaline phase (lower) and the liquid eutectic phase (upper). (**c**) Scanning electron micrograph of a SiNW synthesized using VLS (100 nm scale bar). **c** reprinted with permission from Okamoto & Massalski, 1983[58].

In addition to VLS growth, precursor gases can also undergo spontaneous decomposition in the absence of a metal growth catalyst, depositing solid non-catalytically onto exposed surfaces in the reaction chamber. This process, named in a similar vein to the VLS mechanism, is usually called a vapor-solid (VS) reaction, as it

only involve the vapor and solid phases, as opposed to the liquid phase. In the case of silane precursor gas, this decomposition follows the form of[61]:

$$2\ SiH_{4\,(g)} \rightarrow\ Si_2H_{6\,(g)} + H_{2\,(g)} \quad \textbf{1.1}$$

$$Si_2H_{6\,(g)} +\ (*) \rightarrow\ \left(Si_2H_{6\,(g)}{}^{*}\right) \quad \textbf{1.2}$$

$$\left(Si_2H_{6\,(g)}{}^{*}\right) \rightarrow\ 2\ Si_{(s)} + (*) + 3\ H_{2\,(g)} \quad \textbf{1.3}$$

where $(*)$ denotes an active reaction center, such as small deviations in the solid substrate. As both VLS and VS growth can occur under similar reaction conditions, these two mechanisms are in direction competition with one another, and in practice are often observed simultaneously. However, different reaction conditions can be used to favor one process over another. For instance, the use of higher growth temperatures and lower vapor pressures can be used to selectively deposit solid silicon shells via the VS mechanism, while limiting VLS directed growth; a process which can be used to grow co-axial SiNW structures[44]. The interplay between these two reaction mechanisms allows for an expanded design space which can be used to synthesize novel nanostructures.

While it's possible to use many different setups to enable both VLS and VS assisted growth of SiNWs, one of the most common is chemical vapor deposition (CVD). In CVD, volatile gaseous silicon precursors, such as silane, SiH_4, are continuously flowed through a heated reaction chamber (**Figure 1.3**). To prevent fouling, it is crucial to reduce the background oxygen pressure, as the growth catalyst can easily oxidize if exposed to air at high temperature. As a result, a vacuum chamber is needed to maintain uniform growth conditions, where high-vacuum equipment (base pressure around 10^{-6} mbar) is sufficient for SiNW growth when using Au as a catalyst [59]. However,

the use of a vacuum chamber creates a clean environment, which allows precise control over the precursor gas supply, pressure and temperature, ensuring synthetic reproducibility, while enabling a variety of different growth conditions. During CVD growth, precursor gases are carried to the growth substrate via a carrier gas, usually hydrogen, where they catalytically decompose on the gold surface, inducing growth using the VLS mechanism.

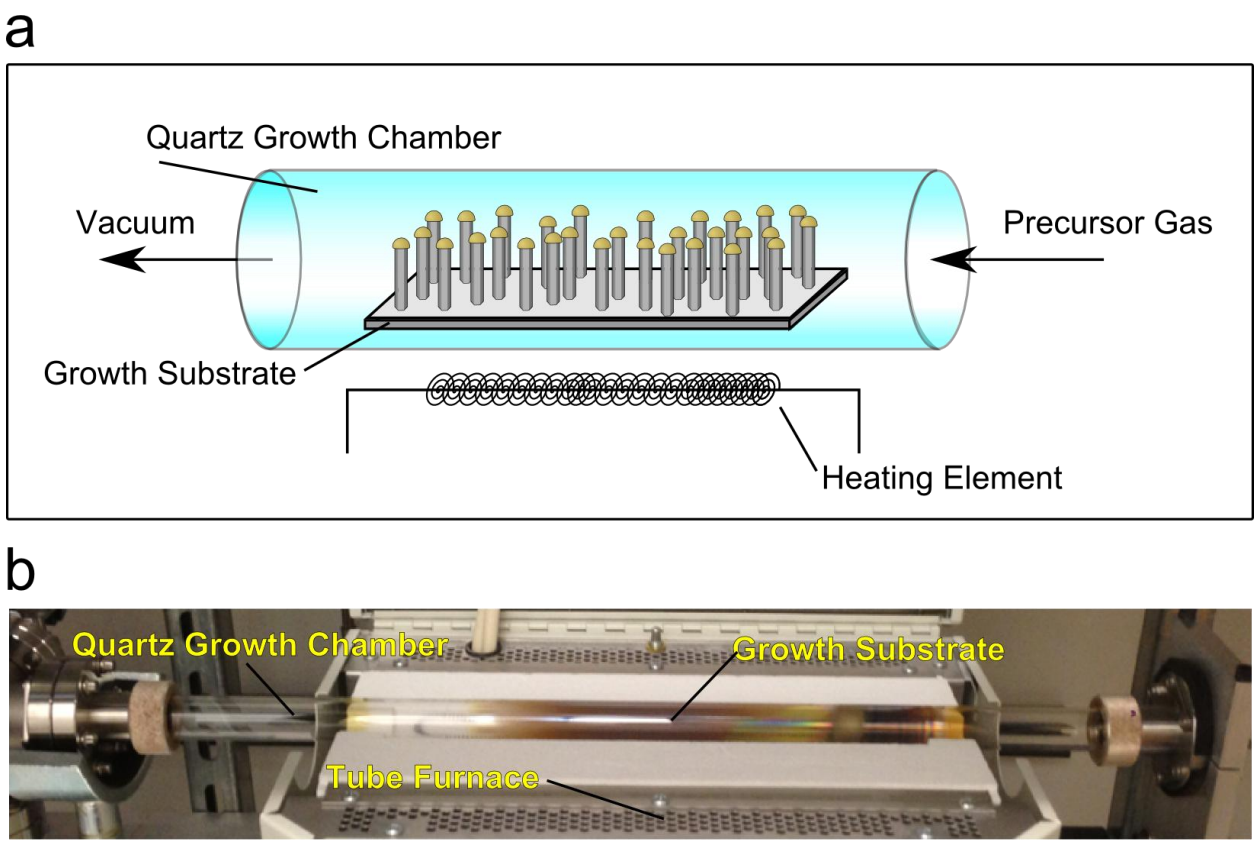

Figure 1.3 Chemical Vapor Deposition (CVD) System.
(**a**) Schematic diagram of a CVD system, showing SiNWs being synthesized in a heated quartz vacuum chamber. (**b**) Picture of an actual CVD system, showing the tube furnace and quartz growth chamber. Location of the growth substrate indicated, but not actually visible through the deposited silicon on the sidewall of the chamber.

Using CVD synthesis, it is also possible to dope silicon nanowires directly from the vapor phase[42]. To this end, both phosphine, PH_3, and diborane, B_2H_6, are commonly used precursors gases for silicon devices, inserting phosphorous and boron

respectively into the silicon lattice. The introduction of these slight impurities injects extra electrons or holes into the semiconductor, altering its electronic properties. This allows for the controllable introduction of positively (p-doped) and negatively (n-doped) regions, enabling a modulated nanowire composition[62]. This property of CVD has been used to great effect to generate a variety of nanoscale electronics, including photovoltaic[44] and transistor devices[63,64]. Overall, synthesizing nanowires in this way offers the advantage of gaining precise control over synthetic growth conditions, allowing CVD synthesis to be used to create a host of different nanowire based materials, such as kinked[37], morphologically encoded[38,65] and dopant modulated[43,44,66] nanowires.

1.2.2 Solution Phase Synthesis

In addition to the VLS assisted growth of silicon nanowires, there are also several solution based strategies. While no method to date has been able to present the same level of synthetic control and flexibility provided by vapor-phase growth, solution based methods offer the potential advantages of surface passivation and ease of implementation, on both the laboratory and industrial scales, while avoiding the use potentially hazardous air combustible gases[67]. Drawing an analogy from the VLS mechanism, these methods are often coined solution-liquid-solid (SLS) mechanisms, making use of a solid catalyst suspended in a liquid precursor solution[68]. In the past, these methods have been largely avoided for use in biology, as most applications to date have required an attached, electronically addressable substrate (**Section 1.3**). However, for substrate free devices, solution phase synthesis presents a possible alternative.

One strategy for growing silicon nanowires, presented by Korgel, uses super critical hexane as a solvent[69]. In their original setup diphenylsilane, $SiH_2(C_6H_5)_2$, was used as a Si precursor. When mixed with hexane and alkanethiol coated gold nanoparticles in a high pressure (200-270 bar), high temperature (500 °C) reactor, this resulted in a super critical hexane solution and the formation of single crystalline silicon nanowires. One advantage of this technique is that nanowire preparation can be performed continually, rather than in a single batch process. Additionally, it was shown that multiple precursors could be used, giving rise to some synthetic flexibility[70].

Korgel's group has also presented a strategy using the SLS growth mechanism at atmospheric pressures[71]. Using trisilane, Si_3H_8, dissolved in octacosane, $C_{28}H_{58}$, as the Si precursor and gold as the growth catalyst, researchers were able to grow primarily <111> and <110> silicon nanowires. However in this case, temperatures exceeding 400 °C were needed and the resulting SiNW morphologies were poor, forming large clumped aggregates. However, the main advantages of this method is that it can synthesize thin nanowires in large amounts, using only comparably simple equipment.

A more recent technique presented by P. Yang's group[72] allows for the low temperature (~200 °C) solution phase growth of silicon nanowires using a gallium catalysts. In this report, tris(trimethylsilyl)silane, $(TMS)_3SiH$, was catalytically decomposed in the presence of triethylgallium dissolved in a hexadecane solution. The resulting nanowire formations were found to be weakly oxidized, and grew primarily in the <111> growth direction. Using this technique they were also able to show the growth

of hybrid Si and GaP structures, indicating that this method can be used to incorporating Si into other semiconductor lattices at low temperatures.

Silicon nanorods are also achievable using solution phase techniques. In a recent report by Song et al.[73] photostable fluorescent nanorods with tunable optical characteristics were prepared via a one-pot microwave assisted synthesis. Here, $C_6H_{17}NO_3Si$ molecules were reduced using trisodium citrate and oddly enough milk albumen. In this work, Song and co-workers proposed an entirely different mechanism of nanowire growth, using microwave assisted micelle and CaP crystal format to guide nanorod growth. This technique offered the advantage of using mild reaction conditions, and providing quick sample preparations. Researchers also presented results indicating that nanorods prepared this way were relatively biocompatible and did not negatively impact cell viability.

Taken together, solution based synthesis of semiconductor nanowires is still a young field. Compared to other synthetic methods, many of these reports lack the ability to introduce structural modulations or chemical dopants in a controllable fashion. Additionally, the ability to epitaxialy grow silicon nanowires would be difficult to realize in solution based methods. While this limits selectivity over nanowire growth directions, in the case of bio-integration the lack of substrate can actually be viewed as a potential advantage, as additional preparation is not needed to distribute nanowires into solution; a process which can give rise to heterogeneous structures. Additionally, solution based techniques also hold great promise in enabling easy to access, cost-effective methods of producing silicon nanowires. So while there are still some hurdles left in solution

based processing, such methods could potentially hold an important place in the future of generating nanomaterials for use in biological systems.

1.3 Nanowires in Biology

In recent years, semiconductor nanowires have increasingly been used in biological applications, with their small dimensions and flexible device design making them minimal invasive tool for sensing and manipulating cellular behavior. So far we have discussed methods of producing silicon nanowires. Here we will show how substrate bound devices have been be used as sensitive electrical and mechanical sensors, and as a platform for bio-molecule delivery, before exploring some strategies for incorporating these diverse functionalities into substrate free devices.

1.3.1 Nanowire Field Effect Transistors

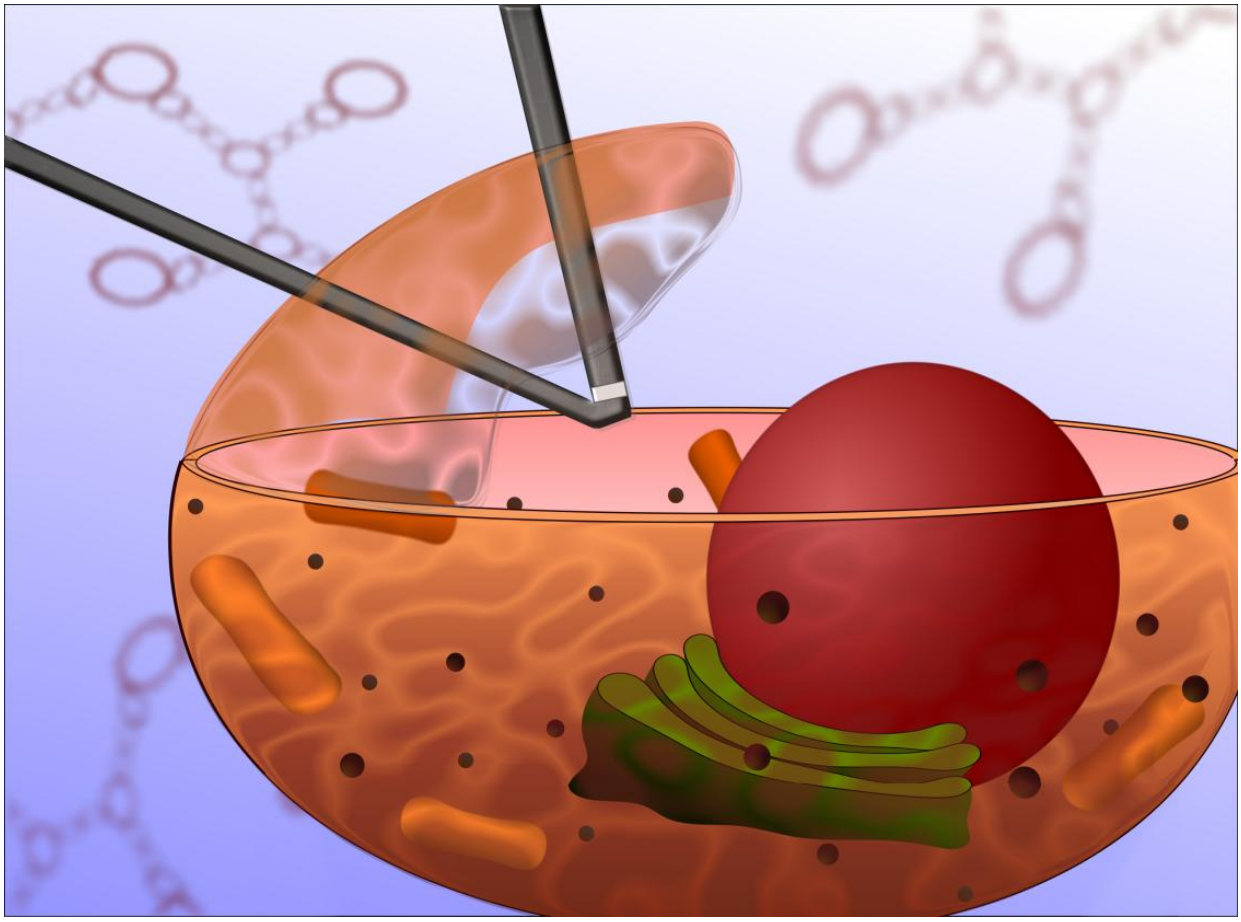

Figure 1.4 Cellular Nanowire Probe.
Artistic rendition of a kinked NWFET being inserted into a cell, probing it's intracellular electrical potential. Adapted from Zimmerman J. F. et. al. , Biomater. Sci. 2, 619 (2014), with permission from the Centre National de la Recherche Scientifique (CNRS) and The Royal Society of Chemistry.

In the past, research on integrating nanoscale semiconductor devices with biology has primarily focused on using substrate bound devices, and in particular nanowire field effect transistors (NWFETs) (**Figure 1.4**). NWFETs are a highly sensitive and selective platform for detecting minute changes in chemical concentrations and electrochemical potentials[7,31,49], with a detection sensitivities down to femto-molar concentrations[9,18] (i.e. parts-per-quadrillion 'ppq' detection) and switching speeds as fast as 2 THz[74], allowing for responses on the picosecond timescale. The ability of NWFETs

to operate under physiological conditions in a non-destructive and highly non-invasive manner makes them a useful candidate for in-vivo studies.

In addition to being sensitive chemical probes, NWFETs allow for multiplexed bio-marker detection, or the use of multiple semiconductor devices for the simultaneous measurement of a single sample. This correlated detection can cut down on electrical cross-talk and/or false-positives[9], while individual nanoscale detectors within an array can be configured through surface modification to monitor for distinct targets[8,75]. This allows for the simultaneous measurement of multiple biomarkers and can give insight into how chemical systems dynamically evolve in real-time[9,76]. Additionally, coupling NWFETs with proximal porous systems can be used to measure a variety of markers and has been used for DNA Sequencing[77]. While there are certain practical challenges in device implementation preventing the current commercialization of these devices[76], recent advancements in fabrication techniques such as patterned positioning[78–80], robotic spotting[81], ink-jet printing[82], heat selective functionalization[83], site specific electrochemical deposition[84], and dip-pen nanolithography[85] present promising opportunities for future implementations.

Nanoscopic devices are also capable of extreme flexibility when compared to bulk materials allowing for the construction of uniquely pliable electronic devices [25,50,86]. This enables the design of free standing three dimensional device configurations and allows for the dynamic response to changes in tissue positioning and conformation. In an analogous fashion to existing engineered active components in tissue culture[87,88], flexible nanoelectronics allow for the observation and modulation of tissue behavior in a three dimensional volume.

1.3.2 Nanowire Arrays as a Bio-molecule Delivery Platform

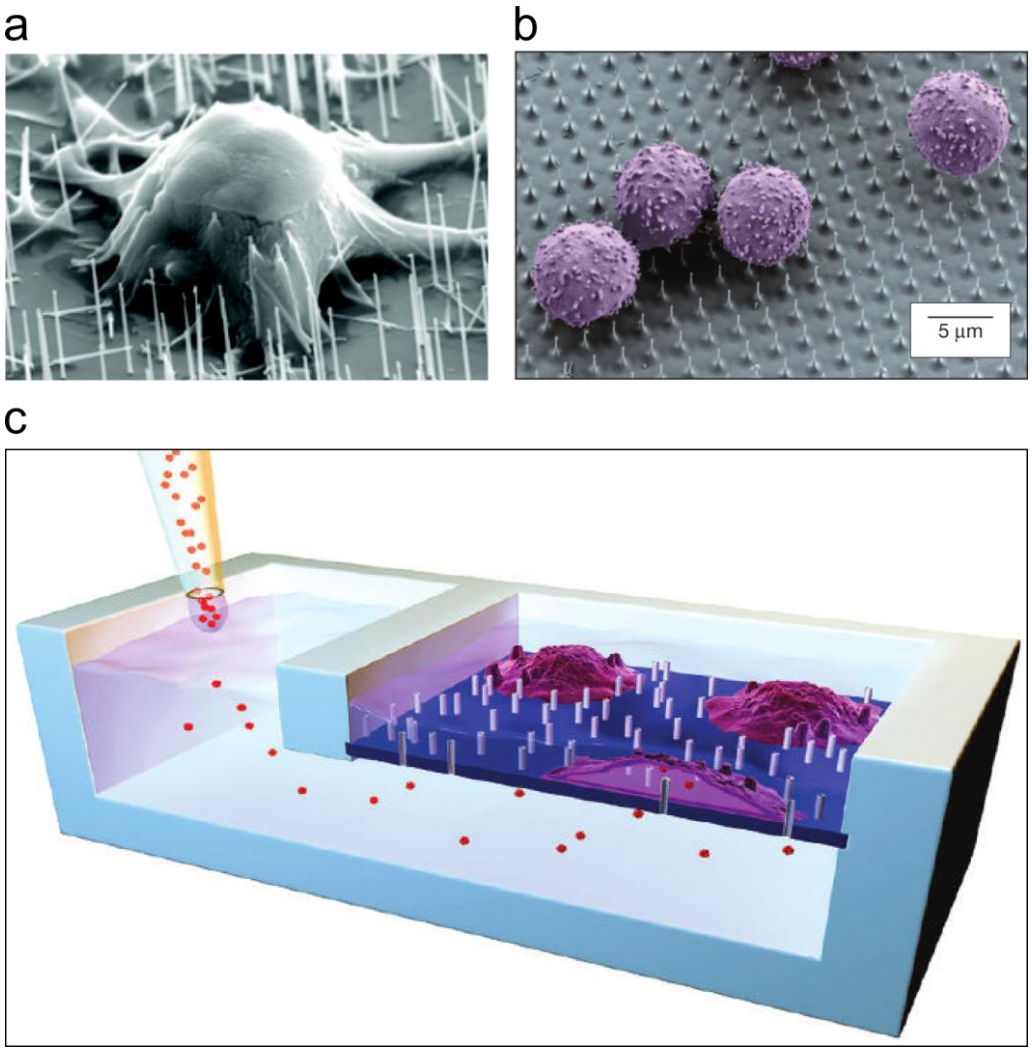

Figure 1.5 SiNW Bio-Molecule Delivery Platforms.
(**a**) SEM micrograph of a vertical SiNW array penetrating mouse embryonic stem (mES) cells, delivering GFP-DNA. (**b**) SEM micrograph of primary T cells (false-colored purple) cultured on vertical silicon nanowires for ssRNA delivery. (**c**) Schematic illustration of intracellular straw delivery system. Figure **a** adapted with permission from Kim et al., 2007[31]. Figure **b** adapted with permission from Yosef et al., 2013[89]. Figure **c** adapted with permission from VanDersarl et al., 2012[90].

In addition to acting as electrical sensors, vertical nanowire arrays have also been used as bio-molecule delivery platforms. First presented by P. Yang's group[31] in 2007, mouse embryonic stem (mES) cells and human embryonic kidney (HEK 293T) cells were transfected with GFP (**Figure 1.5a**) using an array of SiNWs. To achieve this, cells were simply cultured on vertical nanowire arrays which were preconditioned with

electrostatically deposited GFP-DNA. Growing cells in this way, nanowires were observed to be able to penetrate the cell membrane, allowing the release of bio-molecules into cytosol, with the SiNWs acting as a transfection vector. While, these initial reports showed very little characterization of the cell interface, and extremely low delivery levels (<1%), they concretely demonstrated that SiNWs could form a unique interface with cellular systems.

This was later improved by Shalek et al.[33], who showed that nanowires could be used to deliver a variety of biomaterials intracellularly, including ssRNA, proteins, and DNA, with an over 95% reported cells transfection rate (**Figure 1.5b**). Additionally, researchers demonstrated the ability to micropattern nanowire arrays, allowing site-specific delivery of the targeted molecules. One of the primary advantages of this method, is that it can be used to promote bio-molecule delivery into traditionally difficult to transfect cell lines, such as primary T-cells[89]. To optimize this process, this group showed that nanowire geometry could play an important role in mediating cell-nanowire interactions[91], with longer (2−3 μm), sharper (diameter <150 nm), and denser (0.3−1 per μm^2) nanowires providing improved delivery to non-adherent T-cells.

Another approach for delivering bio-molecules uses nanostraws to gain access to intracellular regions[90] (**Figure 1.5c**). This method uses a tube-like structure, which allows media and other molecules to be flowed directly into the cytosol, without the need for linkage breaking of conjugated groups. This approach offered several advantages. First, it allows the use of bio-molecules that are difficult to conjugate to nanowire surface. Second, the use of flow system, means that the introduction of separate bio-molecular species can be temporally separated, allowing for a sequential

addition of different bio-molecules and more direct control over sample concentrations. One problem with this setup, was that the pore openings could potentially be detrimental to cell health, and that the cell would eventually seal the nanowstraw's hole. To subsequently combat this issue, systems incorporating electrical and chemical poration have been introduced[92,93].

1.3.3 Extracellular Nanowire Force Probes

Nanowires have also been used as a platform for mechanosensing, studying the dynamics of extracellular mechanical forces. In these studies, typically an array of nano to micro sized posted are fabricated onto a substrate's surface. Cells are then seeded onto the posts, and the shifts in post positions gives rise to force measurements, as the extent of post deformation depends on the forces exerted by the cell. In this manner, these arrays can act as a series of independent cantilever devices whose precise devices parameters depend only on the cantilever's materials properties. This follows the relation[94]:

$$P = \frac{3EI}{L^3}\Delta x \qquad \textbf{1.4}$$

where P is the force load, E is the Young's modulus, I is the cross-sectional moment of inertia, D is the post's diameter, L is the length of the cantilever and Δx is the displacement of the cantilever's tip.

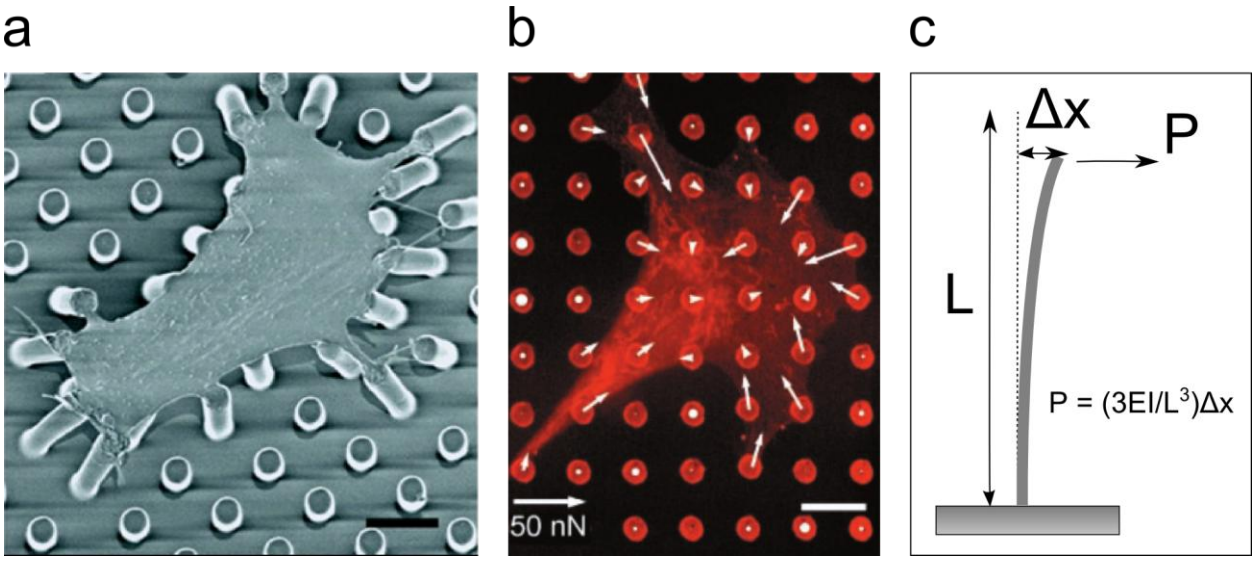

Figure 1.6 Micro-post Traction Force Microscopy.
(**a**)SEM micrograph of smooth muscle cells attached to PDMS posts, deflecting the tip position..(**b**) Confocal image of immunofluorescence stained smooth muscle cell, showing the extent of post deflection, and the calculated force vectors (10 µm scale bars). (**c**) Schematic diagram of cantilever post deflection. Figures adapted with permission from tan et al., 2003[95].

Initial studies focused on using larger micro-post arrays, often fabricated out of PDMS[95,96] **(Figure 1.6)**. This provided an easy to implement fabrication process, using materials with well known mechanical properties. As a result, micro-post studies have been used to study a wide range of biological phenomenon, including the force dynamics of focal adhesion sites[97], and epithelial cell migration[96]. However, the force ranges that can be probed are directly related to the material properties and the size of the micro-post. Additionally, larger cantilever sizes inherently limit the spatial resolution of these traction force microscopy techniques. Therefore, a natural extension of this work has been to move to smaller length scales, decreasing the size of individual posts while increasing the post density, a task which was readily achievable using synthetic nanomaterials.

This was demonstrated by Le et al. in 2009, when they first used arrays of silicon nanowires to quantifying the contractile and traction forces of cancer cells[98]. This

approach allowed for a more densely packed array, providing for a higher spatial resolution of force data. A similar method was adopted by the Prinz group in 2010, using gallium phosphide, GaP, nanowires[94]. By changing the type of nanomaterial, they were able to adjust the range of the force probes, giving rise to a minimum reported detection limit of ~15 pN. Additionally, as GaP nanowires can fluoresce, shifts in nanowire locations were easily discerned without additional staining, marking this as a convenient approach for optical microscopy. While still in its infancy, the use of nanowires as extracellular force probes provided inspiration for our later work, show that nanowires can be used as intracellular force probe, a process which will be discussed in greater detail (**See Chapter 4**).

1.3.4 Substrate-Nanowire Interface

One result of the these nanowire applications is that there has been an increased interest in the interface of semiconducting nanowires with biological systems[6]. More specifically, how cells respond to high aspect ratio nanomaterials, and by what method nanowires are able penetrate cell membranes, gaining access to intracellular regions. These questions are of significant importance, as they govern the ability of NWFETs to probe biologically relevant species and determine the efficacy of using nanowires as a bio-molecule delivery platform[91]. Additionally, as more commercial products begin to incorporate nanomaterials, understanding these interfaces could play an important role in shaping both the biocompatibility and environmental impact of these devices.

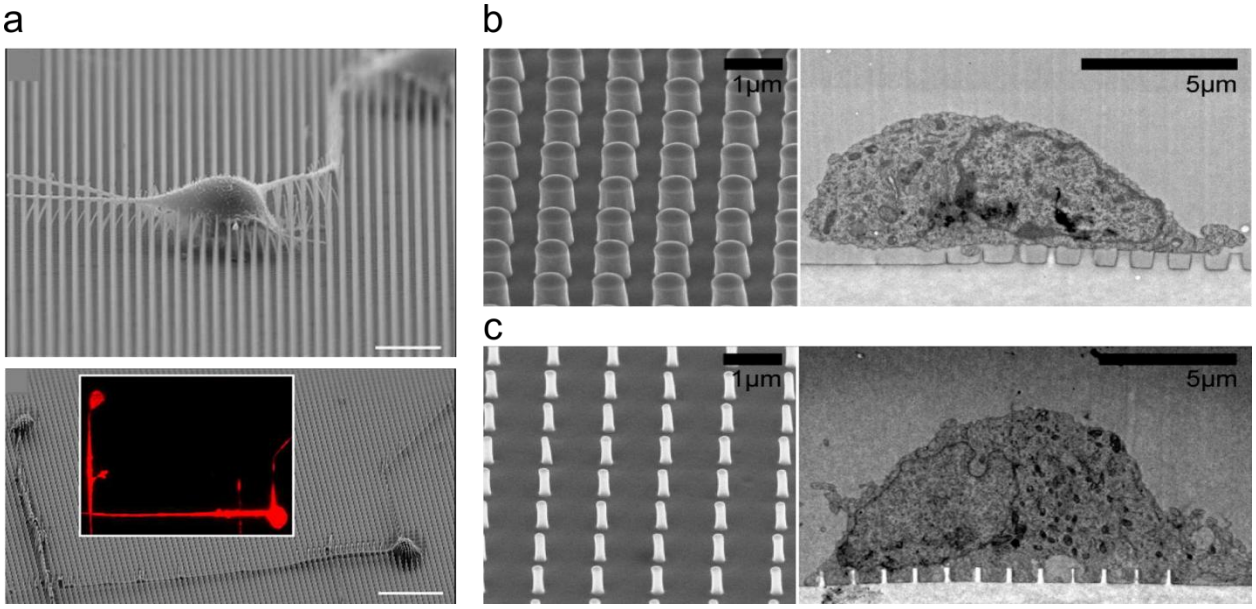

Figure 1.7 Nano Pillar Spacing and Diameter Impacts Cell Growth.
(**a, upper**) SEM micrograph of a stem cell positioned on top of an array of nano-pillars (10 µm scale bar). (**a, lower**) SEM and live optical inset of a stem cell one day after growth, showing oriented growth and polarization (20 µm scale bar). (**b**) Schematic diagram of cantilever post deflection. Figure **a** adapted with permission from Bucaro et al., 2012[99]. Figures **b**&**c** adapted with permission from Hanson et al., 2012[100].

One key aspect of the nanowire's interface with biological systems, is the interplay between micro-post spacing and the size of individual posts within array. Understanding how cells respond to these factors is an important step in calibrating precise device design. It has been shown that in dense array, cells will grow exclusively on top of the post structures, without extending to the underlying substrate surface, a behavior that can even impact cell differentiation and growth directions[99] **(Figure 1.7a)**. However, for bio-molecule delivery to be effective, nanowires need to be able to penetrate cells, fully integrating into the cell body. It was noted earlier, that different diameter nanowires, with different spacing parameters, could impact the ability of nanowires to penetrate cells, determining delivery efficiency[91]. As a result, this suggested that there was trade off between these parameters, where a cell would either grow above the nanowire array, or become integrated with it. Hanson et. al. observed

exactly this[100], showing that when nanopillar diameters were large and densely packed, cells grow over the wires, while reducing either of these parameters caused cells to become interdigitated with nanowire arrays. This confirmed that array packing and size are critical factors in nanowire device functionality.

When nanopillars were examined further using electron microscopy studies however, minimal cell penetration was observed, even for sharp nanowires[100–102]. Instead, the membrane was found to be pliable, and capable of accommodating the long nanowire protrusions. This suggested that there was an additional requirement for nanowire cell penetration. Flow studies conducted on similar structures confirmed this, showing that cell penetration was a rare event, comprising only ~7% of the nano-posts interfacing with the cell[103]. While for bio-delivery, this was still an acceptable amount, as the high density of arrayed materials meant that on average some wires would be able to deliver their cargo, it also suggested that in addition to gravity, other force were needed to initiate nanowire penetration[104]. One proposed mechanism, was the addition of adhesion forces, which would pull the cell membrane further down onto the wire[105]. Alternatively, it has been suggested that cellular recognition events could play a critical role[104,106]. To further complicate this matter, it has been shown that in addition to the plasma membrane, the cytoskeleton can also act as a barrier to nanowire entry[92]. Overall, this is still an open question that has yet to be fully addressed.

While there is there is still much to be known about how nanowires access the cytosol, several strategies have been adapted to facilitate this process, including electrical and chemical poration, as well as lipid coatings. Electroporatoin, the ability to generate small holes in the cell membrane using electrical pulses, is a commonly known

biological phenomena, that has been widely used for gene and drug delivery. Nanowire electrodes are well suited for this method of entry as they can deliver the electrical spike trains needed with high spatial-temporal resolution. This allows for the local electroporation at the point of the nanowire electrode[93,107–109]. Chemical poration methods on the other hand consist of delivering compounds capable dissolving the plasma membrane. To maintain cell viability, these compounds are best delivered locally, making this method most conducive to nanomaterials capable of storing and distributing drugs in a point-like fashion. For example, this method has been demonstrated using dimethyl sulfoxide (DMSO) delivered through nanostraws[92] and saponin delivered through hollow nanoneedles[110]. Finally, lipid coating methods employ a phospholid layering capable of enabling seamless integration. This method was demonstrated using intracellular electrodes[10] and has been shown to be repeatable, where devices can be inserted and removed multiple times without detrimental effects[111]. In summary, all three of these methods can be used to gain entry to the cytosol, however, in each case an important piece of information missing. Namely, the survival time of cells integrated with nanowires. Therefore the relative biocompatibility of these methods is still indeterminate[6], and could play an important role in future device implementations.

1.3.5 Substrate Free Nanowires

Another proposed method for gaining access to the cytosol is to use substrate free devices. While removing the device from substrate makes some applications challenging, such as individually addressed electoral sensors, it also opens up many other opportunity, allowing devices to be completely internalized. This has the potential

of enabling devices capable of independent operation within individual cells, such as active-drug like therapeutics and biophysical probes. Some examples of this class of material have already emerged, with high-aspect nanomaterials seeing use as intracellular rheology systems[112,113], and as 'bionic' enhancements in plant cells for photosynthesis[114]. Additionally, silicon based materials can also be used as both cellular probes[115,116] and as tools for bio-imaging[73].

Prior to starting this project, little work had been done on studying silicon based internalization events, with the main strategy of internalization involving the use of surface modification to functionalize nanowires for specific receptor recognition. In 2006, Bohach's group showed that silica nanowires modified with fibronectin could be internalized in epithelial cells[117]. Later this work was adapted to act as a delivery system for the cytotoxic protein Shiga toxin[118], with the idea of using this as a platform for treating various diseases. In both cases, researchers cited an endocytosis mechanism of integrin binding, but showed little characterization of the internalization process.

A similar strategy was adopted by C. Yang's group in 2012, showing that both amine and folate modified SiNWs could be internalized by CHO-β cells[119]. Here, the group targeted folate receptors transfected onto the surface immortalized Chinese hamster ovaries, as many malignant cell lines express foliate receptors, and similar to the silica nanowire case, these wires could be used as a therapeutic reagent. Prior to this, the same group had also shown that SiNWs injected into the blood stream could be optically observed in-vivo[120], suggesting that nanowires could also be used as a cancer visualization technique. This work offered great promise, showing for the first time that high-aspect ratio nanowires could be internalized in a substrate free manner. However,

one of the main challenges of this work, was that limited quantification was available for studying this form of material interaction.

Since this time, several papers have been published on the subject. Notably, Wierzbicki et. al. showed that SiNWs grown on a substrate could be torn off by fibroblasts and clustered into small vessicles[121]. Using focused ion beam scanning electron microscopy (FIB-SEM), they were able to provide a detailed look at the cellular position of these wires, however little information was provided on how these devices were collected by the cell. Expanding on this, in 2014 Cacchioli et al. showed that a similar material, silicon carbide nanowires, could be internalized in multiple cell lines[122]. Evaluating this material's cytotoxicity, they showed that nanowires did not induce apoptosis or arrest the cell cycle in any of cell line surveyed, but that they did cause a temporary increase in oxidative stress, which returned to basal levels after several days. Overall this suggested that nanowires were well tolerated by multiple cell lines. Additionally, they also presented information on the uptake mechanism, citing a mix of receptor-mediated endocytosis, pinocytosis, and phagocytosis. This provided some useful insight into the substrate free nanowire internalization process, however at this time, it's unclear how much the incorporation of carbon impacts the cellular recognition process, and whether or not these results remain valid for pure silicon analogs. Additionally, this report depended heavily on morphological characterization for the identification of the endocytosis pathway, where transfection and drug-inhibitors studies can provide more detailed information[123124].

Finally, another report by Lee et al. earlier this year has shown the peptide modified SiNWs can be internalized by neuronal cells[125]. To achieve this, SiNWs were

surface modified with a trans-activating transcriptional activator (TAT) protein which helps facilitate nanowire internalization. Using confocal microscopy, they were able to show that nanowires could be spontaneously internalized, offering a brief examination of the single nanowire dynamics. This approach is exciting as it offers a potential platform for addressing primary neurons, however we note that nanowires were internalized with a limited yield (~15%). This is likely the result of poor protein surface coverage, and in the future improved optimization strategies may be needed to increase nanowire incorporation.

1.4 Conclusions

In summary, as a minimally invasive and synthetically flexible class of materials, semiconducting nanowires offer many exciting opportunities for use with biological systems. Here we have shown how these devices have already been used as chemical, and mechanical sensors, in addition to serving as a platform technology for bio-molecule delivery. However the interface between nanowires and cells is a complex system, and it is still unclear how nanowire composition, morphology, and concentration impact device performance. Yet, understanding the interplay between soft biological systems and hard inorganic devices is an important step in developing future nanowire based biomedical applications. As a result, several questions still remain. Notably, the ability of nanowires to penetrate the cell membrane is still an open question, as there are conflicting reports as to how substrate bound nanowires gain entrance to the cytosol[104–106].

In this regard, substrate free silicon nanowires have great potential to be used as a platform technology for designing intracellular devices. In addition to the applications

that we have previously mentioned, substrate free nanowires have the benefit of reducing gravitational and adhesive contributions to internalization. As a result, substrate free wires can act as a minimalist system for understanding the cell penetration process, meaning that they have some potential insight to offer. In the following report, we will show have these label free wires can be internalized by multiple cell lines through an endogenous endocytosis process. This suggests that while adhesion forces may play an important role for vertical nanowire arrays, that endogenous processes may also be a critical factor to consider in future studies.

1.5 References:

1. Gautieri, A., Vesentini, S., Redaelli, A. & Buehler, M. J. Hierarchical structure and nanomechanics of collagen microfibrils from the atomistic scale up. *Nano Lett.* **11,** 757–66 (2011).

2. Ravasz, E., Somera, a L., Mongru, D. a, Oltvai, Z. N. & Barabási, a L. Hierarchical organization of modularity in metabolic networks. *Science* **297,** 1551–5 (2002).

3. Belmont, a S., Sedat, J. W. & Agard, D. a. A three-dimensional approach to mitotic chromosome structure: evidence for a complex hierarchical organization. *J. Cell Biol.* **105,** 77–92 (1987).

4. Whitesides, G. The'right'size in nanobiotechnology. *Nat. Biotechnol.* **21,** 1161–1165 (2003).

5. Ozin, G. A., Manners, I., Fournier-Bidoz, S. & Arsenault, A. Dream Nanomachines. *Adv. Mater.* **17,** 3011–3018 (2005).

6. Prinz, C. N. Interactions between semiconductor nanowires and living cells. *J. Phys. Condens. Matter* **27,** 233103 (2015).

7. Tian, B. & Lieber, C. M. Synthetic Nanoelectronic Probes for Biological Cells and Tissues. *Annu. Rev. Anal. Chem. (Palo Alto. Calif).* 31–51 (2013).

8. Stern, E. *et al.* Label-free biomarker detection from whole blood. *Nat. Nanotechnol.* **5,** 138–42 (2010).

9. Zheng, G., Patolsky, F., Cui, Y., Wang, W. U. & Lieber, C. M. Multiplexed electrical detection of cancer markers with nanowire sensor arrays. *Nat.*

Biotechnol. **23,** 1294–301 (2005).

10. Xie, C. *et al.* Three-dimensional macroporous nanoelectronic networks as minimally invasive brain probes. *Nat. Mater.* 1–8 (2015). doi:10.1038/nmat4427

11. Choi, C. L. & Alivisatos, a P. From artificial atoms to nanocrystal molecules: preparation and properties of more complex nanostructures. *Annu. Rev. Phys. Chem.* **61,** 369–89 (2010).

12. Yin, Y. & Alivisatos, a P. Colloidal nanocrystal synthesis and the organic-inorganic interface. *Nature* **437,** 664–70 (2005).

13. Lieber, C. Semiconductor nanowires: A platform for nanoscience and nanotechnology. *Nanoelectron. Conf. (INEC), 2010 3rd …* **36,** 1052–1063 (2010).

14. Law, M., Goldberger, J. & Yang, P. Semiconductor Nanowires and Nanotubes. *Annu. Rev. Mater. Res.* **34,** 83–122 (2004).

15. Li, Y., Qian, F., Xiang, J. & Lieber, C. Nanowire electronic and optoelectronic devices. *Mater. today* **9,** 18–27 (2006).

16. Wang, J. Carbon-Nanotube Based Electrochemical Biosensors: A Review. *Electroanalysis* **17,** 7–14 (2005).

17. Thostenson, E. T., Ren, Z. & Chou, T.-W. Advances in the science and technology of carbon nanotubes and their composites: a review. *Compos. Sci. Technol.* **61,** 1899–1912 (2001).

18. Li, B.-R. *et al.* Biomolecular recognition with a sensitivity-enhanced nanowire transistor biosensor. *Biosens. Bioelectron.* **45,** 252–9 (2013).

19. Korin, N., Kanapathipillai, M. & Matthews, B. Shear-Activated Nanotherapeutics for Drug Targeting to Obstructed Blood Vessels. *Science (80-.).* 738–742 (2012). at <http://www.sciencemag.org/content/337/6095/738.short>

20. Cherukuri, P., Glazer, E. S. & Curley, S. a. Targeted hyperthermia using metal nanoparticles. *Adv. Drug Deliv. Rev.* **62,** 339–45 (2010).

21. Gómez-Martínez, R. *et al.* Silicon chips detect intracellular pressure changes in living cells. *Nat. Nanotechnol.* **8,** 517–521 (2013).

22. Tian, B. *et al.* Macroporous nanowire nanoelectronic scaffolds for synthetic tissues. *Nat. Mater.* **11,** 986–994 (2012).

23. Javey, A., Nam, S., Friedman, R. S., Yan, H. & Lieber, C. M. Layer-by-layer assembly of nanowires for three-dimensional, multifunctional electronics. *Nano Lett.* **7,** 773–7 (2007).

24. Fan, Z. *et al.* Toward the Development of Printable Nanowire Electronics and Sensors. *Adv. Mater.* **21,** 3730–3743 (2009).

25. Fan, Z. & Ho, J. Large-scale, heterogeneous integration of nanowire arrays for image sensor circuitry. *Proc. …* **105,** 11066–70 (2008).

26. Boettcher, S. W. *et al.* Energy-conversion properties of vapor-liquid-solid-grown silicon wire-array photocathodes. *Science* **327,** 185–7 (2010).

27. Kelzenberg, M. D. *et al.* Enhanced absorption and carrier collection in Si wire arrays for photovoltaic applications. *Nat. Mater.* **9,** 239–44 (2010).

28. Qin, Y., Wang, X. & Wang, Z. L. Microfibre-nanowire hybrid structure for energy scavenging. *Nature* **451,** 809–13 (2008).

29. Patolsky, F., Zheng, G. & Lieber, C. M. Nanowire sensors for medicine and the life sciences. *Nanomedicine (Lond).* **1,** 51–65 (2006).

30. Timko, B. P., Cohen-Karni, T., Qing, Q., Tian, B. & Lieber, C. M. Design and Implementation of Functional Nanoelectronic Interfaces With Biomolecules, Cells, and Tissue Using Nanowire Device Arrays. *IEEE Trans. Nanotechnol.* **9,** 269–280 (2010).

31. Kim, W., Ng, J. K., Kunitake, M. E., Conklin, B. R. & Yang, P. Interfacing silicon nanowires with mammalian cells. *J. Am. Chem. Soc.* **129,** 7228–9 (2007).

32. Chevrier, N. *et al.* Systematic discovery of TLR signaling components delineates viral-sensing circuits. *Cell* **147,** 853–67 (2011).

33. Shalek, A. K. *et al.* Vertical silicon nanowires as a universal platform for delivering biomolecules into living cells. *Proc. Natl. Acad. Sci.* **107,** 1870–1875 (2010).

34. Xie, C., Hanson, L., Cui, Y. & Cui, B. Vertical nanopillars for highly localized fluorescence imaging. *Proc. Natl. Acad. Sci. U. S. A.* **108,** 3894–9 (2011).

35. Tian, B. *et al.* Three-dimensional, flexible nanoscale field-effect transistors as localized bioprobes. *Science* **329,** 830–4 (2010).

36. Gao, R. *et al.* Outside looking in: nanotube transistor intracellular sensors. *Nano Lett.* **12,** 3329–33 (2012).

37. Tian, B., Xie, P., Kempa, T. J., Bell, D. C. & Lieber, C. M. Single-crystalline kinked semiconductor nanowire superstructures. *Nat. Nanotechnol.* **4,** 824–829 (2009).

38. Luo, Z. *et al.* Atomic gold-enabled three-dimensional lithography for silicon mesostructures. *Science* **348,** 1451–1455 (2015).

39. Björk, M. T. *et al.* One-dimensional heterostructures in semiconductor

nanowhiskers. *Appl. Phys. Lett.* **80,** 1058 (2002).

40. Gudiksen, M. S., Lauhon, L. J., Wang, J., Smith, D. C. & Lieber, C. M. Growth of nanowire superlattice structures for nanoscale photonics and electronics. *Nature* **415,** 617–20 (2002).

41. Wang, D., Qian, F., Yang, C., Zhong, Z. & Lieber, C. M. Rational Growth of Branched and Hyperbranched Nanowire Structures. *Nano Lett.* **4,** 871–874 (2004).

42. Cui, Y., Duan, X., Hu, J. & Lieber, C. M. Doping and Electrical Transport in Silicon Nanowires. *J. Phys. Chem. B* **104,** 5213–5216 (2000).

43. Yang, C., Zhong, Z. & Lieber, C. M. Encoding electronic properties by synthesis of axial modulation-doped silicon nanowires. *Science* **310,** 1304–7 (2005).

44. Tian, B. *et al.* Coaxial silicon nanowires as solar cells and nanoelectronic power sources. *Nature* **449,** 885–889 (2007).

45. Algra, R. E. *et al.* Twinning superlattices in indium phosphide nanowires. *Nature* **456,** 369–72 (2008).

46. Caroff, P., Dick, K. & Johansson, J. Controlled polytypic and twin-plane superlattices in III–V nanowires. *Nat. …* **4,** (2008).

47. Schwarz, K., Tersoff, J., Kodambaka, S., Chou, Y.-C. & Ross, F. Geometrical Frustration in Nanowire Growth. *Phys. Rev. Lett.* **107,** 1–5 (2011).

48. Tian, B., Xie, P., Kempa, T. J., Bell, D. C. & Lieber, C. M. Single-crystalline kinked semiconductor nanowire superstructures. *Nat. Nanotechnol.* **4,** 824–9 (2009).

49. Qing, Q. *et al.* Nanowire transistor arrays for mapping neural circuits in acute brain slices. *Proc. Natl. Acad. Sci. U. S. A.* **107,** 1882–7 (2010).

50. McAlpine, M., Friedman, R., Jin, S. & Lin, K. High-performance nanowire electronics and photonics on glass and plastic substrates. *Nano …* **3,** 1531–1535 (2003).

51. Tian, B. *et al.* Three-Dimensional, Flexible Nanoscale Field-Effect Transistors as Localized Bioprobes. *Science* **329,** 830–834 (2010).

52. Cohen-Karni, T., Timko, B. P., Weiss, L. E. & Lieber, C. M. Flexible electrical recording from cells using nanowire transistor arrays. *Proc. Natl. Acad. Sci. U. S. A.* **106,** 7309–13 (2009).

53. Timko, B., Cohen-Karni, T., Yu, G. & Qing, Q. Electrical recording from hearts with flexible nanowire device arrays. *Nano …* **9,** 914–8 (2009).

54. Whang, D., Jin, S., Wu, Y. & Lieber, C. M. Large-Scale Hierarchical Organization

of Nanowire Arrays for Integrated Nanosystems. *Nano Lett.* **3,** 1255–1259 (2003).

55. Yu, G., Cao, A. & Lieber, C. M. Large-area blown bubble films of aligned nanowires and carbon nanotubes. *Nat. Nanotechnol.* **2,** 372–7 (2007).

56. Wagner, R. S. & Ellis, W. C. Vapor-Liquid-Solid Mechanism of Single Crystal Growth. *Appl. Phys. Lett.* **4,** 89 (1964).

57. Schmidt, V., Wittemann, J. V., Senz, S. & Gösele, U. Silicon Nanowires: A Review on Aspects of their Growth and their Electrical Properties. *Adv. Mater.* **21,** 2681–2702 (2009).

58. Okamoto, H. & Massalski, T. B. The Au−Si (Gold-Silicon) system. *Bull. Alloy Phase Diagrams* **4,** 190–198 (1983).

59. Schmidt, V., Wittemann, J. V. & Gösele, U. Growth, thermodynamics, and electrical properties of silicon nanowires. *Chem. Rev.* **110,** 361–388 (2010).

60. Nebol'sin, V. a. & Shchetinin, a. a. Role of Surface Energy in the Vapor – Liquid – Solid Growth of Silicon. *Inorg. Mater.* **39,** 899–903 (2003).

61. Peev, G., Zambov, L., Shanov, V. & Tserovski, L. Kinetics of polysilicon film growth by thermal decomposition of silane. *Semicond. Sci. Technol.* **6,** 281–286 (1999).

62. Christesen, J. D., Pinion, C. W., Zhang, X., Mcbride, J. R. & Cahoon, J. F. Encoding Abrupt and Uniform Dopant Pro fi les in Vapor À Liquid À Solid Nanowires by Suppressing the Reservoir E ff ect of the Liquid Catalyst. 11790–11798 (2014).

63. Patolsky, F. *et al.* Detection, stimulation, and inhibition of neuronal signals with high-density nanowire transistor arrays. *Science* **313,** 1100–4 (2006).

64. Cui, Y. & Lieber, C. M. Functional nanoscale electronic devices assembled using silicon nanowire building blocks. *Science* **291,** 851–3 (2001).

65. Christesen, J. D., Pinion, C. W., Grumstrup, E. M., Papanikolas, J. M. & Cahoon, J. F. Synthetically Encoding 10 nm Morphology in Silicon Nanowires. *Nano Lett.* **13,** 6281–6286 (2013).

66. Yang, C., Barrelet, C. J., Capasso, F. & Lieber, C. M. Single p-Type/Intrinsic/n-Type Silicon Nanowires as Nanoscale Avalanche Photodetectors. *Nano Lett.* **6,** 2929–2934 (2006).

67. Wang, F. *et al.* Solution−Liquid−Solid Growth of Semiconductor Nanowires. *Inorg. Chem.* **45,** 7511–7521 (2006).

68. Trentler, T. J. *et al.* Solution-Liquid-Solid Growth of Crystalline III-V

Semiconductors: An Analogy to Vapor-Liquid-Solid Growth. *Science (80-.).* **270,** 1791–1794 (1995).

69. Holmes, J., Johnston, K., Doty, R. & Korgel, B. Control of thickness and orientation of solution-grown silicon nanowires. *Science* **287,** 1471–3 (2000).

70. Lee, D. C., Hanrath, T. & Korgel, B. A. The Role of Precursor-Decomposition Kinetics in Silicon-Nanowire Synthesis in Organic Solvents. *Angew. Chemie Int. Ed.* **44,** 3573–3577 (2005).

71. Heitsch, A. T., Fanfair, D. D., Tuan, H.-Y. & Korgel, B. a. Solution-liquid-solid (SLS) growth of silicon nanowires. *J. Am. Chem. Soc.* **130,** 5436–7 (2008).

72. Sun, J. *et al.* Low-Temperature Solution-Phase Growth of Silicon and Silicon-Containing Alloy Nanowires. *J. Phys. Chem. C* acs.jpcc.5b08289 (2015). doi:10.1021/acs.jpcc.5b08289

73. Song, B. *et al.* One-Dimensional Fluorescent Silicon Nanorods Featuring Ultrahigh Photostability, Favorable Biocompatibility and Excitation Wavelength-Dependent Emission Spectra. *J. Am. Chem. Soc.* jacs.6b00479 (2016). doi:10.1021/jacs.6b00479

74. Hu, Y., Xiang, J., Liang, G., Yan, H. & Lieber, C. M. Sub-100 nanometer channel length Ge/Si nanowire transistors with potential for 2 THz switching speed. *Nano Lett.* **8,** 925–30 (2008).

75. Cui, Y., Wei, Q., Park, H. & Lieber, C. M. Nanowire nanosensors for highly sensitive and selective detection of biological and chemical species. *Science* **293,** 1289–92 (2001).

76. He, B., Morrow, T. & Keating, C. Nanowire sensors for multiplexed detection of biomolecules. *Curr. Opin. Chem. Biol.* **12,** 522–528 (2008).

77. Goldberger, J., Fan, R. & Yang, P. Inorganic nanotubes: a novel platform for nanofluidics. *Acc. Chem. Res.* **39,** 239–248 (2006).

78. Fan, Z. *et al.* Wafer-scale assembly of highly ordered semiconductor nanowire arrays by contact printing. *Nano Lett.* **8,** 20–5 (2008).

79. Yao, J., Yan, H. & Lieber, C. M. A nanoscale combing technique for the large-scale assembly of highly aligned nanowires. *Nat. Nanotechnol.* **8,** 329–335 (2013).

80. Takei, K. *et al.* Nanowire active-matrix circuitry for low-voltage macroscale artificial skin. *Nat. Mater.* **9,** 821–6 (2010).

81. Auburn, R. P. *et al.* Robotic spotting of cDNA and oligonucleotide microarrays. *Trends Biotechnol.* **23,** 374–9 (2005).

82. Bietsch, A., Zhang, J., Hegner, M., Lang, H. P. & Gerber, C. Rapid functionalization of cantilever array sensors by inkjet printing. *Nanotechnology* **15,** 873–880 (2004).

83. Park, I., Li, Z., Pisano, A. P. & Williams, R. S. Selective surface functionalization of silicon nanowires via nanoscale joule heating. *Nano Lett.* **7,** 3106–11 (2007).

84. Bunimovich, Y. L. *et al.* Electrochemically programmed, spatially selective biofunctionalization of silicon wires. *Langmuir* **20,** 10630–8 (2004).

85. Salaita, K., Wang, Y. & Mirkin, C. a. Applications of dip-pen nanolithography. *Nat. Nanotechnol.* **2,** 145–55 (2007).

86. McAlpine, M. C., Friedman, R. S. & Lieber, C. M. High-Performance Nanowire Electronics and Photonics and Nanoscale Patterning on Flexible Plastic Substrates. *Proc. IEEE* **93,** 1357–1363 (2005).

87. Dvir, T., Timko, B. & Brigham, M. Nanowired three-dimensional cardiac patches. *Nat. …* **6,** 720–5 (2011).

88. Dvir, T., Timko, B. P., Kohane, D. S. & Langer, R. Nanotechnological strategies for engineering complex tissues. *Nat. Nanotechnol.* **6,** 13–22 (2011).

89. Yosef, N. *et al.* Dynamic regulatory network controlling TH17 cell differentiation. *Nature* **496,** 461–468 (2013).

90. Vandersarl, J. J., Xu, A. M. & Melosh, N. A. Nanostraws for direct fluidic intracellular access. *Nano Lett.* **12,** 3881–3886 (2012).

91. Shalek, A. K. *et al.* Nanowire-Mediated Delivery Enables Functional Interrogation of Primary Immune Cells: Application to the Analysis of Chronic Lymphocytic Leukemia. *Nano Lett.* **12,** 6498–6504 (2012).

92. Aalipour, A., Xu, A. M., Leal-Ortiz, S., Garner, C. C. & Melosh, N. a. Plasma membrane and actin cytoskeleton as synergistic barriers to nanowire cell penetration. *Langmuir* **30,** 12362–7 (2014).

93. Xie, X. *et al.* Nanostraw–Electroporation System for Highly Efficient Intracellular Delivery and Transfection. *ACS Nano* **7,** 4351–4358 (2013).

94. Hallstrom, W. *et al.* Fifteen-piconewton force detection from neural growth cones using nanowire arrays. *Nano Lett.* **10,** 782–787 (2010).

95. Tan, J. L. *et al.* Cells lying on a bed of microneedles: an approach to isolate mechanical force. *Proc. Natl. Acad. Sci. U. S. A.* **100,** 1484–9 (2003).

96. du Roure, O. *et al.* Force mapping in epithelial cell migration. *Proc. Natl. Acad. Sci. U. S. A.* **102,** 2390–2395 (2005).

97. van Hoorn, H. *et al.* The Nanoscale Architecture of Force-Bearing Focal Adhesions. *Nano Lett.* (2014). doi:10.1021/nl5008773

98. Li, Z. *et al.* Quantifying the traction force of a single cell by aligned silicon nanowire array. *Nano Lett.* **9,** 3575–3580 (2009).

99. Bucaro, M. A., Vasquez, Y., Hatton, B. D. & Aizenberg, J. Fine-tuning the degree of stem cell polarization and alignment on ordered arrays of high-aspect-ratio nanopillars. *ACS Nano* **6,** 6222–6230 (2012).

100. Hanson, L., Lin, Z. C., Xie, C., Cui, Y. & Cui, B. Characterization of the Cell–Nanopillar Interface by Transmission Electron Microscopy. *Nano Lett.* **12,** 5815–5820 (2012).

101. Hanson, L. *et al.* Vertical nanopillars for in situ probing of nuclear mechanics in adherent cells. *Nat. Nanotechnol.* **10,** 554–562 (2015).

102. Persson, H. *et al.* Fibroblasts cultured on nanowires exhibit low motility, impaired cell division, and DNA damage. *Small* **9,** 4006–4016 (2013).

103. Xu, A. M. *et al.* Quantification of nanowire penetration into living cells. *Nat. Commun.* **5,** 1–8 (2014).

104. Yi, X., Shi, X. & Gao, H. A universal law for cell uptake of one-dimensional nanomaterials. *Nano Lett.* **14,** 1049–1055 (2014).

105. Xie, X. *et al.* Mechanical Model of Vertical Nanowire Cell Penetration. *Nano Lett.* **13,** 6002–6008 (2013).

106. Shi, X., von dem Bussche, A., Hurt, R. H., Kane, A. B. & Gao, H. Cell entry of one-dimensional nanomaterials occurs by tip recognition and rotation. *Nat. Nanotechnol.* **6,** 714–9 (2011).

107. Robinson, J. T. *et al.* Vertical nanowire electrode arrays as a scalable platform for intracellular interfacing to neuronal circuits. *Nat. Nanotechnol.* **7,** 180–184 (2012).

108. Xie, C., Lin, Z., Hanson, L., Cui, Y. & Cui, B. Intracellular recording of action potentials by nanopillar electroporation. *Nat. Nanotechnol.* **7,** 185–90 (2012).

109. Han, S.-W. *et al.* High-efficiency DNA injection into a single human mesenchymal stem cell using a nanoneedle and atomic force microscopy. *Nanomedicine* **4,** 215–225 (2008).

110. Peer, E., Artzy-Schnirman, A., Gepstein, L. & Sivan, U. Hollow nanoneedle array and its utilization for repeated administration of biomolecules to the same cells. *ACS Nano* **6,** 4940–4946 (2012).

111. Jiang, Z., Qing, Q., Xie, P., Gao, R. & Lieber, C. M. Kinked p-n junction nanowire

probes for high spatial resolution sensing and intracellular recording. *Nano Lett.* **12,** 1711–6 (2012).

112. Berret, F. Local viscoelasticity of living cells measured by rotational magnetic spectroscopy. *Nat. Commun.* **7,** 1–18 (2016).

113. Fakhri, N. *et al.* High-resolution mapping of intracellular fluctuations using carbon nanotubes. *Science (80-.).* **344,** 1031–1035 (2014).

114. Giraldo, J. P. *et al.* Plant nanobionics approach to augment photosynthesis and biochemical sensing. *Nat. Mater.* 1–9 (2014).

115. Zimmerman, J. F. *et al.* Free-Standing Kinked Silicon Nanowires for Probing Inter- and Intracellular Force Dynamics. *Nano Lett.* **15,** 5492–5498 (2015).

116. Zimmerman, J. F., Murray, G. F. & Tian, B. Optical Determination of Silicon Nanowire Diameters for Intracellular Applications. *J. Phys. Chem. C* **119,** 29105–29115 (2015).

117. Beaux, M. F. *et al.* Fibronectin Bonding to Nanowires and Their Internalization by Epithelial Cells. *J. Biomed. Nanotechnol.* **2,** 23–28 (2006).

118. Kwon, N. H. *et al.* Nanowire-Based Delivery of Escherichia coli O157 Shiga Toxin 1 A Subunit into Human and Bovine Cells. *Nano Lett.* **7,** 2718–2723 (2007).

119. Zhang, W., Tong, L. & Yang, C. Cellular Binding and Internalization of Functionalized Silicon Nanowires. *Nano Lett.* **12,** 1002–1006 (2012).

120. Jung, Y., Tong, L., Tanaudommongkon, A., Cheng, J.-X. & Yang, C. In Vitro and In Vivo Nonlinear Optical Imaging of Silicon Nanowires. *Nano Lett.* **9,** 2440–2444 (2009).

121. Wierzbicki, R. *et al.* Mapping the complex morphology of cell interactions with nanowire substrates using FIB-SEM. *PLoS One* **8,** e53307 (2013).

122. Cacchioli, a *et al.* Cytocompatibility and Cellular Internalization Mechanisms of SiC/SiO 2 Nanowires. *Nano Lett.* **14,** 4368–4375 (2014).

123. Lakadamyali, M., Rust, M. J., Babcock, H. P. & Zhuang, X. Visualizing infection of individual influenza viruses. *Proc. Natl. Acad. Sci. U. S. A.* **100,** 9280–5 (2003).

124. Gratton, S. E. a *et al.* The effect of particle design on cellular internalization pathways. *Proc. Natl. Acad. Sci.* **105,** 11613–11618 (2008).

125. Lee, J.-H., Zhang, A., You, S. S. & Lieber, C. M. Spontaneous Internalization of Cell Penetrating Peptide-Modified Nanowires into Primary Neurons. *Nano Lett.* **16,** 1509–1513 (2016).

Chapter 2. Internalization and Single SiNW Dynamics•

2.1 Introduction

To date SiNW-cell interactions have been primarily studied from the perspective of substrate bound wires[1–5] (i.e. those wires still joined to an underlying material) using gravity, electroporation and/or adhesive forces to access the cell interior[6,7] or form invaginations[5]. While these configurations allow nanoscale devices to be connected directly to external macroscopic electronics, they lead to bulkier designs which can be detrimental for several reasons. First, larger devices can exacerbate the mismatch in material properties (i.e. Young's modulus, curvature, etc.) between typical inorganic semiconductors and biological samples, leading to poor device integration and increased irritation[8,9]. Second, the incorporation of macroscopic substrates negates many of the benefits of using nanoscale materials in the first place, such as surgery-free device distribution and point-like localized probing. Finally, many of these devices require extensive wiring extending outside of the body, which can be disruptive to existing biological architecture, and hinders the use of such devices at the single cell level. Therefore, a more desirable approach would be to use substrate independent devices capable of being dispersed in a drug-like manner and of being wholly internalized within a single cell. Such materials could act as precursors for future

• A portion of this work has been adapted with permission from Zimmerman J. F. et. al. Nano Lett. 15, 5492–5498 (2015). Copyright 2015 American Chemical Society.

'artificial bionanomachines'[10] or as therapeutic devices and probes that can operate independently at the sub-cellular level.

Prior to our study, previous work has shown that surface modified[11,12] SiNWs can be internalized at the single cell level in a substrate free manner and that such devices could be imaged in an in-vivo setting[13]. This makes SiNWs a promising candidate for use as an active drug-like material, however, to date little has been known about how these devices enter cells, especially in a time-dependent manner. Additionally, label free particles are particularly difficult to study, as labeling reagent can help elucidate the nano-bio interface, but can also be disruptive to the native device functionalization, leading to altered surface recognition and nanowire-cell interactions. Yet, such knowledge is critical in informing future device design, and in implementing cell specific targeting. To expand on this outlook, here we will discuss how label free SiNWs can be spontaneously internalized in cellular systems. An overview of this can be seen in **Figure 2.1**, where a cell is depicted initiating nanowire internalization. To study this process, first we will show that label free SiNWs can be internalized at the individual cell level. From here, we will demonstrate a new technique, Scatter Enhanced Phase Contrast (SEPC) microscopy, which allows for the simultaneous visualization of both SiNWs and cellular systems. Using this setup, we will track individual SiNW internalization in a dynamic manner, showing that wires undergo a 'burst like' active transport process. Collectively, this behavior suggests a endogenous internalization process, which will be discussed in further detail in later sections.

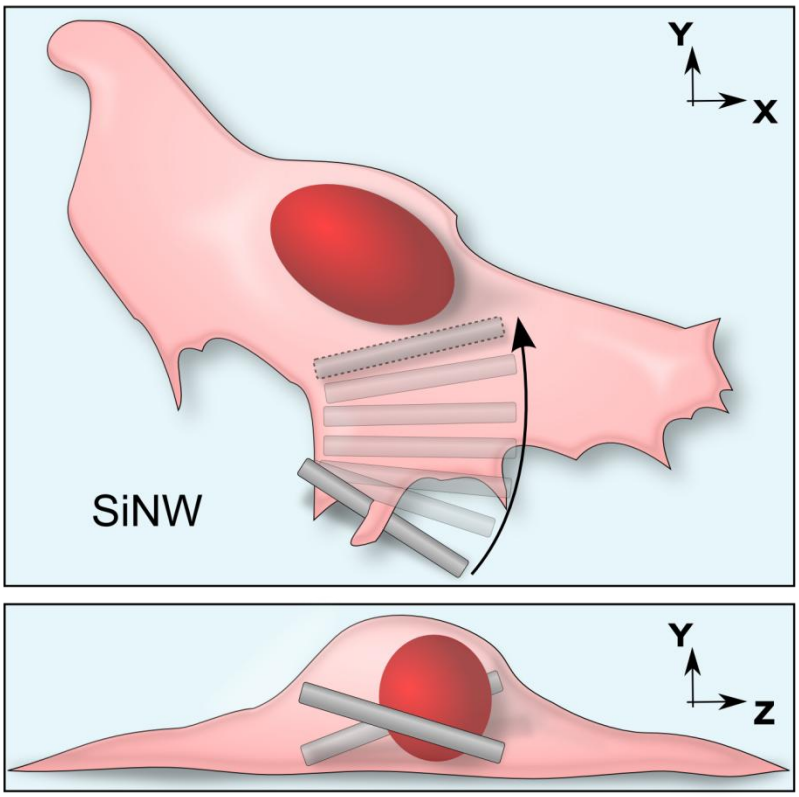

Figure 2.1 SiNW Internalization Schematic.
Illustration depicting internalization on the single nanowire length scale**.**

2.2 Results and Discussion

2.2.1 Confirming Nanowire Internalization

To study substrate free SiNW endocytosis, human umbilical vascular endothelial cells (HUVECs) and Human aortic smooth muscle cells (HASMCs) were selected as a model cell line. Serving as the inner lining of blood vessel walls, endothelial cells act as a filtration system between the blood stream and the rest of the body, helping regulate the uptake of drugs, and clearing apoptotic blood cells and other extracellular materials. As SiNWs can potentially be distributed in a drug like fashion, endothelial cells play a key role in mediating biointegration, with HUVECs in particular having been shown to recapitulate many of features found in native vascular endothelial cells[14]. HASMCs on

the other hand can undergo contraction, making them an ideal target for future force studies.

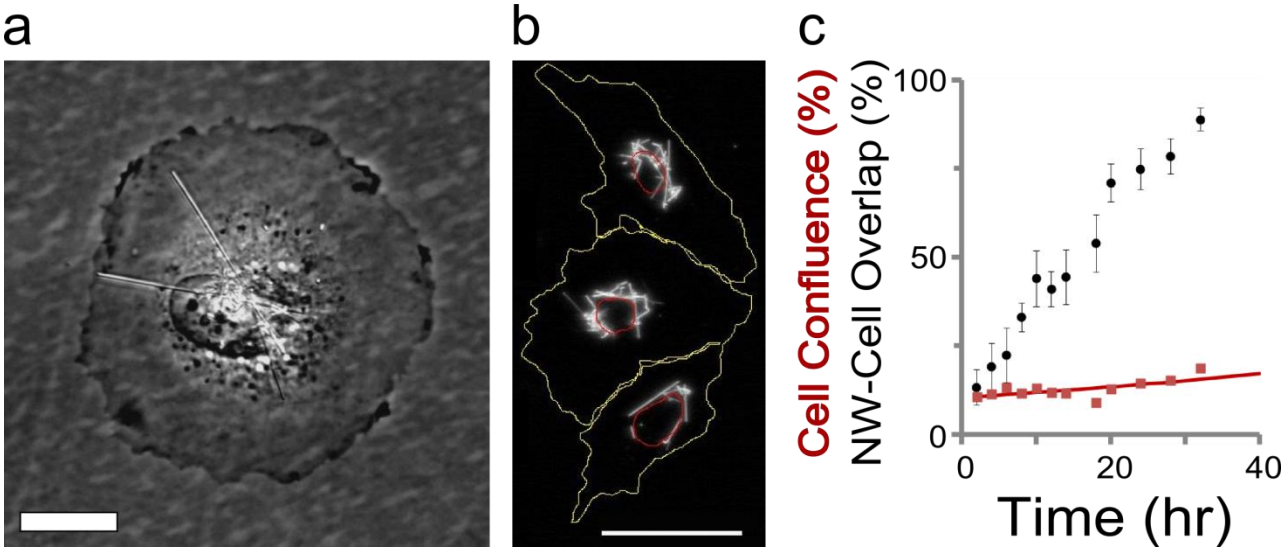

Figure 2.2 Initial SiNW Internalization Studies.
(**a**) Phase contrast micrograph of a HUVEC co-incubated with SiNWs, retaining it's nanowires after trypsinization (20 µm scale bar). (**b**) Darkfield micrograph of SiNWs clustering in the perinuclear region, but excluded from the nuclear envelope (yellow cell outline, red nucleus outline) (50 µm scale bar). (**c**) Ensemble rate of NW-cell overlap (black line) as compared to cell confluence (red line) indicating preferential NW-cell interactions. Adapted with permission from Zimmerman J. F. et. al. Nano Lett 2015. Copyright 2015 American Chemical Society.

When first co-incubated with cells, several initial observations suggested that SiNWs were being internalized. First, NWs were shown to preserve their colocalization with cells after removing the extra cellular matrix. To cleave extracellular adhesions, HUVECs were treated with EDTA/ trypsin and then templated onto a fresh NW free substrate. Under these conditions, NWs were shown to retain their initial colocalization (**Figure 2.2a**). If NW interactions were purely extracellular, such connects should be severed during trypsinization and no NWs would be expected to carry over to the new substrate. Additionally, SiNWs were observed to cluster in the perinuclear region (**Figure 2.2b**) but were excluded from the nucleus. This further suggested internalization, as extracellular nanowires would have no reason to be excluded, and

should be free to orient in any direction, while internalized SiNWs would be restricted due to the presence of the nuclear envelope. Finally, while not a direct reporter of internalization, colocalization studies showed that SiNWs exhibited a preferential overlap with cells (**Figure 2.2c**), with HUVECs and HASMCs presenting ~86% and ~56% NW colocalization, respectively, after 24 h. In contrast, in a non-coupled system would be expected to see no better colocalization than random (i.e., no better than cell confluence; depicted in red) (For an expanded look on this, see **Section 3.2.1** Ensemble Nanowire Dynamics). Taken together, these observations all suggested that HUVECs were capable of internalizing label free SiNWs.

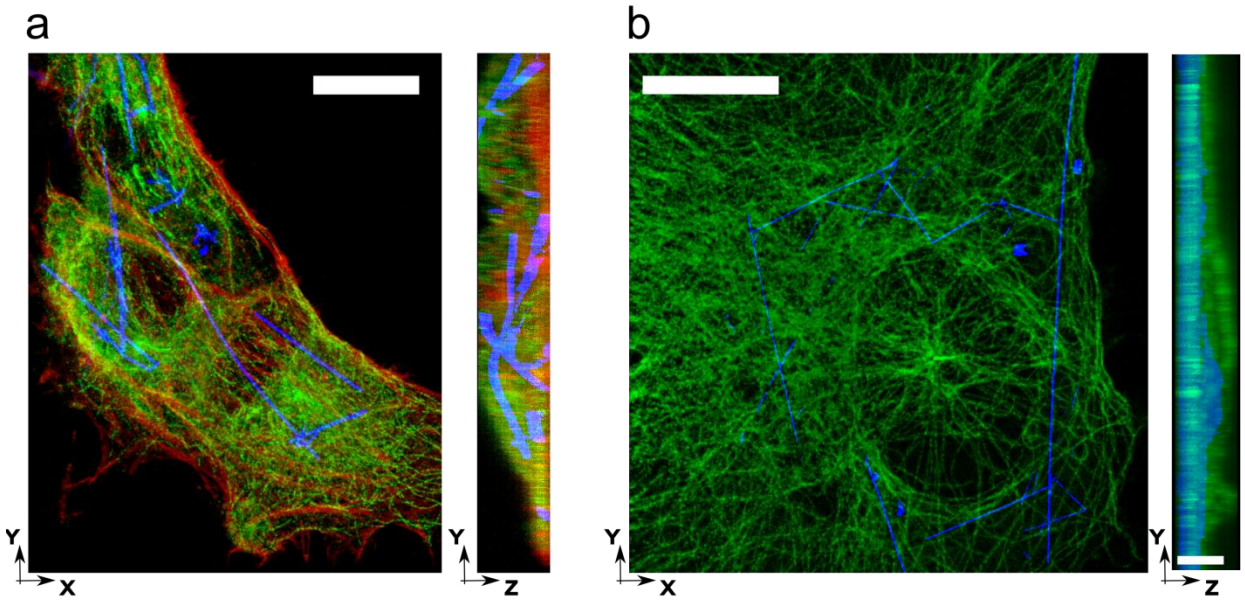

Figure 2.3 Confocal Confirmation of SiNW Internalization.
Confocal fluorescence micrographs of (**a**)HUVECs and (**b**)HASMCs (red-actin, green-tubulin) demonstrating SiNW internalization (blue-scattering). Maximum projection in the x-y plane (**a**&**b** left, both scale bars: 10 µm), and interpolated projection in the y-z plane (**a**&**b** right, height 3.5 µm and scale bar 3.5 µm respectively).

To confirm that label free SiNWs could be internalized by HUVECs both optical and electron microscopy techniques were used. First, confocal fluorescent microscopy was used to reconstruct three dimensional (3D) volumes containing HUVECs with

internalized SiNWs (**Figure 2.3a**). Cells were incubated with SiNWs for 24 h and the cytoskeleton was labeled using fluorescent markers TRITC-phalloidin (actin, red) and anti-α tubulin AlexaFluor 488 (microtubules, green), with the label free SiNWs visualized using optical scattering[15]. The resulting 3D volumes were seen to contain SiNWs, demonstrating that SiNWs could be spontaneously internalized by HUVECs. A similar result can be seen in human aortic smooth muscle cells (HASMCs), where SiNWs were also observed to be contained within the cell volume (**Figure 2.3b**).

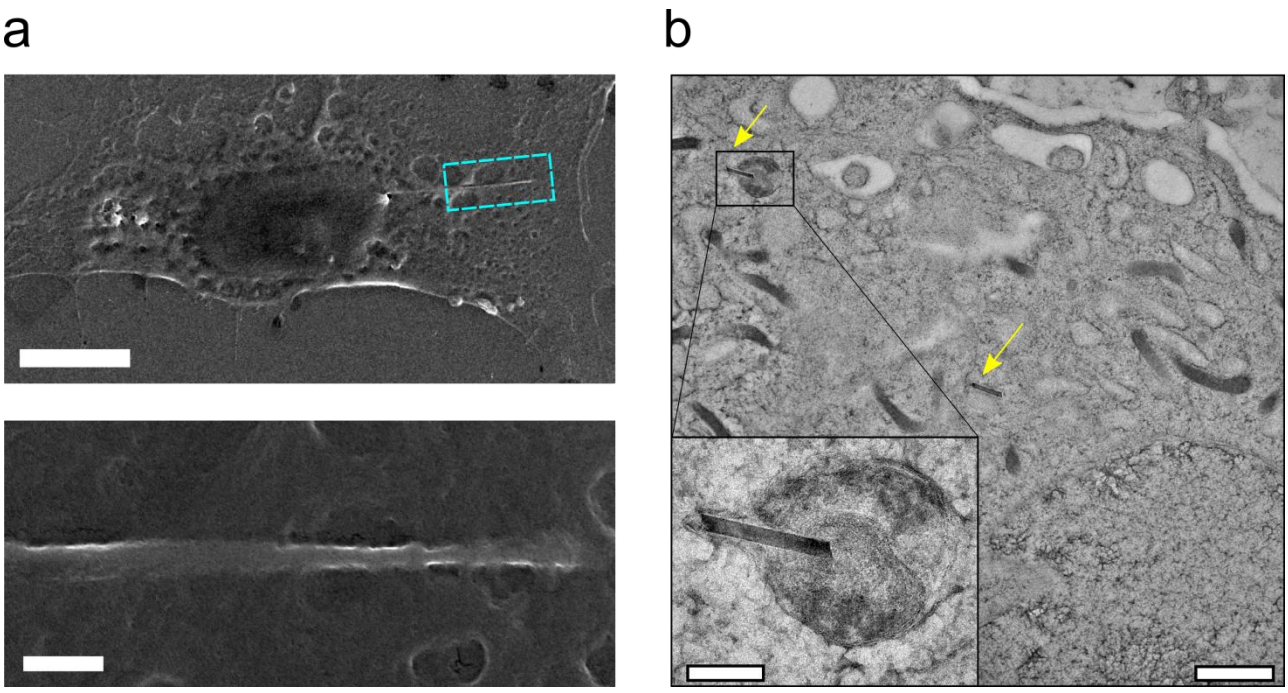

Figure 2.4 Electron Microscopy Data.
(**a**) SEM micrograph of a HUVEC containing a SiNW (Upper, 10 µm scale bar). Magnified highlighted region, indicating the SiNW is embedded under the cell's membrane (Lower, 300 nm scale bar). (**b**) Representative TEM micrograph of a HUVEC thin section (~250 nm thick), with higher magnification inset, illustrating that there is a distribution of internalized wires, both in vesicles and the cytosol (yellow arrows indicate NW locations) (1 µm scale bar, inset 200 nm scale bar).

This was examined in greater detail using electron microscopy (EM) techniques. First, HUVECs cultured with SiNWs were chemically fixed, critical point dried and then imaged using a scanning electron microscope (SEM). The resulting samples were observed to contain SiNWs beneath the cell membrane (**Figure 2.4a**). To show that the

cells were not simply sitting above of the wires, but that the SiNWs were actually contained within the cell body, cryopreserved thin cell sections were imaged using transmission electron microscopy (TEM). To prepare these samples, trypsinized cells were rapidly fixed using high pressure freezing and processed using freeze substitution techniques[16]. The resulting samples were then segmented using an ultramicrotome, yielding thin cell sections (~200-300 nm). TEM measurements revealed that internalized SiNWs showed a mixed distribution, with some wires floating free in the cytosol, while others were contained in small vesicles (**Figure 2.4b**). This confirmed that SiNWs could be spontaneously internalized by HUVECs without additional surface modification, independent of external mechanical forces or electroporation. Additionally, the formation of encapsulation vesicles suggested the SiNWs were entering the cells via an endogenous endocytosis process, rather than through mechanical abrasion (i.e. puncturing the cell membrane). It was also observed that multiple SiNWs could be contained within a single larger vesicle, reminiscent of a lysosome (**Figure 2.5**), causing SiNWs to become clustered in the perinuclear region. This suggested a dynamic process was occurring, where SiNWs could be shuttled to a specific cellular regions.

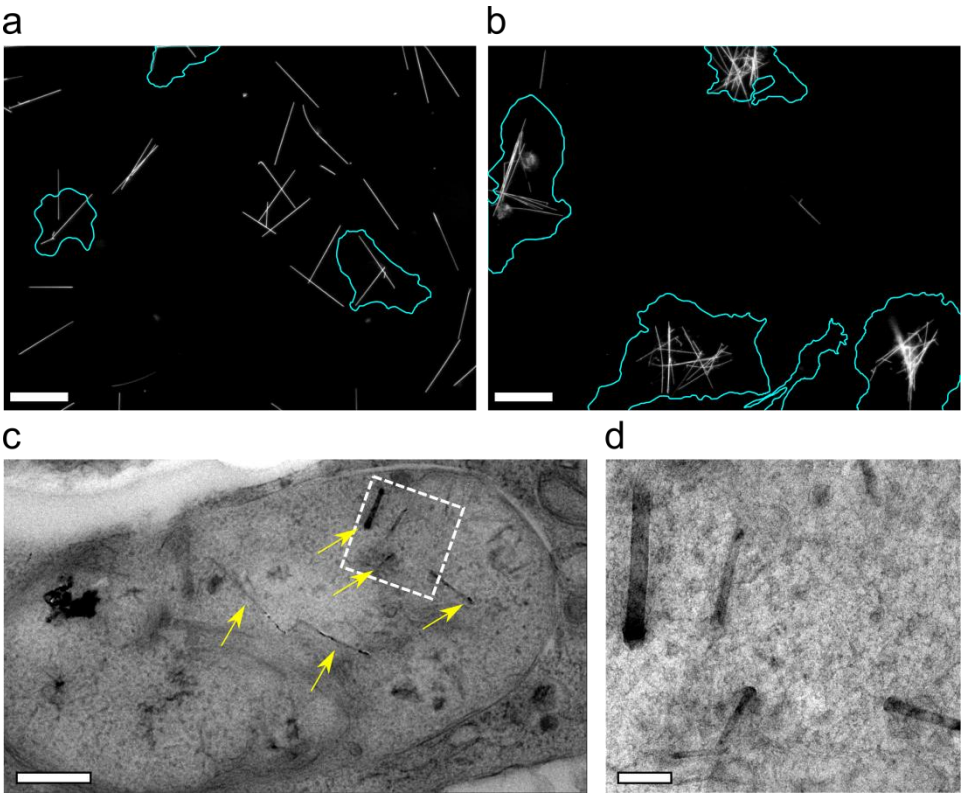

Figure 2.5 SiNW Clustering.
(**a&b**) Darkfield micrograph of SiNWs with HUVECs after 3h and 48h of incubation respectively, showing that cells cluster SiNWs over time. Highlighted teal regions indicate cell boarders as determined by phase contrast microscopy (50 µm scale bars).(**c**) Single large lysosomal type vesicle containing multiple SiNWs, with corresponding (**d**) higher magnification micrograph of the indicated region. Yellow arrows indicating the location of example SiNWs (Scale bars: 750 nm & 150 nm respectively).

While confocal techniques display clear SiNW and cellular features, they are prone to photo-bleaching and other undesirable consequences of laser/Si interactions such as the local SiNW-induced photothermal heating of cells[17]. Similarly, the extreme environments (i.e. high vacuum, large electron flux, etc) needed for electron microscopy measurements makes them poorly suited for use with living biological samples. As a result, EM studies can provide detailed structural information, however they only offer a static view of the internalization process. Therefore, to further characterize SiNW uptake, it would be ideal to study nanowire-cell interactions in a time-dependent fashion. However, to achieve this we first needed a method for consistently visualizing both

SiNWs and cellular systems at he same time. To bridge this gap, we developed a method of optical visualization we call scatter enhanced phase contrast (SEPC) microscopy, which enabled the simultaneous visualization of SiNWs and cellular systems.

2.2.2 Scatter Enhanced Phase Contrast Microscopy

To enable the extended noninvasive study of the nano-bio interface, we introduced a simple optical microscopy technique, Scatter Enhanced Phase Contrast (SEPC), which uses the one-shot acquisition of both SiNWs and cells (**Figure 2.6**), allowing for a clear visualization of the nano-bio interface. The main principle behind the operation of this method is the coordinated use of two different light sources. A bright field source, which can used for differential interference contrast (DIC) or phase contrast (PC) microscopy, allowing for high fidelity cellular imaging and a high angle ring emitter light source, which can used for darkfield (DF) microscopy, allowing for the visualization of SiNWs. Making use of both a transmitted and scattered light source, allows for the projection of a composite image which contains information from both systems, while maintaining little interference between the two signals. Using SEPC alleviates the need for manually alternating between DF and PC condensers, which would not only prove time consuming for researchers, but also allows for greatly expedited acquisition times, as no physical change is needed in the light path during imaging.

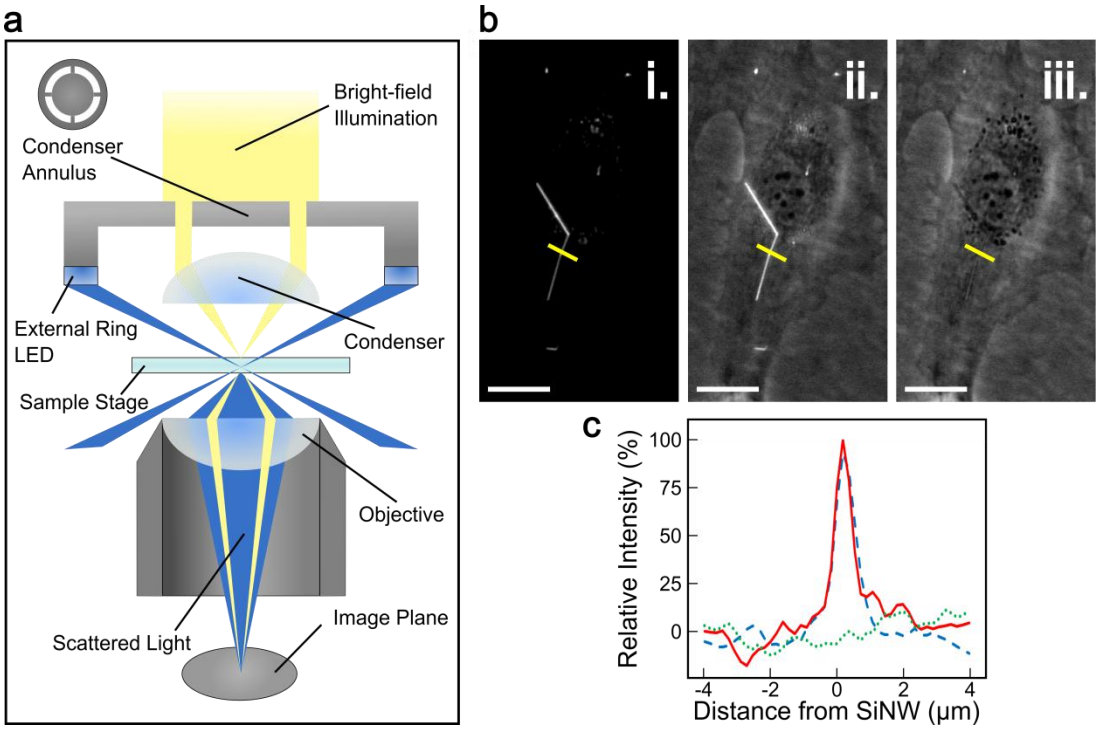

Figure 2.6 Scatter Enhanced Phase Contrast (SEPC) Imaging Modality.
(**a**) SEPC light path diagram. (**b, c**) Images and line plots taken over the same region in b (yellow line) (**c**), indicating the relative signal intensity of NWs under: dark-field (**b**, left; **c**, blue), SEPC (**b**, middle; **c**, green), and phase contrast (**b**, right; **c**, black). (10 μm scale bars). Adapted with permission from Zimmerman J. F. et. al. Nano Lett 2015. Copyright 2015 American Chemical Society.

To understand how SEPC allows for the simultaneous visualization of both cells and nanomaterials, we need to take a closer look at how light interacts with these materials. SiNWs are axially above the optical resolution limit, but are radially diffraction limited, meaning that they can be visualized using bright field techniques (*e.g.* PC) but that variation in the NW orientation can lead to large deviations in the signal-to-noise (S/N) ratio (6.8±7) to the point where some wires are unobservable (**Figure 2.7c.i**) in some cases. Due to this high standard deviation, the quantitative analysis of SiNWs can be challenging using purely bright field techniques. Additionally, when interacting with cellular systems, SiNWs can be difficult to distinguish from naturally occurring folds in cellular membranes under bright field, especially in highly polarized cells where the folds can maintain a straight edge for several microns. However, they also possess a

high refractive index, giving them a large mismatch with the refractive index of the aqueous media around them. As a result they scatter a large amount of light and appearing readily under DF techniques (For a more detailed look at SiNW light scattering, see **Section 5.2.2** Calculations of Optical Scattering using Lorentz-Mie Theory). Adherent cells on the other hand, have a low refractive index and are obscured using DF. To bridge this gap, an oblique angle ring emitter was employed (**Figure 2.6a**), using simultaneously transmitted DF and PC projections to create a single SEPC image. This allowed for the clear visualization of both SiNWs and cellular features at the same time (**Figure 2.6b & Figure 2.7c**).

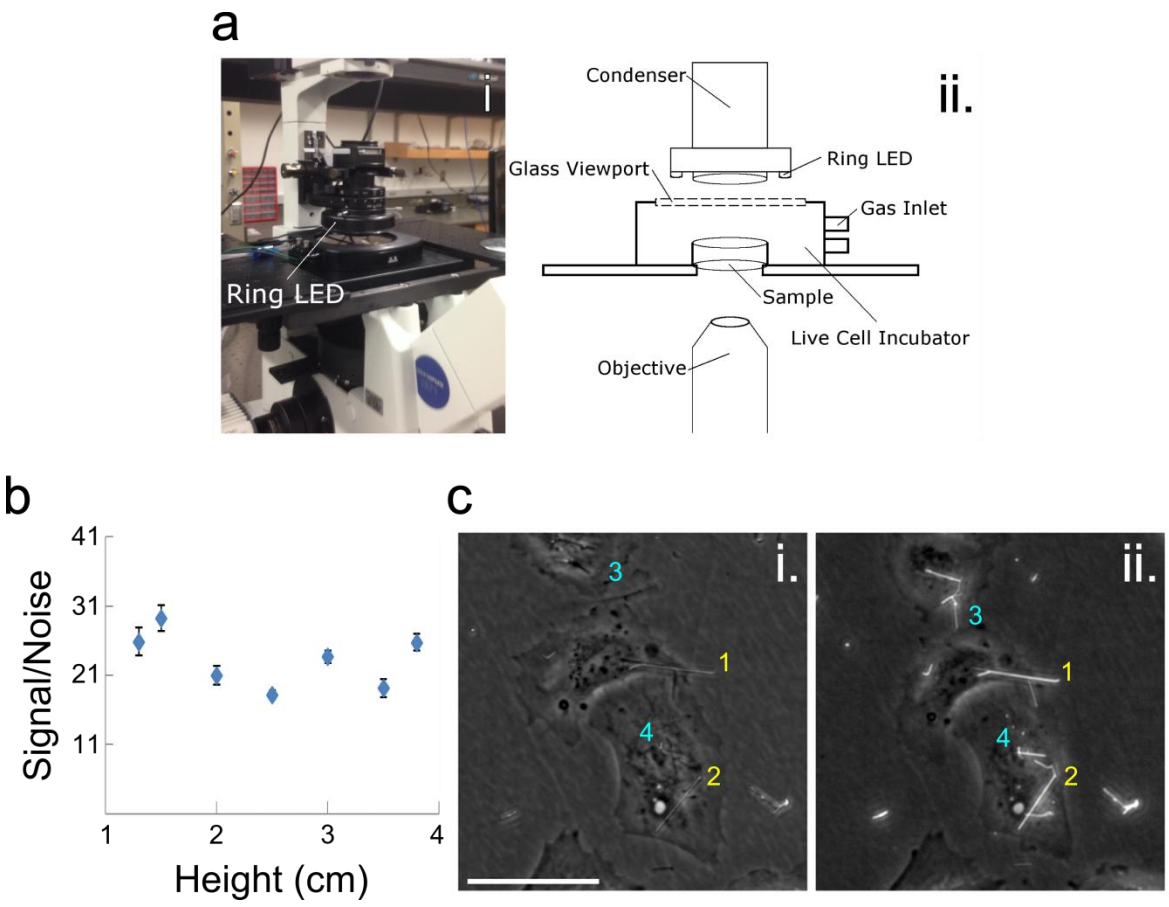

Figure 2.7 SEPC Experimental Setup.
(**a**) SEPC imaging station. A picture of the real setup (i) and the corresponding schematic illustration (ii) for live cell imaging, including illumination ring for SEPC. (**b**) Dark-field Signal to Noise Ratios for an Amscope LED-144-YK ring lamp as a function of height. Values obtained measures the light scatter intensities for 100 nm SiNWs at 15% of maximum power. (**c**) Comparison of PC (i) and SEPC (ii) images in live cell recording. Some wires are visible in both modes (1&2), however some can only be distinguished using SEPC (3&4). Using purely PC can be misleading and can lead to false quantification of nanomaterial interactions (50 µm scale bar). Adapted with permission from Zimmerman J. F. et. al. Nano Lett 2015. Copyright 2015 American Chemical Society.

To image cells using SEPC, an Olympus IX71 inverted microscope was used with LUCPlanFLNPh 20x and 40x objectives with a numerical aperture (NA) of 0.4 and 0.65 respectively. The relatively low NA cut down on background scattering, allowing for a clear DF image. For live cell imaging a INUB-ONICS-F1 Takai Hit stage top incubator was employed, maintaining physiological conditions (i.e. 95% humidity, 37 °C internal temperatures, 5% CO_2). To obtain simultaneous high angle transmitted DF, an

Amscope LED-144-YK ring lamp LED was fitted to the bright field condenser. Typical LED power was set to 15%-20% of maximum power. Images were recorded on a Hamamatsu ORCA-R2 C10600-10B digital CCD camera at 16bit depth with 0.3 µm x 0.3 µm pixel resolution.

The high angle ring illuminator provided an alternative method for obtaining transmitted dark field (DF) as compared to traditional DF condensers which have very small working distances. This large working distance permitted the use of liquid submerged samples and a stage top incubator. The DF S/N ratio was shown to be relatively height independent, with smaller angles initially providing lower background illumination (**Figure 2.7b**), but with the S/N ratio leveling off almost immediately at ~2 cm, still allowing relatively long working distances. In our experiments, typical working distances of approximately 3.6 cm were used to preserve Köhler illumination for the corresponding phase contrast modality. Under these working conditions, there was a measured ~14% destructive interference between the two imaging modes (*i.e. PC and DF*), as determined by measuring the absolute background intensities for PC and DF modes, and comparing the sum intensities to SEPC intensities for the same region.

	Signal/Noise	Standard Deviation
PC	6.8	7.0
SEPC	24.7	11.4

Table 2.1. SEPC Signal-to-noise Ratios
Experimentally determined signal to noise ratios for 100 nm SiNWs internalized in HUVECs. Values obtained at a 3.6 cm condenser height at 15% power for LED ring illuminator. Adapted with permission from Zimmerman J. F. et. al. Nano Lett 2015. Copyright 2015 American Chemical Society.

The S/N ratio of HUVECs internalized 100 nm SiNWs was determined for each imaging modality. To compare these values, both PC and SEPC micrographs were

collected under the same imaging settings (I.e. exposure, condenser height, focus, bright field light intensity, etc.) (n=17), with the addition of the ring LED for SEPC images. *NIH ImageJ* was used to measure the average background light intensity, as well as the signal intensity from 100nm SiNWs interacting with HUVECs. These two values were compared to produce the corresponding S/N ratio, which on average showed a 3.6 fold increase for SEPC compared to PC images. Additionally, a minimum 7.5 S/N ratio was observed for SEPC images, meaning that all NWs were discernible under these conditions, using DF as a reference to determine the total number of NWs present. The PC modality on the other hand, displayed a minimum S/N ratio of 1.0, which as previously stated, meant that not all SiNWs could be readily distinguished from cellular systems, limiting its use in quantitative experiments.

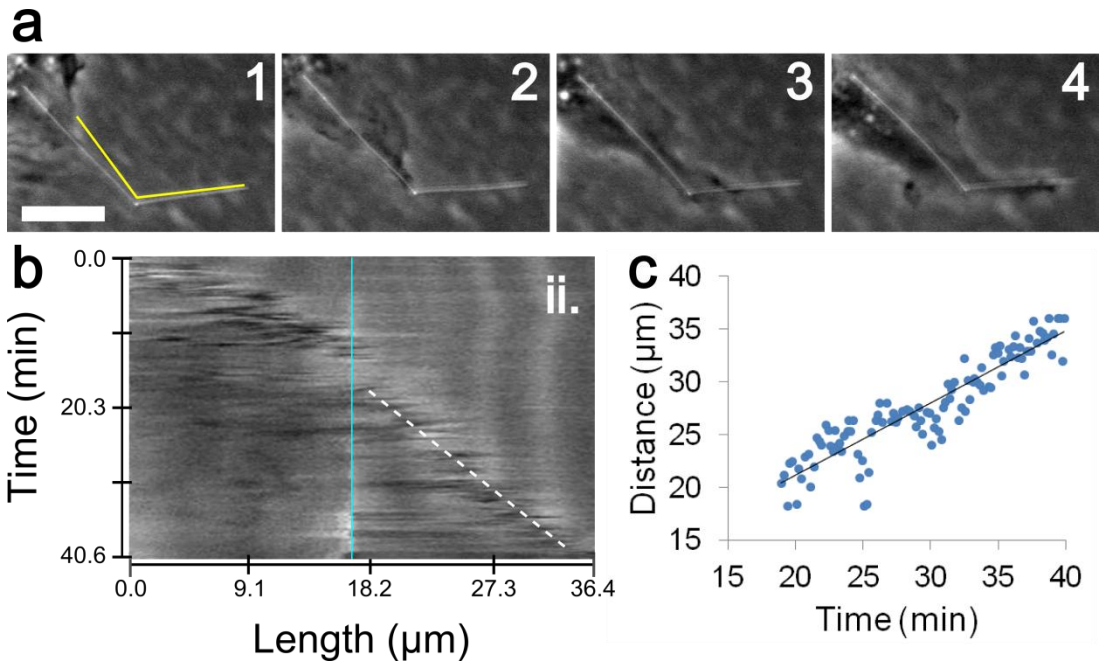

Figure 2.8 Long Nanowire Engulfment.
(**a**) Time-lapse SEPC micrograph of a membrane extending along a kSiNW (HUVEC, 10 min elapsed/frame), with associated kymograph (**b**) (dashed cyan line - kink location) taken from the indicated path (dashed yellow in d) (10 μm scale bar). (**c**) Membrane extension along the kSiNW extracted from the kymograph. The slope of the linear fit yields the rate of 11.34±0.05 nm/s (R^2=0.84). Adapted with permission from Zimmerman J. F. et. al. Nano Lett 2015. Copyright 2015 American Chemical Society.

The ability of SEPC to dynamically track both cells and nanomaterials in a label-free manner allows SiNW interactions to be linked to specific cellular processes. One example is the recording of HUVEC membrane extension along a single kinked SiNW (**Figure 2.8**, **Video S.1**). Using SEPC, a kymograph was obtained of the cell membrane. By mapping the leading edge position, a linear relationship was established showing that the wire is engulfed at an average rate of 11.34±0.05 nm/s (**Figure 2.8b**, white dashed line, and **Figure 2.8c**), after pausing at the kinked joint for ~9 min (yellow arrows). The observation that the leading edge of the cell membrane tightly follows the orientation of the kinked SiNW highlights the ability of the cell to recognize nanoscale topographies, a fact which will become important when examining the mechanism of internalization and one that will be discussed in more detail (See **Section 3.2.3** Cellular Uptake Morphology).

In addition to being able to track SiNW uptake, we note here that SEPC is not strictly limited to silicon devices, but can be readily adapted to work in conjunction with other nanomaterials. As a result, this technique has strong implications for other forms of biological nanoparticle tracking, such as carbon nanotubes and gold nanoparticle internalization studies. Also, this technique can be adapted to work with existing equipment, requiring only slight modification (i.e. the installation of an inexpensive, commercially available ring LED emitter), making it easily implemented using most conventional microscopy setups. Finally. this approach is also well suited for long term monitoring, requiring only low intensity light sources and no fluorescent tags, marking this method as being resistant to both photobleaching and photothermal effects[17]. To demonstrate this, we will show how this method can be used for prolonged (>1hr)

continues intracellular force studies using kinked SiNWs (See **Section 4.2.3**). Therefore, given the range of devices that can be monitored, the relative ease of implementation, and the extended time-scales, we believe that this technique offers substantial promise for researchers interested in exploring nano-bio interactions where both inorganic and biological components can be imaged simultaneously.

2.2.4 Single Nanowire Dynamics

SEPC allowed for the dynamic study of individual SiNWs during internalization[18]. For this study, SiNWs were sonicated into growth media and allowed to settle before being introduced to HUVECs. Internalization dynamics were then monitored using a custom tracking algorithm, returning the position of each SiNW tip as a function of time (See **Section 2.4.4**). Nanowire dynamics were approximated as being two-dimensional (2D), a reasonable assumption given the large aspect ratio of the nanowires, and the thin volume of the lamellipodium, where transport is initiated. Tracking the nanowire's tip positions allowed for a precise determination of both the SiNW's velocity and mode of transport. To correct for stage drift, stationary particles were simultaneously tracked and used to adjust the SiNW's relative path. Tracking individual SiNWs revealed an active transport process, where nanowires are shuttled to the perinuclear region within ~30 min of coming into contact with the internalizing cell (**Figure 2.9**)(See **Video S.2**).

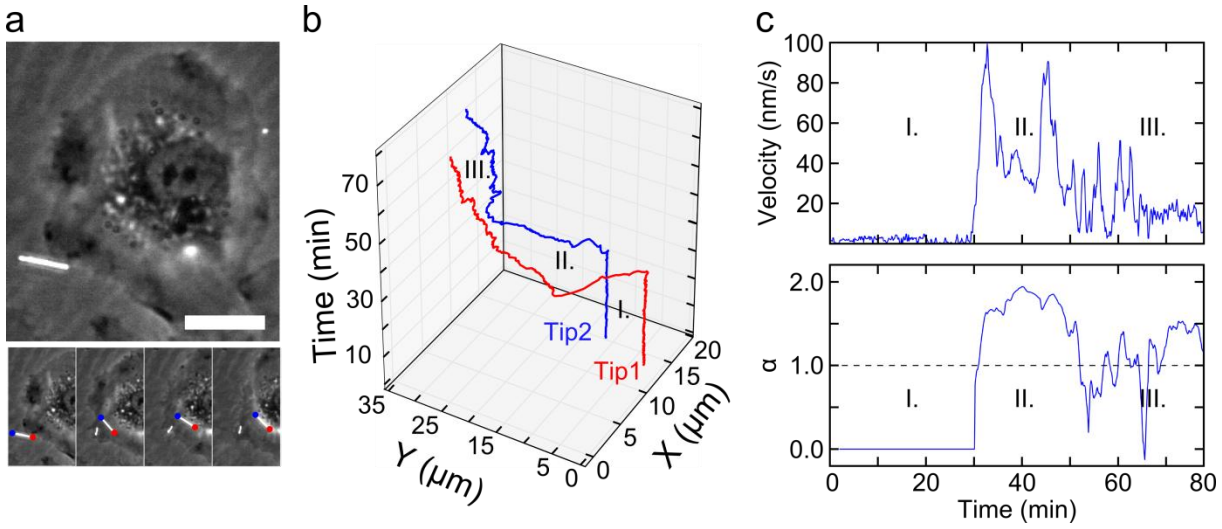

Figure 2.9 SiNW Active Transport.
(a) SEPC micrograph of a SiNW before (upper) and during (lower, t= ~7min/frame) internalization (15 μm scale bar), with tips 1&2 indicated by red and blue markers respectively. (b) Path of travel for both tips of the SiNW as a function of time. (c) Instantaneous velocity of the SiNW before (15 frame interval) (I), during (II) and after (III) active transport, with the corresponding rolling MSD 'diffusivity exponent', α, indicating an active transport process. Diffusivity exponent, α. was obtained over a rolling 50 frame period. All values given for tip 1 (red).

Briefly summarizing this process, initially settled SiNWs remained stationary on the underlying substrate (**Figure 2.9.c, Region I**). Upon contacting the SiNWs, cells were seen to 'grab' the nanowires (**Region II**), shuttling them from the lamellipodium to the perinuclear region (**Figure 2.9.b&c, Region II**). Here SiNWs displayed 'burst-like' velocities, where the nanowire would be transported in sudden large spurts of speed, punctuated by brief pauses (up to five minutes), during which the SiNWs would display Brownian or restricted diffusion, before continuing active transport. In the present study, NW transport begins almost immediately (**Region II**), displaying a relatively high mobility, with a maximum instantaneous velocity of 99.4 nm/s (velocities averaged over a 15 frame interval). In the majority of studies transport trajectories were linear, proceeding along an approximately straight track, however in some cases SiNWs could also undergo rotational rearrangements (**Figure 2.10**). After transport, SiNWs would

eventually settle around the nucleus (although excluded from the nuclear envelope), displaying only small diffusive movements (**Figure 2.9.b, Region III**).

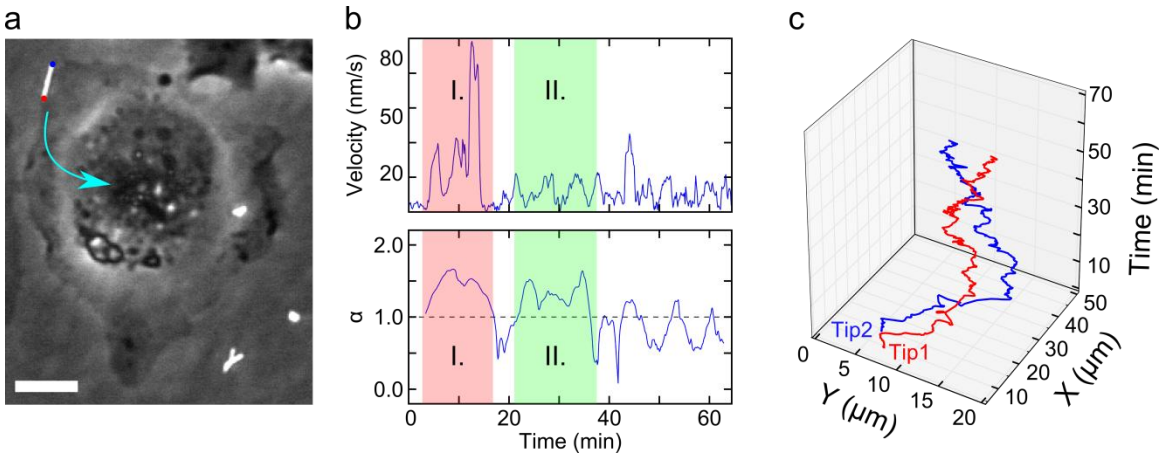

Figure 2.10 Cell Migration and Rotational Transport.
(**a**) SEPC micrograph of a SiNW being internalized by a HUVEC. (5 μm scale bar). SiNW tip 1 and 2 indicated by red and blue dots respectively, with the teal arrow indicating the general direction of SiNW travel. (**b**) Instantaneous velocity of the SiNW during active transport (15 frame average), with the corresponding rolling MSD 'diffusivity exponent', α, showing active transport process (Rolling 50 frame period). Highlighted regions indicate motor protein linked (I) active transport where SiNW tip velocity is greater than baseline, and cell motility (II) linked active transport where NW velocities are minor, but directional transport is given by the cell's general motility. All values given for tip 1 (red). (**c**) Path of travel for each tip of the SiNW as a function of time. SiNW rotation can be seen in where the paths cross over one another.

To distinguish between different modes of SiNW transport, a rolling frame mean squared displacement (MSD) metric was used, where the MSD is the average distance that a particle travels as a function of lag time, given by:

$$MSD = < \Delta r^2(\tau) > = q\tau^{\alpha} \qquad \textbf{2.1}$$

where Δr, τ, q, and α are the NW displacement, lag time, diffusion coefficient and the "diffusive exponent" respectively[19]. The diffusive exponent, α, can be used as a metric of transport properties, distinguishing between Brownian diffusion (α=1), restricted diffusion (α<1), and active transport (α>1) processes. Values for α were obtained by fitting the log-log plot of the MSD with a linear regression over a rolling 30 frame interval, with the slope yielding the relative diffusivity (For more detailed description see

Section 2.4.4). Using the MSD of the SiNW, different modes of cellular transport can be assessed, providing some insight into the underlying mechanism.

The present case strongly suggests that SiNWs are being treated as cargo by the cell and are being actively shuttled by cellular machinery. First, this is suggested by the relatively high velocities and active transport (α= 1.94) (**Figure 2.9.b, Region II**), distinguishing it from other modes of active cellular transport, for instance motion coupled to cell motility (**Figure 2.10.b, Region II**) which also displayed directional motion (α=1.6) but had relatively low velocities (~20nm/s). Second, the 'burst like' transport displayed here is reminiscent of other motor protein powered intracellular transport[20]. Finally, both the linear trajectories and previously observed vesicle formation are phenotypical of intracellular cargo transport.

2.2.5 Serum Free SiNWs

So far we have discussed SiNW internalization in the context of serum proteins. However, during internalization a process called opsonization can occur, where non-specific serum proteins can adsorb to the nanomaterial's surface, priming it for internalization[21–23]. In the case of SiNWs, proteins were observed to be able to bind non-specifically to SiNW surfaces (see **Section 3.2.7**), suggesting that this could be a possibility. Single nanowire transport studies however can also be used to examine the role of serum on SiNW internalization. Therefore, to see if opsonization effected SiNW internalization, we also tracked single SiNW internalization in the absence of serum proteins (**Figure 2.11**). To accomplish this, SiNWs and cells were co-incubated in a similar fashion as previous experiments, but without the addition of fetal bovine serum

(FBS) to the culture media. As the initial internalization of nanowires can happen within the first hour of co-culture, cells were not adversely effected by the lack of serum.

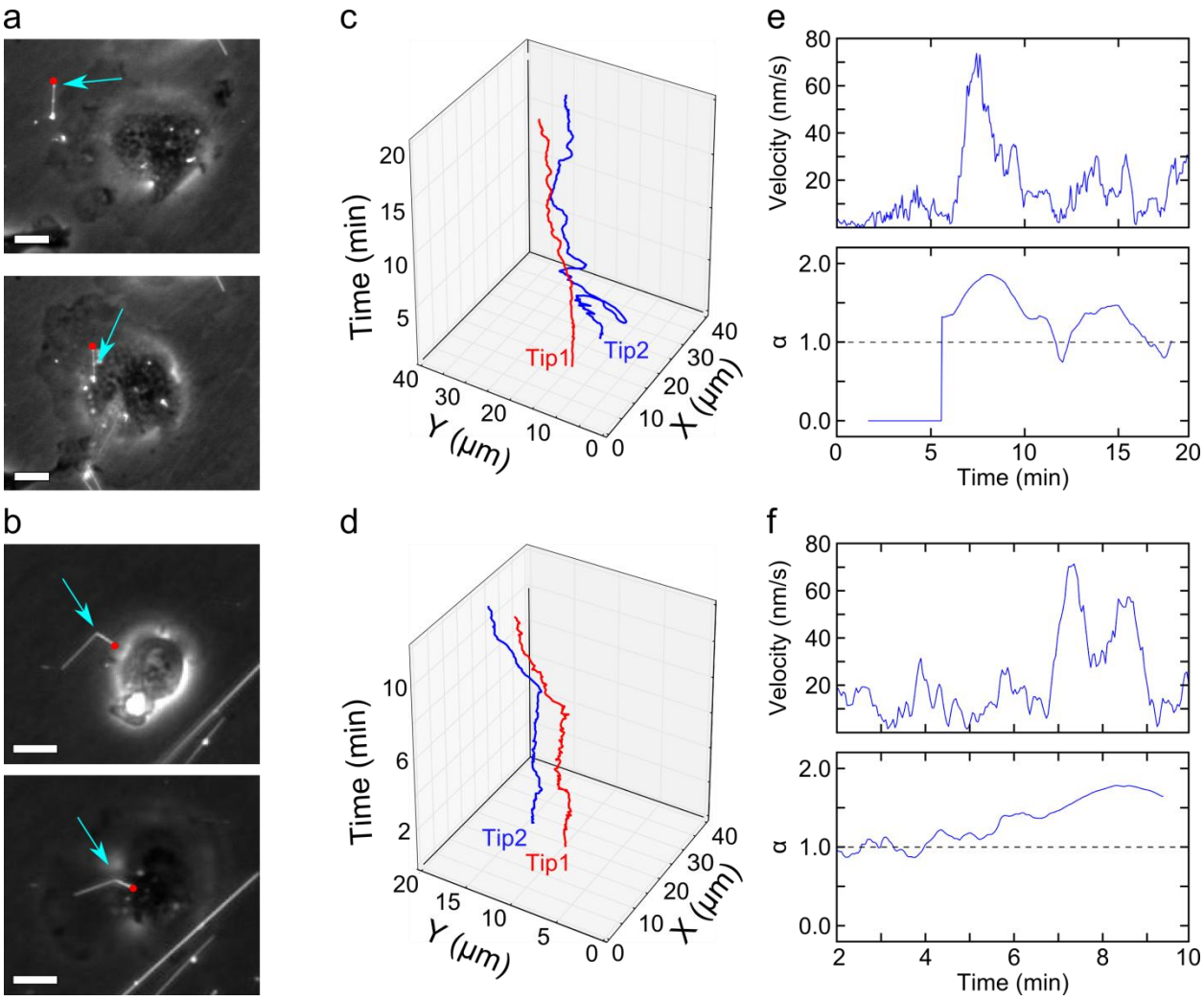

Figure 2.11 Serum Free SiNW Internalization.
(**a&b**) SEPC micrograph of a straight (**a**) and kinked (**b**) SiNW, before (upper) and after (lower) being internalized by a HUVEC in a serum free solution (10 μm scale bars). Teal arrow indicating the location of the tracked wire. Tip 1 indicated by red highlight (**c&d**) Path of travel of the SiNWs as a function of time for the straight and kinked SiNWs respectively. (**e&f**) Instantaneous velocity of the SiNW's tip during active transport (15 frame average), with the corresponding rolling MSD 'diffusivity exponent', α, showing active transport process (Rolling 55 frame period). (All values given for the highlighted red tip).

In the absence of serum proteins, nanowires internalization was seen to consistent with previous experiments, suggesting that opsonization does not play a major role in SiNW uptake. While internalization did appear to take less time in the case of the kinked SiNW, taking ~4 minutes rather than the ~20 min, it's likely that this is the

result of reduce cellular distance, as the SiNW in the serum free case starts closer to the perinuclear region. This is further suggested by examining the serum free SiNW's transport velocities, which were comparable to those previously observed, with kinked and straight wires reaching a maximum velocity of ~70 and ~74 nm/s respectively. Additionally, examining the diffusive exponent, α, we can see that serum free wires undergo an active transport process (Kinked: α=1.78, straight: α=1.86), confirming that the HUVECs were able to internalize these wires, even in the absence of serum proteins. As a whole, this suggests that the dynamics and process of SiNW internalization is not greatly impacted by the adsorption of serum proteins.

2.3 Conclusions

In this section we have shown that SiNWs can be internalized in a label free manner, developing a new microscopy method, SEPC, for visualizing these systems in a dynamic manner. Using single nanowire tracking, we have shown that SiNWs undergo an active 'burst like' transport process, suggesting an endogenous mechanism of nanowire internalization. To examine this processes in more depth, we will turn to ensemble studies, probing the precise mechanism of nanowire internalization, however before moving on we note that the current work raises several intriguing possibilities.

First, we believe that SEPC is a generalizable method which can be used in conjunction with other nanoscale devices to help elucidate how nanomaterials interact with cells in a dynamic manner. For instance, one can imagine using SEPC to study gold and quantum dot nanoparticle uptake, tracking both the particle and cell's position simultaneously, allowing improved sampling rates compared to other. As researchers

begin to push into this field, we feel that SEPC will serve as a simple to implement platform for expanded device characterization. One example of this we will explore later, is using SiNWs in conjunction with SEPC as kinked probes for studying inter and intracellular forces. By using a low intensity light source and avoiding fluorescent markers, SEPC is able to offer a method that is resistant to both photobleaching and photothermal effects[17], making it appropriate for long term continuous force studies. Overall, this suggests that SEPC can serve as useful technique for study the bio-nano interface far into the future.

Second, we believe that this work is of interest as it offers some insight into the rising debate over the role of endogenous and adhesive forces in granting nanowire's access to intracellular regions. Namely, in the past it had been observed that substrate bound wires were able to penetrate cell membranes[4,24–27], while other reports have shown that membrane invaginations can occur[3,5]. As a result, there is a growing debate over the role of gravity, endogenous and/or adhesive forces in creating these nanowire-cell interfaces[27]. In this section we have removed the SiNWs from the substrate, mitigating gravity and adhesive forces, however we have shown that label free SiNWs are still able to be internalized through an active transport process. This suggests that endogenous endocytosis mechanism play a more important role in mediating the cell-nanowire interface than previously reported. To examine this in more detail, in the next section we will discuss ensemble internalization measurements, and methods for study the specific route of endocytosis.

2.4 Experimental Details

2.4.1 Nanowire Growth

SiNWs were grown using the vapor-liquid-solid mechanism in a homebuilt chemical vapor deposition system. Silicon growth substrates were first rinsed with acetone and isopropyl alcohol (IPA), and then dried using N_2 gas. Substrates were then oxygen plasma cleaned (Plasma Etch PS-100LF) for 10 minutes at 100 watts, and coated in 1:3 dilute poly-L-lysine for 15 minutes, and then rinsed with deionized (DI) water. For SiNW growth, gold nanoparticles between 20-250 nm (Ted Pella Inc.) were allowed to settle for 15 minutes and then rinsed once more with DI water before being then using N_2 gas. SiNW growth conditions were as follows: 480 ^{o}C, 40 torr, 60 sccm hydrogen carrier gas, and 2 sccm silane. To prepare samples for use with cells, SiNWs were first rinsed with hydrofluoric acid (HF, Sigma Aldrich)(9.8%) for 10-30 second, before being washed in DI water. To sterilize the SiNWs, they were then transferred to a 70% ethanol solution, and kept under an ultraviolet lamp for ~30 minutes. After this samples were then transferred to the appropriate cell media and sonicated for 7 minutes to suspend the SiNWs into solution. Media solutions were then transferred to the appropriate container and SiNWs were allowed to settle before the media was aspirated off, and cell samples were added to the culture.

2.4.2 Confocal Fluorescent Microscopy

Cells were cultured until approximately 40-50% confluent. Prior to staining, cells were incubated with SiNW for 24 h and fixed with 4% paraformaldehyde in PBS for 20 min at room temperature. The cells were then stained with TRITC-phalloidin (Millipore, FAK100, excitation laser 532 nm) and anti-α tubulin Alexa Fluor 488 (322588, Excitation

laser 488 nm) following the manufactures' protocol. A leica SP5 confocal microscope was used with an oil immersion objective (Leica 63x). SiNW scattering was monitored in a separate channel, using an 458 nm excitation laser, with scattered "emission" light detected at the same wavelength, between 454-468 nm. At this wavelength, the scattering intensity from SiNWs was much greater than the underlying cells, and wires were readily distinguished using simple image intensity thresholding in NIH ImageJ.

2.4.3 Scanning Electron Microscopy Sample Preparation.

SiNWs were sonicated into M200 growth media and transferred to a Petri dish containing an glass cover slip which had previously been sterilized using ethanol (30 s wash in 70% EtOH). SiNWs were allowed ~16 h to settle, before the media was removed and trypsinized HUVECs were introduced. After ~18 h of incubation, samples were fixed using 4% paraformaldehyde in a phosphate buffered saline (PBS) solution. Samples were then washed twice using fresh PBS and dehydrated using subsequent ethanol substitution steps (20%, 40%, 60%, 80%,90%,95%,100% x2, 15 min). Samples were then dried using a CO_2 critical point dryer (Leica EM CPD300 Critical Point Dryer), and a 6 nm Pt/Pd layer was deposited onto the fixed cells using a sputter coater (Ted Pella). The glass substrate was then mounted using conductive carbon tabs and imaged using a FEI Nova NanoSEM 230. For transmission electron microscopy studies, samples were prepared and processed as previously reported[18].

2.4.4 Single Nanowire Transport

Individual SiNWs were tracked using Scattered Enhanced Phase Contrast (SEPC). imaging. To prepare samples, SiNWs were first rinsed with hydrofluoric acid (HF, Sigma

Aldrich)(9.8%) for 10-30 s, before being washed in DI water. To sterilize the SiNWs, they were then transferred to a 70% ethanol solution, and kept under an ultraviolet lamp for ~30 min. After the SiNW substrate was then transferred to the appropriate cell media and sonicated for 7 min to suspend the SiNWs into solution. The media containing the SiNWs was the transferred to a glass-bottom petri dish, and allowed to settle for ~16 h. During this period, media was stored in a cell incubator at 37 °C and 5% CO_2. Next, the media was then aspirated but before the samples could fully dry, cells were seeded onto the petri dish. Cells were then given ~20 min to attach to the petri dish before being transferred to a stage top incubator (INUB-ONICS-F1 Takai Hit) which maintained physiological conditions (i.e. 95% humidity, 37 °C internal temperatures, 5% CO2) during sample imaging. Internalization was then monitored using SEPC, where images were recorded on a Hamamatsu ORCA-R2 C10600-10B digital CCD camera at 16bit depth with pixel resolutions between 0.3 µm x 0.3 µm to 0.1 µm x 0.1 µm, depending on the objective used.

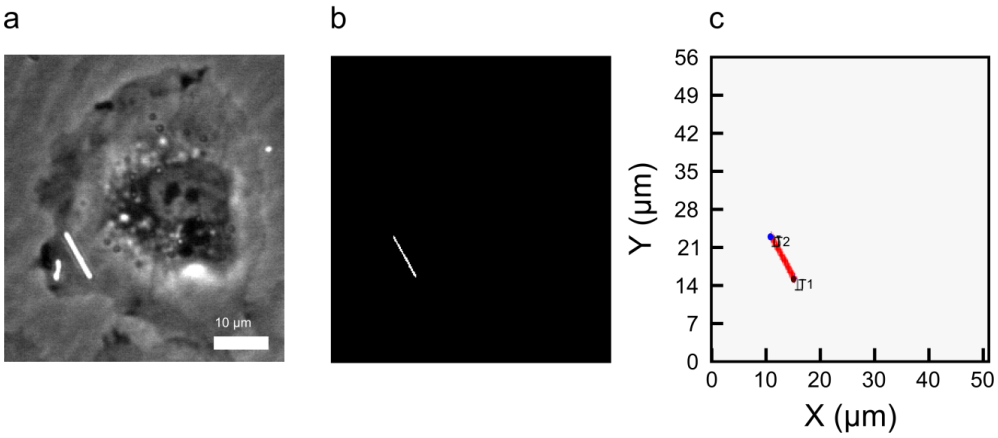

Figure 2.12 SiNW Tracking Algorithm.
(**a**) Example SEPC micrograph of a SiNW mid internalization. (**b**) An intensity threshold filter is applied to the SEPC micrograph, and turned into a binary image containing only the SiNW of interest. SiNW coordinates are extracted using NIH imageJ, and (**c**) fit using a linear regression in python to return internalized tip 1 (IT1, maroon) and internalized tip 2 (IT2, blue) positions.

To resolve the SiNW's position, SEPC images were first thresholded using NIH ImageJ, yielding binary images of just the SiNW (**Figure 2.12**). The SiNW's profile was approximated as linear and was fit on a per frame basis using a linear least squares regression in python, returning the position of each nanowire tip. For SiNW profiles with slopes greater than 45°, the profiles were rotated 90° to preserve them as a function, before fitting. The resulting tip positions were then rotated back into the original coordinate system. All SiNW trajectories were corrected for stage drift by also recording the "motion" of stationary particles external to the SiNW-Cell system (**Figure 2.13**), which was fit using a similar process. Instantaneous velocities were determined on a rolling frame basis, by averaging the distance travelled by particles over a 15 frame interval, to smooth sample noise. Mean squared displacements (MSD) were determined by calculating the distance that an individual NW was displaced after a given lag time, τ , averaged for an entire trajectory. In this case trajectories were segmented into rolling 30 frame intervals, centered on the reported time point. Values for α were obtained by fitting the log-log plot of the MSD with a linear regression (**Figure 2.14**), with the slope yielding the relative diffusivity exponent α. Slopes with negative values of the log-log plot were observed for the stationary case, and were approximated as being zero.

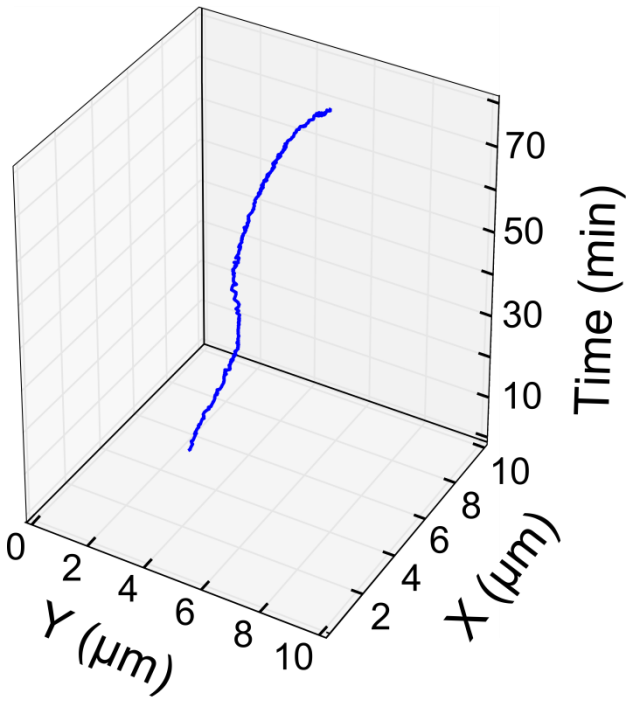

Figure 2.13 Stage Drift Correction.
Example path of a 'stationary particle', indicating the amount of stage drift for a SiNW tracking experiment. Relative movement was subtracted to accommodate for drift of the stage.

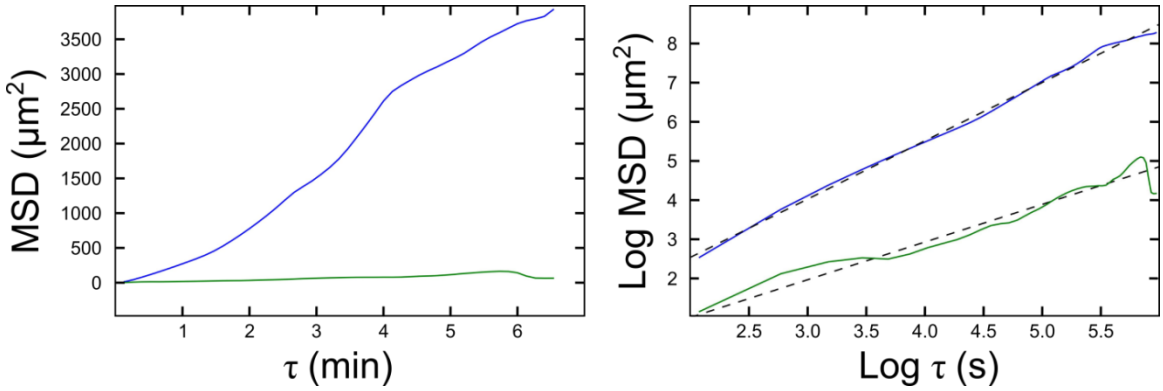

Figure 2.14 Example MSD Calculation.
The MSD of a SiNW that is being internalized at 13.5 min (blue) and 60 min (green) respectively, with corresponding log-log plot used to calculate the diffusivity exponent, α. Linear fits given as dashed line (Slopes: 1.49 & 0.96 respectively).

2.5 References

1. Kim, W., Ng, J. K., Kunitake, M. E., Conklin, B. R. & Yang, P. Interfacing silicon nanowires with mammalian cells. *J. Am. Chem. Soc.* **129,** 7228–9 (2007).

2. Xu, A. M. *et al.* Quantification of nanowire penetration into living cells. *Nat. Commun.* **5,** 1–8 (2014).

3. Hanson, L. *et al.* Vertical nanopillars for in situ probing of nuclear mechanics in adherent cells. *Nat. Nanotechnol.* **10,** 554–562 (2015).

4. Wierzbicki, R. *et al.* Mapping the complex morphology of cell interactions with nanowire substrates using FIB-SEM. *PLoS One* **8,** e53307 (2013).

5. Hanson, L., Lin, Z. C., Xie, C., Cui, Y. & Cui, B. Characterization of the Cell–Nanopillar Interface by Transmission Electron Microscopy. *Nano Lett.* **12,** 5815–5820 (2012).

6. Shalek, A. K. *et al.* Vertical silicon nanowires as a universal platform for delivering biomolecules into living cells. *Proc. Natl. Acad. Sci.* **107,** 1870–1875 (2010).

7. Han, S.-W. *et al.* High-efficiency DNA injection into a single human mesenchymal stem cell using a nanoneedle and atomic force microscopy. *Nanomedicine* **4,** 215–225 (2008).

8. Kim, D.-H. *et al.* Materials and noncoplanar mesh designs for integrated circuits with linear elastic responses to extreme mechanical deformations. *Proc. Natl. Acad. Sci.* **105,** 18675–18680 (2008).

9. Kim, D.-H. *et al.* Stretchable and Foldable Silicon Integrated Circuits. *Science* **320,** 507–511 (2008).

10. Ozin, G. A., Manners, I., Fournier-Bidoz, S. & Arsenault, A. Dream Nanomachines. *Adv. Mater.* **17,** 3011–3018 (2005).

11. Zhang, W., Tong, L. & Yang, C. Cellular Binding and Internalization of Functionalized Silicon Nanowires. *Nano Lett.* **12,** 1002–1006 (2012).

12. Lee, J.-H., Zhang, A., You, S. S. & Lieber, C. M. Spontaneous Internalization of Cell Penetrating Peptide-Modified Nanowires into Primary Neurons. *Nano Lett.* **16,** 1509–1513 (2016).

13. Jung, Y., Tong, L., Tanaudommongkon, A., Cheng, J.-X. & Yang, C. In Vitro and In Vivo Nonlinear Optical Imaging of Silicon Nanowires. *Nano Lett.* **9,** 2440–2444 (2009).

14. Park, H.-J. *et al.* Human umbilical vein endothelial cells and human dermal microvascular endothelial cells offer new insights into the relationship between lipid metabolism and angiogenesis. *Stem Cell Rev.* **2,** 93–102 (2006).

15. Zimmerman, J. F., Murray, G. F. & Tian, B. Optical Determination of Silicon Nanowire Diameters for Intracellular Applications. *J. Phys. Chem. C* **119,** 29105–29115 (2015).

16. Austin II, J. R. in *Arabidopsis Protocols* (eds. Sanchez-Serrano, J. J. & Salinas, J.) **1062,** 473–486 (Humana Press, 2014).

17. Roder, P. B., Pauzauskie, P. J. & Davis, E. J. Nanowire heating by optical electromagnetic irradiation. *Langmuir* **28,** 16177–16185 (2012).

18. Zimmerman, J. F. *et al.* Free-Standing Kinked Silicon Nanowires for Probing Inter- and Intracellular Force Dynamics. *Nano Lett.* **15,** 5492–5498 (2015).

19. Nelson, S. R., Ali, M. Y., Trybus, K. M. & Warshaw, D. M. Random Walk of Processive , Quantum Dot-Labeled Myosin Va Molecules within the Actin Cortex of COS-7 Cells. *Biophysj* **97,** 509–518 (2009).

20. Wang, B., Kuo, J. & Granick, S. Bursts of Active Transport in Living Cells. *Phys. Rev. Lett.* **111,** 208102 (2013).

21. Wu, Y., Tibrewal, N. & Birge, R. B. Phosphatidylserine recognition by phagocytes: a view to a kill. *Trends Cell Biol.* **16,** 189–197 (2006).

22. Gottstein, C., Wu, G., Wong, B. & Zasadzinski, J. Precise Quantification of Nanoparticle Internalization. *ACS Nano* 4933–4945 (2013). at <http://pubs.acs.org/doi/abs/10.1021/nn400243d>

23. Mortensen, N. P. *et al.* Dynamic development of the protein corona on silica nanoparticles: composition and role in toxicity. *Nanoscale* **5,** 6372–80 (2013).

24. Vandersarl, J. J., Xu, A. M. & Melosh, N. A. Nanostraws for direct fluidic intracellular access. *Nano Lett.* **12,** 3881–3886 (2012).

25. Duan, X., Gao, R., Xie, P. & Cohen-Karni, T. Intracellular recordings of action potentials by an extracellular nanoscale field-effect transistor. *Nat. …* **7,** 174–179 (2011).

26. Duan, X. *et al.* Intracellular recordings of action potentials by an extracellular nanoscale field-effect transistor. *Nat. Nanotechnol.* **7,** 174–9 (2012).

27. Prinz, C. N. Interactions between semiconductor nanowires and living cells. *J. Phys. Condens. Matter* **27,** 233103 (2015).

Chapter 3. SiNW Mechanistic Studies

3.1 Introduction

Our results in the previous section suggested that rather than through exogenous manipulation, Silicon Nanowires (SiNWs) are internalized primarily through an endogenous endocytosis pathway. While the internalization of the low aspect ratio nanoparticles has been well studied, the dynamics of cellular entrance and intracellular behavior of nanowires with large aspect ratio has remained elusive. In smaller silica spheres (<200 nm), which can have similar surface properties, nanoparticles are primarily internalized via a clathrin mediated mechanism of endocytosis[1–4], Therefore, as SiNWs can have smaller diameters it's possible that they may share a similar fate, however their large aspect ratio also makes it possible that they are internalized through another pathway, as clathrin typically internalizes smaller biological targets. Additionally, it has been shown that size, shape and surface functionalization can all play an important role in nanomaterial uptake[3,5–11]. As a result, a more careful examination is needed for high-aspect ratio nanoconstructs, where such a study could be important for both designing new nanowire based biomedical devices, and in determining the environmental impact of silicon nanomaterials of different configurations.

In an effort to achieve this, here we demonstrate that label free SiNWs can be internalized in multiple cell lines (96% uptake rate), are primarily endocytosed specifically through an endogenous phagocytosis pathway. To study this behavior we have developed a robust set of methodologies for quantitatively examining large aspect ratio nanowire-cell interactions in a time-dependent manner on the ensemble scale.

This approach represents one of the first dynamic studies of semiconductor nanowire internalization and helps fit SiNW uptake into a more familiar biological picture. Finally, we will discuss how this study offers valuable insight into designing devices for bio-molecule delivery, intracellular sensing and photoresponsive therapies.

3.2 Results and Discussion

3.2.1 Ensemble Nanowire Dynamics

Ensemble SiNW uptake was assayed using the rate of SiNW-cell overlap. To achieve this, first SiNWs were allowed to settle on a substrate before seeding cells. During incubation, cells could then migrate over the surface picking up SiNWs as they moved. During this process, both darkfield (DF) and phase contrast (PC) micrographs were collected to determine the percentage of SiNWs overlapping with cells (**Figure 3.3**). While not a direct confirmation of internalization, SiNW-Cell overlap acts as a reporter of nanowire-cell interactions. In a non-interacting random system, we would expect minimal clustering of the wires and an 'overlap reporter' value (β) of one, where β is equal to the percentage of nanowires overlapping with cells ($Y_{(t)}$), divided by the percentage of area covered by cell (i.e. cell confluence, $C_{(t)}$). However, in the case of positive SiNW uptake, we would expect to see wires clustered into small regions corresponding to the position of each cell, resulting in a larger SiNW-Cell overlap reporter value (β>1)(**Figure 3.2**). In this regard, the use of overlap values β enables an easy to perform optical assay for studying a variety of SiNW-cell interactions, including both the cell line and NW length dependence on internalization.

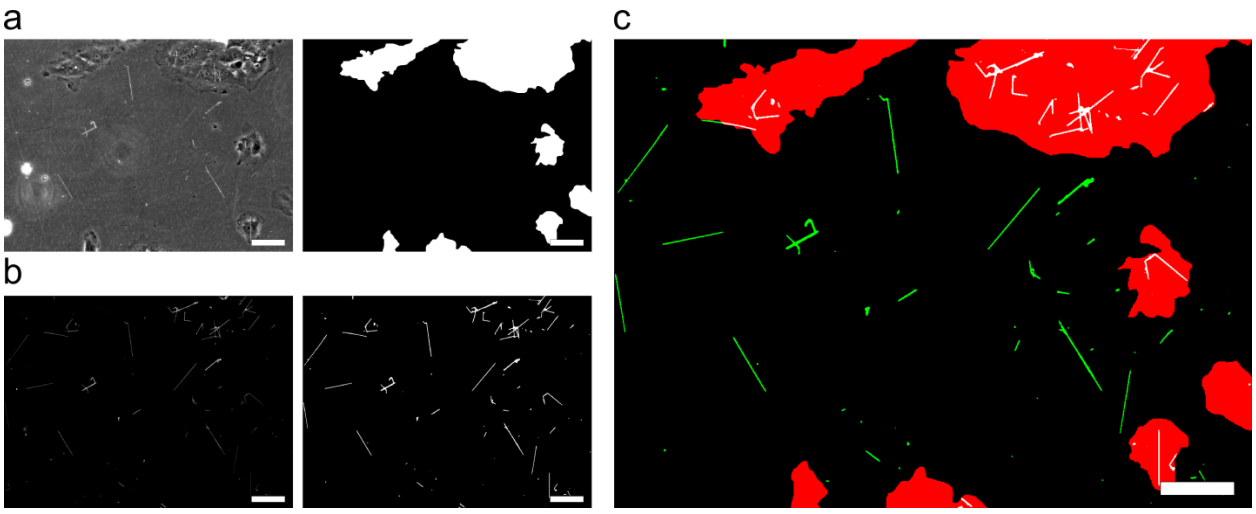

Figure 3.1 Nanowire/Cell Colocalization Determination.
(**a**) Phase contrast micrograph of cells 4h after inoculation (left), and the corresponding binary cell outline (right). (**b**) Darkfield micrograph with the same field of view, highlighting the SiNWs (left), and the corresponding binary image (left). (**c**) The resulting composite overlap image, depicting the cell's position (red), the overlapping SiNWs (white), and the excluded SiNWs (green). The percentage of SiNW-Cell overlap was determined on a per-pixel basis to incorporate wires which were only partially overlapping with cells. (all scale bars: 50 µm).

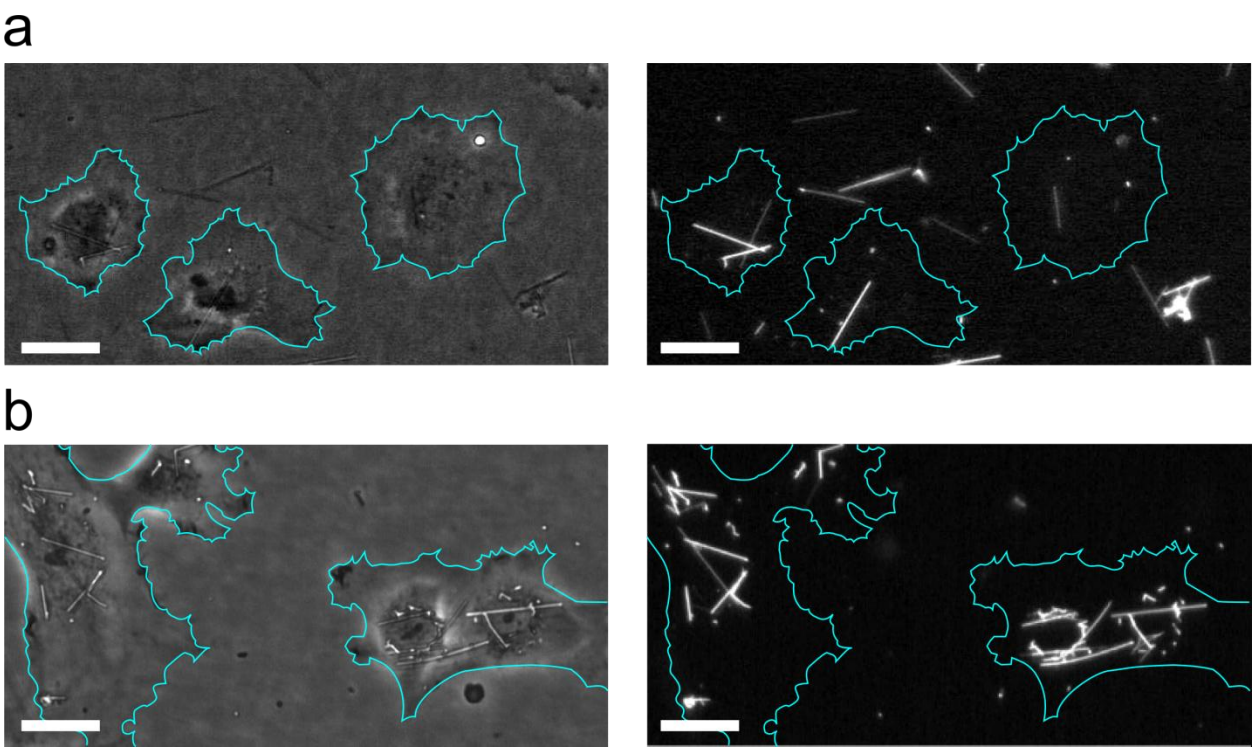

Figure 3.2 Cellular Clustering of SiNWs.
Corresponding PC (left) and DF (right) micrographs taken at 2 hours (**a**) and 20 hours (**b**) after HUVEC incubation with SiNWs (25 µm scale bars), indicating increased SiNW-Cell overlap, and clustering in the perinuclear region. (Cell outline highlighted in teal).

Using this 'overlap reporter' model, we examined the importance of NW length on SiNW uptake (**Figure 3.3b**). SiNWs of different lengths were prepared by varying growth time during synthesis, with increased durations resulting in longer wires on average after sonication. For each sample, β was then determined after 24 h of co-incubation with human umbilical vascular endothelial cells (HUVECs). In all cases, internalization was observed (β>1), with longer wires showing a higher rate of overlap with cells (~45% increase in β). While at first this suggested that HUVECs prefer longer SiNWs, this result is consistent with the fact that longer wires are more likely to come into contact with cells. When normalized by the length of the wire, no significant difference was noted between the longest and shortest growth times (Student's t-test: P>0.9), indicating that SiNW length is not a critical factor in determining which nanowires can be internalized once they are already in contact with a cell.

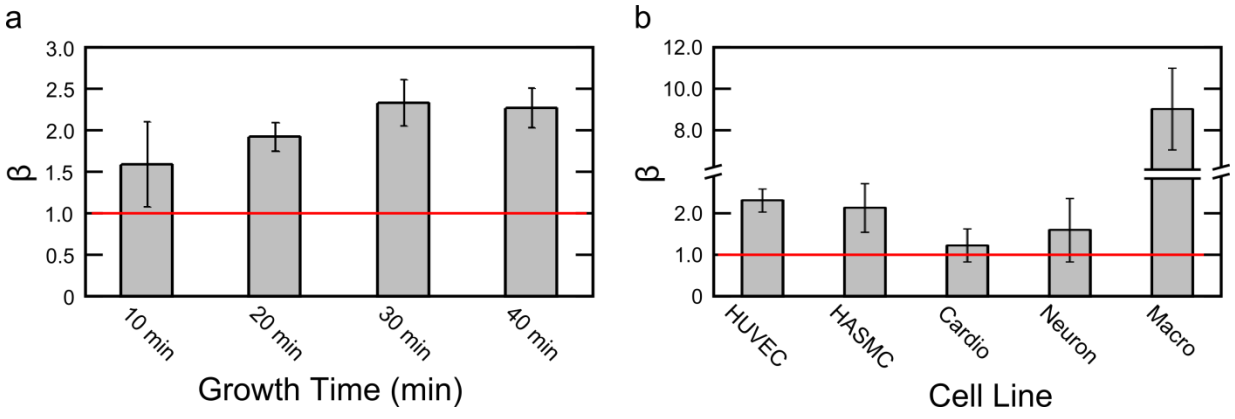

Figure 3.3 Length and Cell Line Dependence on Nanowire Uptake.
Overlap reporter values of SiNWs with varying growth lengths (HUVECs)(**a**), and in multiple cell lines (**b**), after 24h, showing that longer wires are more likely to be internalized based on geometric considerations and that cardiomyocytes and DRG neurons do not internalize unmodified SiNWs, while HUVECs, HASMCs and macrophages do.

The 'overlap reporter' model also provided insight into cell line specific internalization. In the case of both HUVECs and Human Aortic Smooth Muscle Cells (HASMCs), β values in excess of unity (**Figure 3.3b**) (β=2.3±0.3 & 2.15±0.6,

respectively) and clustering (**Figure 3.4a**), were observed, suggesting that both cell lines were capable of internalizing label free SiNWs. Mouse derived J774A.1 monocyte macrophages were also seen to internalize nanowires at high rates, demonstrating clustering and high overlap values after 24h (β=9.0±1.9) (See **Video S3**). However, for primary cardiomyoctes and dorsal root ganglia (DRG) neurons, no clustering was observed and β values did not statistically exceed the baseline (β=1.3±0.4 & 1.6±0.8, respectively), indicating that neither cell line was capable of internalizing label free SiNWs (**Figure 3.4**). While the DRG neurons (as determined by β-tubulin III staining) did show slightly elevated β values, this was ascribed primarily to the neurons close association with other non-neuronal cells retained during primary culture, some of which appeared to be able to internalize SiNWs (Clustering, β= 3.3±1.5). Collectively, these results suggest a heterogeneity in the cell specific response to SiNWs. Namely, that only certain cells types are capable of internalizing label free wires. This is consistent with the fact that are many different routes of entry for particles to be internalized[12,13], however not all of these endocytosis pathways are expressed across all cell types.

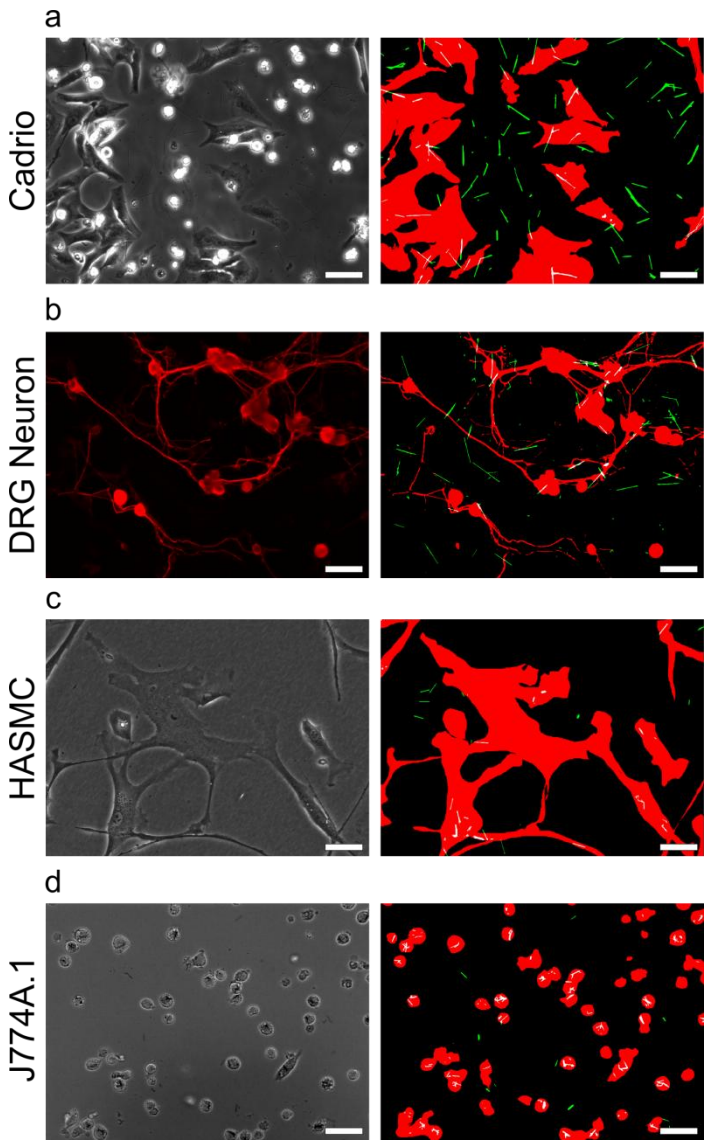

Figure 3.4 Cell Line Specific SiNW/Cell Colocalization.
Phase contrast micrograph of primary cardiomyocytes (**a, left**),Human Aortic Smooth Muscle Cells (HASMCs)(**c, left**) and J774A.1 macrophage cells (**d, left**) and the TxRed channel of β-tubulin III stained DRG Neurons (**b, left**), 24 hours after co-incubation with SiNWs, with the corresponding composite overlap image (**a,b,c & f, right**) depicting the cell's position (red), the overlapping SiNWs (white), and the excluded SiNWs (green) (all scale bars: 50 µm).

To delineate between different endocytosis pathways, we turned to a dynamic model looking at the SiNW-Cell overlap as a function of time; a method reminiscent of previous phagokinetics studies[14,15]. To understand the resulting dynamics we parameterized the system using a 2D random walker model, which we derived from the Dvoretzky & Erdös's equations[16] (for the derivation see **Section 3.4.9** Two-Dimensional

Random Walker Model), with the ensemble percentage of SiNWs overlapping cells, $Y_{(t)}$, being given by the following:

$$Y_{(t)} = M_w - Be^{\frac{-\pi D_t \cdot C_{(t)} \cdot t}{A_{Cell}}} \quad 3.1$$

Where t is time, D_t is the effective cell migration constant, M_w is the maximum percentage of SiNWs available for internalization, A_{cell} is the average area covered by a single cell, $C_{(t)}$ is the percent cell confluence as a function of time, and $B = M_w - C_{(0)}$. This model differs significantly from other drug delivery kinetics model, which typically assume that cells are stationary and the small molecular drug targets are free to diffuse throughout the solution, however in the present case the settled SiNWs are assumed to be stationary while the cells' innate motility brings them into contact with new SiNWs.

This model was observed to be in good agreement with experimental values (**Figure 3.5**), and it's use presented several advantages. First, as a relatively constrained system, this model offers distinct physical insights into the ensemble internalization process, as all of the terms refer to directly measureable quantities. For instance, the maximum percentage of internalizable wires, M_w, was found to be ~96%, while using Dt as the single free fit parameter in a least squares regression, an average effective cell migration rate of 437±36 $\mu m^2/h$ (R2 = 0.89, N=7) was determined for HUVECs. Second, this model can be used to create an expected rate of SiNW internalization in the absence of perturbations. Using known endocytosis inhibitors to block specific routes internalization, this information can be used to gauge how SiNW internalization is effected by different treatment regimes, in turn pointing towards a specific method of

endocytosis.

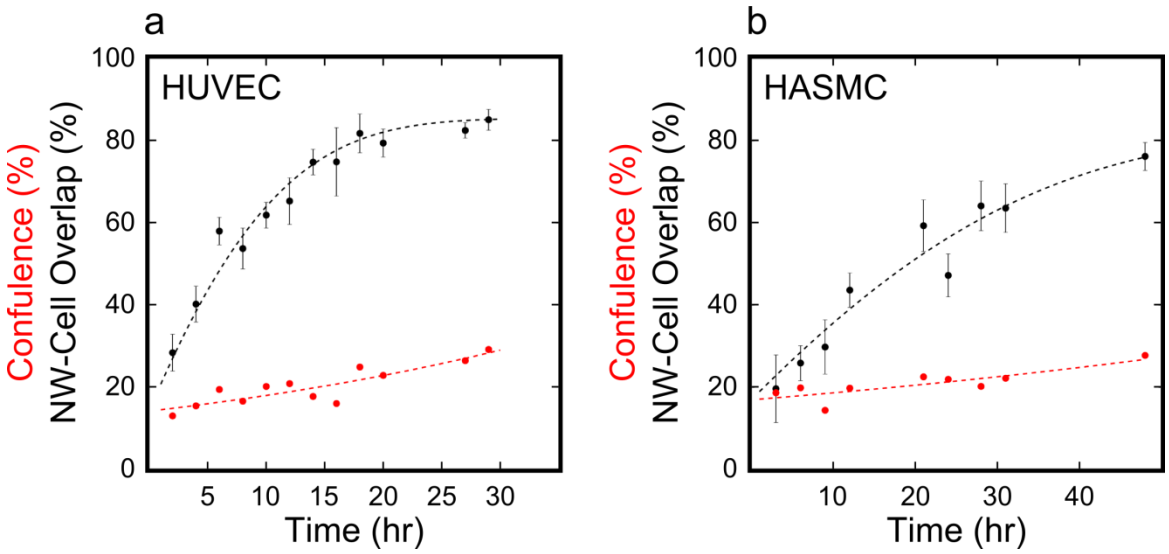

Figure 3.5 Nanowire Colocalization Over Time.
Example SiNW-Cell overlap (black dots) & cell confluence (red dots) traces as a function of time for unmodified SiNWs in HUVEC (**a**) and HASMCs (**b**). Expected overlap trend (black line) fit using 2D random walker model (HUVEC: D_t = 410 μm^2/h, R^2 = 0.93) (HASMC: D_t = 206 μm^2/h, R^2 = 0.88). Cell confluence modeled as an exponential fit (red line).

3.2.2 Mechanistic Studies

To determine the specific route of endocytosis several strategies were adopted. Initially lysosome tracking was pursued (**Figure 3.6**), however due to the relatively large size of the SiNWS, it was difficult to couple SiNW motion with individual lysosomes, as the SiNWs overlapped multiple vesicles, and any correlation in movement was difficult to distinguish from the overall cell motility. Therefore, we turned to an ensemble model based on the SiNW-Cell overlap. Using the SiNW-Cell overlap allowed for both a simple to implement single time point measurement to asses cell-type dependent internalization and for a dynamic model based on 2D random walkers to determine the specific mechanism of internalization.

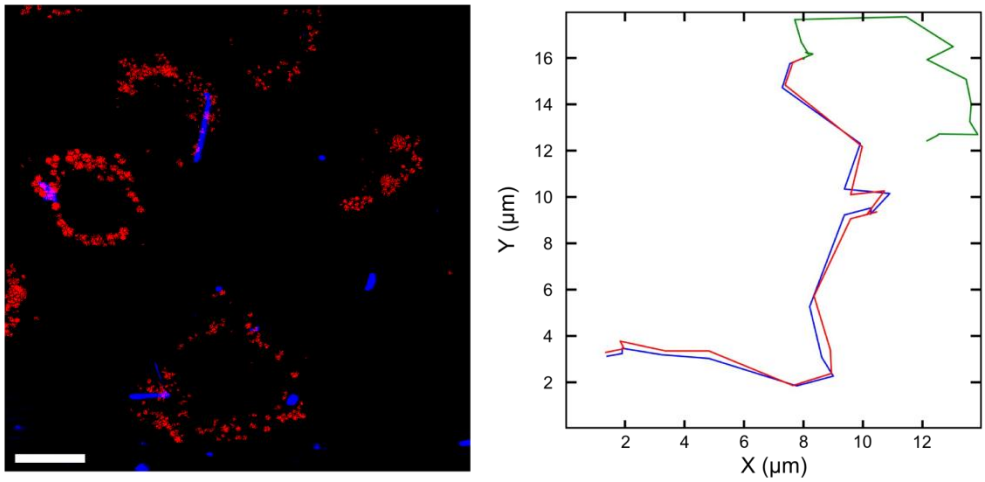

Figure 3.6 Lysosome Tracking.
(**left**) Fluorescently labeled lysosome (red) of HUVECs with internalized SiNWs (scattering, blue). SiNWs overlap a large number of lysosomes, hindering identification of an individual internalizing lysosome (10 µm scale bar). (**right**) trajectories of an individual lysosome (red), the tip of a nearby SiNW (blue), and a free particle in solution (green) (5 min/frame, total time = 90 min). SiNW movement is closely coupled to the lysosome, however both are driven by the underlying cell motility.

While using the dynamic SiNW-Cell overlap model, an internal control was adopted to help correct for deviations in the rate of NW internalization, which was found to be sensitive to the initial seeded cell population (**Figure 3.7a**). To establish this internal control, HUVECs were co-cultured with SiNWs a minimum of 7.5 h prior to administering drugs, monitoring the SiNW-Cell overlap. Then using equation **3.1**, the projected SiNW-Cell overlap was determined in the absence of any perturbations. The resulting projection was found to be in good agreement with experimentally observed values present in the negative control, where no inhibitors were administered (R^2 = 0.91) (**Figure 3.7b**), suggesting the validity of this internal control model. To quantitate the significance of a drugs impact on internalization, a Pearson Chi-squared test was employed, using the projection from the internal control model as the expected result and the experimentally measured overlaps as the observed trend. In the case of the negative control, a non-significant deviation from the projected trend was observed χ^2

(7,N = 6) = 1.62, P>0.95 (**Figure 3.7b**), with a ΔY_{29} of only 0.6%, where ΔY_t is the difference between the expected and experimentally observed SiNW-cell overlap values after t hours.

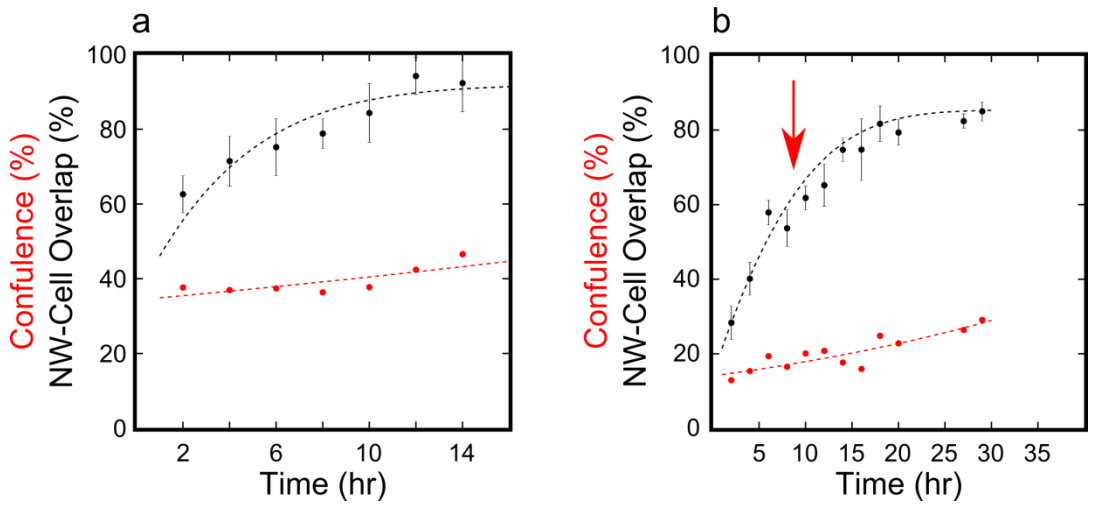

Figure 3.7 Initial Cell Confluence Effects Uptake Dyanmics.
(**a**) Increased initial HUVECs concentration, showing cell confluence plays an important role in ensemble uptake dynamics. SiNW/Cell overlap (black dots) & cell confluence (red dots) as a function of time with modeled fit (black line). (**b**) Negative internal control of SiNW/Cell overlap, indicating the internal control model matched well with the resulting overlap in the absence of inhibitors. Expected rate of overlap (black line) modeled on the first 8 hours of internalization (red arrow for comparison, no inhibitor present), shows good fitting with the remainder of the data (R^2 = .91, $\chi 2$ = 1.62, P<0.95).

As a positive control for drug efficacy, cell migration was halted using the potent actin polymerization inhibitor, Cytochalasin D (Cyto D), restricting the cell's motility and their ability to access new SiNWs. This resulted in the abrupt termination of NW internalization (ΔY_{23} = 28.4%), showing significant deviation from the expected SiNW-Cell overlap, χ^2 (4,N = 6) = 35.26, P<0.01 (**Figure 3.8a**). A similar trend was observed using dynasore (**Figure 3.8b**), a cell-permeable dynamin inhibitor, which yields a statistically significant change from the internal control (ΔY_{23} of 29.2%), χ^2 (4,N = 12) = 23.5, P<0.01, indicating that dynamin, a protein that is responsible for regulating membrane curvature and vesicle scission[17], plays a critical role in NW internalization. This observation is important, as it concretely links SiNW uptake to cell regulated

endocytosis, showing that the nanowires are being actively internalized through a protein dependent process, rather than passively through mechanical abrasion. To examine this in more detail, both clathrin dependent and independent mechanisms were probed.

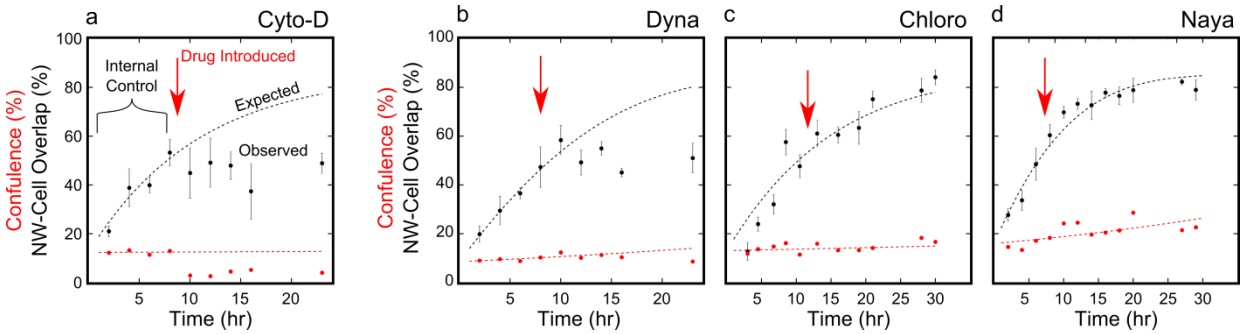

Figure 3.8 Mechanistic Study of SiNW Internalization Using Endocytosis Inhibitors.
Each graph depicts the observed SiNW/Cell overlap (black dots), cell confluence (red dots) and the expected overlap trend (black line), which is modeled on the first 8h of internalization (Internal control), prior to drug introduction (red arrow). Cell confluence modeled as an exponential fit (red line). Endocytosis inhibitors studied: Cytochalasin D (**a**)(actin-positive control), Dynasore (**b**)(Dynamin), Chlorpromazine (**c**)(Clathrin), and Nyastatin (**d**)(Lipid-Rafts), indicating that the protein dynamin plays a critical role in SiNW internalization.

Using chloropromazine as a clathrin blocker (**Figure 3.8c**), no significant change was noted in NW internalization (ΔY_{30} = 6.1%), χ^2 (6,N = 6) = 1.75, P = 0.94, suggesting a clathrin independent pathway. This result is surprising considering clathrin coated pits are one of the dominate routes of entry for many spherical inorganic nanoparticles (NPs), including AuNPs[2] and SiO_2 NPs (<200 nm)[18]. To confirm that clathrin pathways were effectively blocked at the present inhibitor concentrations, fluorescently labeled transferrin was used as a positive control, resulting in observable clathrin inhibition (~40%) (**Figure 3.9**). This means that despite the nano-scale diameter of the SiNWs (20-250 nm), cells were able to distinguish the high-aspect ratio of the material, suggesting a mechanism of topological sensing where a cell is able to gauge a material's aspect ratio and thereby delineate it's mode of cellular entry. One such

pathway which shows shape sensitive internalization at the nanoscale is caveolae-mediated endocytosis[19]. While the role of caveolae is still controversial[20], we examined this route by administering the drug Nystatin (**Figure 3.8d**), which disrupts lipid raft and caveolae formation by cholesterol binding[21], however this showed no significant change in NW internalization (ΔY_{29} = 5.7%), χ^2 (7,N = 6) = 1.73, P > 0.95.

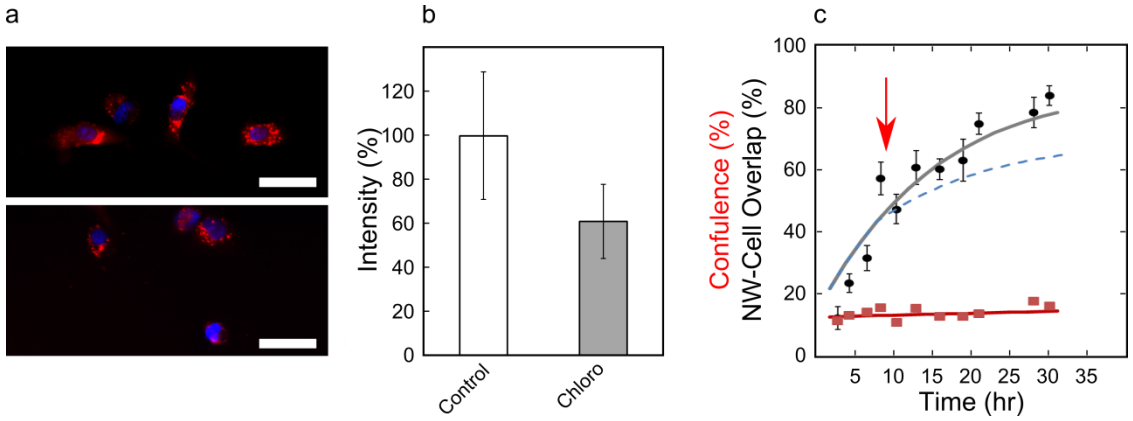

Figure 3.9 Chloropromazine Positive Control.
(**a**) Example fluorescent staining micrograph after TXred conjugated transferrin incubation in a control sample (upper) and chloropromazine (lower) treated cells (50 µm scale bar)(Red-Transferrin) (Blue-Dapi). (**b**) Relative signal intensity of transferrin per cell treated with 2.5 µg/mL of chloropromazine (14 hrs) compared to a control, showing effective clathrin dependent endocytosis inhibition (P<<0.01). (**c**) Observed SiNW/Cell overlap (black dots) & cell confluence (red dots) as a function of time for chloropromazine drug studies, with modeled fit (black line). Blue-dashed line gives the expected rate of SiNW internalization if the uptake process was clathrin dependent given the measured blocking levels. Experimentally observed overlap deviates significantly from the projected blocking (χ2 (6,N = 6) = 16.9, P < 0.01), suggesting the observed process was not clathrin dependent.

Another pathway which is particle size dependent, is phagocytosis, as it requires particles to be completely encapsulated prior to internalization. Reviewing the cell line dependent internalization we noted that macrophages, primary phagocytes, were able to readily internalize the wires (**Figure 3.4c**). Additionally, reagents for blocking phagocytosis include actin inhibitors, such as cytochalasin D, which showed a significant decrease in SiNW uptake (**Figure 3.8a**). Together this suggested that phagocytosis may play an key role in nanowire endocytosis. However, macrophages

can present multiple endocytosis pathways, while actin polymerization can restrict cell migration, potentially leading to false positives. Therefore, to study this pathway in more detail we first examined the cell's morphology during internalization, before using the competitive surface binding protein Annexin V, that can inhibit phagocytosis without restricting cell migration.

Condition	Inhibits	χ^2	P
Control (No Drug)	--	1.62	0.95
Chloropromazine	Clathrin	1.75	0.94
Nystatin	Lipid Rafts	1.73	0.97
Cyto D (Positive Control)	Actin Polymerization	35.3	<<0.01
Dyansore	Dynamin	23.5	<<0.01
Annexin V (16 nM)	Phagocytosis	8.35	0.14

Table 3.1 Summary of Inhibitor Action on SiNW Internalization.

3.2.3 Cellular Uptake Morphology

To see if particles were being engulfed prior to internalization, we examined the morphology of HUVECs using EM and SEPC studies (**Figure 3.10**). When examined under SEM, cells co-incubated with SiNWs were seen to extend their membrane along the entire length of the wire (**Figure 3.10**). This suggested phagocytosis, as one necessary step in nanowire uptake is particle encapsulation, however the static view offered by SEM meant that we couldn't be sure if this was an internalization event, or some other nanowire-cell interaction. To supplement this viewpoint, SEPC was used to observe the real-time dynamics of membrane extension along a single SiNW (**Figure 3.10b**). This was achieved using relatively high-aspect ratio SiNWs (~33 μm in length), with longer wires requiring greater extension distances, enabling easier optical characterization. When using these wires, we observed that starting at the base of the membrane, the cell would extend a protrusion along the entire length of the wire at a

maximum rate of ~120 nm/s, eventually reaching past the wire's tip, before pausing briefly and then being retracted back to the basal level at similar speeds (~140 nm/s) (**Figure 3.10c**) (See **Video S.4**). This membrane engulfment is phenotypical of phagocytosis, further suggesting this route of internalization.

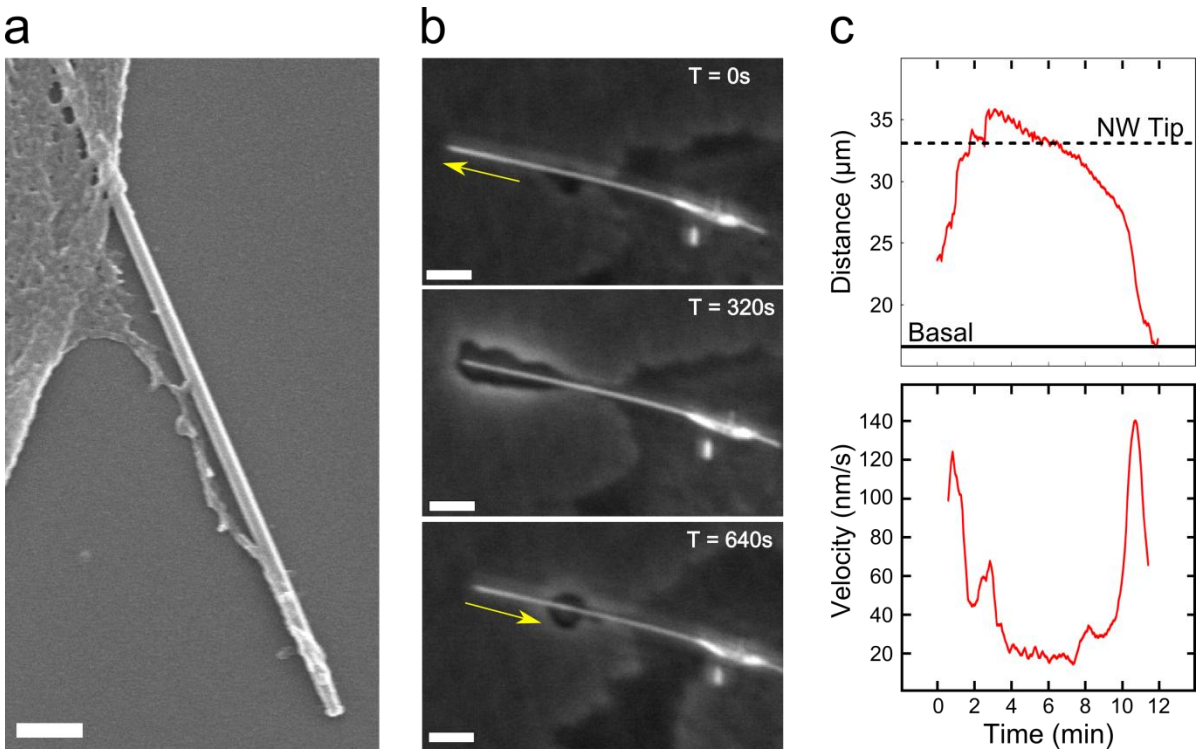

Figure 3.10 SiNW Membrane Engulfment.
(**a**) SEM micrograph showing the cell membrane extending along a SiNW (200 nm scale bar). (**b**)Time lapse SEPC micrographs of a membrane protrusion extending along a single SiNW prior to cellular uptake (left)(5 µm scale bars). (**c**) Distance of the membrane protrusion's leading edge from the base of the SiNW as a function of time (upper), with the corresponding instantaneous velocity of the membrane (lower). Base membrane distance and protruding NW tip distance given as solid and dotted lines respectively. Velocities smoothed over an 11 frame interval.

Surprisingly, during this process we observed that in some cases the membrane would not bring the entire SiNW into the cell, but would instead retract as a punctured vesicle. Such behavior has been noted before in other high aspect ratio particles, such as carbon nanotubes[22,23] and silver nanowires[24], and is often referred to as 'frustrated phagocytosis'. This partial encapsulation was further confirmed using TEM (**Figure 3.11**), showing that for longer SiNWs, a portion of the sample can extend past the

internalization vesicle. Overall, these observations reinforced phagocytosis as a mechanism for SiNW internalization, however it also suggests that there is a maximum length at which cells can healthily internalize wires. This will be discussed briefly in **Section 3.2.6**, however this process should be examined in further detail in future studies.

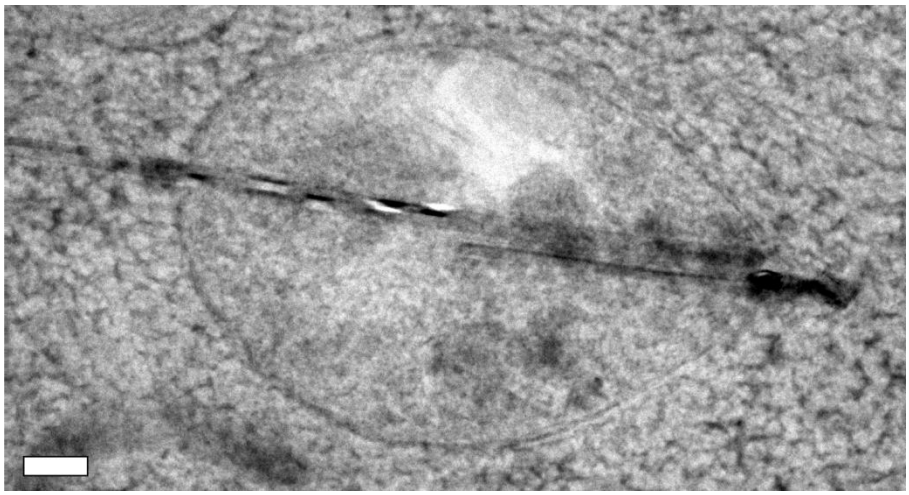

Figure 3.11 Partial Encapsulation.
TEM micrograph of a long SiNW inside of a HUVEC, showing that only the tip of the wire is contained in the vesicle (250 nm scale bar).

3.2.4 Annexin V as a Phagocytosis Inhibitor

To confirm phagocytosis as the route of SiNW internalization, Annexin V (A5) was used as a competitive surface-binding inhibitor[25–27], with A5 binding to the SiNW rather than directly to the cell. Compared to other phagocytosis inhibitors like Cytochalasin D (**Figure 3.8a**) that work by polymerizing actin, A5 offered the advantage of not restricting cell migration which can potentially lead to a false identification using stationary particles. In the past, A5 has been used as a phagocytosis inhibitor by binding to the membranous protein phosphatidylserine (PS), interfering with phagocytosis by screening apoptotic cells[26,28,29] (**Figure 3.12**). To briefly describe this

process, in healthy cells phosphatidylserine (PS), a negatively charged phospholipid that makes up a significant portion of the cell membrane, is concentrated to the inner leaflet by the ATP dependent protein flippase. (Fp)[30] (**Figure 3.12a**). During apoptosis, cells lose the ability to regulate the heterogeneity of their membrane composition, resulting in a mixed distribution of PS between the inside, and outside of the cell. Phagocytes are then able to recognize these exposed PS moieties, resulting in the clearance of the apoptotic cell[31,32]. In this context, A5 can be used as a phagocytosis inhibitor by ligand binding to PS, screening the apoptotic cells from the phagoctyes[32] (**Figure 3.12b**). A similar approach is pursued here, using the positively charged A5 protein to the non-specifically bind to the surface of the negatively charged SiNW, effectively screening the SiNWs from the phagocytosis internalization pathway (**Figure 3.12c**). As a result, if phagocytosis is the primary mechanism of SiNW uptake, then HUVECs should be unable to uptake the modified wires.

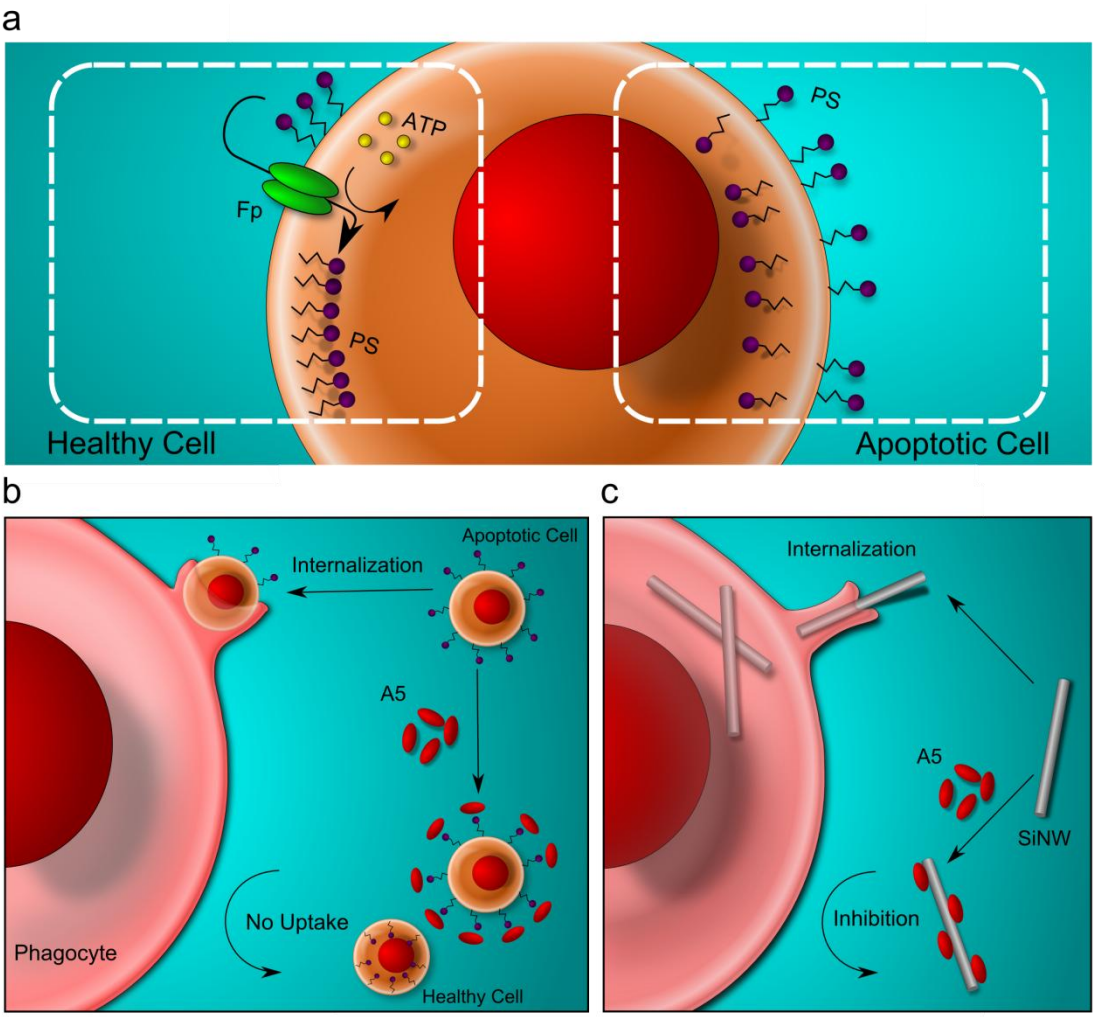

Figure 3.12 Mechanism of Annexin V Inhibition.
(**a**) Schematic illustration showing A5's mechanism of inhibition. In a healthy cell, PS (purple) is concentrated to the inner leaflet by the ATP (yellow) dependent protein Fp (green). In apoptotic cells, Fp can no longer control PS distribution, letting them diffuse to the outer leaflet. (**b**) A5 (red) can inhibit phagocytosis of apoptotic cells via ligand binding to PS, screening them from phagocytes. (**c**) An analogous mechanism can be considered in SiNWs. Just like A5 screens apoptotic cells from uptake, it can also screen SiNWs when bound to the nanowire surface. Unlike other inhibitors which work by disrupting the phagocyte's behavio, the non-specific binding of A5 to the negatively charged SiNW surface can screen the SiNW from uptake.

In this way, A5 was found to be able to inhibit SiNW uptake when introduced during internalization, showing a modest reduction in the percentage of internalized NWs (ΔY_{38} = -13.4%), χ^2 (10,N = 6) = 9.38, P = 0.49 (**Figure 3.13b**), reinforcing phagocytosis as the primary route of endocytosis, however, the observed inhibition was rather mild and during this process we noted a significant lag period before taking effect

(~10 h). Increasing the concentration of A5 (from 4 to 16 nM), led to decreased a lag period (~3 h) (**Figure 3.13**) and a further suppression in SiNW-cell overlap (ΔY_{22} = -17.8%), χ^2 (5,N = 6) = 8.35, P = 0.14. This confirmed that A5 could inhibit SiNW uptake, however, the observed lag period and the initial limited activity suggested that this method was only partially effective. To understand this behavior, we examined how A5 proteins were binding to SiNWs in solution.

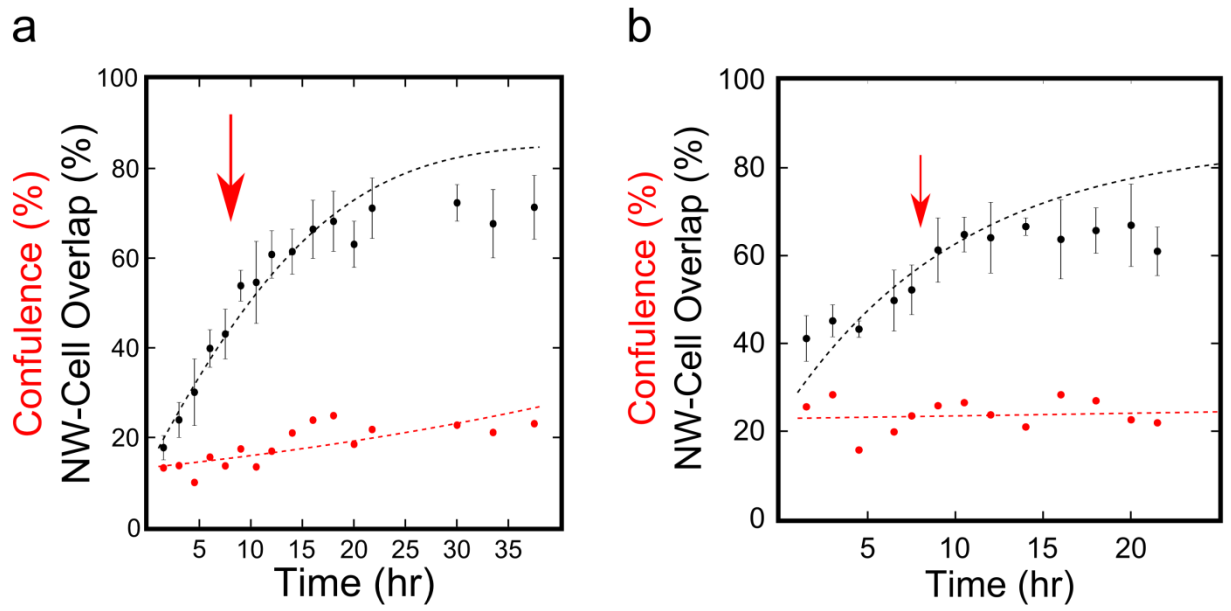

Figure 3.13 Annexin V Inhibitor Studies.
Observed SiNW/Cell overlap (black dots) & cell confluence (red dots) as a function of time for (**a**) 4nM and (**b**) 16nM A5 drug studies, with internal control modeled fit (black line). Experimentally observed overlap shows that higher concentrations of A5 lead to a reduced lag time, and greater inhibition.

In the case of apoptotic cells, A5 acts as an inhibitor by ligating exposed PS residues, reducing the rate of phagocytosis by effectively screening the apoptotic cell[32]. However, in the case of SiNWs, this binding would be nonspecific, occurring primarily from electrostatic interactions. This means that while in solution, A5 would be in competition with other positively charged serum proteins to bind the nanowire's surface. This competition has been observed before in other systems, with positively charged

serum proteins binding non-specifically in spherical silica particles[33–35]. Upon inspection a similar phenomenon was observed for the label-free SiNWs (See **Section 3.2.7**), with cytosolic wires forming 'protein sheaths' or elongated protein coronas. Such proteins could possibly interfere with A5 binding to the SiNW surface, leading to the observed lag-time and mild inhibition rates. To see if this was the case, we examined the role of serum proteins in the nonspecific binding of A5 to SINWs.

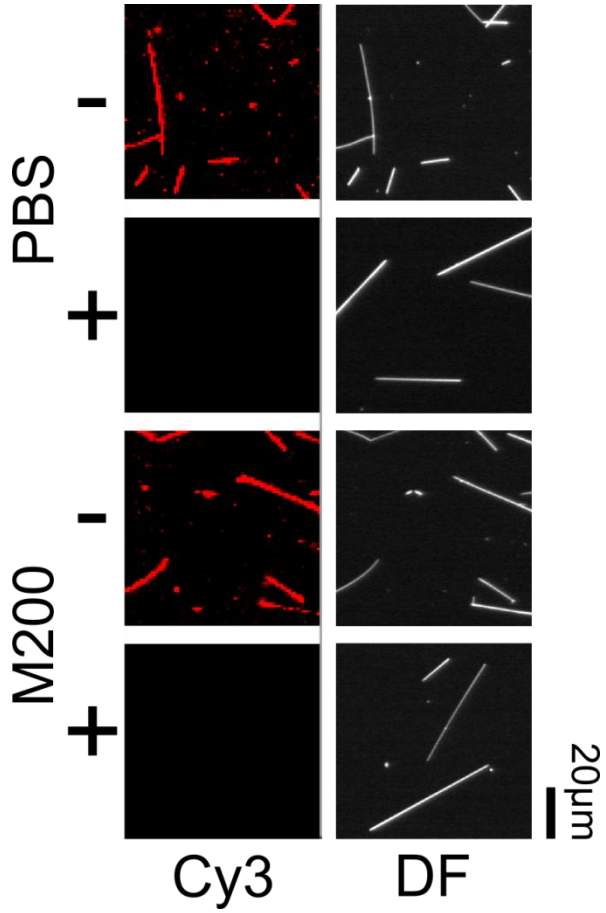

Figure 3.14 Nonspecific Binding of Annexin V to SiNWs.
Fluorescent (left) and DF (right) micrographs indicating the level of binding of A5-Cy3 in the presence (+) and absence (-) of serum in PBS and M200 solutions, indicating that A5 is competition with serum proteins to bind with the SiNW surface. (20 μm scale Bar).

For the non-specific A5 binding experiments (**Figure 3.14**), SiNWs were incubated with Cyanine labeled Annexin V (A5-Cy3) at 37 °C for ~24 h in the absence and presence of serum proteins (2%, Fetal Bovine Serum) in both phosphate buffered

solution (PBS) and M200 media. In the absence of serum, A5-Cy3 was observed to bind to the SiNW surface in PBS, showing strong fluorescent signal intensity, while the samples containing serum were only minimally binding; with a relative fluorescent signal intensity of only 0.29±0.03% (background subtracted using unlabeled SiNWs and normalized by SiNW concentration). A similar trend was observed in M200 media, with serum free and serum rich media showing a relative signal intensity of 87±16% and 0.54±0.04% respectively, as compared to the PBS bound A5. These results show that serum is sufficient in restricting A5-Cy3's access to SiNW's surface, and supports a competitive model of binding between A5 and other serum proteins. This explains the lag period and mild inhibition, as A5 would take some time to displace other proteins from the SiNW's surface.

To circumvent this competition and show that surface bound A5 was enough to disrupt nanowire uptake, both SiNWS pretreated with electrostatically absorbed A5-Cy3 and surface functionalized SiNWs specifically conjugated with A5-Cy3, were examined. For pre-treated samples, SiNWs were first incubated with A5-Cy3 in PBS in the absence of serum for 1h at 37 °C, while for surface functionalized samples, A5-Cy3 was conjugated to the SiNW surface using an aldehyde-silane modification step[36]. In both cases, wires were then sonicated into an M200 solution and allowed to settle, before HUVECs were introduced. After 24h of co-incubation, samples were then chemically fixed and the SiNW-Cell overlap was monitored optically in the Cy3, PC and DF channels. After incubation in the serum containing media, many of the pre-treated SiNWs lost their A5-Cy3 coating, however those wires that did retain their coating (as determined by fluorescent imaging), showed a significantly reduced rate of overlap with

HUVECs as compared to an external control of unmodified wires (β = ~28% of control, Student's t-test: P<0.01). This indicated that when pre-deposited onto the nanowire surface, A5 was able to effectively disrupt SiNW uptake by screening the nanowires from the internalizing cell.

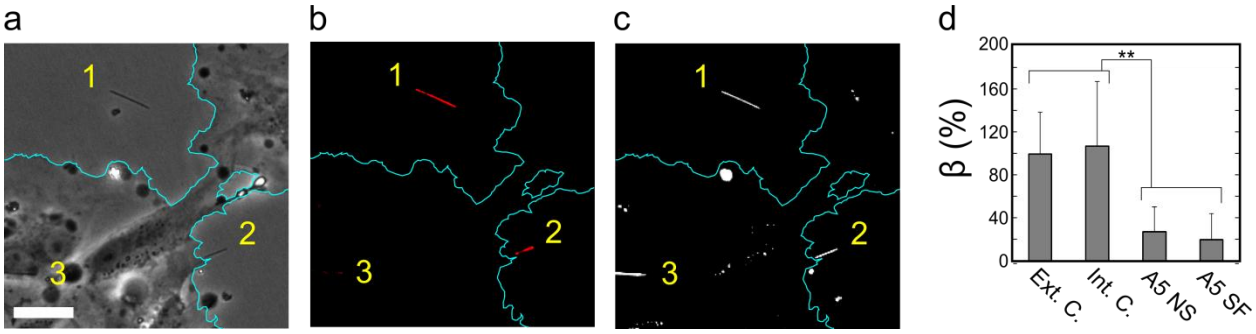

Figure 3.15 A5-Cy3 Functionalized SiNW Uptake.
Example micrograph showing the same region in the PC (**a**), DF (**b**), and Cy3 (**c**, artificial color) channels, indicating that SiNW surface modified with Cy3-A5 (1,2) are excluded from the cell while the internal controls (3) are endocytosed. (Artificial Cell Outline-teal) (30 µm scale bar). (**d**) SiNW-Cell overlap in HUVECs after 24h of SiNWs with non-specifically bound A5-Cy3 (A5 NS) and surface functionalized A5-Cy3 (A5 SF) relative to an external (Ext. C.) and internal (Int. C.) control of unmodified SiNWs. (β given as a percent of external control) (**, P<0.01).

This was further confirmed studying the uptake of SiNWs with covalently linked A5-Cy3, which showed a similar reduction in uptake (β = ~20.5% of control, Student's t-test: P<0.01) (Determined using the Cy3 fluorescence overlap of labeled SiNWs with HUVECs). Additionally, the use of surface conjugated A5-Cy3 also allowed for an internal control of unmodified wires, which wasn't available using non-specifically bound A5, as the electrostatically adsorbed surface coating can be transient and in equilibrium with other unmodified wires. By using specifically modified wires, A5-Cy3 coating could be maintained throughout the entire incubation, allowing for a study of the distribution of labeled versus unlabeled SiNWs within the same solution (**Figure 3.15**). When compared to an internal control of unmodified SiNWs, A5-Cy3 labeled wires showed highly reduced overlaps (β = ~19.1% of control, Student's t-test: P<0.01), while the

internal standards showed no significant difference from external controls in (β = 4.1±2.3 & 3.8±1.5 respectively) (**Figure 3.15d)**. This offered several valuable insights. First, this indicates that HUVECs are able to discriminate between SiNWs conjugated with A5-Cy3 and those with no surface modification, allowing the cell to selectively determine which nanowires will be internalized. Second, it indicated that the presence of A5-Cy3 SiNWs in solution did not inhibit cell activity in other ways, such as hindering cell motility, as unmodified wires were able to be internalized as normal. Collectively, this strongly shows that A5 is capable of selectively inhibiting SiNW uptake, and when combined with the high rate of macrophage uptake, and cell morphology analysis, clearly demonstrate that SiNWs are primarily internalized via a phagocytosis mechanism, concretely linking SiNW uptake with an endogenous endocytosis mechanism. This result is promising, as it links SiNW uptake to a well understood biological phenomenon, and helps explain how label free SiNWs interact with cellular systems.

3.2.5 Proposed Overview

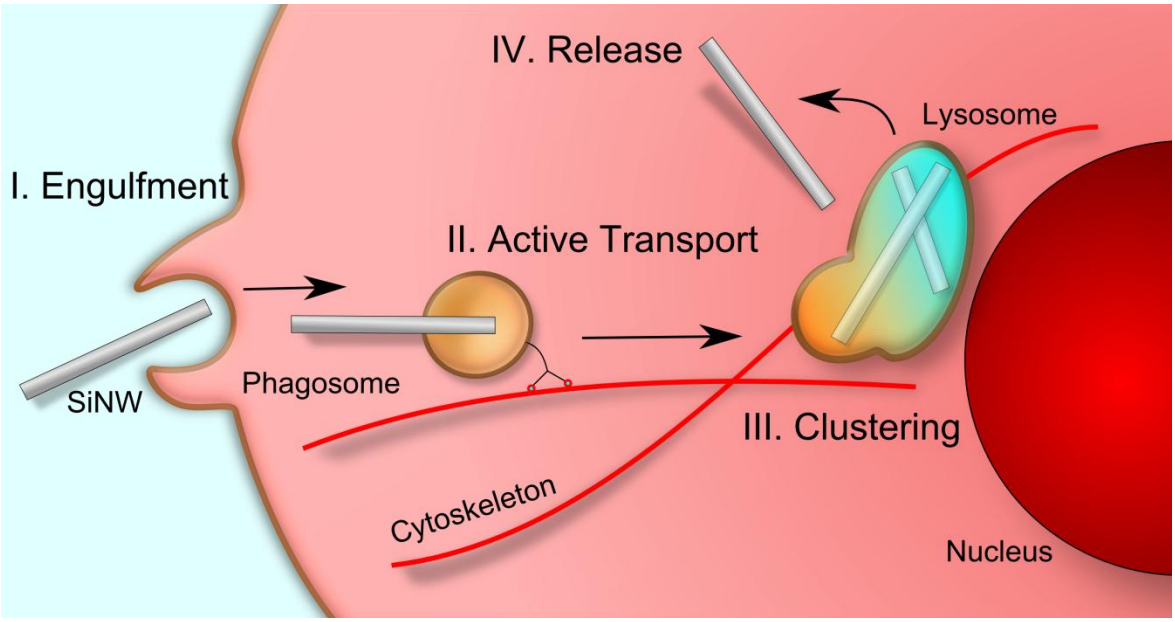

Figure 3.16 Schematic Overview of the Proposed SiNW Internalization Pathway.
After first coming into contact with the SiNW, the cell membrane extends along the entire length of the SiNW, engulfing the particle. This result in either complete or partially encapsulation of the SiNW into a small vesicle. The SiNW is then transported to the perinuclear region for processing. Eventually the particle, through an yet unknown processes, is able to leave the lysosome and is released to the cytosol.

In this report we have we have demonstrated that high-aspect ratio SiNWs can be internalized in a label free fashion, developing a robust set of methodologies to allow for the dynamic study of label free nanowire-cell interactions, showing for the first time that nanowires are endocytosed through the phagocytosis pathway. The identification of phagocytosis as the primary mechanism of SiNW internalization is an important step in several ways. First, it demonstrates that nanowire morphology plays an important role internalization, and distinguishes high-aspect ratio nanowires from nanospheres with similar diameters[18,37]. Second, it helps fit nanowire internalization into a broader, more familiar biological picture. Namely, our results suggest a very specific time-dependent pathway (**Figure 3.16**), where SiNWs are first internalized by a membrane extension engulfing the particles (**Figure 3.10**). From here the SiNWs undergo active transport to

the perinuclear region, presumably along cytoskeleton filaments as indicated by the 'burst like transport' and relatively linear trajectories (**Figure 2.9**). This results in the nanowires becoming clustered as they are collected into larger lysosomal compartments (**Figure 2.5**). In this study, we have carefully examined each of these components, placing SiNW internalization into a larger picture, which may appear familiar from other endocytosis studies[5,38], however has hitherto been connected to SiNW internalization. In turn this pathway raises several intriguing possibilities. For instance, it appears that SiNWs undergo an as yet unstudied release process from the lysosome, resulting in a distribution between the cytosol and vesicles (**Figure 2.4d**). However, at this point it is not clear if this release process is the result of mechanical abrasion, as SiNWs appear to be able to puncture vesicle membranes (**Figure 3.10d**), or if this process is directed by the native cellular architecture. Additionally, studying this pathway has important implications in designing and implementing new functional devices in biology and medicine which will be discussed later in this section.

3.2.6 Cytotoxicity

In addition to SiNW uptake, a preliminary study of SiNW cytotoxicity was pursued. To examine the metabolic rate of HUVECs containing SiNWs, an MTT colorimetric assay was used. MTT (3-[4,5-dimethylthiazol-2-yl]-2,5- diphenyltetrazolium bromide; thiazolyl blue) is a water soluble dye, that is yellowish in color when prepared in a transparent media solution. When exposed to NAD(P)H-dependent oxidoreductase enzymes present in the mitochondria, MTT is converted to an insoluble purple formazan by cleavage of the tetrazolium ring[39,40]. This distinct color shift allows for an easy measurement of metabolic activity using a UV-Vis spectrometer, and is often taken as a

marker of cell viability. In the case of HUVECs incubated with SiNWs, initially 30 nm wires showed no significant deviation from control samples, while 100 nm wires presented initially lowered viability rates (**Figure 3.17a**). In both case however, after 7 days the samples showed greatly increased rates of activity. This type of behavior is consistent with additional oxidative stress and possibly the generation of reactive oxygen species (ROS), which has been reported for silicon carbide nanowires[41], and suggests that the presence of the SiNW may place an increased metabolic burden on the cell. However, in the case of silicon carbide wires, activity were reported to eventfully return to basal levels, suggesting that longer studies may be needed in the case of silicon nanowires.

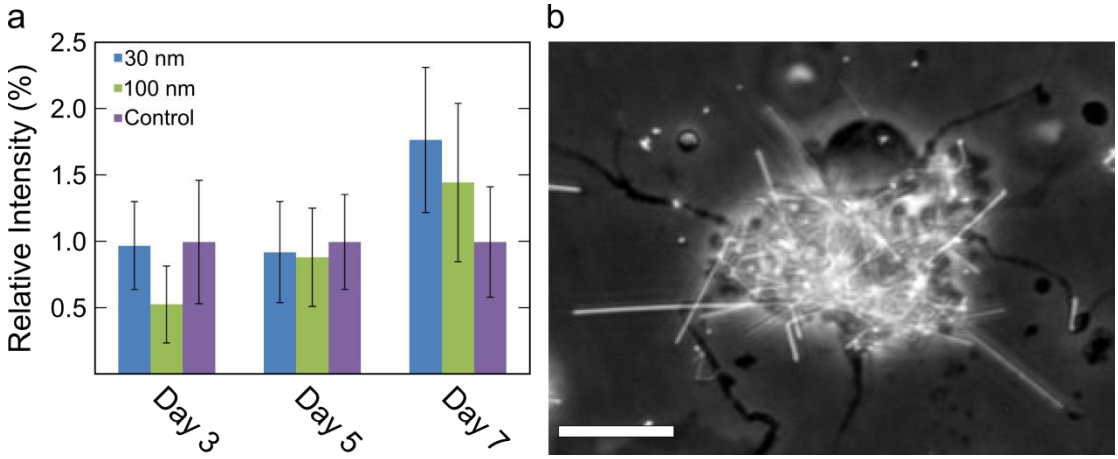

Figure 3.17 Cytotoxicity Assay.
(**a**) MTT colorimetric metabolic activity assay of HUVECs co-incubated with 100 nm and 30 nm SiNWs, indicating that SiNWs can induce metabolic stress (**b**) SEPC micrograph of an unhealthy HUVEC containing a large concentration of long 100 nm SiNWs (20 µm scale bar).

Additionally, MTT results should not be taken at face value in the case of nanowires samples. As previously mentioned, SiNW light scattering is strongly dependent on the orientation of the wire with respect to the incident light, with the transversal electric (TE) and transversal magnetic (TM) modes of polarization offering distinctly different optical spectrums[42,43] (See S**ection 5.2.2**). As a result, readings of

ensemble SiNWs, randomly oriented and suspended in solution, using UV-Vis spectroscopy gives widely varying baselines, even within a single sample and is therefore notoriously unreliable. As a UV-Vis spectroscopy based technique, this pulls the value of MTT and other colorimetric assays into question when evaluating nanowire cytotoxicity, and suggests that a more careful approach is needed, for instance using a proteomic assay to determine protein expression levels.

Despite initial MTT results, some less direct evidence suggests that SiNWs are well tolerated by cellular systems. First, healthy cell morphology is well persevered for HUVECs and HASMCs in the presence of a moderate amount of SiNWs. In unhealthy, hypoxic, cells "blebs" or erratic cellular protrusions are a common feature[44]. For samples containing SiNWs, we can see that 'blebbing' can occur at large concentrations, using long SiNWs (**Figure 3.17b**), however for the majority of samples this morphology isn't present. Anecdotally, this transition appears to occur when single wires reach a length that is ~4/5th the diameter of the underlying cell. This makes sense as long fibers can be detrimental to cell health, due to processes such as frustrated phagocytosis[22,24], however in the future, a more quantitative study, is needed to asses cytotoxicity dependence on the length of SiNWs. We also note that this dependence on length, makes nanowire diameter an important secondary factor, as the length of nanowires after sonication is moderately dependent on nanowire diameter[45]. This can be controlled to a certain extent using varying synthetic conditions, however it still means that diameter can be an important factor when comparing synthetically similar samples. Overall however, cell morphology points towards relatively healthy cells for the majority of samples surveyed.

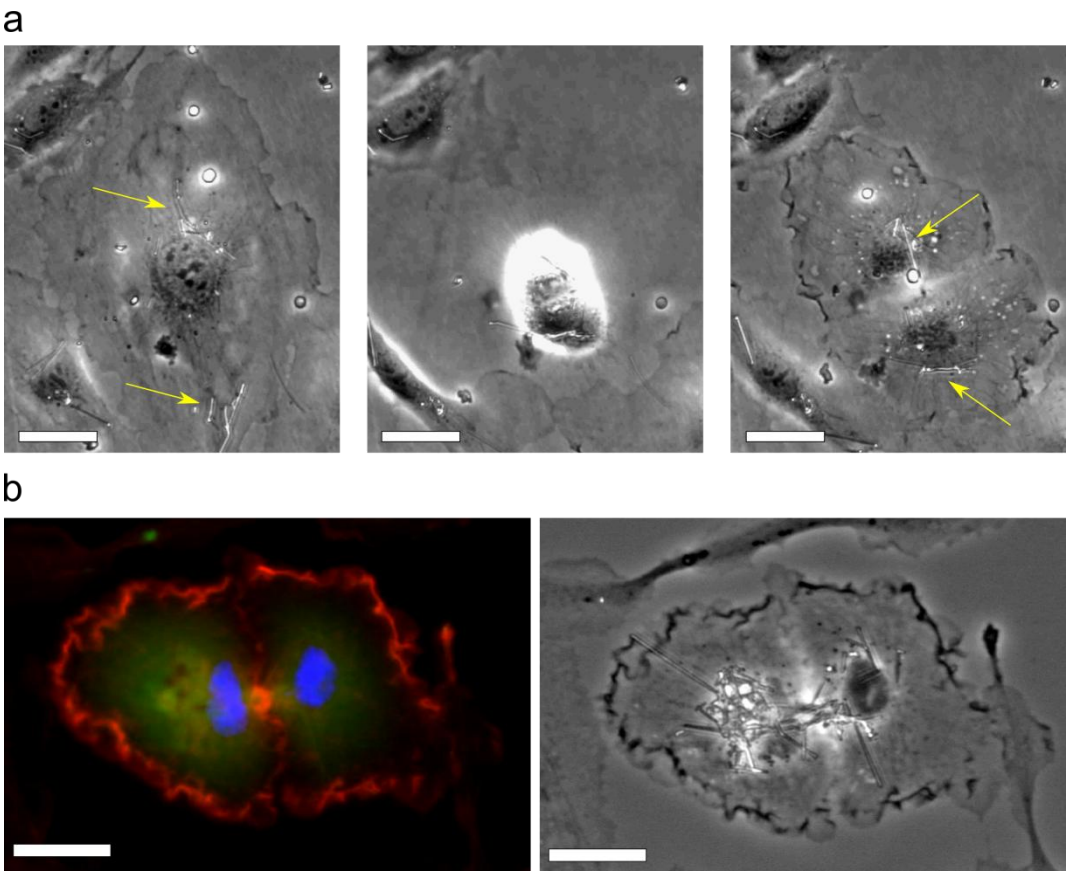

Figure 3.18 SiNW Mitosis.
(**a**) PC micrographs of a HUVEC with 30 nm SiNW present before (left), during (middle), and after (right) mitosis, indicating that cells are still able to proceed in the cell cycle. SiNWs are distributed to both daughter cells after mitosis. (Location of wires indicated with yellow arrow) (30 µm scale bars). (**c**) Fluorescent (left) and PC (right) micrographs of a HUVEC right after mitosis, with SiNWs seen to be bridging the two daughter cells (red = phallodin stained actin, green = antibody stained vinculin, blue = DAPI) (20 µm scale bars).

Another indicator that SiNWs are well tolerated by cellular systems, is that the cell cycle is able to proceed in the presence of nanowires. This can be seen in cells undergoing mitosis while containing internalized SiNWs (**Figure 3.18**). This is a good indicator of health, as the cell needs to pass certain "cell cycle checkpoints" for it to undergo mitosis, which are a critical part of the cell's ability to defend against adverse environmental conditions, such as ROS. The G1 check point in particular monitors the cell's general health and the ability to proceed along the cell cycle, by regulating proteins involved in DNA repair and apoptosis[4647]. During hypoxia, in response to the

oxidative stress, protein kinases can arrest the cell cycle preventing it from moving forward. As a result, the fact that HUVECs are able to undergo mitosis in the presence of SiNWs is good marker of cell health, as it indicates that these natural defense mechanisms have not been tripped, and that the cells are functioning normally.

As a brief aside, we can see that nanowires tend to bridge daughter cells immediately following mitosis (**Figure 3.18b**), with actin clustering at the point of the connection. Later we will discuss how intracellular nanowires can become entangled in the cytoskeleton (see **Section 4.2.5**). In this case, it appears that SiNWs may be able to also become entangled in mytotic spindles, and that cells are able to rearrange the nanowire's orientation during mitosis. Additionally, we note that SiNWs were well distributed between both daughter cells, indicating that the cell has a way of splitting nanowire populations. Both of these factors hint at interesting dynamics occurring for SiNWs during mitosis, and that nanomaterials could act as novel indicators in future biophysical studies of mitosis.

While still a preliminary study of cytotoxicity, our initial results indicate that the majority of wires were not problematic for cellular health. At this juncture it seems probable that some elevated levels of metabolic activity are present in cells with internalized SiNW, but that ROS are not generated at levels which are deleterious to cell health. Additionally, it appears that wire length plays an important role in determining nanowire cytotoxicity but that more information is needed to pin down this exact transition. To this end, more basic studies are needed for examining cell health using high-aspect ratio nanomaterials, as spectroscopy based methods can be

misleading. This means that in the future, more detailed methods such as proteomic studies will be needed to asses cell health.

3.2.7 Non-specific Protein Binding to SiNW Surfaces

Previous reports have shown that serum proteins binding to the surface of nanomaterials can play an important role in mediating cellular interactions[33–35]. While we have shown that serum proteins are not needed to initiate SiNW uptake (**Section 2.2.5**2.2.5 Serum Free SiNWs), our work with annexin V suggested proteins were being adsorbed onto the SiNW surface during co-incubation with cells. One way to probe this system is to use the intensity of optical scattering of SiNWs. Later we will show that the amount of light that a nanowire scatters is extremely sensitive to its size, scaling to the fourth power with respect to the nanowire's diameter (**Section 5.2.2**). This means that as proteins are adsorbed onto the SiNW's surface, it's diameter should fluctuate, a process which should be measurable using optical scattering. To monitor this process, we co-incubated SiNWs with HUVECs, and recorded the ensemble DF scattering, as compared to samples stored in deionized water for the same duration. Using this method we could see that the optical scattering of SiNWs incubated with cells would increase, before becoming saturated over a period of ~72 h (**Figure 3.19**) (Maximum 187% scattering of control). We note here that this timescale is not entirely inconsistent with other nanoparticle studies, which show that corona dynamics can evolve on the day timescale[48]. Additionally, during this time period, SiNWs were also being endocytosed by HUVECs, with the observed saturation timescale being consistent with ensemble internalization dynamics. This suggested that not only were proteins from the solution binding to the SiNW surface, but that cellular interactions were also occurring.

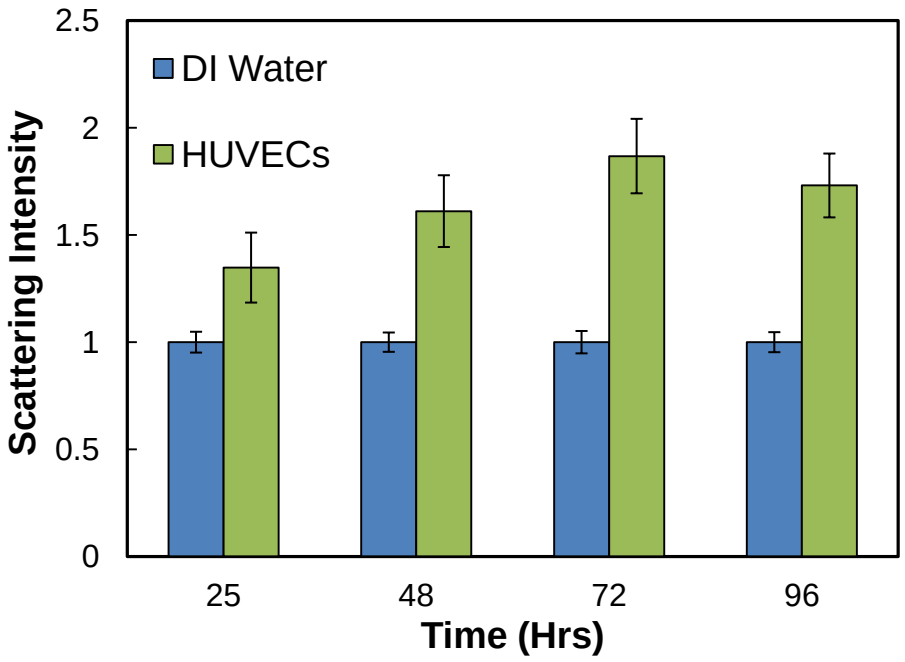

Figure 3.19 Optical Scattering of SiNWs Incubated with Cells.
Scattering intensity of 100 nm SiNWs incubated with HUVECs over time compared. Values normalized using similar SiNWs incubated in DI water for the same duration. (Error bars given as the standard error of measurement).

The role of cellular modification of SiNWs was examined using TEM studies. Cryopreserved thin cell sections were prepared by trypsinizing HUVECs co-incubated with SiNWs for 24 h. Cells were than rapidly fixed using high pressure freezing, processed using freeze substitution techniques[49], and segmented using an ultramicrotome. The resulting thin cell sections (~200-300 nm) were then heavy metal stained and imaged under a transmission electron microscope. Cells processed this way were observed to contain SiNWs with an attached protein shell (**Figure 3.20**). These 'sheath' like protein coronas were morphologically distinct from vesicles, in that they formed long wrappings around the SiNWs rather than circular structures. Measuring these protein formations by TEM, the coating around cytosolic SiNWs ranged from approximately 4 to 40 nm in size (Mean:16.2±9.6 nm, N=21), with large

variations observed even along a single wire. This large deviation in thickness, and shape suggested a heterogeneity in the composition of proteins coating the wires.

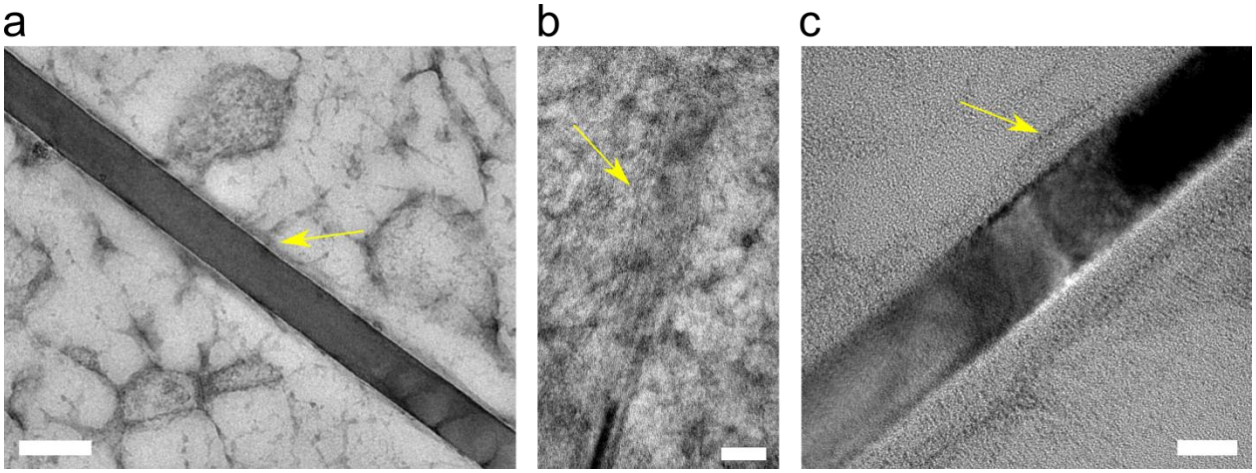

Figure 3.20 'Protein Sheath' Formation on Cytosolic SiNWs.
Example TEM micrographs of internalized cytosolic SiNWs surrounded by a thin layer of proteins, or a protein corona, extending from the wire's surface. Yellow arrows help indicate the location of the protein envelope (Scale bars: 200 nm, 50 nm, & 25 nm respectively).

Briefly probing this composition, we used confocal fluorescent microscopy in conjunction with antibody staining to look at some proteins bound to the SiNW surface (**Figure 3.21**). Using this technique we could see that both actin and vinculin were bound to the SiNW surface. Later we will discuss how SiNWs can become entangled in the actin network (**Section 4.2.5**). This entanglement helped motivate our choice of fluorescent stains, prompting an examination of actins' interaction with SiNWs, while vinculin was chosen as a surrogate for 'random' protein binding. Vinculin is a integrin-related protein that is recruited to focal adhesion plaques by specifically binding to talin head groups[505152]. This makes it a reasonable marker for non-specific protein binding, as it would normally only be dynamically recruited to focal adhesion sites or be found floating in the cytosol. In the case of SiNWs, we can see that in both HUVEC (**Figure 3.21a)** and HASMCs (**Figure 3.21b)**, actin and vinculin were found to be able to adsorb

to the nanowire surface. This suggested that in addition to cytoskeletal entanglement, nanowires could bind to a large host of proteins inside the cell. Additionally, the presence of vinculin suggested that this was larger nonspecific in nature, rather than being a directed by cellular process, as vinculin typically only clusters at focal adhesion sties.

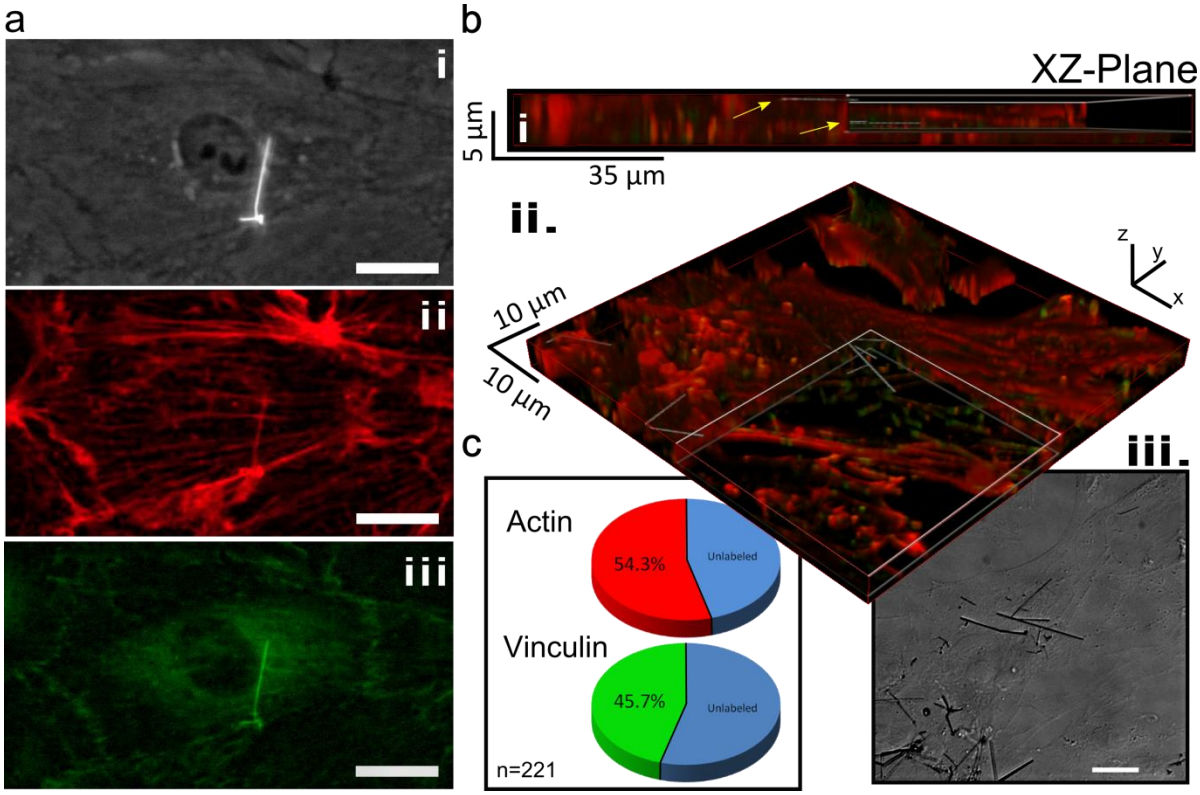

Figure 3.21 Non-Specific Protein Binding.
(**a**) Optical microscopy images of a stained HUVEC, showing the same cell in the SEPC (i), actin (ii, txred-phalloidin), and vinculin channel (iii, GFP-antibody staining), showing non-specific protein binding to the SiNWs (25 µm scale bars). (**b**) Confocal cross section of a HASMC(i&ii) containing SiNWs (white), stained for vinculin (green) and actin (red), showing similar non-specific binding, and that the SiNWs are internalized. Accompanying DIC image showing the location of each SiNW (iii) (10 µm scale bar). (**c**) Pi-Chart depicting the percentage of labeled and unlabelled SiNWs in HUVECs for actin and vinculin.

To ensure that the observed binding was the result of fluorescent labeling, rather than an artifact of optical scattering, an internal control was adopted. SiNWs which were contained in the same samples, but were not internalized by HASMCs were imaged (**Figure 3.22**). These micrographs were seen to contain SiNWs under DIC, but no

significant fluorescent intensity was associated with them (i.e. above background levels), suggesting that the observed non-specific protein bind was a result of optical artifacts. This allowed us to examine the percentage of SiNWs showing discernible levels of protein binding, with ~54% and 46% of SiNWs contained in HUVECs showing actin and vinculin binding respectively (**Figure 3.21c)**. This indicated that even among similarly internalized wires there was a heterogeneous distribution of protein coating. Overall these results indicate that there is a significant level of interaction between SiNWs and proteins contained in the cytosol. However, actin and vinculin offer only a brief glimpse of possible interactions forming at the nanowire surface. In the future more dynamic studies are needed to see how these formations evolve over time, and more in-depth proteomic studies are needed, to examine the range of proteins binding events[48].

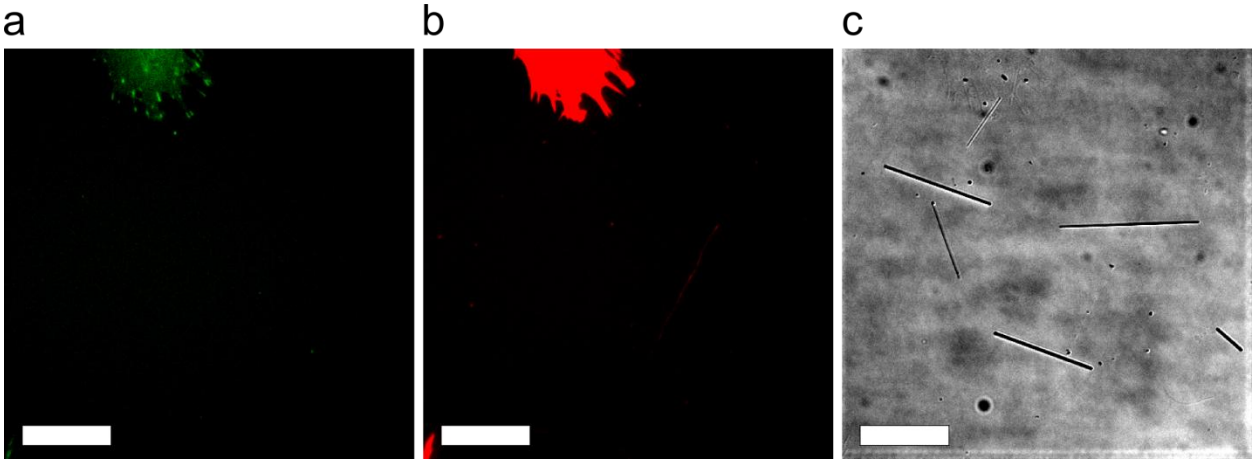

Figure 3.22 SiNW Scattering Internal Control.
Confocal fluorescent micrograph of an internal control of SiNWs, showing that SiNWs outside of cells do not 'fluoresce', indicating that the observed signal is not an artifact of optical scattering. GFP (**a**)(Vinculin), TxRed (**b**) (Actin), and DIC (**c**) channels shown for the same corresponding region. (Control images taken at double exposure time to emphasis point) (30 µm scale bars).

3.3 Conclusions

SiNWs are of particular interest for bio-integration because of their excellent electronic properties, biocompatibility, and potential to incorporate a diverse set of surface functionalities, structural morphologies, and dopant compositions. This allows for the realization of a large library of nanowire based tools and devices. For example, using nanowires as inter- and intracellular force probes[53]. Understanding the SiNW internalization pathway offers key insights into the single cell level interactions, and helps inform future device design. For example, one can image designing devices capable of differentiating between cell types. The fact that neurons and cardiomyocytes rejected SiNWs, while other cells were capable of internalizing these materials, implies that SiNW based therapeutic devices can be designed to specifically target certain cell types over others. Additionally, it may be possible to implement a pH or force responsive device capable of modulating cellular activity at specific points in the pathway, based on vesicle and cytoskeleton interactions. Alternatively, the partial encapsulation, or 'frustrated phagocytosis', of the particles raises the possibility of using the portion of the nanowire that is exposed to the cytosol as a delivery vector for bio-molecules which would traditionally be degraded in the harsh environment of the endosome. While these are just a few examples, understanding the pharmacokinetics of SiNWs helps pave the way for new and exciting opportunities in using nanowire based devices as active 'drug-like' therapeutic and diagnostic techniques, with the ability to distribute these devices in a substrate free manner marking an important milestone in developing next-generation bio-molecule delivery vectors, intracellular electrodes and photoresponsive therapies.

3.4 Experimental Details

3.4.1 Cell Culture

HUVEC and HASMCs were cultured using the same protocol as previously reported[53]. For J774A-1 cells (Sigma Aldrich) samples were cultured under sterile conditions in Dulbecco's Modified Eagle Medium (DMEM) with 4.5 g/L glucose, L-glutamine and sodium pyruvate (Corning) supplemented with 10% Fetal Bovine Serum and 0.04 mg/mL Gentamicin solution (Sigma Aldrich). Cell cultures were maintained at 37 °C and under 5% CO2, with media exchanged after 24 h, and every 48 h thereafter. For DRG neuron and cardiomyocte culture, see the below protocols.

3.4.2 Neonatal Rat Ventricular Cardiomyocytes Isolation

Hearts were excised from decapitated P2 neonatal Sprague-Dawley rats and placed into HBSS without Ca2+ or Mg2+ on ice. Hearts were washed in HBSS on ice six times to eliminate as many red blood cells as possible. Atria were sliced off of the hearts over ice, and each heart was minced into 3-4 pieces and transferred into 0.05 mg/mL trypsin in HBSS. Hearts were incubated overnight in trypsin on a 4 °C cold room shaker. Hearts were then transferred to a 37 °C water bath. 2 mg/mL soybean trypsin inhibitor in HBSS was added to the hearts followed by 1 mg/mL collagenase type II in L15 medium. Hearts were incubated in the water bath with collagenase for 45 min, with manual shaking and inverting every 5 min. Slow mechanical trituration of the cells was then performed in the tissue culture hood ten times with a plastic pipette. Next, cells were passed through a 70 µm filter and allowed to rest for 30 min at room temperature. Cells were then centrifuged and resuspended into DMEM + 10% FBS + 100 U/mL penicillin +

100 µg/mL streptomycin cardiac culture medium. Cells were platted on 10 cm TC treated petri dishes in a 37 °C 5% CO_2 cell culture incubator for 2 h in order to adhere the smooth muscle and fibroblast cells to the plastic and exclude them from the cardiac culture. After the incubation, the cardiac cells in the supernatant were counted via trypan blue staining. Cardiac cells were platted on glass bottom petri dishes coated with fibronectin and pre-settled SiNWs at a concentration of $5*10^5$ cells/dish. All rats were used in accordance with the University of Chicago's Animal Care and Use Protocol (ACUP: 72378) and the National Institutes of Health guidelines.

3.4.3 Dorsal Root Ganglia Culture

Dorsal root ganglia were dissected from decapitated P1 neonatal Sprague-Dawley rats into DMEM on ice. Ganglia were resuspended into 2.5 mg/mL trypsin in EBSS for digestion in a 37 °C shaker for 20 min. Following the digestion, cells were spun down and resuspended into 10% FBS in EBSS to inhibit any remaining trypsin. Mechanical trituration of the cells was then performed using three glass pipettes of decreasing size. Cells were centrifuged and resuspended into culture media consisting of DMEM + 5% FBS + 100 U/mL penicillin + 100 µg/mL streptomycin. They were then seeded onto the Poly-L-lysine coated glass bottom dishes with pre-settled SiNWs and left in a 37 °C 5% CO_2 cell culture incubator for 25 min to adhere to the glass. After the adhesion incubation, dishes were flooded with the same media until further use. Glass bottom dishes were prepared by soaking in Poly-L-lysine for ~25 min, before being rinsed twice in PBS. SiNWs were then sonicated into DMEM + 5% FBS, and allowed to settle ~18 h before being used for cell culture. All rats were used in accordance with the University

of Chicago's Animal Care and Use Protocol (ACUP: 72378) and the National Institutes of Health guidelines.

3.4.4 Ensemble Nanowire Studies

The ensemble rate of NW internalization was approximated using the SiNW-Cell colocalization as a function of time. To achieve this, a series of both phase contrast and dark field micrographs were obtained at each time point (**Figure 3.1a&b, left**) Samples were imaged at predetermined locations, prior to viewing, to prevent sampling bias. In a typical experiment, eight locations were examined for each time point. These images were then post-processed using NIH ImageJ and converted to binary, highlighting the area encompassed by cells and nanowires (**Figure 3.1a&b, right**). For each image, a histogram was obtained, yielding information on cell confluence and NW population respectively. Using ImageJ's built in batch processing, a corresponding "AND" image was produced, which contains only those NWs which were overlapping cellular regions. A histogram of this image was then used to determine the relative SiNW-Cell overlap. A representative composite overlap image (**Figure 3.1.c**) shows the population of SiNWs considered outside the cell, and those considered overlapping with the cells. For SiNW length studies and alternative cell line studies, SiNWs grown from 100 nm seed AuNPs were used and overlap reporter values were recorded 24h after the cells were seeded. In the length dependent study, the average length of the wires after sonication, measured via DF microscopy were as follows: 10min: 9.81 µm, 20min: 14.5 µm, 30min: 23.1 µm, 40min: 31.7 µm.

3.4.5 Endocytosis Inhibitor Studies

For inhibitor studies, SiNWs grown from 100 nm seed AuNPs were sonicated (7 min) into M200 media with growth supplement (Life technologies) and then allowed to settle overnight. After settling, HUVECs were introduced at ~15% initial confluence, and drugs were administered after 8 hours of incubation. All drugs were obtained from Sigma Aldrich, and were administered at the following concentrations (Dissolved in dimethyl sulfoxide, DMSO): Chloropromazine (2.5 µg/mL), Nyastatin (50 ng/mL), Dynasore (80 µM), Cytochalasin D (5 ng/mL), Annexin V (4 nM & 16 nM). Throughout this process, the cell/NW overlap was monitored by taking alternating DF and PC micrographs ever ~2 h at random substrate locations (selected prior to viewing to avoid sampling bias).

3.4.6 Annexin V Binding Assay

SiNWs were incubated with A5-Cy3 (Sigma Aldrich, from Human Placenta) at 37 °C in 5% CO_2 for ~24 h in the absence and presence of serum proteins (2%, Fetal Bovine Serum) in both phosphate buffered solution (PBS) and M200 media. After incubation, samples were rinsed twice in fresh PBS and imaged under the same optical conditions (i.e. exposure, light intensity, etc). Fluorescent signal intensities were quantified using NIH's imageJ. To correct for background scattering, the signal intensity from a control sample containing only SiNWs and no A5-Cy3 was also measured (~9% relative signal intensity). Additionally, as the glass substrate could also be stained by the A5 protein, DF images were used as a mask to selectivity measure intensities only from the regions containing SiNWs. Reported signal intensities were also normalized by the relative SiNW population.

3.4.7 Chloropromazine Positive Control Drug Studies

To confirm that clathrin was successfully inhibited at these drug concentrations, Txred conjugated transferrin (from human Serum, Life Technologies) was used as a positive control. HUVECs were transferred to fresh glass substrates via trypsinization and allowed to incubate for 8 hours (Figure 3.9). For the inhibitor samples, 6.45 µL of chloropromazine (3.1 mg/mL) dissolved in DMSO was added to 8 mL of M200 growth media, which was then distributed to the HUVEC growth culture for 30 minutes, before adding a final working concentration of 25 µg/mL of conjugated trypsin dissolved in deionized water. For the control samples, a similar process was followed, using blank DMSO containing no chloropromazine. Both samples were then allowed to incubate for 14 hours, before being washed twice in 1x PBS, and then fixed using 4% paraformaldehyde (20 min). The samples were then rinsed twice more in PBS and then imaged at random locations (determined prior to viewing to prevent sample bias) using the same exposure and intensity settings on an Olympus IX71 inverted microscope under a Texas red filter. The mean fluorescent intensity of each image was then obtained using NIH's ImageJ.

3.4.8 MTT Assays

30 nm and 100 nm SiNWs were sonicated (7 minutes) into M200 growth media and transferred to a 96 well plate. Samples were then allowed to settle overnight, before removing the supernate and adding HUVECs to give a final volume of 100 µL per well. After cells were co-cultured with the SiNWs (95% humidity, 37 °C, 5% CO_2) for 3, 5 and 7 days respectively, to each well 20 µL of 5 mg/mL MTT was added. Samples were then incubated with MTT for an additional 3.5 h at 37 °C. Being careful to not disturb the cells,

the media was then gently removed, and 120 µL of DMSO was added to well. Samples were then covered and agitated for 15 minutes, before being place into a plate reader and imaged at 570 nm and 590 nm. For each reading, a control sample of HUVECs cultured under the same conditions, but containing no SiNWs was used. Additionally, blank samples containing only media, and containing only SiNWs in growth media were also run alongside the cellular samples, and were used as a background subtraction metric.

3.4.9 Two-Dimensional Random Walker Model

While monitoring ensemble rates of SiNW internalization, we observed a pattern of nanowire internalization where SiNWs remain stationary on the substrate, while cells migrate across the surface picking up nanowires. This mode of internalization is distinct from normal routes of drug delivery, where the cells are stationary and drugs are mixed ubiquitously into a solution. As a result, this internalization process would be expected to follow a distinct model of kinetics, differing drastically from other drug delivery mechanisms.

The present case of NW internalization can be considered in terms of a two dimensional (2D) random walk model, where cells are diffusive walkers that crawl over the surface of a lattice, with equal probability of moving in any direction. As a cell visits a new lattice site, this area has the chance of containing a nanowire, which the cell can then internalize. Once internalized, a NW will remain with the cell as it moves to new lattice sites, marking the previous site as having been visited. In this case, the

percentage of NWs internalized should be proportional to the total number of sites visited by all of the cells inside of the system. What follows is a model for the number of unique sites visited by an ensemble of random walkers, which we show is in good agreement with experimental data for nanowire internalization.

Variable Definitions:

n = number Density of Walkers (# walkers/ # lattice sites)

τ = Number of steps

$A_1(\tau)$ = Expected number of distinct sites that have been visited by **an individual** walker after τ steps

$A_N(\tau)$ = Expected number of distinct sites that have been visited by **all** walker after τ steps

Pr(τ) = Probability that an individual site has **not** been visited after τ steps

Y(τ) = Probability that an individual site **has** been visited after τ steps

The number of nanowires internalized should be proportional to the total number of distinct sites visited by all of the random walker as a function of time, while the percentage of nanowires, $\mathrm{Y}(\tau)$, should be equal to this value divided by the total area ($A_N(\tau)/A_{total}$), where A_{total} is the total number of lattice sites. A direct solution for $A_N(\tau)$ is not available but we can use the following formulation.

The probability that a site has not been visited by a single random walker can be taken to be,

$$\mathrm{Pr}(\tau) = 1 - \frac{\mathrm{A}_1(\tau)}{A_{total}} \qquad \textbf{3.2}$$

Therefore, if there are N_w number of walkers it follows that,

$$\Pr(\tau)_N = \prod_{i=1}^{N_w} \Pr(\tau)_i = \left(1 - \frac{A_1(\tau)}{A_{total}}\right)^{N_w} \quad \textbf{3.3}$$

N can also be defined in terms of walker density, such that $N_w = n \cdot A_{total}$, such that

$$\Pr(\tau)_N = \left(1 - \frac{A_1(\tau)}{A_{total}}\right)^{n \cdot A_{total}} = \left(1 - \frac{n \cdot A_1(\tau)}{n \cdot A_{total}}\right)^{n \cdot A_{total}} \quad \textbf{3.4}$$

using the property of Euler's number, e, such that,

$$\lim_{n \to \infty} \left(1 + \frac{x}{n}\right)^n = e^x \quad \textbf{3.5}$$

it can be shown that for a large number of lattice sites, such that $A_{total} \to \infty$ than the probability that an individual site has not been visited by a random walker after τ steps is given by:

$$\Pr(\tau)_N = e^{-n \cdot A_1(\tau)} \quad \textbf{3.6}$$

This value while useful, is dependent on the nebulous term $A_1(\tau)$, the expected number of distinct sites that have been visited by a single 2D random walker after τ steps. A rigorous determination of this function is beyond the scope of this manuscript, however in 1951 Dvoretzky & Erdös[16] demonstrated that in a 2D system this follows the form of:

$$A_1(\tau) = \frac{\pi \tau}{\log \tau} + B_o \quad \textbf{3.7}$$

where B_o is a higher order correction term, which we have taken to be constant over the duration of the experiment. As the probability that a given site will have been visited, $Y(\tau)$, is defined by the function $Y(\tau) = 1 - \Pr(\tau)_N$, it follows that,

$$Y(\tau) = \frac{A_1(\tau)}{A_{total}} = 1 - e^{\frac{-n\pi\tau}{\log \tau} + B_o} \quad \textbf{3.8}$$

However, this formulation assumes that all lattice sites contain SiNWs and that each visible wire is available for internalization, an assumption which may prove improbable

due to morphological restrictions or limitations in surface functionalization of the NWs. Therefore, this result is better expressed as,

$$\mathrm{Y}(\tau) = \mathrm{M_w} - e^{\frac{-n\pi\tau}{\log\tau} + B_o} \qquad \textbf{3.9}$$

where M_w is the maximum percentage of NWs available for internalization. In practice, M_w is found to have values of ~0.96 in HUVECs, suggesting that it's substitution is not completely unwarranted, however this distinction could prove useful when looking at future nanoconstructs which have less ubiquitous rates of internalization.

This function than gives us the probability for a NW to internalized, which should be reflected in the percentage of nanowires that will have been internalized after τ steps, however this function only holds in the discreet site limit and over a large number of step. Therefore to use this in a real world situation, it becomes desirable to take this into the continuum limit. While a rigorous expansion to the continues case is beyond the scope of this manuscript, some features of the continues model are readily apparent. For example, τ must be proportionate to time, t, such that $\tau = D_t \cdot t$, where D_t is a diffusion constant relating the amount of time it takes to move a single step across the lattice. In other words, the time it takes for a cell to migrate a single body length away from its initial site. Similarly, the value of $\log\tau$, applies only in the long term limit, and is therefore inappropriate for modeling real world experiments, as cells have a relatively slow migration rate. Finally, the density of random walkers does not remain constant over the duration of the experiment, as cells are able to undergo mitosis, therefore the number density of walkers is more appropriately measured as function of percent confluence, C(t), (the percentage of the surface covered by cells) which can be related to number density by the function $n = C(t)/A_{Cell}$, where A_{Cell} is the average area

covered by an individual cell. All of these factors taken into account result in continuum model equation of the form:

$$\mathrm{Y(t)} = \mathrm{M_w} - \mathrm{B}e^{\frac{-\pi D_t \cdot C(t) \cdot t}{A_{Cell}}} \qquad \textbf{3.1}$$

where the rate constant, D_t , can be used as the single free fitting parameter. This yields us a good expression for the rate of NW internalization. However, there is an additional boundary conditions to consider. At time zero we know that the expected overlap, $Y_{(0)}$, should be equal to initial confluence $C_{(0)}$. That is to say that the number of sites initially occupied by walkers is proportional to the initial number of walkers. Additionally, at t=0, the right side of equation **3.1** collapses, giving the expression:

$$\mathrm{Y_{(0)}} = C_{(0)} = \mathrm{M_w} - \mathrm{B} \qquad \textbf{3.10}$$

which upon rearrangement yields, $B = M_w - C_{(0)}$. This allows B, which was initially conceived of as a higher order correction term, to be expressed in terms of the experimentally determined constants M_w and $C_{(0)}$. For simplicity we leave the expression for NW internalization in the form of equation **3.1**, however noting that the correction term, B, can be substituted for experimentally determined values.

3.5 References

1. Harush-Frenkel, O., Debotton, N., Benita, S. & Altschuler, Y. Targeting of nanoparticles to the clathrin-mediated endocytic pathway. *Biochem. Biophys. Res. Commun.* **353,** 26–32 (2007).

2. Chithrani, B. D. & Chan, W. C. W. Elucidating the mechanism of cellular uptake and removal of protein-coated gold nanoparticles of different sizes and shapes. *Nano Lett.* **7,** 1542–50 (2007).

3. Herd, H. *et al.* Nanoparticle Geometry and Surface Orientation Influence Mode of Cellular Uptake. *ACS Nano* **7,** 1961–1973 (2013).

4. Zhu, J. *et al.* Size-dependent cellular uptake efficiency, mechanism, and

cytotoxicity of silica nanoparticles toward HeLa cells. *Talanta* **107,** 408–415 (2013).

5. Nel, A. E. *et al.* Understanding biophysicochemical interactions at the nano-bio interface. *Nat. Mater.* **8,** 543–57 (2009).

6. Geng, Y. *et al.* Shape effects of filaments versus spherical particles in flow and drug delivery. *Nat. Nanotechnol.* **2,** 249–55 (2007).

7. Gratton, S. E. a *et al.* The effect of particle design on cellular internalization pathways. *Proc. Natl. Acad. Sci.* **105,** 11613–11618 (2008).

8. Kelly, P. M. *et al.* Mapping protein binding sites on the biomolecular corona of nanoparticles. *Nat. Nanotechnol.* **10,** 472–479 (2015).

9. Ge, C. *et al.* Binding of blood proteins to carbon nanotubes reduces cytotoxicity. *Proc. Natl. Acad. Sci. U. S. A.* **108,** 16968–73 (2011).

10. Lee, J.-H., Zhang, A., You, S. S. & Lieber, C. M. Spontaneous Internalization of Cell Penetrating Peptide-Modified Nanowires into Primary Neurons. *Nano Lett.* **16,** 1509–1513 (2016).

11. Beaux, M. F. *et al.* Fibronectin Bonding to Nanowires and Their Internalization by Epithelial Cells. *J. Biomed. Nanotechnol.* **2,** 23–28 (2006).

12. Conner, S. D. & Schmid, S. L. Regulated portals of entry into the cell. *Nature* **422,** 37–44 (2003).

13. Doherty, G. J. & McMahon, H. T. Mechanisms of Endocytosis. *Annu. Rev. Biochem.* **78,** 857–902 (2009).

14. Albrecht-Buehler, G. The phagokinetic tracks of 3T3 cells. *Cell* **11,** 395–404 (1977).

15. Scott, W. N., McCool, K. & Nelson, J. Improved Method for the Production of Gold Colloid Monolayers for Use in the Phagokinetic Track Assay for Cell Motility. *Anal. Biochem.* **287,** 343–344 (2000).

16. Dvoretzky, A. & Erdös, P. Some problems on random walk in space. in *Proceedings of the Second Berkeley Symposium on Mathematical Statistics and Probability* 353–367 (University of California Press, Berkeley, Calif., 1951).

17. Mayor, S. & Pagano, R. E. Pathways of clathrin-independent endocytosis. *Nat. Rev. Mol. Cell Biol.* **8,** 603–612 (2007).

18. Blechinger, J. *et al.* Uptake kinetics and nanotoxicity of silica nanoparticles are cell type dependent. *Small* **9,** 3970–80, 3906 (2013).

19. Agarwal, R. *et al.* Mammalian cells preferentially internalize hydrogel nanodiscs over nanorods and use shape-specific uptake mechanisms. *Proc. Natl. Acad. Sci. U. S. A.* **110,** 17247–52 (2013).

20. Kirkham, M. & Parton, R. G. Clathrin-independent endocytosis: New insights into caveolae and non-caveolar lipid raft carriers. *Biochim. Biophys. Acta - Mol. Cell Res.* **1745,** 273–286 (2005).

21. Chen, C.-L. *et al.* Inhibitors of clathrin-dependent endocytosis enhance TGFbeta signaling and responses. *J. Cell Sci.* **122,** 1863–71 (2009).

22. Brown, D. M. *et al.* An in vitro study of the potential of carbon nanotubes and nanofibres to induce inflammatory mediators and frustrated phagocytosis. *Carbon N. Y.* **45,** 1743–1756 (2007).

23. Boyles, M. S. P. *et al.* Multi-walled carbon nanotube induced frustrated phagocytosis, cytotoxicity and pro-inflammatory conditions in macrophages are length dependent and greater than that of asbestos. *Toxicol. Vitr.* **29,** 1513–1528 (2015).

24. Schinwald, A. & Donaldson, K. Use of back-scatter electron signals to visualise cell/nanowires interactions in vitro and in vivo; frustrated phagocytosis of long fibres in macrophages and compartmentalisation in mesothelial cells in vivo. *Part. Fibre Toxicol.* **9,** 34 (2012).

25. Fan, X. Macrophage Surface Expression of Annexins I and II in the Phagocytosis of Apoptotic Lymphocytes. *Mol. Biol. Cell* **15,** 2863–2872 (2004).

26. Xie, R. *et al.* Phagocytosis by macrophages and endothelial cells inhibits procoagulant and fibrinolytic activity of acute promyelocytic leukemia cells. *Blood* **119,** 2325–2334 (2012).

27. Callahan, M. K. Phosphatidylserine expression and phagocytosis of apoptotic thymocytes during differentiation of monocytic cells. *J. Leukoc. Biol.* **74,** 846–856 (2003).

28. Callahan, M. K., Williamson, P. & Schlegel, R. a. Surface expression of phosphatidylserine on macrophages is required for phagocytosis of apoptotic thymocytes. *Cell Death Differ.* **7,** 645–653 (2000).

29. Kolb, S., Vranckx, R., Huisse, M.-G., Michel, J.-B. & Meilhac, O. The phosphatidylserine receptor mediates phagocytosis by vascular smooth muscle cells. *J. Pathol.* **212,** 249–259 (2007).

30. Holthuis, J. C. M. & Levine, T. P. Lipid traffic: floppy drives and a superhighway. *Nat. Rev. Mol. Cell Biol.* **6,** 209–20 (2005).

31. Wu, Y., Tibrewal, N. & Birge, R. B. Phosphatidylserine recognition by phagocytes:

a view to a kill. *Trends Cell Biol.* **16,** 189–197 (2006).

32. van Engeland, M., Nieland, L. J., Ramaekers, F. C., Schutte, B. & Reutelingsperger, C. P. Annexin V-affinity assay: a review on an apoptosis detection system based on phosphatidylserine exposure. *Cytometry* **31,** 1–9 (1998).

33. Tenzer, S. *et al.* Rapid formation of plasma protein corona critically affects nanoparticle pathophysiology. *Nat. Nanotechnol.* **8,** 772–81 (2013).

34. Lesniak, A. *et al.* Effects of the presence or absence of a protein corona on silica nanoparticle uptake and impact on cells. *ACS Nano* **6,** 5845–5857 (2012).

35. Cedervall, T. *et al.* Understanding the nanoparticle-protein corona using methods to quantify exchange rates and affinities of proteins for nanoparticles. *Proc. Natl. Acad. Sci. U. S. A.* **104,** 2050–2055 (2007).

36. Patolsky, F., Zheng, G. & Lieber, C. M. Fabrication of silicon nanowire devices for ultrasensitive, label-free, real-time detection of biological and chemical species. *Nat. Protoc.* **1,** 1711–24 (2006).

37. Hsiao, I.-L. *et al.* Size and Cell Type Dependent Uptake of Silica Nanoparticles. *J. Nanomed. Nanotechnol.* **05,** (2014).

38. Flannagan, R. S., Jaumouillé, V. & Grinstein, S. The Cell Biology of Phagocytosis. *Annu. Rev. Pathol. Mech. Dis.* **7,** 61–98 (2012).

39. Mosmann, T. Rapid colorimetric assay for cellular growth and survival: Application to proliferation and cytotoxicity assays. *J. Immunol. Methods* **65,** 55–63 (1983).

40. Gerlier, D. & Thomasset, N. Use of MTT colorimetric assay to measure cell activation. *J. Immunol. Methods* **94,** 57–63 (1986).

41. Cacchioli, a *et al.* Cytocompatibility and Cellular Internalization Mechanisms of SiC/SiO 2 Nanowires. *Nano Lett.* **14,** 4368–4375 (2014).

42. Brönstrup, G. *et al.* Optical Properties of Individual Silicon Nanowires for Photonic Devices. *ACS Nano* **4,** 7113–7122 (2010).

43. Brönstrup, G. *et al.* A precise optical determination of nanoscale diameters of semiconductor nanowires. *Nanotechnology* **22,** 385201 (2011).

44. Gores, G. J., Herman, B. & Lemasters, J. J. Plasma membrane bleb formation and rupture: A common feature of hepatocellular injury. *Hepatology* **11,** 690–698 (1990).

45. Huang, Y. Y., Knowles, T. P. J. & Terentjev, E. M. Strength of Nanotubes, Filaments, and Nanowires From Sonication-Induced Scission. *Adv. Mater.* **21,**

3945–3948 (2009).

46. Kastan, M. B. & Bartek, J. Cell-cycle checkpoints and cancer. *Nature* **432,** 316–323 (2004).

47. Gehen, S. C., Staversky, R. J., Bambara, R. a, Keng, P. C. & O'Reilly, M. a. hSMG-1 and ATM sequentially and independently regulate the G1 checkpoint during oxidative stress. *Oncogene* **27,** 4065–4074 (2008).

48. Mortensen, N. P. *et al.* Dynamic development of the protein corona on silica nanoparticles: composition and role in toxicity. *Nanoscale* **5,** 6372–80 (2013).

49. Austin II, J. R. in *Arabidopsis Protocols* (eds. Sanchez-Serrano, J. J. & Salinas, J.) **1062,** 473–486 (Humana Press, 2014).

50. Giannone, G. Super-resolution links vinculin localization to function in focal adhesions. *Nat. Cell Biol.* **17,** 845–847 (2015).

51. Burridge, K. & Mangeat, P. An interaction between vinculin and talin. *Nature* **308,** 744–746 (1984).

52. Horwitz, A., Duggan, K., Buck, C., Beckerle, M. C. & Burridge, K. Interaction of plasma membrane fibronectin receptor with talin—a transmembrane linkage. *Nature* **320,** 531–533 (1986).

53. Zimmerman, J. F. *et al.* Free-Standing Kinked Silicon Nanowires for Probing Inter- and Intracellular Force Dynamics. *Nano Lett.* **15,** 5492–5498 (2015).

Chapter 4. Silicon Nanowire As Intracellular Force Probes•

4.1 Introduction

As has been previously discussed, synthetically-enabled silicon nanowires (SiNWs) are of particular interest, as they can be rationally designed[1,2] and have well-defined structural and material properties,[3–5] while silicon is one of the few semiconductor materials to display low cytotoxicity.[6,7] This diverse set of functionalities makes SiNWs a promising class of material for designing a wide set of nanoscopic "building blocks" for use in a biological context. This has the potential of leading to a host of possible device designs, which could be used in a range of applications such as intracellular electronic stimulators or biosensors. So far we have shown that these devices are capable of being internalized, and that they are endocytosed primarily through a phagocytosis pathway, however we have yet to demonstrate a discreet application. To show that devices capable of substrate-independent operation are achievable, here we demonstrate that SiNWs can serve as free-standing inter- and intracellular probes capable of continuous extended (>1hr) force monitoring. In doing this, we hope that this work can serve as a prelude to other nanowire based sensors and therapeutic devices.

Mechanical forces were chosen as a target of study, as they play an important role in regulating physiological processes, with the extracellular matrix (ECM) and cytoskeletal filaments providing mechanical cues for inter- and intracellular signaling[8–10]. Correct cell functionality often depends on the precise molecular integration of both

• A portion of this work has been adapted with permission from Zimmerman J. F. et. al. Nano Lett. 15, 5492–5498 (2015). Copyright 2015 American Chemical Society.

force-generating and force-transducing machinery, including such examples as cell migration and cytokinesis, where the controlled interplay between motor proteins, cytoskeletal filaments and the ECM result in dramatic morphological and chemical changes for the entire cell.[11] Force generation and transduction can also play an important role in local processes, such as vesicle and organelle transport,[12] or in the small-scale reorganization of the cytoskeleton network during molecular internalization and vessicular secretion processes.[13,14] Finally, cells also use force transduction to sense their environment, responding to external stimuli by activating mechanoreceptors, converting forces into chemical signals, or by transferring information directly to the nuceleus via the cytoskeleton, a process which is believed to directly modulate gene transcription[15].

As mechanical cues can play an important role in regulating cell shape, function and fate[9], understanding these forces is an important step in regulating bio-functionality and plays an important role in designing new therapeutic tissue regeneration and drug delivery systems[16]. To date our ability to probe these systems in a minimally invasive way is limited. Deformable substrate,[17–19] molecular probe,[20–22] and optical tweezer[22] methods can measure cellular force dynamics with high spatio-temporal resolution. However, there is still a need to develop a simple system capable of continuously probing inter- and intracellular forces over long periods of time. To achieve this such a system would need to be resistant to both localized photothermal heating[23,24] and fluorescent bleaching,[25] as these limit experimental time-scales.

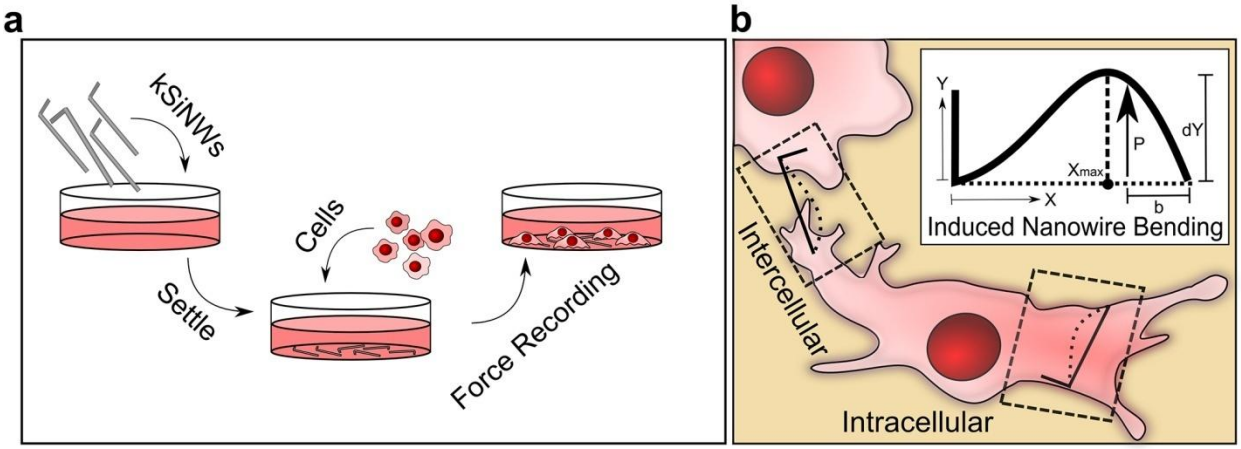

Figure 4.1 kSiNW-based Force Sensing Schematics.
(**a**) Overview schematic, showing the drug like distribution of kSiNWs to cells, and their internalization for use as as intra- and inter-cellular force sensors. (**b**) Possible interactions between kSiNW and cytoskeletal filaments, with entanglement enabling force transduction dynamics. (b, inset) Model of kSiNW deformation. The short arm (vertical beam, left) anchors the kSiNW, while the longer arm experiences cellular induced bending. P, b and dY are the load, its distance from the tip and the deflection respectively, while x_{max} is the x-position of the maximum deflection. Adapted with permission from Zimmerman J. F. et. al. *Nano Lett 2015*. Copyright 2015 American Chemical Society.

With this in mind, kinked silicon nanowires (kSiNWs) were selected as potential cellular force probes. First, as kSiNWs are easily distributed in a drug-like fashion to cellular systems (**Figure 4.1a**), they are relatively simple to implement, and can be used in wide array of experimental conditions to monitor both inter- and intracellular force processes (**Figure 4.1b**). Second, the kinked structure serves as both a visual and physical anchor, limiting device rotation and translation, ensuring that force is transduced primarily to mechanical strain. The operational principle of this platform, relies on the maintained force-strain relationship between nanowires and their microenvironment (**Figure 4.1**). Nanowire crystal deformation results in the buildup of stress and the generation of an elastic restorative force. To prevent relaxation a consistent force must be applied to the wire. Therefore, by monitoring the structural deformations of the SiNW, the present force being applied to the wire can be

determined. As a result, kSiNWs can be used as a platform for studying the spatial-temporal evolution of forces within the cellular microenvironment.

kSiNW force probes are also promising as they only require structural deformation information, which can be obtained optically. Using the previously introduced Scatter Enhanced Phase Contrast (SEPC) microscopy (See **Section 2.2.2**), a simple to implement Dark-field/Phase Contrast optical imaging modality, allows for the long term monitoring of kSiNW/cellular interactions. As this method requires only low intensity light sources, it is easily implemented using most conventional microscopy setups, requiring only slight modification (i.e. the installation of an inexpensive, commercially available ring LED emitter). Additionally, the use of low intensity light sources and the avoidance of fluorescent tags, mark this method as being resistant to both photobleaching and photothermal effects,[26] making it appropriate for long term continuous force studies. Here we demonstrate studies of >1 h durations with sampling on the single second time scale. This provided long duration probing with high fidelity temporal information, however in principle this period could be substantially expanded. Given the relative ease of implementation, and extended time-scales of these studies, this technique offers substantial promise for researchers interested in exploring mechanical signal transduction, as both inorganic and biological components can be imaged simultaneously. Finally, while this approach demonstrates that we can use SiNWs as probes for intracellular forces, in broader terms, these results shows that nanowire based devices capable of substrate independent operation are achievable, not just in the future, but right now.

4.2 Results and Discussion

4.2.1 Beam Bending and Euler-Bernoulli Beam Theory

Before exploring their use as intracellular force probes, we will first examine the underlying principles of beam bending, understanding how these materials respond to forces in their local environment and how they can be used as intracellular devices. The operational principle behind kinked silicon nanowires as force probes is relatively straightforward. The length of the silicon nanowire can be treated as a beam, with analogous properties to those used on the macroscopic scale by architects and engineers. When a load is applied to a beam, the structure will undergo a deformation, with one portion of the beam being stretched and the other being compressed. This creates stress in the beam, with the beam experiencing both compression and tension (**Figure 4.2a**). In the static case, these tensile forces are in equilibrium with the materials intermolecular forces, which act as a restorative force, giving the deformed beam a defined shape which is dependent only on the beam's materials properties and the applied load. This means that once the external load is removed, the beam will return to its initial state as long as the material underwent only an elastic deformation. One result of this is that the shape of bent beam can be used to measure external forces, as long as the initial state is known, and the beam's material properties are well understood. In the case of silicon nanowire, the initial beam's shape[1,27,28] and material's properties[29,30] are both well defined, making them a good candidate for studying external forces using beam deformation.

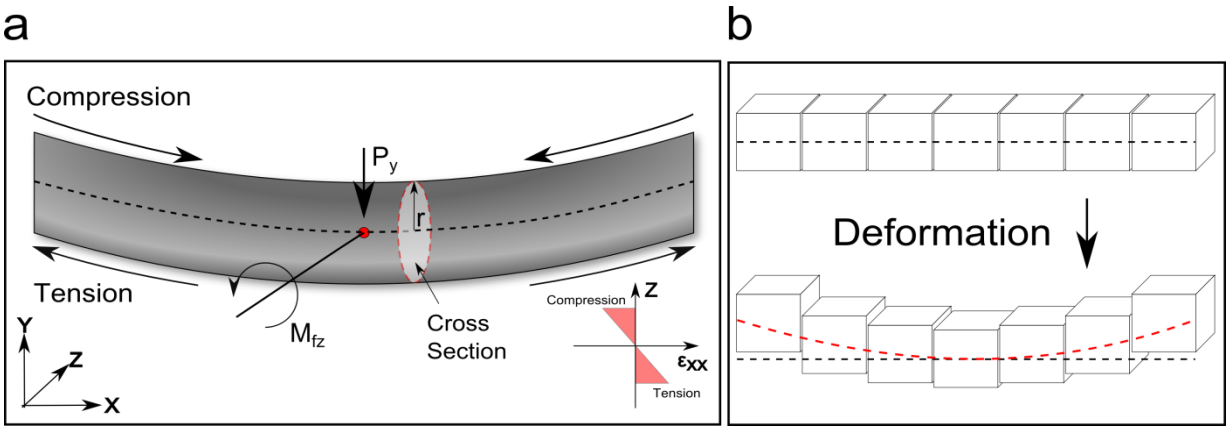

Figure 4.2 Beam Bending Schematic
(**a**) A cylindrical beam with an applied force load, P, experiencing both compression and tension. Neutral axis displayed as a dashed line. Inset showing the corresponding strain, ε_{xx}, above and below the neutral axis. As the beam deforms, it experiences a bending moment, $M_{fz,}$. (**b**) Deformation of parallel plates, as the neutral axis deforms.

To understand the forces being applied to the kinked probe, we need a working understanding of how beams deform under a load, and the resulting curvatures. This behavior is well explained using Euler-Bernoulli beam theory, which as work horse of the civil engineering world, offers the advantage of being able to analytically determine the load-carrying and deflection characteristics of a beam. This allows for quick calculations while making only minor assumptions about the system.

Euler-Bernouli theory's main driving equation is that the beam's bending moment, $M_{(x)}$, which describes how much a beam bends as a function force and distance (**Figure 4.6a**) in a x,y Cartesian plane, can be approximated for linearly elastic beams as[31]:

$$M(x) \approx -EI\frac{d^2y}{dx^2} \qquad \textbf{4.1}$$

where E and I are the material's young's modulus and the cross-sectional moment of inertia respectively, with the cross-sectional moment of inertia depending on a beam's geometric shape; relating to its cross sectional area, and the geometric distribution of its perimeter about an axis. This property, which is given in units of meters to the fourth

power, is useful in beam bending, as it relates how different shaped beams, such as rectangles, cylinders and I-beams, will deform under pressure as defined by:

$$I = \iint r^2 dA \qquad \textbf{4.2}$$

where r is the distance between the centroid of an object and it's perimeter (**Figure 4.6a**), and A is the object's area. In the case where the desired reference frame is the x-axis, r^2 can be further substituted for y^2.

To derive equation **4.1**, we start by using the assumptions that beams deform as solid parallel cross sections, where cross sections that were originally normal to the longitudinal axis of the beam remain planar and normal after deformation (**Figure 4.2b**). This provides an approximation for the load strain, ε_{xx}, which is the relative displacement of two points across an object after deformation with respect to the x-axis, such that:

$$\varepsilon_{xx} = -y/\rho \qquad \textbf{4.3}$$

where ρ is the radius of curvature. In a linearly elastic material, strain can be related to the stress, σ, of a material through its Young's modulus, E, as (**Figure 4.3**):

$$\sigma_{xx} = \mathrm{E}\varepsilon_{xx} \qquad \textbf{4.4}$$

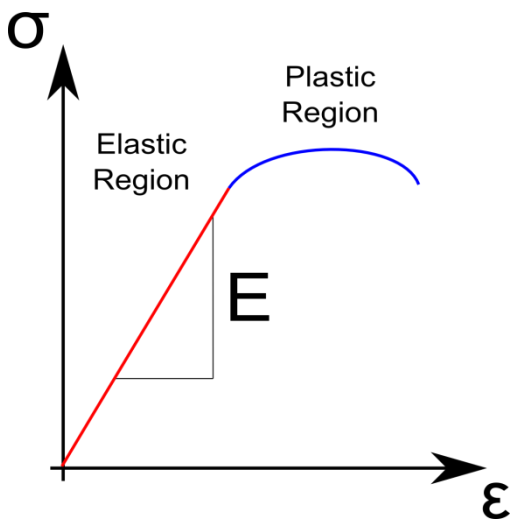

Figure 4.3 Stress-Strain Curve of An Elastic Material
Stress (σ), is shown as a function of strain (ε) for a typical elastic material, with the elastic (red) and plastic (blue) regions indicated. The slope of the linear elastic region yield's the materials Young's modulus, E.

In turn, both of these values can be related back to the beams bending moment, which when in static equilibrium, is defined as the stress being applied over an area such that:

$$M(x) = \iint \sigma_{xx} \cdot y \, dA \qquad \textbf{4.5}$$

Substituting equations **4.8** and **4.3** into equation **4.9**,then yields,

$$M(x) = \frac{-E}{\rho} \iint y^2 \, dA = -EI/\rho \qquad \textbf{4.6}$$

From here we can recall from the calculus of variations, that the curvature of a plane at point Q(x,y) is given by,

$$\frac{1}{\rho} = \frac{\frac{d^2y}{dx^2}}{\left[1 + \left(\frac{dy}{dx}\right)^2\right]^{3/2}} \approx \frac{d^2y}{dx^2} \qquad \textbf{4.7}$$

for elastic beams, we can make a "small angle" approximation when deformations are not extreme, where the square of the slope, dy/dx, can be taken as negligible as

compared to unity. Upon rearrangement of **4.7**, this result can be used with **4.6** to show that you can obtain the second order differential equation **4.1**, the governing equation for Euler-Bernoulli elastic beam theory.

The resulting expression is a powerful tool for understanding structural deformations, and can be used to analyze a large variety of materials, geometric shapes, and force loads, marking its flexibility and general use for a wide range of configurations. To see if this is applicable to kSiNWs, we can review the approximations needed for this governing equation, noting that each is reasonable for our system:

1. Minimal Cross Sectional Variation. The cross section is either constant or varies smoothly across the beam segment.

2. Planer Cross Sections. Cross sections that were originally normal to the longitudinal axis of the beam remain planar and normal after deformation.

4.Negligable Strain Energy. The bending moment of deformation accounts for all internal strain energies of the member. All other contributions, including transverse shear and axial force, are considered negligible.

5. Small Angle Approximation. All transverse rotations, deflections and deformations are considered small such that the beams are considered continues and the approximation of infinitesimal deformations applies.

6. Usual Material Properties. The material is assumed to be an isotropic and elastic material which obeys Hook's laws, allowing the use of Young's modulus.

4.2.2 Simply Supported Asymmetric Beams

To determine the force being applied to a SiNW, we need to go from the governing Euler-Bernouli equation (**4.1**) to an equation for the deflection of the beam, Y(x),

expressed in terms of the applied force load, P. For our force probes, we have assumed a 2D static model of interactions, where the forces being applied to the beam are in equilibrium with the beam's restorative forces. While this may seem strange for measuring forces over time in a cell, an inherently dynamic process, this acts as a reasonable assumption due to the differences in time scale. Namely, relaxations of stress in silicon nanowires happen on the millisecond to second timescale, while cellular forces propagate over the span of minutes. Therefore, from a materials perspective, the cell is acting as a relatively static environment. Additionally, for this model we have also assumed a simply-supported beam with an asymmetric load, an assumption whose merits will be discussed in further detail. By assuming a simply supported beam, we are stating that the ends of the nanowire are fixed in space, such that they are unable to move from a spatial pinned x, y, coordinate, but are free to rotate about that point. This spatial pinning results in a different morphology of beam deformation, that is consistent with those observed during intracellular force processes.

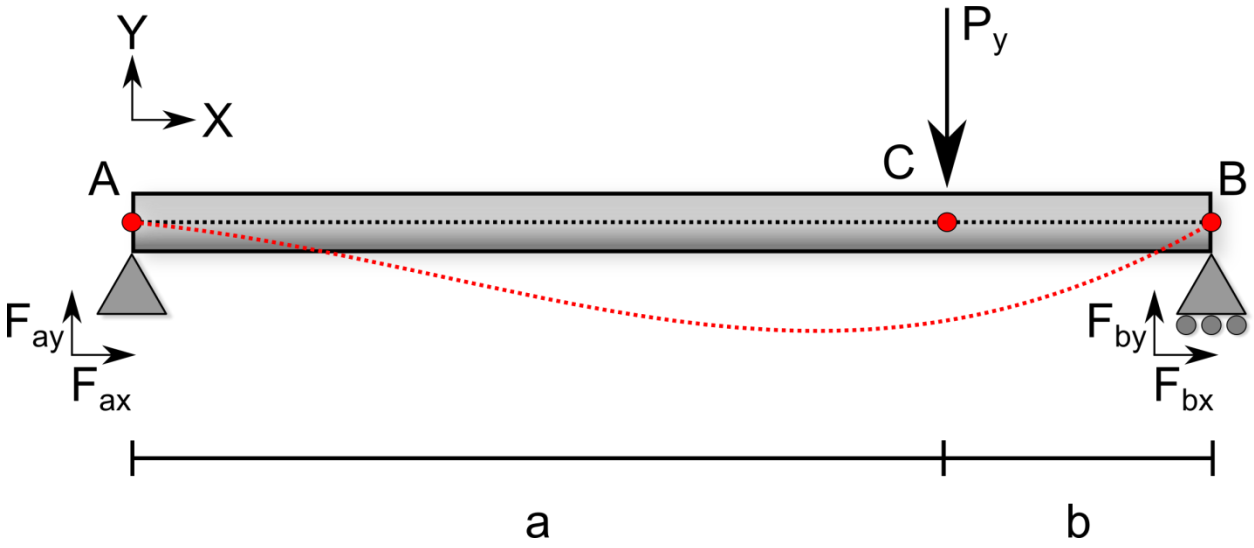

Figure 4.4 Simply Supported Beam Free Body Diagram
Diagram depicting a load (P_y) being applied transverse to a simply supported beam's neutral axis (black line) at position C, with the resulting beam deflection (red). Free body forces (F_x &F_y) are given for the supports at point A and B.

For simply supported beam, a derivation for the deformation of the beam, Y(x), can be found by summing the forces over a free body diagram (**Figure 4.4**) and using the Euler-Bernoulli formulation for the beam's internal bending moment M(x), which are derived as:

$$M(x) = -EI\frac{d^2y}{dx^2} \tag{4.1}$$

Drawing the free body diagram, and taking the moments about the portions AC and BC, the bending moments can also be defined as:

$$M(x) = F \cdot \mathrm{d} = \begin{cases} \mathrm{F_{ay}} \cdot \mathrm{x} & \text{if} \quad 0 \leq \mathrm{x} \leq \mathrm{a} \\ \mathrm{F_{by}} \cdot (\mathrm{L} - \mathrm{x}) & \text{if} \quad \mathrm{a} < x \leq L \end{cases} \tag{4.8}$$

with L giving the length of the entire beam, such that L = a+b. To find the forces being applied at each point, we can use the free body diagram, assuming in the static case that all forces must sum to zero, or that $\sum F = 0 = F_{ay} + F_{by} - P$. Using this expression, in combination with geometric considerations, yields:

$$M(x) = \begin{cases} \frac{\mathrm{Pb}}{\mathrm{L}} \cdot \mathrm{x} & \text{if} \quad 0 \le \mathrm{x} \le \mathrm{a} \\ \frac{\mathrm{Pa}}{\mathrm{L}} \cdot (\mathrm{L} - \mathrm{x}) & \text{if} \quad \mathrm{a} < x \le L \end{cases} = \begin{cases} \frac{\mathrm{Pbx}}{\mathrm{L}} & \text{if} \quad 0 \le \mathrm{x} \le \mathrm{a} \\ \frac{\mathrm{Pbx}}{\mathrm{L}} - \mathrm{P}(\mathrm{x} - \mathrm{a}) & \text{if} \quad \mathrm{a} < x \le L \end{cases} \qquad \textbf{4.9}$$

This alternate expression for the bending moment **4.9**, can then be compared to that offered through Euler-Bernoulli beam theory, **4.1**. Treating this as an ordinary differential equation (ODE), and taking the integral then provides the following four equations:

$$-EI \cdot Y_a'(x) = \frac{\mathrm{Pbx}^2}{2\mathrm{L}} + \mathrm{C}_1 \qquad \textbf{4.10}$$

$$-EI \cdot Y_b'(x) = \frac{\mathrm{Pbx}^2}{2\mathrm{L}} - \frac{\mathrm{P}(\mathrm{x} - \mathrm{a})^2}{2} + \mathrm{C}_2 \qquad \textbf{4.11}$$

$$-EI \cdot Y_a(x) = \frac{\mathrm{Pbx}^3}{6\mathrm{L}} + \mathrm{C}_1\mathrm{x} + \mathrm{C}_3 \qquad \textbf{4.12}$$

$$-EI \cdot Y_b(x) = \frac{\mathrm{Pbx}^3}{6\mathrm{L}} - \frac{\mathrm{P}(\mathrm{x} - \mathrm{a})^3}{6} + \mathrm{C}_2\mathrm{x} + \mathrm{C}_4 \qquad \textbf{4.13}$$

where $\mathrm{C_i}$ stands for the respective constants of integration. For ease of notation, the piecewise function has been separated into its corresponding segments, with $Y_a(x)$ and $Y_a'(x)$ giving the deflection of the beam and it's first order derivative with respect to x, for the segment $0 \le \mathrm{x} \le \mathrm{a}$, while $Y_b(x)$ and $Y_b'(x)$ describe the $\mathrm{a} < x \le \mathrm{L}$ segment.

These four governing equations then provide four unknowns. To solve for these, we need to bring in additional information, using the system's boundary conditions. As we have assumed a simply supported beam we can use our knowledge of fixed ends, such that $Y_a(0) = 0$ and $Y_b(L) = 0$. Additionally, Euler-Bernoulli beam theory assumes continues deflection, such that $Y_a(a) = Y_b(a)$ and $Y_a'(a) = Y_b'(a)$. Using these four boundary conditions, we can then substitute them into equations **4.10-13** to solve for the four unknowns.

Working through this, the boundary condition $Y_a(0) = 0$ with equation **4.12** yields

$$C_3 = 0 \tag{4.14}$$

and $Y_b(L) = 0$ with equation **4.13** gives,

$$0 = \frac{\mathrm{PbL}^2}{6} - \frac{\mathrm{Pb}^3}{6} + \mathrm{C_2L} + \mathrm{C_4} = \frac{\mathrm{Pb(L^2 - b^2)}}{6} + \mathrm{C_2L} + \mathrm{C_4} \tag{4.15}$$

Using $Y_a'(a) = Y_b'(a)$, let's us compare equations **4.10** and **4.11** revealing,

$$C_1 = C_2 \tag{4.16}$$

while $Y_a(a) = Y_b(a)$, with equations **4.12** and **4.13** gives,

$$C_4 = C_3 = 0 \tag{4.17}$$

Having used these boundary conditions, we can then substitute equation **4.17** back into equation **4.15** to obtain an expression for C_1 and C_2, solving for all of the unknowns in the system:

$$C_1 = C_2 = \frac{-\mathrm{Pb(L^2 - b^2)}}{6\mathrm{L}} \tag{4.18}$$

Substituting these back into equations **4.12** and **4.13**, we can recombine the piecewise polynomial to yield a final expression for the deflection of the beam in terms of force,

$$Y(x) = \begin{cases} \dfrac{\mathrm{Pbx(L^2 - b^2 - x^2)}}{6\mathrm{LEI}} & \text{if} \quad 0 \le \mathrm{x} \le \mathrm{a} \\ \dfrac{\mathrm{Pbx(L^2 - b^2 - x^2)}}{6\mathrm{LEI}} + \dfrac{\mathrm{P(x - a)^3}}{6\mathrm{EI}} & \text{if} \quad \mathrm{a} < x \le L \end{cases} \tag{4.19}$$

Equation **4.19**, a solution for the deflection of a simply-supported beam under an asymmetric point load, can be used to solve for the forces that a kSiNW beam experiences during intracellular contraction, and will serve as one of the driving equations for our sensors.

In using this mechanical model there are a few considerations. First, the exact load configuration of a real system is a three-dimensional composite of both cytoskeleton and cytosolic forces, however here we have assumed a two-dimensional point like load. Assuming a point like load is a fine approximation as it provides a good

estimate for the total sum of the component forces experienced by the SiNW in the x,y dimension, however additional out of plane forces may be also be experienced, which this model does not account for. Second, our method assumes pinned edges, an assumption which is reasonable given the NWs are ~30 µm long with the tips showing an average velocity of less than 1.4 µm/min (<5% displacement/minute) (**Figure 4.5**). This demonstrated limited spatial movement which is on par with the underlying cell's motility. Additionally, we have found that the deformations predicted using these boundary conditions matched well with experimentally observed values (See **Section 4.4.2**). Finally, while the current model is robust to a wide range of load conditions and is of relative computational ease, we note that other force models could also be considered for future use, for instance local curvature,[32,33] and finite element[34] analysis methods.

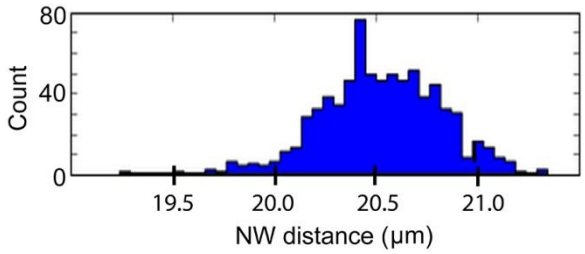

Figure 4.5 Distribution of SiNW Arm Length Changes.
Distribution of SiNW arm length changes. The distance between left tip and kink of a single wire does not vary much during intercellular interactions, indicating a minor buckling and torque contribution. Adapted with permission from Zimmerman J. F. et. al. *Nano Lett 2015*. Copyright 2015 American Chemical Society.

4.2.3 Kinked Force Probes

Kinked Silicon Nanowires (kSiNWs) were selected in particular over straight wires as they offer several distinct advantages. In a previous section we briefly mentioned that

kinked SiNWs were selected as force probes because they served as "physical and visual" anchors. In the case of visual anchors, the kinked structure acts as a marker for SiNW rotation as opposed to SiNW bending. As each process requires a fundamentally different applications of force by the cell, we need a method for distinguishing between these two events. The kink offers a simple method for overcoming this challenge by providing an additional frame of reference. A more precise definition would be that the "kinked" structure acts as an orthogonal basis vector for the projection of the 3D object's shape onto the 2D imaging plane, allowing for the distinguishability of rotations events from deformations (**Figure 4.6**). To understand how the kinked structure achieves this, we need to first look at what information is available using traditional optical microscopy. Namely, the deformation information we collect on the SiNW, is based on the two dimensional projection of the SiNW onto the imaging plane. However, the SiNW is a 3D object which can also be deformed transverse to the imaging plane. We can then imagine, that if a bent object is rotated into the plane of view using only a single "straight" nanowire, this rotation event would be indistinguishable from bending (**Figure 4.6a**). Additionally, transition states between the fully in plane and fully out of plane rotations would appear as smaller "deformations", resulting in misleading force information.

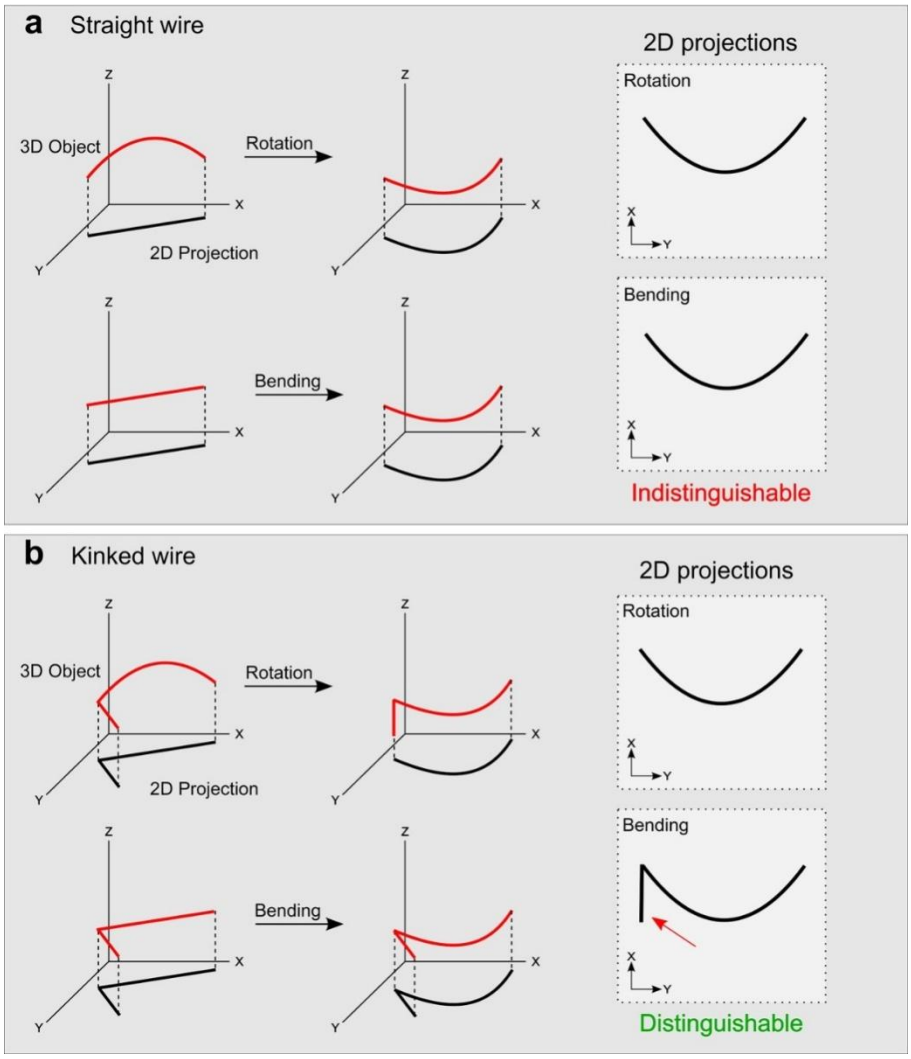

Figure 4.6 Kinked Nanowires as a Visual Anchor.
(**a**) The two dimensional (2D) projection of a curved wire undergoing rotation is similar to a straight wire undergoing structural deformation, however significantly different forces can be at work in each case. (**b**) In kinked wires, the second arm acts as an orthogonal basis, allowing rotation events to be more easily distinguished from bending events. Adapted with permission from Zimmerman J. F. et. al. *Nano Lett 2015*. Copyright 2015 American Chemical Society.

By including the kinked structure into the nanowire, you have introduced an additional reference frame, or an orthogonal vector, which you can be used to distinguish rotations. Namely, that as a wire rotates, you would expect the projection of the secondary axis to change in length, either increasing as it aligns tangentially, or diminishing as it becomes normal to the imaging plane, eventually disappearing to a point. This helps make rotation events clearly distinguishable from bending events, a

process which can be observed in live cells (**Figure 4.7**). In turn this allows for kSiNWs to be used as precise force probes.

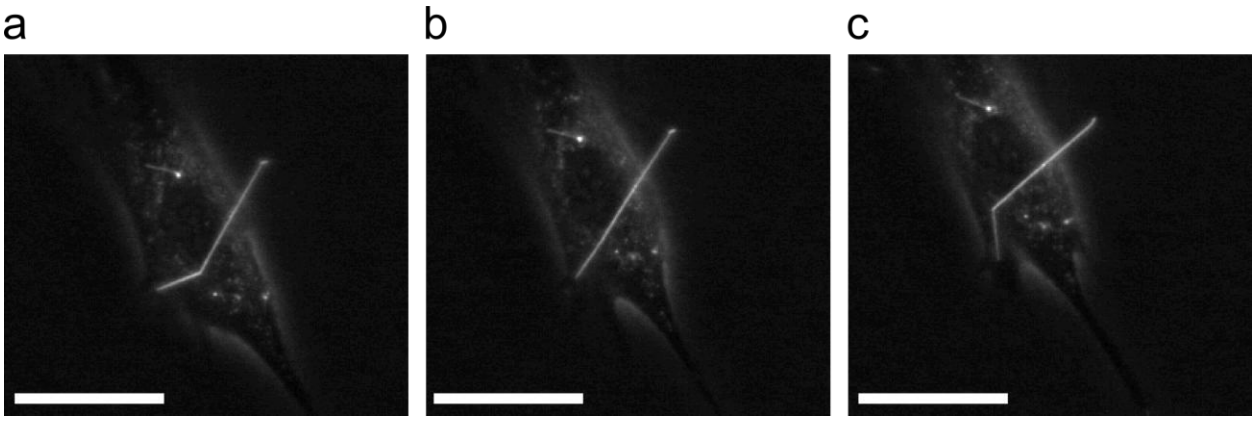

Figure 4.7 Cellular Rotation of a Kinked Silicon Nanowire
SEPC micrograph of a HUVEC with a kSiNW, which undergoes rotational rearrangement. The nanowire before (a), during(b) and after rotation has an easily distinguishable projection profile, indicating that a rotation event is occurring. ~8 min between frames (20 μm scale bars).

Using SEPC microscopy, time-lapse force dynamics were extracted from kSiNW conformations, with the NWs coordinates (x,y) determined using a custom built-script in NIH's ImageJ (**Figure 4.17**, **Figure 4.16**). kSiNWs were modeled as simply-supported beams with an asymmetric load, using Euler-Bernoulli beam theory. This model provided a good match between predicted and experimentally observed deflections, is generalizable to a wide range of load conditions, is computationally quick, and yields information on the position of the force load, with the deformation of the wire, Y(x), being given by:

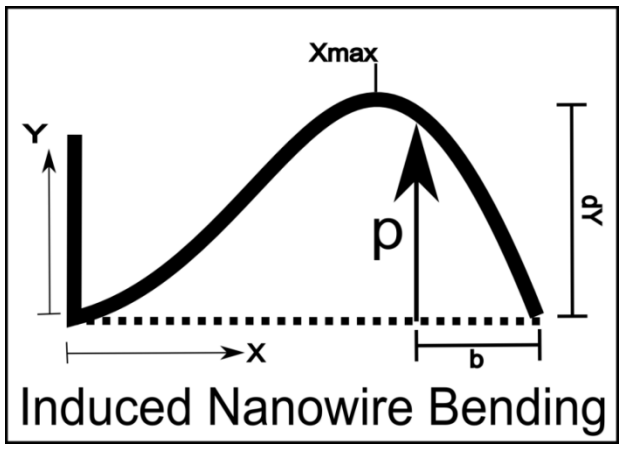

Figure 4.8 Kinked Silicon Nanowire Deflection Schematic
Nanowire undergoing deflection with the applied point load, P. Adapted with permission from Zimmerman J. F. et. al. *Nano Lett 2015*. Copyright 2015 American Chemical Society.

$$Y(x) = \begin{cases} \dfrac{\mathrm{Pbx}(\mathrm{L}^2 - \mathrm{b}^2 - \mathrm{x}^2)}{6\mathrm{LEI}} & \text{if} \quad 0 \le \mathrm{x} \le \mathrm{a} \\ \dfrac{\mathrm{Pbx}(\mathrm{L}^2 - \mathrm{b}^2 - \mathrm{x}^2)}{6\mathrm{LEI}} + \dfrac{\mathrm{P}(\mathrm{x} - \mathrm{a})^3}{6\mathrm{EI}} & \text{if} \quad \mathrm{a} < x \le L \end{cases} \qquad \textbf{4.19}$$

where P is the force of the load, L is the length of the wire, b is the position of the point-load (**Figure 4.8**), E and I are the elastic Young's modulus and the beams' cross sectional moment of inertia respectively ($I = (5\sqrt{3})/(144)D^4$ for hexagonal cross sections, where D is the NW diameter). We note here, that the large dependence of deflection on nanowire diameter makes this a critical parameter for determining absolute forces, with even small uncertainties in diameter leading to large uncertainty in force values; a fact which will be discussed in great detail in Chapter 5. kSiNWs were grown primarily in the <112> direction and a Young's modulus of 169 GPa[3,29] was used, with the location of the point load, b, determined on a frame-by-frame basis using the geometric relationship:

$$b = \sqrt{L^2 - 3x_{max}^2} \qquad \textbf{4.20}$$

where x_{max} is the x coordinate of maximum deflection (**Figure 4.8**); whose value was obtained by fitting the neutral axis of the SiNW using a 10-point moving average.[33]

Force was determined by fitting for the load parameter, P, using a least-squares regression of equation. **4.19**. An average diameter of ~28.1 nm (as measured by TEM) was selected for force probe growth, as this afforded a wide detection range, with a maximum observed force of ~5400 pN and a minimum detection limit of ~1.8 pN. However, we note here that this range can also be tuned for specific biological processes by controlling the nanowire diameter, as the diameter plays an important role in determining the material's second moment of area and its size dependent modulus of elasticity[3,4], impacting the amount of force it takes to deform the SiNW. Tuning the material in this way is readily achievable synthetically, by selecting different sized precursor gold nanoparticles. This allows for kSiNW probes to be used across a wide set of force range, extending its potential as an intracellular probe.

To test these probes, first we wanted to see if devices would decompose over time in solution. In air, silicon can oxidize into silica and then further decompose into silicic acid in phosphate buffered solution[3536]. As a result, nanowire decomposition could impact force measurements. To make sure that devices were stable over the measurement period, optical scattering profiles were extracted in both DI water and growth media (**Figure 4.9**). As we will show later, the optical scattering of SiNWs is greatly impacted by device diameter (**Section 5.5.2**5.2.2 Calculations of Optical Scattering using Lorentz-Mie Theory), making their scattering profiles a useful metric for understanding device decomposition. Under these conditions, no significant difference was found for force probes, suggesting that they were moderately stable under physiological conditions.

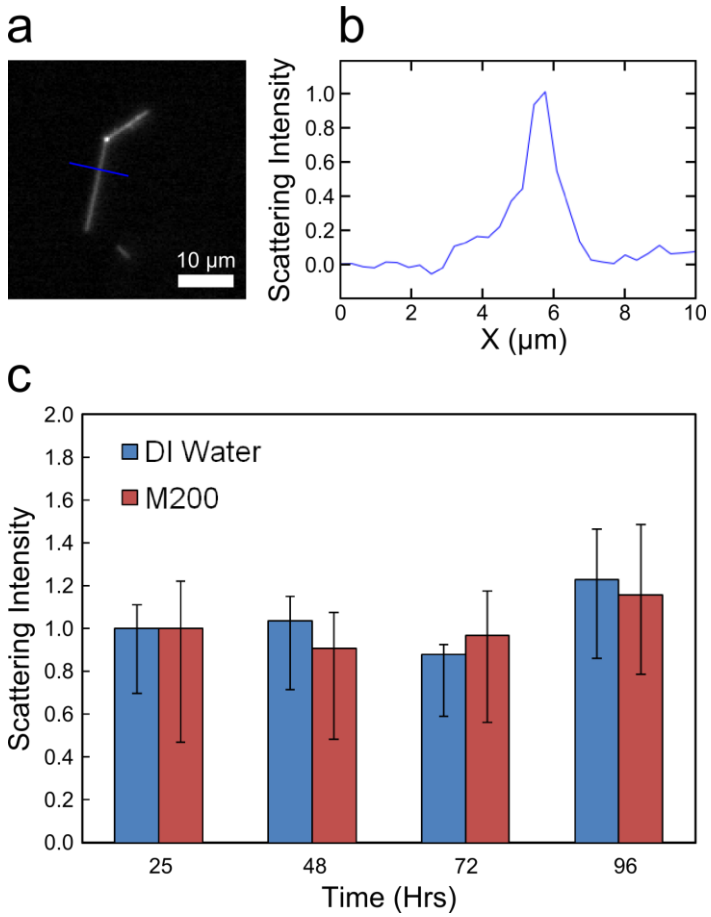

Figure 4.9 kSiNW Probe Integrity Under Physiological Conditions.
(**a**) Example DF micrograph of a kSiNW in deionized (DI) water with the accompanying (**b**) line-scan used to determine NW's maximum scattering intensity, $I(\lambda)_s$, taken over the highlighted region (blue). (**c**) Mean scatter intensity of kSiNWs over incubation period (37 ^oC, 5% CO_2), in both DI water and M200 growth media. Scattering intensities normalized using the equation $I(\lambda)_{norm} = (I(\lambda)_s - I(\lambda)_{bkg})/I(\lambda)_{25}$, where $I(\lambda)_{bkg}$ is the background intensity, and $I(\lambda)_{25}$ is the mean scattering intensity of kSiNWs at 25hours in their respective media. Error bars given for the 33rd and 66th population percentiles respectively. No significant change in kSiNW scattering was noted over the experimental duration. Adapted with permission from Zimmerman J. F. et. al. *Nano Lett 2015*. Copyright 2015 American Chemical Society.

4.2.4 Inter and Intracellular Force Probes

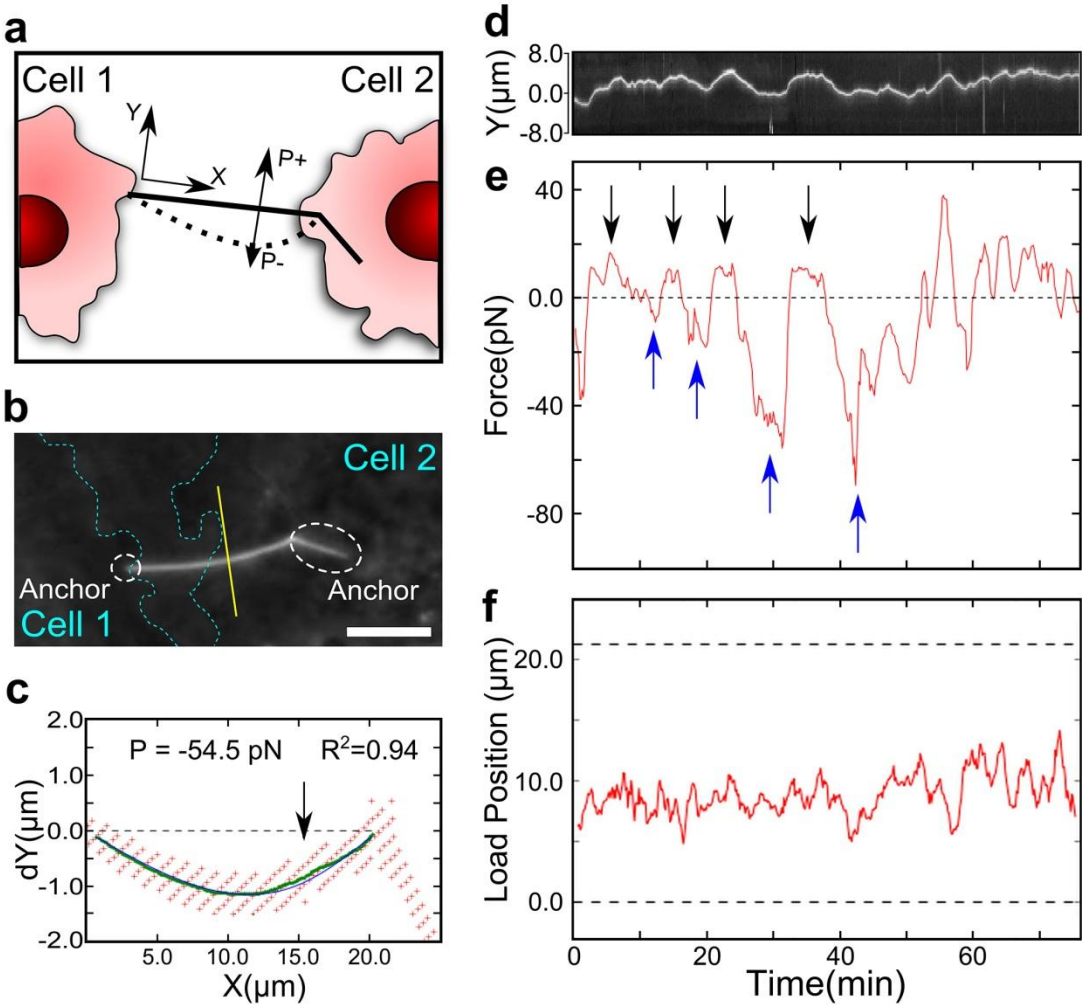

Figure 4.10 Intercellular Force Sensing.
(**a**) Illustration of HUVEC kSiNW intercellular interactions with associated SEPC micrograph (**b**), showing a bent SiNW state (dashed cyan lines - cell membranes) (5 μm scale bar). (**c**) Example single-frame force fitting data for the displayed NW bending (T = 31min) (red, raw coordinates; green, curve average; blue, fit to the curve average; arrow, estimated load position). (**d**) Kymograph and time-lapse (**e**) force data (from yellow line segment in b), with coincident load position (**f**), showing ratcheting force behavior (shared time axis) (arrows indicating ratcheting force peaks). Adapted with permission from Zimmerman J. F. et. al. *Nano Lett 2015*. Copyright 2015 American Chemical Society.

Using this model we examined the intercellular forces exerted on a kSiNW by two HUVECs working to internalize the same SiNW and the intracellular forces exerted by HASMC during drug-induced constriction. For HUVECs, a kSiNW was captured midway through the internalization process (**Figure 4.10**), with both ends pinned, one on the membrane of an adjacent cell (Cell 1) and the other connected to the internalizing cell

(Cell 2)(**Figure 4.10b**). Force was recorded perpendicular to the axis of the extended kSiNW arm, with HUVECs exhibiting unexpected ratcheting like behavior (**Figure 4.10c-f**), jostling the NW back and forth by applying forces with increasing amplitude and/or duration (**Figure 4.10e**, highlighted with arrows). The load force fitting (**Figure 4.10c**), and load position predictions for a typical frame are given (**Figure 4.10c**), showing that the Euler-Bernoulli model yields reasonable results and predictions. Force dynamics (**Figure 4.10e**) were smoothed using a 5-frame moving average, resulting in a force profile similar to the corresponding kymograph of SiNW position (**Figure 4.10d**). Under these conditions the kSiNW was observed to experience a maximum averaged force peak of 69.6 pN (**Figure 4.10e**). The load position dynamics (**Figure 4.10f**) suggests that the lamellipodium was the primary location where NW bending occurred, a reasonable outcome given focal adhesions exhibit high density at lamellipodium.[10] Additionally, the NW length (*i.e.* the distance between the left tip and the middle kink) variation was only ~2.5% (Standard deviation, **Figure 4.5**), suggesting that possible force contributions due to NW buckling and torque are minor. The observed ratcheting behavior is likely exhibited by the cell (cell 2), in an attempt to free the kSiNW from the underlying substrate and the 'competing' cell (cell 1).

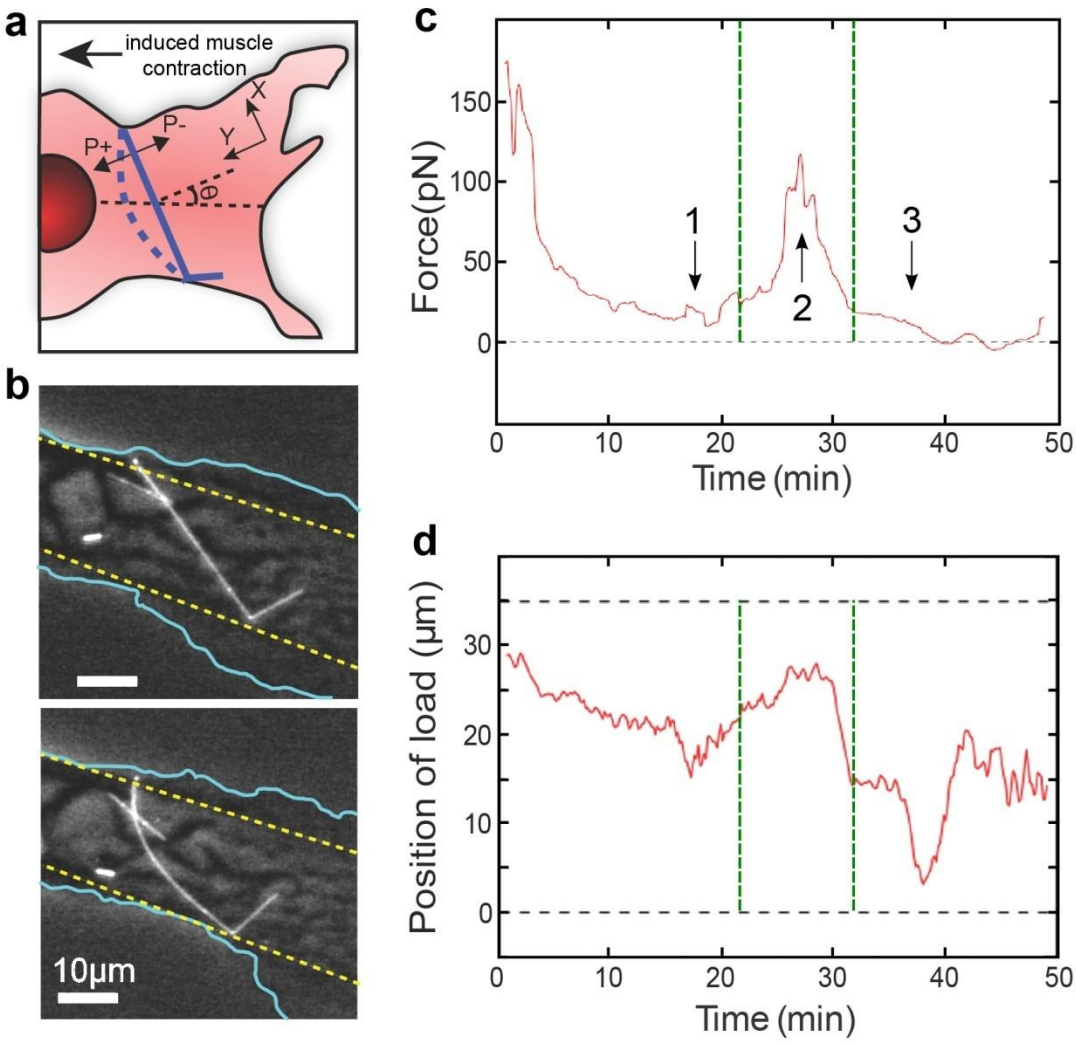

Figure 4.11 Intracellular Force Sensing.
(**a**) Schematic of HASMC contraction. (**b**) Associated SEPC micrographs, showing straight (upper)/bent (lower) states (cyan, cell membranes; yellow, lamella boundary). Time-lapse force data (**c**) with coincident load position (**d**), showing well-defined contraction peak (between dashed green lines). Adapted with permission from Zimmerman J. F. et. al. *Nano Lett 2015*. Copyright 2015 American Chemical Society.

Using kSiNWs, we also studied the intracellular force dynamics of HASMCs undergoing vasoconstriction (**Figure 4.11**)(**Video S.5**). Here, SiNWs were totally internalized, and contraction was induced using the hormone angiotensin II (ANGII). In the present case, a kSiNW located in the lamella was observed (**Figure 4.11b**), with force data recorded intracellularly at an angle of 52.6° (**Figure 4.11a**). Upon the introduction of ANGII (t=0 min), a relaxation of tension was observed (**Figure 4.11c)**,

reaching a minimum force of 11.0 pN (**Figure 4.11c**, arrow 1). This relaxation was likely the result of a rearrangement of cytoskeleton filaments preparing for contraction, as this relaxation was followed by a significant force peak (t = ~30 min, between dashed green lines, **Figure 4.11c**) with a maximum force of 116.9 pN (**Figure 4.11c**, arrow **2**) before returning to a minimally strained state (**Figure 4.11c**, arrow 3). Using this information, we can see that while relaxation was almost immediate, it took ~30 minutes for the cells to respond to the hormone dosage, a metric which was relatively consistent across samples. Additionally, we can see that the force of contraction lasted for ~8 minutes. In this way, kSiNWs can provide useful information about the cellular response to external stimuli such as drug or mechanically induced contraction.

Different from the extracellular case (**Figure 4.10d**), the predicted load position dynamics (**Figure 4.11d**) suggests a significant spatial evolution of intracellular forces over a single cytoskeleton-like kSiNW, especially during the peaked force actuation period (between dashed green lines, **Figure 4.11d**). An example frame of the force fitting data is provided (**Figure 4.12**). Unexpectedly, no obvious morphology change was noted in the lamella containing the kSiNW (the region between yellow dashed lines, **Figure 4.11b**) during the observed force cycle. This highlights the usefulness of intracellular force measurements in improving biophysical characterization.

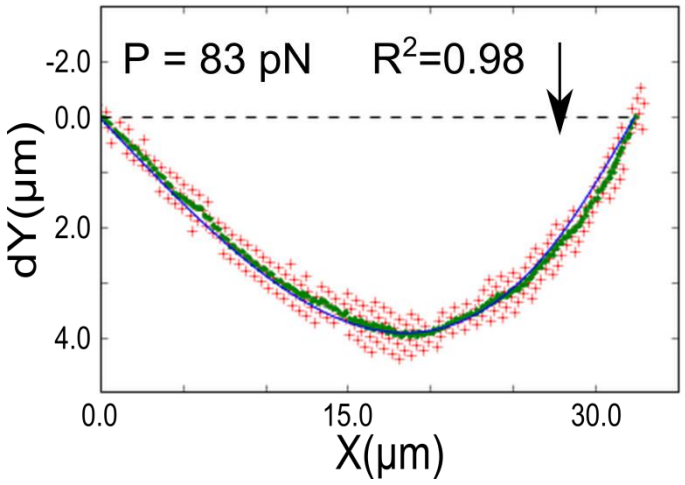

Figure 4.12 Single-frame Intracellular Force Data.
Example of single-frame force fitting data (upper) for a kSiNW probe in a HASMC at T=29 min (red, raw coordinates; green, smoothed curve average; blue, curve fit; arrow, load position). Adapted with permission from Zimmerman J. F. et. al. *Nano Lett 2015*. Copyright 2015 American Chemical Society.

4.2.5 Force Transduction and the Cytoskeleton

The role of filamentous actin and myosin in muscle cell contraction is well established, with the actomyosin cross bridging cycle acting as the fundamental mechanism of tension formation and morphological shortening in all forms of muscle cells, as well as many non-muscular cells[37]. To briefly describe this process, movement in smooth muscle cells is generated by a myosin cross-bridge unit, which cyclically binds to thin filamentous actin and transports these filaments by "sliding" them across thick myosin filaments[38]. To achieve this sliding motion, myosin head groups are propelled forward in a ratcheting motion using ATP hydrolysis to induce a change in the protein's confirmation causing the attached actin filament to slide forward by ~5.0 nm per "power stroke"[39]. The myosin cross-bridge unit can simultaneously pull multiple actin fibers towards it' center, causing an overall 'shrinkage' of the overall chain length. As these actin filaments are connected to the cell's membrane, the reduction in chain length

places a tension on the cell membrane causing the cell to undergo contraction, overall forcing the cell into a tighter bundled, morphology (**Figure 4.13a**).

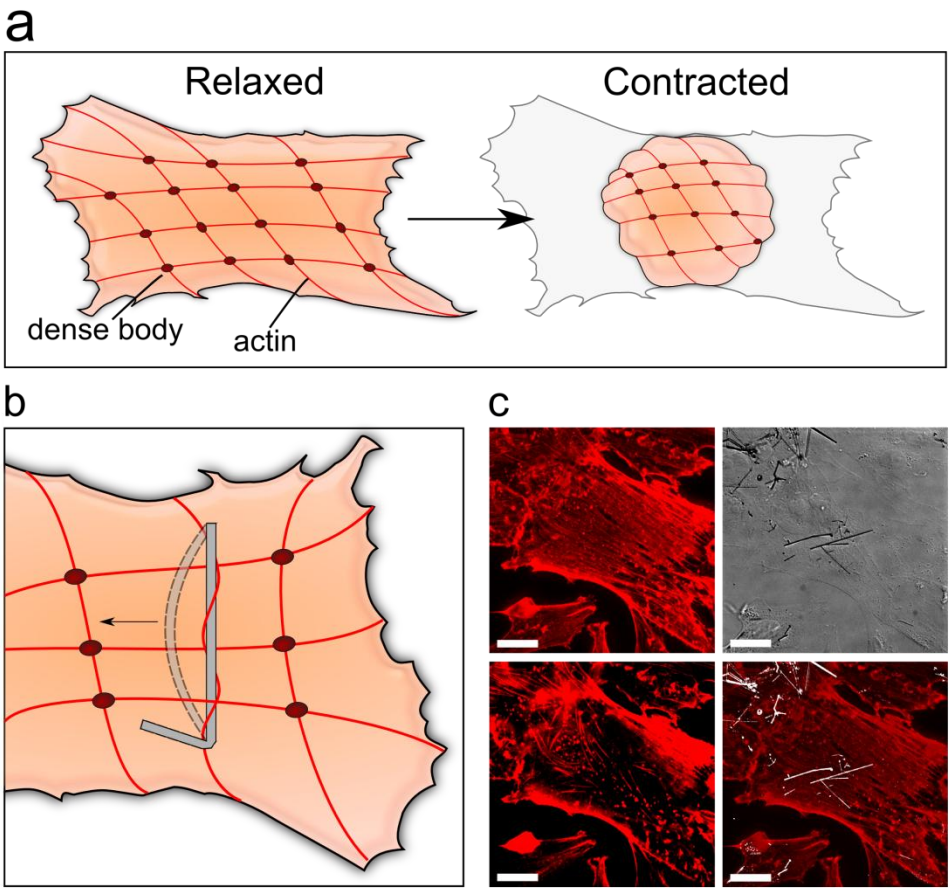

Figure 4.13 Mechanism of Force Transduction.
(**a**) Schematic Illustration showing smooth muscle cell contraction. Cytoskeleton filaments run throughout the cell, and during contraction, molecular motors pull on these filaments, reducing the distance between linking segments. (**b**) Proposed mechanism of force transduction. SiNWs become entangled in the cytoskeletal filaments during internalization. As the cell contracts, it rearranges it cytoskeleton, resulting in an induced force on the anchored SiNW. (**c**) Fluorescent confocal image of the actin network in a HASMC containing SiNWs, indicating that actin primarily forms in filamentous bundles (red, TXred phalloidin) running parallel with main axis of contraction (upper left, maximum projection), although some filaments run at odd angles to this (lower left, single confocal plane). The corresponding DIC (upper right) and artificially combined images (lower right), show internalized nanowires (white) running roughly perpendicular with respect to the main axis of contraction (25 μm scale bars).

For kSiNWs acting as intracellular force probes, it's possible for the SiNWs to become entangled in the cytoskeleton both during and subsequent to internalization (**Figure 4.13b**). This would allow force to be transduced to the SiNW via conformational

changes in the cytoskeleton. To understand this behavior, we first note that the cytoskeleton can form large cytoskeletal networks (**Figure 4.13c**), for instance with actin being crosslinked through the filamin dimer[39]. This results in a three-dimensional web like structure, with some actin bundles running in "cross hatch" pattern relative to the main axis of contraction (**Figure 4.13c**). As these cross hatch actin are also coupled to the contractile network, tension can develop in the actin networks during muscle contraction[40], causing non-equilibrium force generation. If we then imagine a SiNW embedded in this network, connected to the cytoskeleton via non-specific protein binding and physical entanglement, then it's possible for tensions to be transduced to the nanowire. This in turn could result in the observed structural changes taking place in the SiNW force probes.

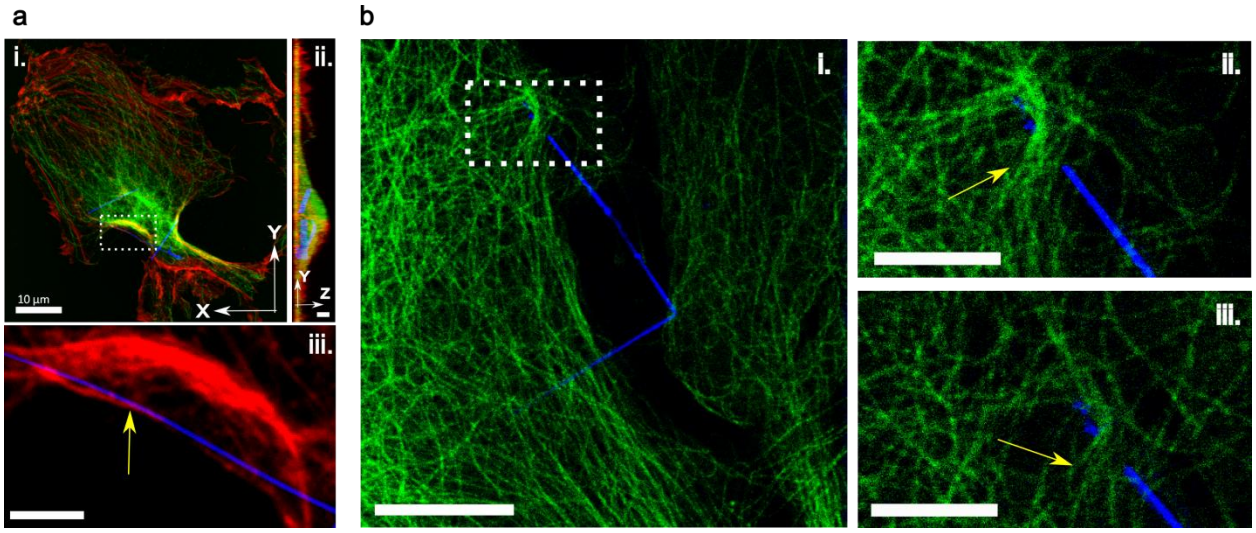

Figure 4.14 SiNWs Entangle in the Cytoskeleton.
(**a**) Confocal fluorescence (HUVEC, red-actin, green-tubulin) micrograph in x-y (left) and y-z (right) planes, containing NWs (blue-scattering). Actin channel inset shows entangled SiNWs. (lower, 2.5 µm scale bar), (right, 2 µm scale bar). (**b**) Time-lapse live cell confocal fluorescence micrograph, showing HASMC microtubule bundles (green) interacting with a kSiNW (blue) at T=0 min (left, and upper right) and T=24min (lower right) (left, 10 µm scale bar) (right, 5 µm scale bars). Adapted with permission from Zimmerman J. F. et. al. Nano Lett 2015. Copyright 2015 American Chemical Society.

To see if a linkage was occurring between SiNWs and the cytoskeleton network, confocal fluorescent microscopy was used, exploring the interface between SiNWs and

intracellular proteins. During this processes kSiNWs were found to be entangled in the cytoskeleton network, forming junctions with both actin (**Figure 4.14d**, inset**)** and microtubules (**Figure 4.14e**), causing the kSiNWs to become pinned intra- (**Figure 4.14d**) and intercellularly (**Figure 4.14e**). Using live cell staining, we tracked microtubule/kSiNW junctions in contractile muscle cells. While much of the entanglement was transient, as the cytoskeleton can polymerize and depolymerize, some of the connections were maintained over an extended period (≥24 minutes) (**Figure 4.14e**, right). First, this entanglement with the cytoskeleton represents a distinct SiNW-protein interaction, the first of its kind reported, however it also supports our proposed mechanism of kSiNW anchoring and intra-/intercellular force transduction. Using TEM allowed these anchors to be inspected in higher detail. In a previous section we discussed how non-specific proteins could bind to the SiNW surface (See **Section 3.2.7**). Here we can observed a similar phenomenon, where an amalgam of proteins can form at specific point along the length of the nanowire (**Figure 4.15**). It is possible that these proteins bundles can act as a physical anchor, restricting nanowire movement. While it does not confirm that this specific mechanism of cytoskeleton and cytosolic rearrangement is deforming the SiNWs, it at least suggests that this is a distinct possibility.

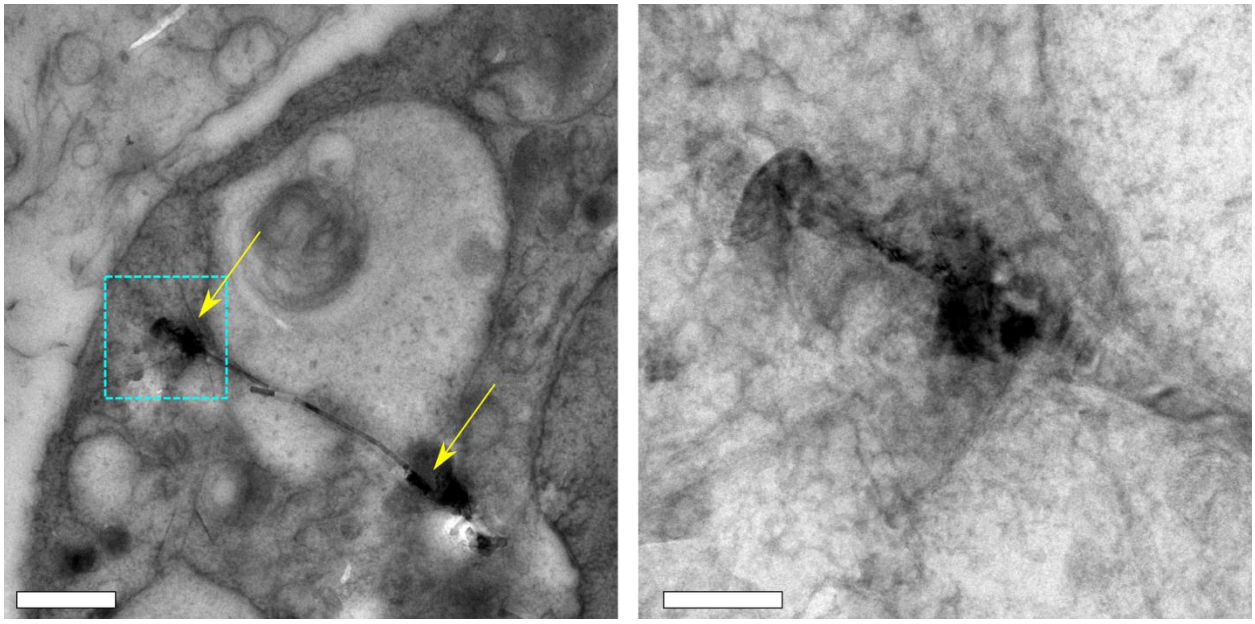

Figure 4.15 Intracellular SiNW Anchoring
(**a**) TEM micrograph of an internalized SiNW inside a HUVEC, showing point like anchoring by dense protein bundles (yellow arrows), with the corresponding (**b**) higher magnification micrograph taken from the highlighted region. (Scale Bars: 1 µm & 175 nm respectively).

4.3 Conclusions

This work demonstrates that rationally designed semiconducting nanowire based devices capable of independent inter- and intracellular operation are achievable, with SiNWs serving as a potential platform technology for designing future constructs. In our work, we have shown that long-term non-invasive probes for force monitoring are possible, and were able to be used for several hours without marked deleterious effects. However, we also note that that this range has the potential to be substantially extended, as kSiNWs are not subject to photobleaching, while the use of conventional light sources produces only negligible localized photothermal heating[23]. When compared to other intracellular force measurement techniques, such as optical trapping, these devices do display some limitations, for instance target specificity, however these devices also offer several distinct advantages. First, this technique is easily

implemented, with the nanoscale force probes being administrated in a similar fashion to drugs. This raises the possibility of using additional force probes within a single experiment, incorporating multiple devices both within an individual cell and across a cellular network. This multiplexed signal detection could be used to studying ensemble force transduction dynamics and is not easily achieved in other intracellular force detection methods. Second, the tunable nature of these probes makes them adjustable to a wide array of force conditions, with the detection range depending on the material properties of the probe, and not the optical setup. This makes adjusting these probes relatively non-invasive compared to optical traps whose detection limits are dependent on laser strength,[41] which can lead to significant localized heating[23,24,41].

This work also raises several intriguing possibilities from a biomaterials perspective, enabling studies into how nanomaterials can affect intracellular force interactions and mechano-signaling. First, the measurements presented here suggest that similar mechanical processes may occur in individual biological filaments, and highlight the mechanical considerations needed for designing future nanoscale probes and therapeutic devices. For instance, one could imagine designing a nanoscale piezo-electric devices,[42] capable of independent intracellular operation, with this work serving as a basis for understanding the limits of such a system. Finally, as SiNWs are observable even through tissue samples,[43] we hope that this work can be used in future *in vivo* experiments, where intracellular forces are particularly difficult to probe.

4.4 Experimental Details

4.4.1 Nanowire Force Probe Growth

Epitaxial crystalline SiNWs were grown on a silicon substrate using the vapor-liquid-solid mechanism in a homebuilt chemical vapor deposition system, with the kink introduced using a 10s purge as previously reported.[1] Typical growth conditions used flow rates of 2 sccm and 60 sccm for SiH_4 and H_2 respectively at 480 °C and 40 torr, with 20nm gold nanoparticle as a catalyst. Typical growth times were 20 min and 10 min before and after the purge, resulting in kSiNWs with an ~2:1 aspect ratio between the two arms. 1.5 cm x 1 cm segments of the substrate were sectioned off, and rinsed using dilute Hydrofluoric acid (%9.8 wt, ~10s) to remove the silicon dioxide layer before being washed in deionized water. kSiNWs were then sterilized in 70% ethanol for at least 30 minutes under UV radiation, before being placed into growth media where they were sonicated (Ficher Scientific FS60D Ultrasonic cleaner). Prior to cell culture, NW suspensions were distributed onto the growth substrate and allowed to settle overnight. For smooth muscle experiments, cells were allowed 48-72 hours to internalize NWs, and working concentrations between 50 nM - 75 nM of Angiotension II human (Sigma-Aldrich) were used to induce vasoconstriction. Nanowire response was monitored using SEPC.

4.4.2 kSiNW Boundary Conditions and Data Extraction

To model the force data, the Euler-Bernoulli model was used, assuming a simply supported beam with an asymmetric point load. An asymmetric point load was assumed because of the asymmetric deflection observed in the kSiNWs deflection during intracellular bending, however there are several ways asymmetric bending can arise.

First, it is possible for asymmetric bending to appear due to asymmetric boundary conditions, even in the presence of a uniform force load. For instance, in the case of one end of the kSiNW being fixed (no displacement or rotation, $M_{(0)}=0$, $\Delta x=\Delta y=0$) and the other being pinned (no displacement but free to rotate, $M_{(L)}\neq 0$, $\Delta x=\Delta y=0$), an asymmetric curve can arise. In this case, if we assume that the kink resists bending, causing the kink associated end to become fixed, rather than pinned, then just such an asymmetric distribution could be observed. However, when we model the force across the wire in this fashion (**Figure 4.16a**), it results in a poor fitting parameter especially when the asymmetry is most closely distributed towards the kink (We note here that the asymmetry was observed to be distributed towards both boundaries, depending on the time). This suggests that the asymmetry observed in the curve is not primarily due to asymmetric boundary conditions, but is formed through some other mechanism. A second possibility is that the asymmetric curve is formed through the uneven distribution of load across an object. When modeling the bending using these boundary conditions, we see that the predicted deflection matches well with the observed NW shape (**Figure 4.16b**), and can be adjusted to fit the time dependent cellular microenvironment. This suggests that the asymmetry observed in the curve is not primarily due to asymmetric boundary conditions, but is formed primarily as a result of an asymmetric load across the wire.

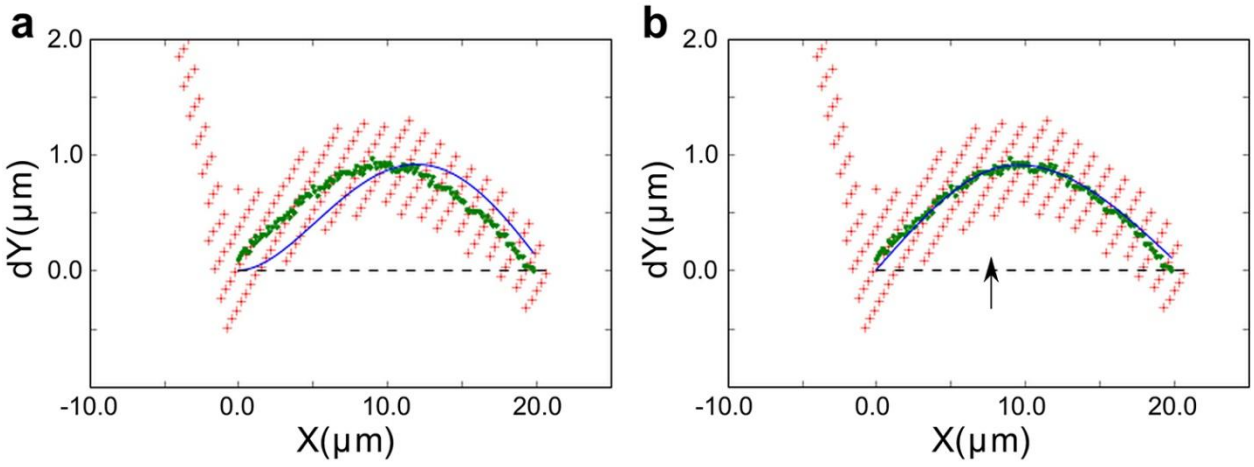

Figure 4.16 kSiNW Boundary Conditions Analysis.
Example kSiNW fit using either (**a**) an asymmetric boundary conditions (R^2 = 0.2, q = 5.82 pN/µm) or (**b**) an asymmetric load (R^2 = 0.96, q = 54.8 pN). Red, raw coordinates; Green, smoothed curve average; Blue, curve fit; Arrow; predicted load position. Adapted with permission from Zimmerman J. F. et. al. Nano Lett 2015. Copyright 2015 American Chemical Society.

To model NW force data, coordinates were extracted on a frame-by-frame basis from a time lapse SEPC micrograph (**Figure 4.17a**) using a custom built NIH ImageJ script. First a region of interest was selected containing a kSiNW, and was then filtered using intensity thresholding to produce a binary image, containing only the highlighted kSiNW (**Figure 4.17b**). NW coordinates were then extracted using the binary image (**Figure 4.175c**) using a custom script in NIH's ImageJ.

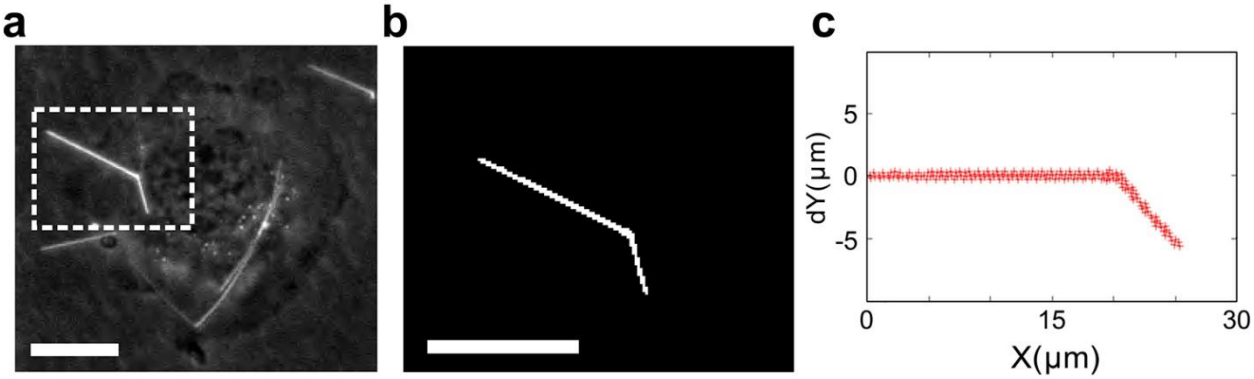

Figure 4.17 Extracting SiNW Position.
(a) SEPC micrograph of kSiNW being internalized by a HUVEC, with accompanying binary image (b) taken from the highlighted region. (c) Graph showing extracted NW aligned onto the x-axis. (20 µm scale bars). Adapted with permission from Zimmerman J. F. et. al. Nano Lett 2015. Copyright 2015 American Chemical Society.

Minimum detection limits were determined by examining the noise associated with unbent wires, with consistent readings of ~1.8 pN or less observed. This established a baseline below witch no accurate readings could be obtained, however, this is primarily a limitation in optical resolution rather than the NW's bent state, and that this minimum detection limit could be improved in multiple ways. First, by improving the spatial resolution at which the NW's coordinates are obtained. This would allow a more minute determination of the NW's shape to be made, in turn improving force detection limits. Second, wire diameters could be changed, in turn changing sectional moment of inertia, to accommodate a different range of force measurements.

4.5 References

1. Tian, B., Xie, P., Kempa, T. J., Bell, D. C. & Lieber, C. M. Single-crystalline kinked semiconductor nanowire superstructures. *Nat. Nanotechnol.* **4,** 824–829 (2009).

2. Tian, B. *et al.* Coaxial silicon nanowires as solar cells and nanoelectronic power sources. *Nature* **449,** 885–889 (2007).

3. Sohn, Y.-S. *et al.* Mechanical Properties of Silicon Nanowires. *Nanoscale Res. Lett.* **5,** 211–216 (2010).

4. Hsin, C.-L. *et al.* Elastic Properties and Buckling of Silicon Nanowires. *Adv. Mater.* **20,** 3919–3923 (2008).

5. Ryu, S. Y. *et al.* Lateral buckling mechanics in silicon nanowires on elastomeric substrates. *Nano Lett.* **9,** 3214–3219 (2009).

6. Fine, D. *et al.* Silicon Micro- and Nanofabrication for Medicine. *Adv. Healthc. Mater.* **2,** 632–666 (2013).

7. Marcon, L. & Boukherroub, R. in *Semiconducting Silicon Nanowires for Biomedical Applications* (ed. Coffer, J. L.) 62–85 (Elsevier, 2014).

8. Wang, N., Butler, J. P. & Ingber, D. E. Mechanotransduction across the cell surface and through the cytoskeleton. *Science* **260,** 1124–1127 (1993).

9. Fletcher, D. a & Mullins, R. D. Cell mechanics and the cytoskeleton. *Nature* **463,** 485–492 (2010).

10. Geiger, B., Spatz, J. P. & Bershadsky, A. D. Environmental sensing through focal adhesions. *Nat. Rev. Mol. Cell Biol.* **10,** 21–33 (2009).

11. Ji, L., Loerke, D., Gardel, M. & Danuser, G. Probing intracellular force distributions by high-resolution live cell imaging and inverse dynamics. *Methods Cell Biol.* **83,** 199–235 (2007).

12. Hirokawa, N. Kinesin and Dynein Superfamily Proteins and the Mechanism of Organelle Transport. *Science (80-.).* **279,** 519–526 (1998).

13. Conner, S. D. & Schmid, S. L. Regulated portals of entry into the cell. *Nature* **422,** 37–44 (2003).

14. Schafer, D. A. Actin puts on the squeeze. *Nat. Cell Biol.* **5,** 693–694 (2003).

15. Ingber, D. E. Tensegrity II. How structural networks influence cellular information processing networks. *J. Cell Sci.* **116,** 1397–1408 (2003).

16. Rehfeldt, F., Engler, A. J., Eckhardt, A., Ahmed, F. & Discher, D. E. Cell responses to the mechanochemical microenvironment--implications for regenerative medicine and drug delivery. *Adv. Drug Deliv. Rev.* **59,** 1329–39 (2007).

17. Legant, W. R. *et al.* Measurement of mechanical tractions exerted by cells in three-dimensional matrices. *Nat. Methods* **7,** 969–971 (2010).

18. Fischer, R. S., Myers, K. A., Gardel, M. L. & Waterman, C. M. Stiffness-controlled three-dimensional extracellular matrices for high-resolution imaging of cell behavior. *Nature Protocols* **7,** 2056–2066 (2012).

19. Li, Z. *et al.* Quantifying the traction force of a single cell by aligned silicon nanowire array. *Nano Lett.* **9,** 3575–3580 (2009).

20. Grashoff, C. *et al.* Measuring mechanical tension across vinculin reveals regulation of focal adhesion dynamics. *Nature* **466,** 263–266 (2010).

21. Wang, X. & Ha, T. Defining single molecular forces required to activate integrin and notch signaling. *Science* **340,** 991–4 (2013).

22. Oddershede, L. B. Force probing of individual molecules inside the living cell is now a reality. *Nat. Chem. Biol.* **8,** 879–886 (2012).

23. Peterman, E. J. G., Gittes, F. & Schmidt, C. F. Laser-induced heating in optical traps. *Biophys. J.* **84,** 1308–1316 (2003).

24. Neuman, K. C., Chadd, E. H., Liou, G. F., Bergman, K. & Block, S. M. Characterization of photodamage to Escherichia coli in optical traps. *Biophys. J.* **77,** 2856–2863 (1999).

25. Marawske, S. *et al.* Fluorophores as optical sensors for local forces. *ChemPhysChem* **10,** 2041–2048 (2009).

26. Roder, P. B., Pauzauskie, P. J. & Davis, E. J. Nanowire heating by optical electromagnetic irradiation. *Langmuir* **28,** 16177–16185 (2012).

27. Schwarz, K., Tersoff, J., Kodambaka, S., Chou, Y.-C. & Ross, F. Geometrical Frustration in Nanowire Growth. *Phys. Rev. Lett.* **107,** 1–5 (2011).

28. Wen, C.-Y., Tersoff, J., Reuter, M., Stach, E. & Ross, F. Step-Flow Kinetics in Nanowire Growth. *Phys. Rev. Lett.* **105,** 1–4 (2010).

29. San Paulo, a. *et al.* Mechanical elasticity of single and double clamped silicon nanobeams fabricated by the vapor-liquid-solid method. *Appl. Phys. Lett.* **87,** 053111 (2005).

30. Miller, R. E. & Shenoy, V. B. Size-dependent elastic properties of nanosized structural elements. *Nanotechnology* **11,** 139–147 (2000).

31. Beer, F. P. & Johnston, E. R. *Mechanics of materials*. (McGraw-Hill, 1981).

32. Strus, M. C. *et al.* Strain energy and lateral friction force distributions of carbon nanotubes manipulated into shapes by atomic force microscopy. *Nanotechnology* **20,** 385709 (2009).

33. Qin, Q. & Zhu, Y. Static Friction between Silicon Nanowires and Elastomeric Substrates. *ACS Nano* **5,** 7404–7410 (2011).

34. Yvonnet, J., Mitrushchenkov, a., Chambaud, G. & He, Q. C. Finite element model of ionic nanowires with size-dependent mechanical properties determined by ab initio calculations. *Comput. Methods Appl. Mech. Eng.* **200,** 614–625 (2011).

35. Anglin, E. J., Cheng, L., Freeman, W. R. & Sailor, M. J. Porous silicon in drug delivery devices and materials. *Adv Drug Deliv Rev* **60,** 1266–1277 (2009).

36. Yin, L., Bozler, C., Harburg, D. V., Omenetto, F. & Rogers, J. A. Materials and fabrication sequences for water soluble silicon integrated circuits at the 90 nm node. *Appl. Phys. Lett.* **106,** (2015).

37. Gunst, S. J. & Zhang, W. Actin cytoskeletal dynamics in smooth muscle: a new paradigm for the regulation of smooth muscle contraction. *Am. J. Physiol. Cell Physiol.* **295,** C576–C587 (2008).

38. Geeves, M. a & Holmes, K. C. STRUCTURAL MECHANISM OF MUSCLE CONTRACTION> *Annu. Rev. Biochem.* **68,** 687–728 (1999).

39. Alberts, B. *et al. Molecular Biology of the Cell*. (Garland Science, 2008).

40. Mizuno, D., Tardin, C., Schmidt, C. F. & Mackintosh, F. C. Nonequilibrium mechanics of active cytoskeletal networks. *Science* **315,** 370–373 (2007).

41. Kuo, S. C. Using optics to measure biological forces and mechanics. *Traffic* **2,** 757–763 (2001).

42. Wang, Z. L. & Song, J. Piezoelectric nanogenerators based on zinc oxide nanowire arrays. *Science* **312,** 242–6 (2006).

43. Jung, Y., Tong, L., Tanaudommongkon, A., Cheng, J.-X. & Yang, C. In Vitro and In Vivo Nonlinear Optical Imaging of Silicon Nanowires. *Nano Lett.* **9,** 2440–2444 (2009).

Chapter 5. Optical Determination of Silicon Nanowire Diameters•

5.1 Introduction

So far we have discussed silicon nanowire (SiNW) internalization and the use of force probes for studying intracellular environments. When using these probes we have previously noted that the SiNW's diameter plated a critical role in predicting the forces being applied to the wire, and that large uncertainties in the absolute magnitude of the force can result from even small deviations in the wires to diameter. Therefore to calibrate this system further, it would be ideal to have a way of measuring the force probe's diameter in-situ. While this is possible to do after taking force measurements using electronic microscopy (EM) techniques, the use of correlative microscopy can be both challenging and time consuming. Therefore, a more ideal technique would be to use the optical properties of the SiNW to determine its diameter. While at first this may seem difficult due to the optical resolution limit, here we will discussed how this calibration can be achieved using the SiNW's optical scattering, which we have determined varies as a function of nanowire diameter.

The optical properties of silicon nanowires has drawn great attention recently, with these structures displaying distinct size-dependent optical properties at both the ensemble,[1–3] and single nanowire scale[4]. As a result, these materials have been

---

• A portion of this work has been reprinted with permission from Zimmerman J. F. et. al. Nano Lett. 15, 5492–5498 (2015). Copyright 2015 American Chemical Society.

A portion of this work has been reprinted with permission from Zimmerman J. F. et. al. J. Phys. Chem. C 119, 29105–29115 (2015). Copyright 2015 American Chemical Society.

considered for a wide range of applications, including photovoltaic devices,[5–9] wave guides,[5,10] colorimetric markers[11] and photodetector[5,12,13]. One critical aspect of these devices is their characteristic nanometer-sized diameters, which play an important role in determining device performance and can impact such properties as charge distribution,[14] temperature sensitivity,[15] and photovoltaic quantum efficiency.[16] This makes the precise determination of nanowire's diameter an important step in many device applications, and a step that needs to be introduced to the quality control process for any potential consumer products using these materials.

Previous work has shown that nanowire diameter can be determined optically using the material's dark field (DF) spectra,[17,18] and has even been used for in-situ monitoring of nanowire growth.[19] To achieve this, an in-optics spectrometer is required, which can collect the optical spectrum of individual nanowires, however these setups can be expensive and are not commonly available in most laboratories. Additionally, the requirement for an optical spectrum can limit access to *in-situ* biological applications, as only certain spectral windows are available in tissue and media samples[20] preventing the collection of a complete spectrum. However, in the previous sections we have discussed how nanowires can be integrated with biological systems,[21] for instance as next generation biosensors[22,23] and drug delivery vectors.[24] Therefore, a more ideal system would be able to monitor both cells and silicon nanomaterials simultaneously, while still being easily achieved at a laboratory scales. To demonstrate that such a system is possible, in this chapter we will discuss how optical scattering intensity is strongly correlated with SiNW diameter. Using ensemble information about the sample's optical scattering intensity, as well as the sample's underlying diameter population

(collected using EM), we are able to construct an optical-EM transform which allows for the precise determination of an individual SiNWs diameter using DF microscopy (**Figure 5.1**).

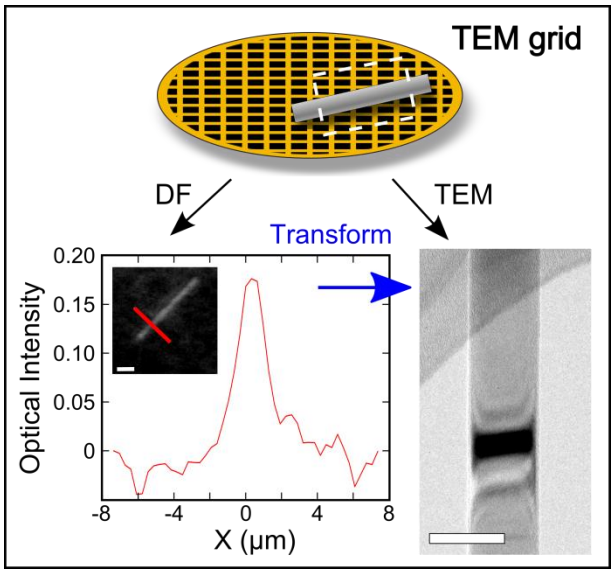

Figure 5.1 Schematic Illustration of Mapping Between Optical and TEM Measured Diameters
The same SiNW is shown both under DF (left) and TEM (right), with the corresponding line scan taken over the highlighted region (scale bars 5 μm and 25 nm respectively). An optical transform function would alleviate the need for individual correlative studies. To obtain the optical-EM transform, ensemble DF and TEM micrographs are used to construct a mapping function, providing an optical method to precisely determine SiNW diameters. Adapted with permission from Zimmerman J. F. et. al. *J. Phys. Chem. C,* 2015. Copyright 2015 American Chemical Society.

Furthermore, here we will show that this work is relevant to the emerging field studying the bio-nanomaterials interface. In previous sections we demonstrated that kinked SiNWs can be used as intracellular force probes to study cell behavior.[25] Using Euler-Bernoulli beam theory, we were able to model SiNW deformation to extract force information from the observed nanowire bending (Figure 5.2)(Chapter 4). However, the force loads, P, modeled this way scale as $P \propto D^{-4}$, where D is the nanowire's diameter. As a result, the absolute values of the predicted forces are very sensitive to even small changes in SiNW diameter. While this still allows for a relative measurement of the time-evolved forces experienced within a cell, it makes a precise determination of the

magnitude of these forces difficult to achieve. Therefore to calibrate this system a careful measurement of the SiNW diameter is needed for each force probe. One way to achieve this is to fix and then stain these samples for examination under transmission electron microscopy (TEM), however this presents several challenges. First, while much work has been recently done on correlative light-electron microscopy,[26] it can still be difficult to track individual cells across microscopes, and requires a significant time investment for each sample. Second, cell fixation can lead to cellular artifacts, limiting the accuracy of these methods. Therefore a more desirable approach to calibrate these probes would be to use an independent technique that allows for the characterization of the underlying nanomaterials, circumventing this time consuming process. To achieve this, we have introduced a method that relies on ensemble population distributions, meaning that individual force probes can be optically calibrated, circumventing the need to use EM methods for each individual force probe.

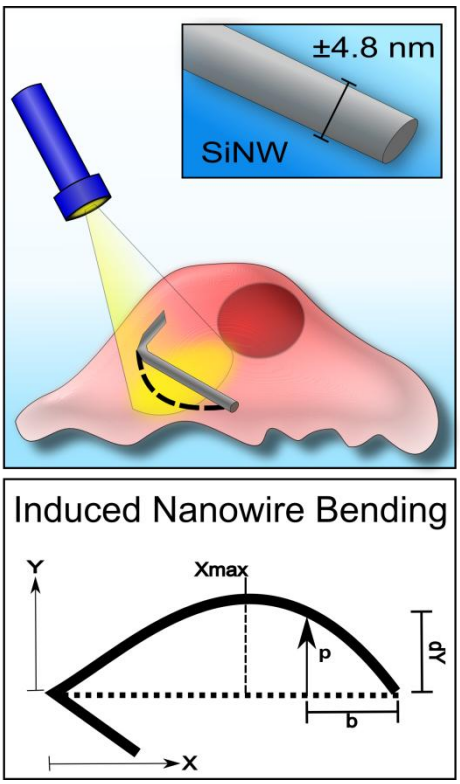

Figure 5.2 SiNW diameter calibration of Intracellular Force Probes.
(**Upper**) Schematic illustration of a kinked SiNW intracellular force probe inside a human aortic smooth muscle cell (HASMC), bending in response to intracellular forces. (**Lower**) Euler-Bernoulli model of a simply supported bending SiNW beam is used to measure the resulting force load, P, which scales as P∝D-4, where D is the SiNW diameter. This makes D a critical parameter for precisely calibrating these intracellular probes. Adapted with permission from Zimmerman J. F. et. al. *J. Phys. Chem. C,* 2015. Copyright 2015 American Chemical Society.

5.2 Results and Discussion

5.2.1 Constructing the Optical Transform.

To optically determine the diameter of an individual SiNW with sub-diffraction precision, we have constructed a non-parametric transform from optical scattering intensity to SiNW diameter, using prior ensemble EM measurements. This method makes use of cumulative distribution functions (CDF), for both optical scattering intensity and sample diameter (**Figure 5.3**). This provides an estimate for the range of possible SiNWs diameters and optical scattering intensities in a given sample preparation. By establishing this range, it's possible to determine where an individual SiNW lies within

this distribution, and enables a prediction of the SiNW's diameter. In other words, this method allows a conversion between two measurements of the same sample population, assuming that the amount of light that a SiNW scatters is related to its diameter. For instance, this method assumes that a wire which scatters light in the 60th percentile also has a diameter in the 60th percentile of the surveyed sample population. By using CDFs, an exact parameterization of the Optical-EM transform is not needed, but instead a statistically driven determination is possible. In general, this method yields reasonable diameter estimates for the majority of wires surveyed, providing diffraction-limited information. Additionally, by avoiding a direct parameterization certain issues like device-substrate photonic interactions, which are difficult to resolve theoretically,[27] can be incorporated into the transform.

Underlying this method is the assumption that a SiNW's scattering intensity scales monotonically with regard to NW diameter. That is to say, that as SiNWs grow in diameter they scatter light more intensely (or at least as intensely). Without this condition, the cumulative mapping function fails to pair optical intensities correctly with their corresponding diameters. To probe this condition, both experimental and theoretical approaches were pursued, using a combination of correlative microscopy and Lorentz-Mie theory based calculations to obtain a theoretical understanding of the principles underlying SiNW optical scattering. Mie theory has previously offered some insight into nanomaterials systems such as germanium[28] and silicon nanowires,[4] and will provide a basis for understanding this underlying assumption, allowing us to establish a range over which the optical-EM transform is valid. Collectively, this duel

experimental and theoretical approach allowed us to map optical scattering intensity to SiNW diameter, enabeling a sub-diffraction determination of a given SiNW's diameter.

To measure ensemble SiNW optical scattering intensities, $I(\lambda)_{norm}$, wires were sonicated and drop cast onto lacy-carbon-coated copper or gold electron microscopy grids. Samples were then submerged in isopropyl alcohol (IPA) and imaged using a DF optical microscopy setup. IPA was selected as a model medium as it has a similar refractive index (RI) compared to cellular systems (RI: 1.378 and 1.402, respectively).[29] To later incorporate this method with cellular systems, DF micrographs were obtained using a ring LED illuminator, enabling the use of scatter enhanced phase contrast (SEPC) imaging (a simultaneously projected DF-phase contrast image) (See **Section 2.2.2**2.2.2 Scatter Enhanced Phase Contrast). For ensemble measurements, a single line scan was taken along the wire body (**Figure 5.3a**), with scattering intensity I(λ) measured transverse to the long SiNW axis, allowing a measurement of both the local background $I(\lambda)_{bkg}$ and SiNW scattering $I(\lambda)_s$ intensities. Intensity measurements were normalized using the equation:

$$I(\lambda)_{norm} = \frac{I(\lambda)_S - I(\lambda)_{bkg}}{I(\lambda)_{s,max}} \quad \textbf{5.1}$$

where $I(\lambda)_{s,max}$ is the maximum observed scattering intensity for all wires within a sample population after background subtraction. To construct the optical scattering intensity CDF (**Figure 5.3b**), peak scattering intensity, $I(\lambda)_{norm}$, were recorded for a representative portion of the SiNWs, providing an optical population distribution. This allowed a transform from optical scattering intensities $I(\lambda)_{norm}$ to population percentile.

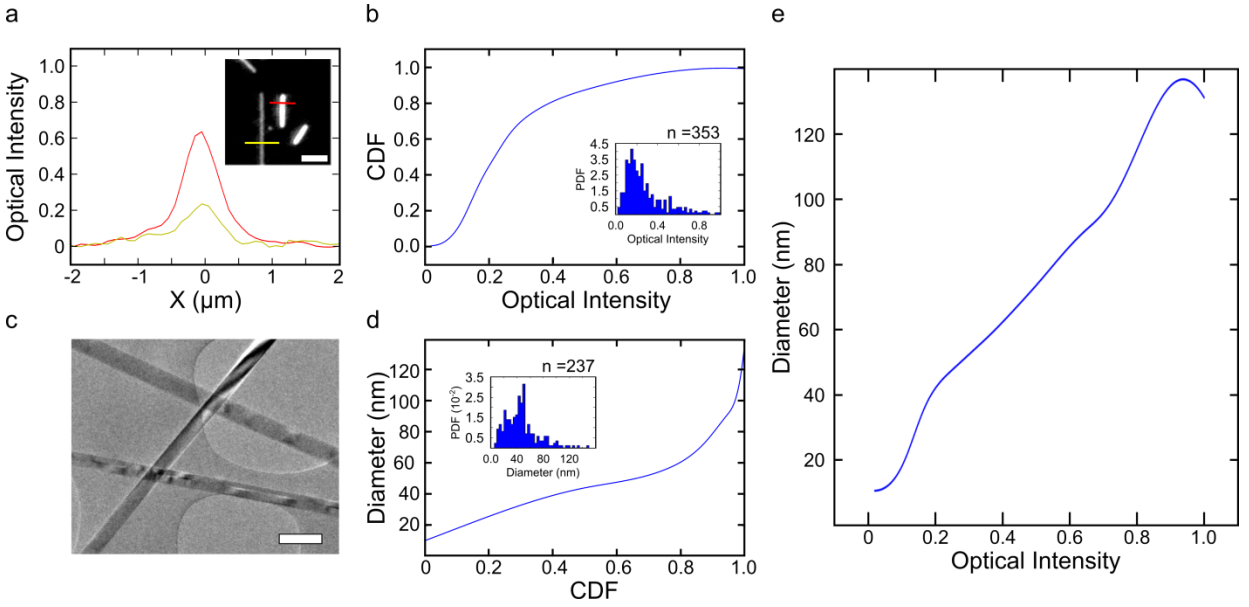

Figure 5.3 Constructing the Optical-EM Transform.
(**a**)Representative line scan measurement of relative SiNW optical intensities, with corresponding DF image (inset, Scale bar 4μm) (region of line scan in yellow and red). (**b**) Cumulative distribution function (CDF) of ensemble SiNW optical scattering intensity, with associated population distribution (inset). (**c**) Representative TEM micrograph of SiNWs used to measure ensemble SiNW diameters (Scale bar 150nm) (**d**) Inverse CDF of ensemble SiNW diameters as measured by TEM (upper), with associated population distribution (Given as a probability density function, PDF) (inset). (**e**) Empirically determined optical-EM transform constructed using the ensemble CDFs. Allows the assignment of individual SiNW diameter using optical intensity data. Adapted with permission from Zimmerman J. F. et. al. J. Phys. Chem. C, 2015. Copyright 2015 American Chemical Society.

To determine the underlying SiNW diameter population, samples were imaged using transmission electron microscopy (TEM), with micrographs taken at random, pre-determined locations prior to viewing to avoid biased sampling (**Figure 5.3c**). TEM provided high-resolution images of the SiNWs with an associated error of ±2.4 nm (~2.0% error), with this uncertainty arising primarily from small inconsistencies in the SiNWs surface morphology formed during the synthetic growth process, rather than imprecision in the measuring process. Collectively, these micrographs were used to measure the distribution of diameters present in the sample, and enabling the construction of the corresponding inverse CDF (**Figure 5.3d**). This allowed a mapping from population percentile into SiNW diameter. We note here that the samples

measured in this way need not be the exact wires imaged under DF (In fact this negates the point, as these wires could be imaged directly under TEM to determine their diameter), but must be wires from the same representative sample population. This enables an independent characterization of the SiNWs, allowing the wires to be optically imaged under conditions that are difficult to probe using electron microscopy, while still permitting a precise determination of the NW's diameter. In this way, this method differs from the exact transform, which would measure the same wires under both techniques, but instead depends on a statistical determination of the wire's diameter. We also note, that, while TEM provides a mechanism for precisely measuring resolution-limited data, this role could be served by other methods, such as atomic force microscopy (AFM), or scanning electron microscopy (SEM), as long as the inverse CDF can be obtained.

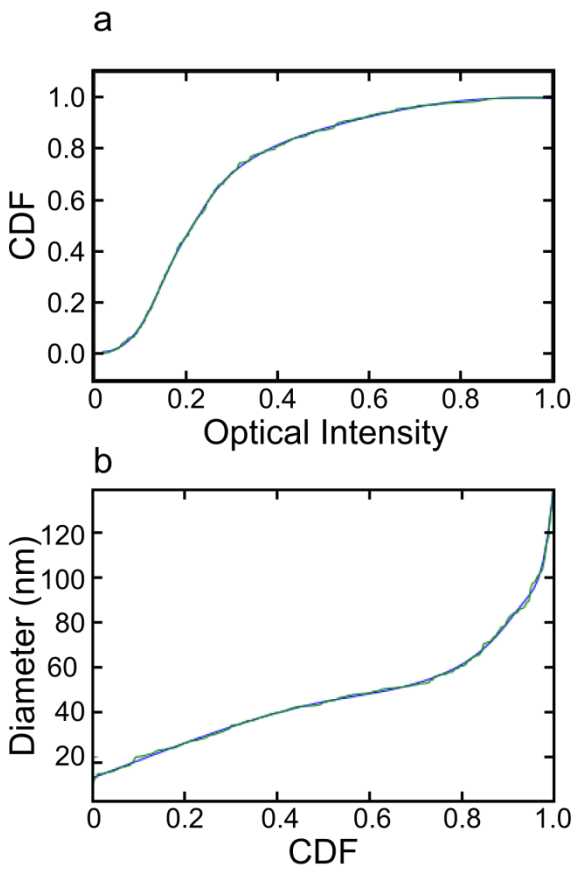

Figure 5.4. CDF Spline Fitting.
The optical CDF (**a**) and the inverse NW diameter CDF (**b**) are given (Experimentally determined values given in green, cubic polynomial spline fitting given in blue). Adapted with permission from Zimmerman J. F. et. al. J. Phys. Chem. C, 2015. Copyright 2015 American Chemical Society.

Taken together, the optical CDF and the inverse NW diameter CDF, allow the construction of a transform from scatter intensity $I(\lambda)_{norm}$ to SiNW diameter (**Figure 5.3e**). To enable a continuous mapping, the optical CDF and the inverse NW diameter CDF, were fit using a piece-wise cubic polynomial spline function (**Figure 5.4**). The resulting population-specific transform was found to be relatively linear, showing only small deviations before 40 nm and after 100 nm. To test this validity of this method, individual wires were measured using both DF and TEM techniques (**Figure 5.5, Figure 5.6**). The optical-EM transform was then applied to the experimentally determined optical

scattering intensities to predict the SiNW diameters, which were then compared to the experimentally measured values obtained via TEM. To account for deviations in the optical intensity profile, both the mean and the mode of the optical scatter intensity $I(\lambda)_{norm}$ distribution were determined for each wire. This was achieved using a custom NIH ImageJ script, which processed iterative line scans across the length of each wire, incorporating multiple DF micrographs (**Figure 5.7**).

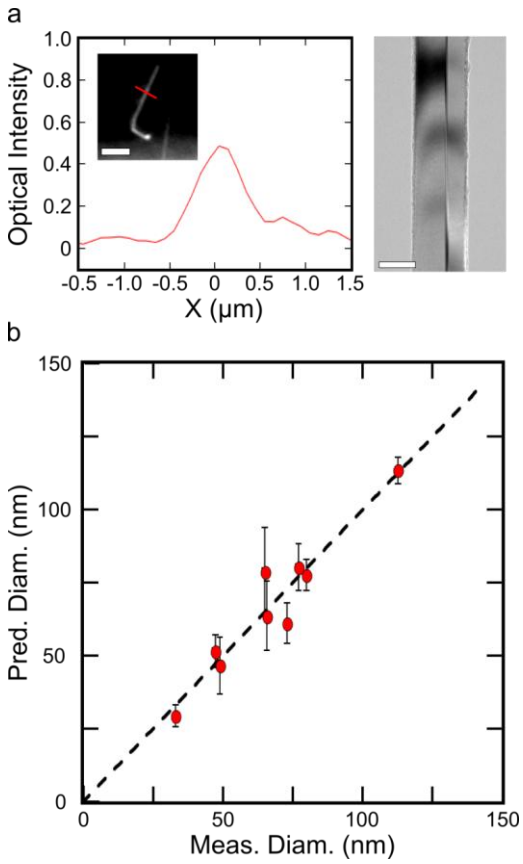

Figure 5.5 Verifying the Optical-EM Transform.
To evaluate the optical-EM transform individual wires were evaluated, measuring their scattering intensity and diameter. (**a**) Example wire's scattering intensity (left) using DF (inset, Scale bar 4μm), and diameter using TEM (right, Scale bar 50nm). The Optical-EM transform was used to predict the SiNW (continued...) diameter (Predicted diameter: 77.7 nm, Measured diameter: 79.8 nm). (**b**) Measured wire diameters compared to optically predicted diameters (unity given as dashed line, Error bars given as the standard deviation of the transformed optical intensity). Adapted with permission from Zimmerman J. F. et. al. J. Phys. Chem. C, 2015. Copyright 2015 American Chemical Society.

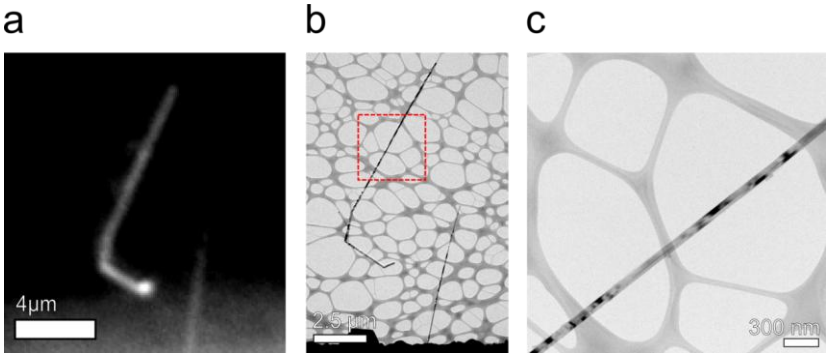

Figure 5.6 SiNW Control Sample.
To test the accuracy of the Optical-EM transform, individual wires were imaged both under DF (**a**) and TEM (**b**). A zoomed in view of the highlighted region is provided (**c**). DF images were acquired using a ring LED illuminator, with SiNWs submerged in an IPA solution. Adapted with permission from Zimmerman J. F. et. al. J. Phys. Chem. C, 2015. Copyright 2015 American Chemical Society.

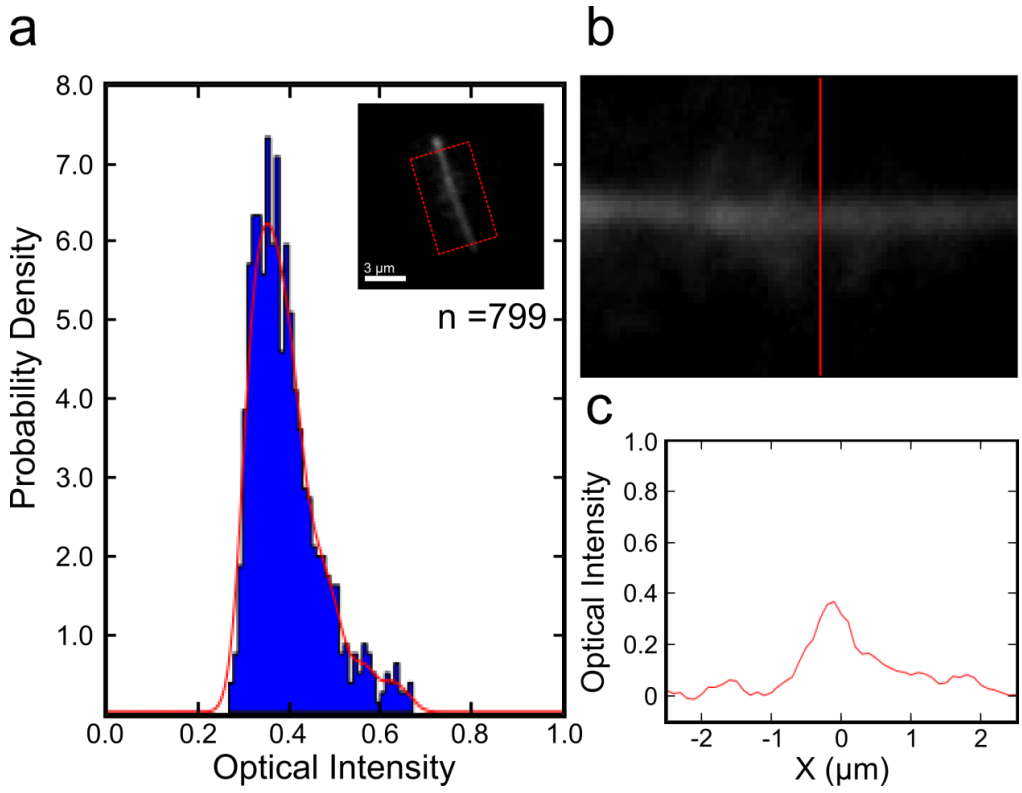

Figure 5.7 Individual SiNW Scattering.
(**a**) Distribution of measured scattering intensities from a single NW (non-parametric fit using a Gaussian kernel density estimate, shown in red) . Wire shown in inset, with region of interest highlighted in red. Ends are excluded due to the presence of gold synthetic catalyst, which displays distinct scattering characteristics. (**b**) Example of a single line scan taken across the NW, with corresponding line plot diagram (**c**). To collect the intensity distribution, a custom NIH ImageJ script was used to process iterative line scans across the entire length of the NW, from multiple micrographs taken under the same exposure conditions. The mode of the distribution was then used in the Optical-EM transform to predict the SiNW's diameter. Adapted with permission from Zimmerman J. F. et. al. J. Phys. Chem. C, 2015. Copyright 2015 American Chemical Society.

Comparing the TEM measured diameters to the predicted values, the optical-EM transform introduced a systematic error, which tended to on average under-predict SiNW diameters by ~8.9 nm, forecasting smaller wires than were actually present. This systematic error suggests that the optical population did not correctly reflect the underlying diameter population; specifically, smaller diameter wires were under-represented optically. This result is well explained through Mie scattering theory, and will be discussed later in further detail. After applying this correction factor, predicted wire diameters were well correlated with experimental results (**Figure 5.5b**), showing on average only a 4.8 nm deviation from the measured values (~8.0% error in SiNW diameter). This demonstrates a predictive capability that is well below the diffraction limit, with measurements remaining reliable across a range of diameters (between ~25-125 nm). The uncertainty associated with an individual SiNW's diameter prediction was estimated using the standard deviation of the transformed optical intensity measurements (shown as error bars for **Figure 5.5b**), which proved to be a reasonable estimate as the expected population of TEM measured diameters fell within a single standard deviation of the optically predicted values. Overall this demonstrates that this method is capable of 'breaking' the optical resolution limit, given some prior information about the sample population.

Before further employing this method, however, we need to consider the maximum range over which we can make reliable predictions. Furthermore, we must address the underlying assumption that scattering intensity scales monotonically with regard to nanowire diameter. To explore these topics, we have turned to Mie scattering theory, which offers some insights into possible experimental limitations.

5.2.2 Calculations of Optical Scattering using Lorentz-Mie Theory

Mie theory offers an analytical approach to solving Maxwell's equations for passive elastic light scattering, and can be used to explore SiNW scattering behavior.[4] As the optical-EM transform uses the intensity of scattered light to determine a SiNW diameter's, it is this measurement that we are most interested in. The intensity of scattered light, $(\lambda)_{norm,}$ is proportional to the product of the illuminating light intensity, $S(\lambda)$, and the dimensionless unit scattering efficiencies, Q_{sca}, such that

$$I(\lambda) \propto S(\lambda) \cdot \mathrm{Q_{sca}}(\mathrm{D}, \lambda) \quad \textbf{5.2}$$

with Q_{sca} defined as

$$\mathrm{Q_{sca}}(\mathrm{D}, \lambda) = \frac{\mathrm{C_{sca}}}{\mathrm{A_{geo}}} \quad \textbf{5.3}$$

where C_{sa} is the effective cross section of scattering, and A_{geo} is the geometric cross section, with materials assuming a Q_{sca} value between 0-1. For very small materials such as SiNWs, whose geometric sizes are below the wavelength of light, it is possible to have scattering efficiencies greater than this, meaning that the scattering cross sections, C_{sca}, is larger than the geometrical area A_{geo} of the object (i.e. the material can scatter light from an area larger than the material itself).

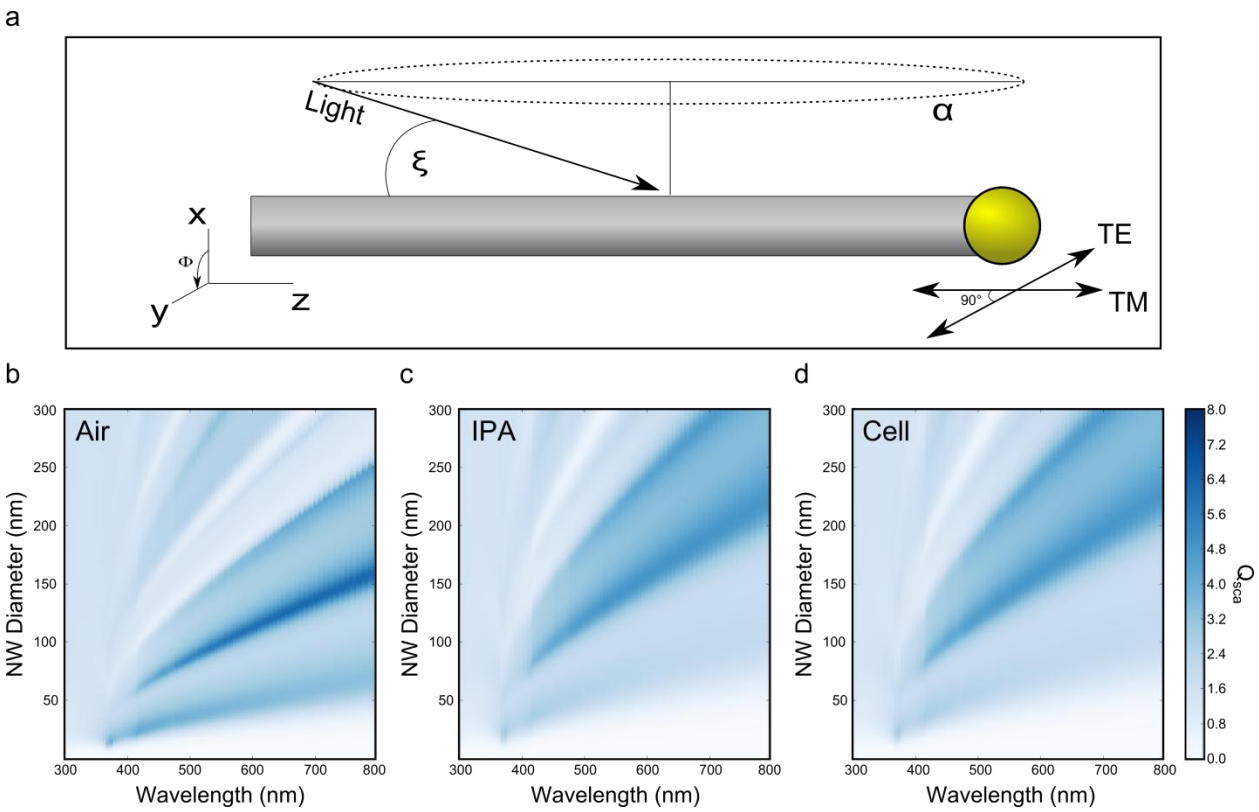

Figure 5.8 Mie Scattering of Silicon Nanowires.
(**a**)Schematic drawing of SiNW light scattering model for Mie theory calculations. Arrows indicates the incident light angle, ξ, and the corresponding plane of the TE and TM fields, with α representing the field of illumination. Calculated scattering efficiencies Q_{sca} of SiNWs for non-polarized light at a normal (ξ=90°) scattering angle in (**b**) air, (**c**) isopropyl alcohol (IPA), and (**d**) cytoplasm as a function of wavelength λ and SiNW diameter D. Adapted with permission from Zimmerman J. F. et. al. J. Phys. Chem. C, 2015. Copyright 2015 American Chemical Society.

The scattering efficiency (Q_{sca}) of SiNWs can be predicted computationally using Mie theory, and is non-linearly dependent on the diameter (D) of the SiNW and on the

illuminating light's incident angle (ξ), wavelength (λ), and polarization. For this model, SiNWs were assumed to behave optically as infinitely long one-dimensional cylinders, with calculations limited to illuminations perpendicular to the nanowire's long axis (ξ=90°). While some angle dependence has been reported for nanowires,[30] this represents the most general case, and has been shown to be in good agreement with experimentally observed SiNW spectra under darkfield.[4] The effective scattering, Q_{sca} (ξ=90°), was determined for the transversal electric (TE) and transversal magnetic (TM) modes of polarized light using the well known expression (**Figure 5.8a**):[4,17,31]

$$Q_{sca,TE} = \frac{2}{x}\left[|a_0|^2 + 2\sum_{i=1}^{\infty}|a_i|^2\right] \quad \textbf{5.4}$$

$$Q_{sca,TM} = \frac{2}{x}\left[|b_0|^2 + 2\sum_{i=1}^{\infty}|b_i|^2\right] \quad \textbf{5.5}$$

where the expansion coefficients (a_i & b_i) are given by:

$$a_i = \frac{\tilde{n}J_i(\tilde{n}x)J_i'(x) - J_i'(\tilde{n}x)J_i(x)}{\tilde{n}J_i(\tilde{n}x)H_i^{(1)\prime}(x) - J_i'(\tilde{n}x)H_i^{(1)}(x)} \quad \textbf{5.6}$$

$$b_i = \frac{J_i(\tilde{n}x)J_i'(x) - \tilde{n}J_i'(\tilde{n}x)J_i(x)}{J_i(\tilde{n}x)H_i^{(1)\prime}(x) - \tilde{n}J_i'(\tilde{n}x)H_i^{(1)}(x)} \quad \textbf{5.7}$$

$$\tilde{n} = n + ik \quad \textbf{5.8}$$

$$x = \frac{2\pi}{\lambda}\frac{D}{2} \quad \textbf{5.9}$$

ñ is the wavelength dependent complex refractive index, J_i is the Bessel function of the first kind of order i, and $H_1^{(i)}$ is the Hankel function of the first kind of order i. For non-

polarized light, the scatter efficiency $Q_{sca,np}$ is given by the expression $Q_{sca,np} = (Q_{sca,TM}+Q_{sca,TE})/2$. Bulk silicon refrence values for the wavelength dependent complex refractive index, ñ, were used[32] and quantum confinement effects were ignored for the present study. These are reasonable assumptions for the majority of wires surveyed; however, they may be problematic for smaller wires (d < 5 nm), as SiNW thickness can begin to dominate optical properties.[33] The infinite sums of the Bessel and Hankel functions were approximated analytically to the 10th order, as beyond this no appreciable changes were noted.

The scattering efficiencies Q_{sca} were calculated for SiNWs in a number of different media, including air, isopropyl alcohol (IPA), and cellular cytoplasmic fluid (**Figure 5.8b,c&d**). For each medium, a series of different peak scattering efficiencies Q_{sca} were observed, with SiNW scattering efficiencies Q_{sca} depending on both the wavelength (λ) and SiNW diameter. The resulting scattering features were similar for both IPA and cytoplasmic fluid as they have a similar RI, however these differed from the scattering predicted in air, with IPA and cytoplamic fluid's displaying a distended scattering efficiency in the (λ,d) plane, while air generally displayed sharper scattering peaks between ~50 nm to ~150 nm in the visible regime. Additionally, larger scattering efficiencies were predicted at larger diameters under IPA and cytoplasmic fluid than was true in the air case and in each medium, for wavelengths smaller than ~350 nm, the scattering efficiencies Q_{sca} did not show a strong dependence on SiNW's diameter.

Mie theory offers some insight into SiNW scattering, and can be used to examine the previously mentioned underlying assumption that SiNW scattering intensity scales monotonically with regard to NW diameter. Examining this in the visible regime for a

given wavelength, it can be seen that multiple NW diameters show the same predicted scattering efficiency (**Figure 5.9**). This suggests that light intensity, at least for a given wavelength, is not a unique metric for determining a SiNW's diameter, and that larger SiNWs don't necessarily scatter light most efficiently. Taken together, this means that single wavelength light does not fulfill our monotonic requirement for using the optical-EM transform.

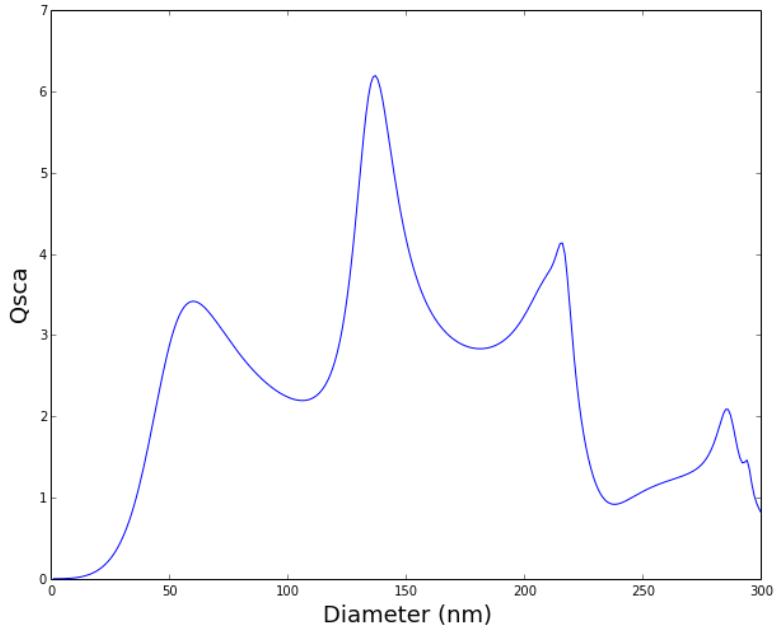

Figure 5.9 Predicted Scattering Efficiency Cross Sections for SiNWs.
For a given wavelength**,** multiple NW diameters show the same predicted scattering efficiency. This suggests that light intensity is not a unique metric for NW diameter, using only a single wavelength of light (Medium = air, λ = 700 nm). Adapted with permission from Zimmerman J. F. et. al. J. Phys. Chem. C, 2015. Copyright 2015 American Chemical Society.

However, with the exception of lasers, few light sources illuminate over such a narrow range of wavelengths. Therefore, a more reasonable prediction of the scattering intensity observed under DF would take into account both the spectrum of the illuminating lamp and the spectral sensitivity of the detector. To incorporate these factors into our model, we constructed a normalized scattering coefficient, Qnsca, which

uses the wavelength dependent intensity of our ring LED source (**Figure 5.18**) and the wavelength dependent quantum efficiency of our recording device as weighting coefficients (See **Section 5.4.2**5.4.2 Correlative Optical and EM Measurements.). Summing these over the spectral range of the illumination source and normalizing, produced a more reasonable estimate of the expected light scattering, Q_{nsca} (**Figure 5.10,** left axis). Using this method, Mie theory predicted scattering efficiencies were compared to the experimentally determined relative optical scattering intensities (**Figure 5.10,** right axis), with the maximum observed scattering intensities (<150 nm) scaled to agree with the maximum predicted Q_{nsca} at ~150 nm (See equation **5.2**). For wires with diameters under 150 nm, the predicted values were seen to be in qualitative agreement with experimentally determined values, with both showing similar scaling and a relatively monotonic increase before ~150 nm in IPA. This validates our earlier approach, suggesting that the Optical-EM transform is well founded in this size range. However, Mie theory also tended to inflate scattering efficiencies, with a predicted scattering peak at ~60 nm in IPA, while experimentally observed values show a more modest scaling in this regime. This is likely the result substrate-SiNW interactions and of assuming a fixed angle (ξ=90°), where a more complete approach would incorporate the setup-dependent darkfield angle, integrating about the circle of illumination (α, **Figure 5.8a**); however, this is beyond the scope of the current paper.

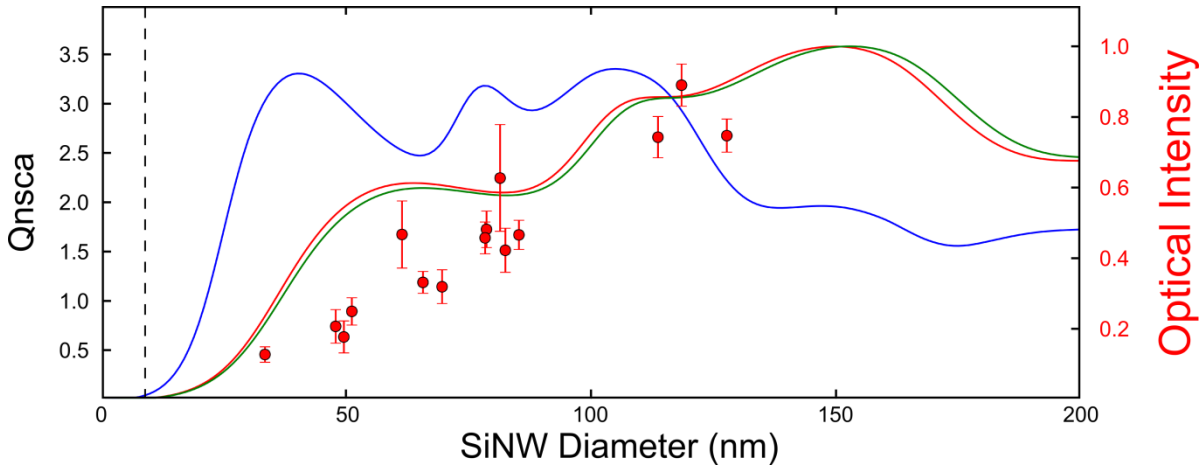

Figure 5.10 Experimental and Predicted Scattering Efficiencies.
Normalized Mie theory predicted scattering efficiencies, Qnsca, of SiNWs using LED illumination in air (Blue-line), IPA (Red-line), and cytoplasmic fluid (Green-line) as a function of SiNW diameter, D (**left axis**), superimposed with relative optical scattering intensity of experimentally measured SiNWs under IPA (Red-Dots, **right axis**). Horizontal (9 nm marker) suggests the origin of the systematic error present in the optical transform. Sub 150 nm diameter wires show qualitative agreement between predictions and experimentation. Adapted with permission from Zimmerman J. F. et. al. J. Phys. Chem. C, 2015. Copyright 2015 American Chemical Society.

Additionally, we noted some limitation in Lorentz-Mie theory's predictive power for larger diameter SiNWs. For larger wires (between ~260-300 nm), observed scattering intensities significantly out-scaled predicted values (**Figure 5.11**) (Scattering intensities normalized to sub 150 nm population). This is the result of an underlying assumption that the wires are embedded in a uniform medium and therefore have minimal interaction with the underlying substrate. For smaller wires whose resonant modes are primarily confined within the wire, this is a reasonable approximation; however, as wires grow larger these modes can extended noticeably beyond the boundary of the wire, creating some discrepancy between experimentation and theory[8]. This shows, that while Lorentz-Mie scattering was useful for understanding certain trends in optical scattering, its application must be carefully considered for larger wires. Additionally, this mismatch between theory and experimentation justifies our experimentally based approach for determining the optical-EM transform, rather than

using a purely theoretical method to produce the mapping function, as the experimental results do not correspond directly with the theoretical model.

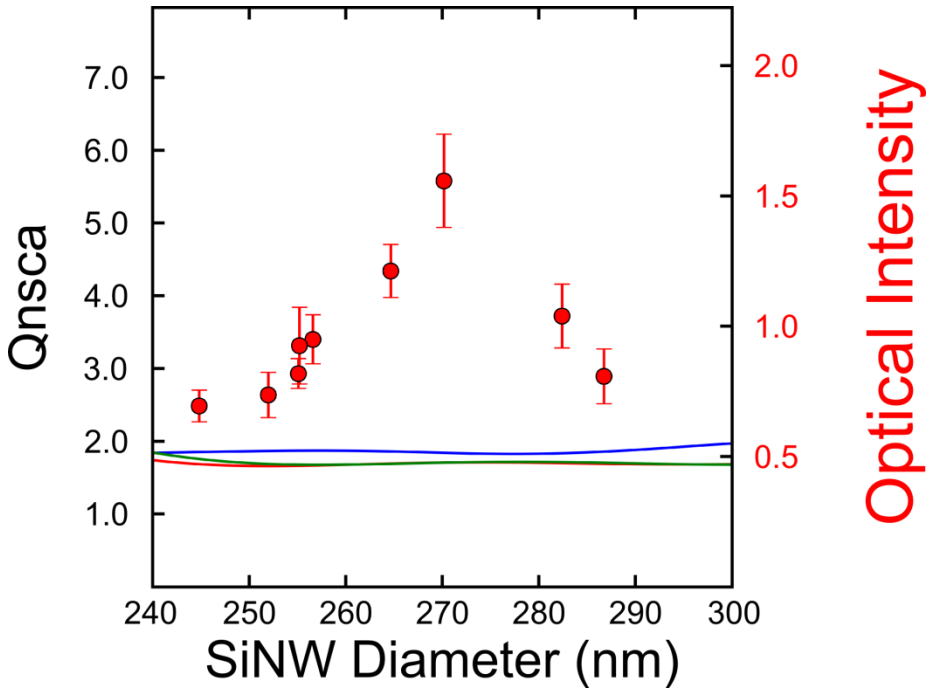

Figure 5.11 Large Diameter SiNW Scattering
Mie theory predicted scattering efficiencies, Qnsca, in air (Blue-line), IPA (Red-line), and cytoplasmic fluid (Green-line) (**left axis**), superimposed with experimentally measured optical scattering intensity of larger diameter SiNWs under IPA (Red-Dots, **right axis**). Mie theory fails to recapitulate experimental values for larger SiNWs. (Relative optical intensities scaled to agree with sub 150 nm population). Adapted with permission from Zimmerman J. F. et. al. J. Phys. Chem. C, 2015. Copyright 2015 American Chemical Society.

Despite these inconstancies, Mie theory offers some potential insight into understanding SiNW scattering. First, it indicates potential ranges over which the optical-EM transform can perform. For each imaging media, the predicted scattering intensities actually decrease after a certain threshold diameter. This indicates the range over which the optical-EM transform can no longer be safely applied, as past this threshold scattering intensity no longer scales monotonically. Second, Mie theory also indicates the important role that imaging media plays in optical scattering. In air, for instance, predicted scattering efficiencies scale sharply between 0 - 40 nm before reaching a maximum plateau, and then drop down again near ~100 nm to a relatively

consistent value. While this limits the range of optical-EM transform to between ~0-40 nm in air, it also suggests that scattering intensity can be used as a very sensitive marker for SiNW diameter in this regime. For IPA and cytosolic fluid, however, a much larger range is predicted, showing a consistent increase in light scattering between ~0-150 nm. While there is slight dip between ~54-84nm, overall this range is relatively monotonic, suggesting that SiNWs fulfill this requirement under real world conditions. The values reported here are specific to the LED ring illuminator used in these experiments, which enabled the simultaneous monitoring of both SiNWs and cellular systems. However more traditional black body irradiators (such as tungsten-cathode lamps) show similar trends, (**Figure 5.12**), even predicting an extended monotonic range of up to ~230 nm in IPA. In this way, Mie theory offers some potential insights into different optical scattering conditions and confirms that our conditions for monotonic scaling are satisfied for wires with diameters under 150 nm in IPA.

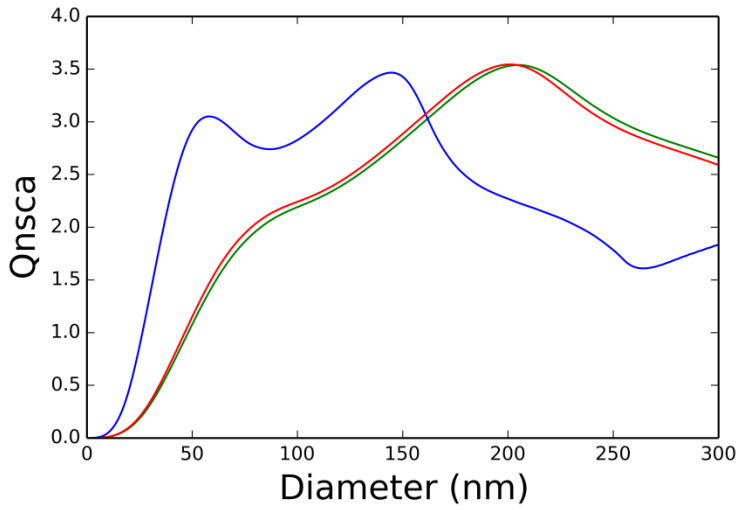

Figure 5.12 Predicted Scattering Efficiencies of SiNWs Under a Blackbody Radiation Source. Predicted scattering efficiencies Q_{nsca} of SiNWs illuminated using blackbody radiation, such as from a tungsten-halogen lamp, in air (blue-line), isopropyl alcohol (red-line), and cytoplasmic fluid (green-line). Spectrum modeled using Planck equation for black body spectral radiance at T=3000 K, and the detectors quantum efficiency, C_{QE}, is taken to be one at all wavelengths. Adapted with permission from Zimmerman J. F. et. al. J. Phys. Chem. C, 2015. Copyright 2015 American Chemical Society.

Mie theory can also help explain why smaller wires were under-represented in the initial optical-EM transform predictions, leading to a systematic error and the need for a correction factor. By examining the predicted scattering efficiencies of very small wires (<9 nm, **Figure 5.10**, dashed line), we can see that these wires showed negligible predicted scattering efficiencies in IPA and cytosolic fluid. This suggests that smaller wires will not be observed appreciably using optical techniques as compared to larger wires, resulting in the previously mentioned population mismatch where smaller wires were under-represented optically compared to the TEM measured values. This threshold appears to occur near ~10.0 nm, which is in good agreement with the experimentally determined correction factor of 8.9 nm.

Before moving on, we note that the Lorentz-Mie theory presented here represents a rapid analytical approach for exploring SiNW optics and has been shown to be in good agreement for multiple material systems including GaAs[17] and germanium[28] nanowires; however more computationally-intensive numerical approaches, such as Finite-difference time-domain (FDTD), can also be pursued to provide a more precise theoretical model[18,34,35]. Such approaches offer the benefit of being able to model explicitly substrate nanowire interactions, however they can also be more time intensive to both implement and run over a large spectral range. As our primary goal in this manuscript was to establish the monotonic range over which the optical-EM transform remains valid, the Lorentz-Mie theory approach offered a valuable tool for rapidly assessing this requirement under multiple conditions.

5.2.3 Calibrated Intracellular Force Probes.

Using this information, we were able to extend the use of the optical-EM transform to intracellular SiNWs, enabling a more precise determination of forces in optically-based SiNW intracellular force probes. Mechanical forces play an important role in regulating cellular behavior, providing cues for intra and intercellular signaling[36,37]. SiNW force probes are a promising class of material for examining these processes, as they can be distributed in a drug like fashion, are relatively easy to implement, offering the potential for long-term continues multiplexed force detection[25]. Additionally, unlike other intracellular force probing mechanisms such as optical tweezers[38], and fluorescent molecular probes[39,40], SiNW force probes are resistant to fluorescent bleaching[41] and localized photothermal heating, both of which can limit experimental time-scales[42].

While the reported probes can precisely predict relative force changes[25], their ability to determine absolute forces was hampered by the accuracy the SiNW diameter measurement, as the force probes reported in this study are extremely sensitive to NW diameters, with forces scaling to the fourth power with respect to SiNW diameter. One way to resolve this issue is using electron microscopy studies in conjunction with these probes; however, such studies are time consuming, and are difficult to link to specific probes within individual cells. The optical-EM transform allows a route to circumvent this requirement, as electron microscopy studies can be performed in an ensemble fashion, using wires prepared from the same sample, rather than the specific force probe itself, while still allowing a precise determination of the NW's diameter.

From here human aortic smooth muscle cells (HASMCs) were selected as a model cell line, as contraction can be easily induced using the hormone angiotension II (**Video S.6**). Kinked SiNW force probes were introduced 72 hours before force

measurements, allowing cells time to internalize the wires, and with samples monitored using scatter enhanced phase contrast (SEPC)[25]. By monitoring the shape of SiNW deformation, we were able to extract force information from the probes, with nanowire bending modeled using the Euler-Bernoulli equations for the deflection of a simple beam supported under an asymmetric point load (See **Section 4.2.3**)

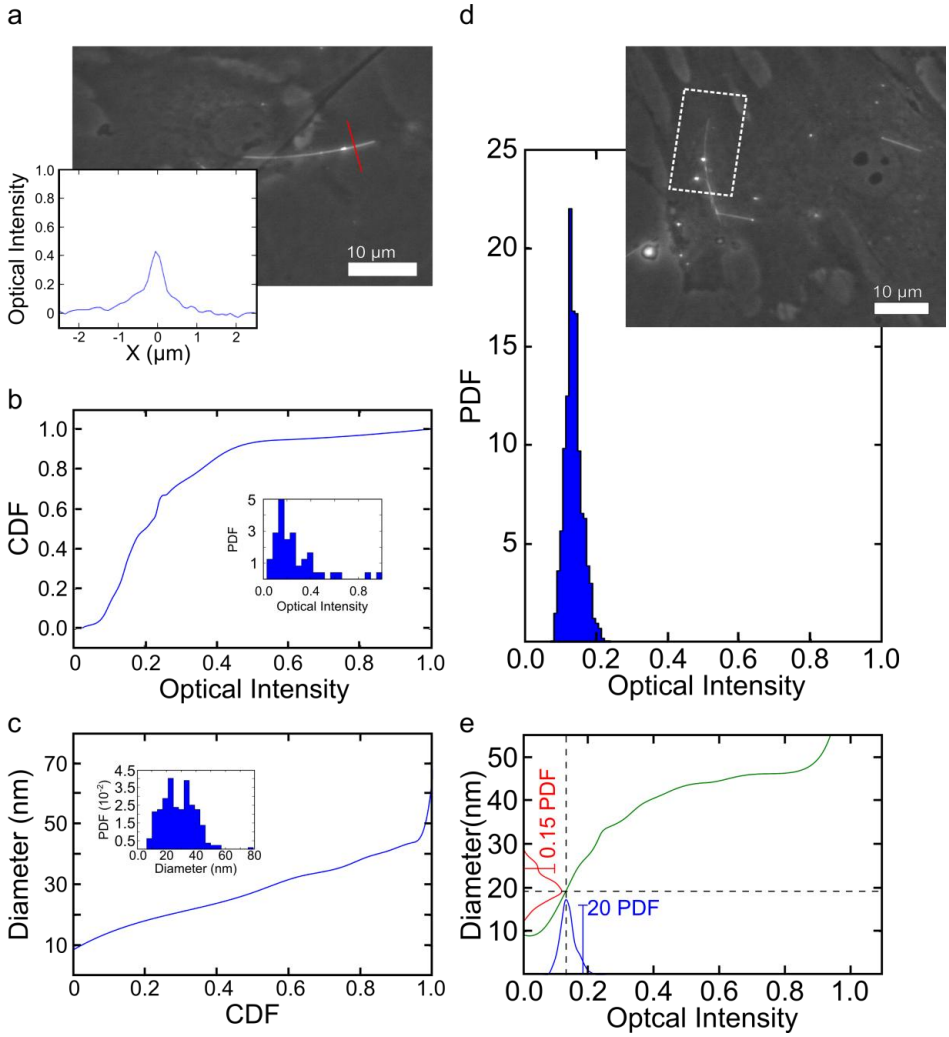

Figure 5.13 Construction of the Live Cell Optical-EM Transform.
(**a**) Example SEPC image of SiNW in cellular microenvironment with resulting line taken over region indicated in red. (**b**) Cumulative distribution function (CDF) of ensemble SiNW optical scattering intensity, with associated population distribution (inset). (**c**) Inverse CDF of ensemble SiNW diameters as measured by TEM, with associated population distribution (inset). (**d**) Measured optical scattering of kinked SiNW force probe, with the associated optical micrograph. Adapted with permission from Zimmerman J. F. et. al. J. Phys. Chem. C, 2015. Copyright 2015 American Chemical Society.

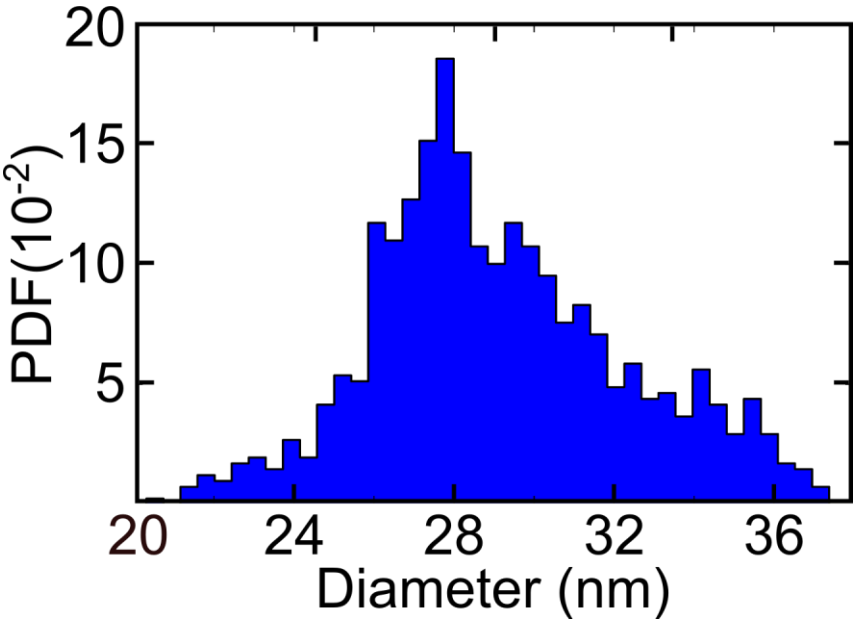

Figure 5.14 Live Cell Predicted SiNW Diameter.
Diameter distribution of the SiNW force probe predicted using the optical-EM transform (mode: 27.7 nm, standard deviation: 3.2 nm). Adapted with permission from Zimmerman J. F. et. al. J. Phys. Chem. C, 2015. Copyright 2015 American Chemical Society.

To precisely measure intracellular forces, the probe's diameter was determined using the optical-EM transform to convert optical intensity measurements into diameter information. The intracellular optical-EM transform was constructed for force probes in an analogous fashion to those previously mentioned (**Figure 5.13**), with the ensemble optical measurements obtained using an internal control model (**Figure 5.13a**) (i.e. other wires present within the sample solution), mitigating the effects of cellular exposure on the optical scattering profile. Control samples were imaged immediately after force measurements, using the same incident light intensity and exposure conditions. The intracellular optical-EM transform was then applied to the optical scattering recorded from the individual probe, yielding a mode diameter prediction of 27.7±3.2 nm (**Figure 5.14**) (error given as the standard deviation of the transformed scattering intensity measurements). Using this diameter, the Euler-Bernoulli equations were found to be in good agreement with experimental determined optical deformations

(**Figure 5.15b**), with HASMCs showing optimal contraction times around ~30 minutes, and maximum predicted force peaks on the order of 171 pN (**Figure 5.15c**).

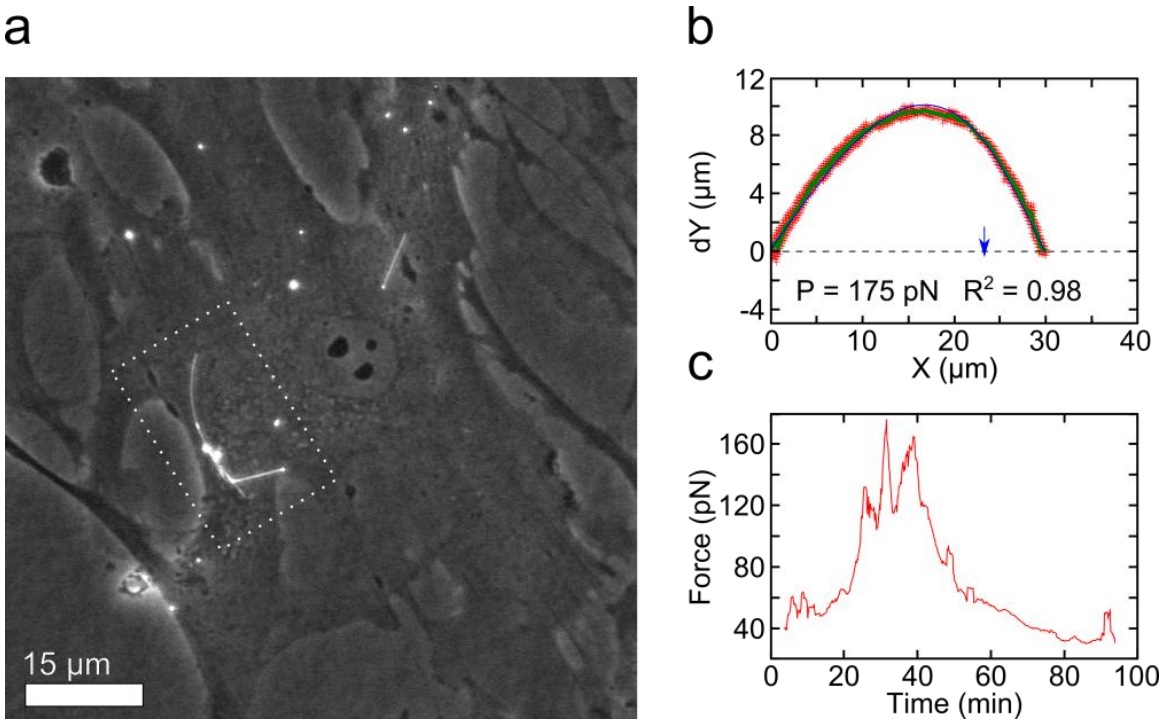

Figure 5.15 SiNWs as Intracellular Force Probes.
(**a**) SEPC micrograph of a Kinked SiNW Force Probe Internalized in a HASMC, with schematic diagram showing SiNW force model (inset). (**b**) Single frame example of SiNW force fitting data. (Red-SiNW coordinates, Green-Averaged center, Blue-Force fitting data, Blue Arrow-Position of Force Load). (**c**) Intracellular force over time, during angiotensin induced muscle contraction. Adapted with permission from Zimmerman J. F. et. al. J. Phys. Chem. C, 2015. Copyright 2015 American Chemical Society.

The use of the optical-EM transform enabled an estimate of uncertainty present in these force measurements. Using the distribution of possible NW diameters, an example frame (**Figure 5.15b**) was re-fit using the modified SiNW diameter and the respective values for the cross sectional moment of inertia **I**. This yielded a range of possible force measurements that could be observed (**Figure 5.16**), estimating a standard deviation of ±102 pN, or an error of ~59%. While this is larger than the ~10% error values reported using magnetic tweezers,[43] this represents a substantial decrease in the error associated with this type of measurement using the base force probe's diameter distribution. Although the standard deviation of the default growth sample was

only ~10 nanometers, this corresponds to standard deviation in force measurements of ~12,672 pN (**Figure 5.17** Uncertainty in Force Measurements Before Optical-EM Transform.). As a result, the optical-EM transform yields a more than 100x fold increase in the accuracy of these force measurements, marking this a substantial improvement, and demonstrating the power of the optical-EM transform in addressing practical biomaterial applications.

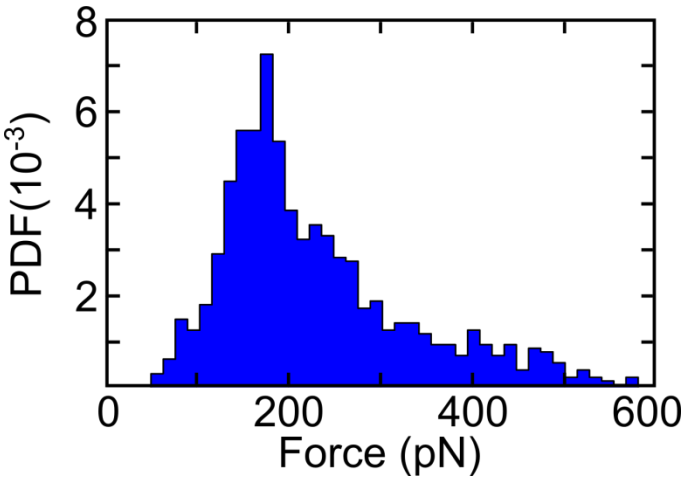

Figure 5.16 Uncertainty in Force Measurements After Optical-EM Transform.
Uncertainty in force measurements determined by fitting an example frame using the distribution of possible SiNW diameters determined by the optical-EM transform (Mode: 171 pN, Mean: 230 pN, Standard Deviation: 104 pN). Adapted with permission from Zimmerman J. F. et. al. J. Phys. Chem. C, 2015. Copyright 2015 American Chemical Society.

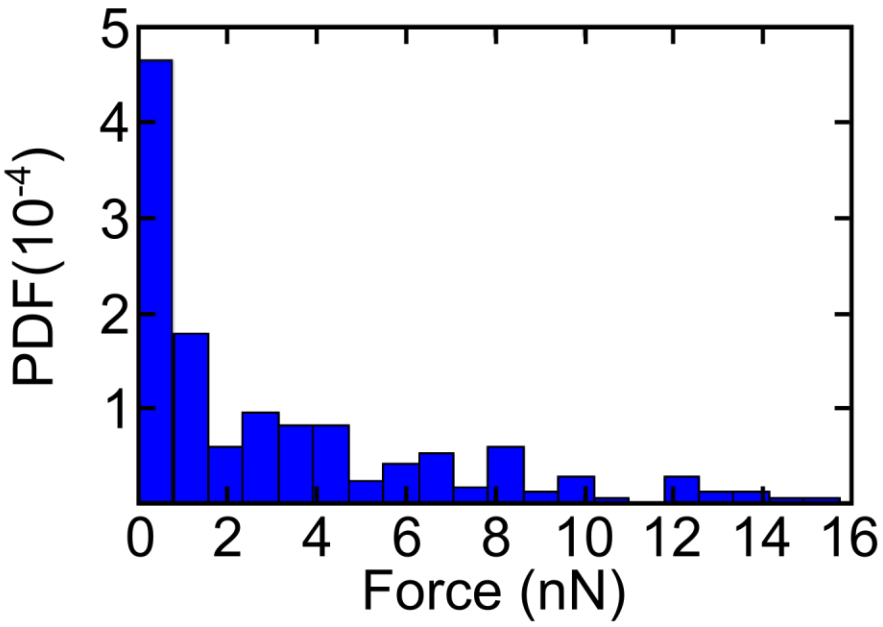

Figure 5.17 Uncertainty in Force Measurements Before Optical-EM Transform.
Histogram of the uncertainty in the force measurements using the base diameter population distribution without using the optical-EM transform. Adapted with permission from Zimmerman J. F. et. al. J. Phys. Chem. C, 2015. Copyright 2015 American Chemical Society.

5.3 Conclusions

A scalable method to optically determine SiNW diameters based on their scattering intensity and ensemble diameter measurements has been presented. This method allows for the determination of a sample's diameter within an accuracy of a few nanometers, providing diffraction-limited information, with an associated error of less than 10%. Although the models presented here are specific to silicon-based devices, we believe that this method could be easily implemented in other nanomaterials, such as germanium and silver nanowires, and that Mie theory offers a powerful tool for understanding how light scattering scales in these systems. By using this method for *in situ* intracellular optical force probes, we have shown how this technique can help

provide resolution-limited information in situations where it might otherwise be challenging to obtain directly, and how such techniques can be important for studying the bionano interface. Finally, we believe that this method has substantial promise for use with SiNW based optoelectronic devices such as sensors, photovoltaics, and photodetectors. By enabling a quick determination of a NW's diameter, this work could be a substantial boon for large-scale quality assurance and device calibration efforts.

5.4 Experimental Details

5.4.1 SiNW Synthesis

SiNWs were grown using the vapor-liquid-solid mechanism in a homebuilt chemical vapor deposition system. To clean the silicon growth substrates, they were first rinsed with acetone and isopropyl alcohol (IPA), and then dried under nitrogen gas. Substrates were then oxygen plasma cleaned (Plasma Etch PS-100LF) for 10 minutes, and coated in 1:3 dilute poly-L-lysine for 15 minutes. After rinsing with deionized water, gold nanoparticles between 20-250 nm (Ted Pella Inc.) were allowed to settle for 30 minutes and were then dried under nitrogen gas. SiNW growth conditions were as follows: 480 ^{o}C, 40 torr, 60 sccm hydrogen carrier gas, and 2 sccm silane. In the case of intracellular force probes, kinks were introduced into the wires as previously reported[44].

5.4.2 Correlative Optical and EM Measurements.

To obtain correlative microscopy images, appropriate wires were sonicated in IPA and dropcast onto lacy carbon coated copper or gold electron microscopy grids (Electron Microscopy Sciences). TEM micrographs were obtained using a 300 kV FEI Tecnai G2

F30 Super Twin Transmission Electron Microscope. After TEM imaging, the grids were then transferred to an Olympus IX71 inverted microscope, and submerged in the appropriate optical media (i.e. air or IPA). LUCPlanFLNPh 20x and 40x objectives were used with a numerical aperture (NA) of 0.4 and 0.65 respectively. High angle transmitted darkfield micrographs were obtained using a using an Amscope LED-144-YK ring lamp LED attached to the brightfield condenser, as previously described.[25] Typical LED power was between 15%-20% of maximum power, with a spectral range as shown (**Figure 5.18**). Images were recorded on a Hamamatsu ORCA-R2 C10600-10B digital CCD camera at 16-bit depth with 0.3 µm x 0.3 µm pixel resolution. For comparative intensity measurements, illuminating light intensity and image exposure times were maintained across all samples.

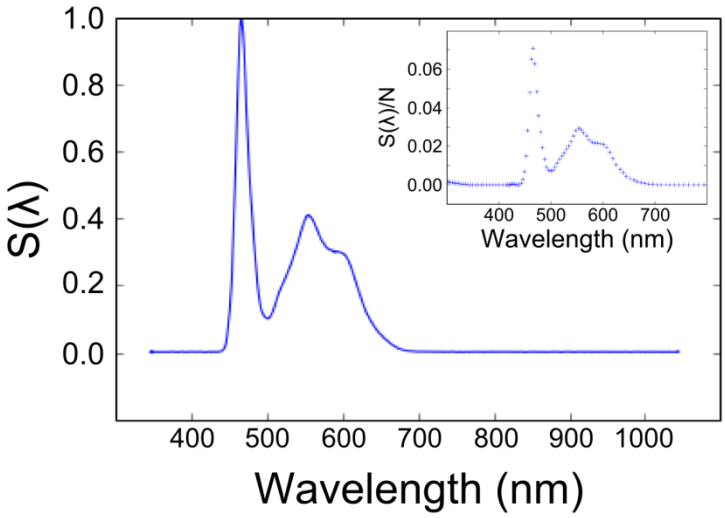

Figure 5.18. Darkfield Lamp Spectrum.
Relative spectral intensity, S(λ), of the illuminating LED light source used for NW measurement experiments, with inset showing the normalized probability density. Adapted with permission from Zimmerman J. F. et. al. J. Phys. Chem. C, 2015. Copyright 2015 American Chemical Society.

5.4.2 Computational Calculations

Mie theory calculations were performed in Python using a custom built script in iPython Notebook 4.0. Kernel density estimates, Bessel and Hankel functions were numerically approximated using the associated stats and special functions available in the open source SciPy functions library.

5.4.3 Scattering Efficiency Normalization

To incorporate the spectral features of the illuminating light source, and quantum efficiency of the detector, the wavelength dependent scattering coefficient, Qsca, was normalized using the following equation:

$$\mathrm{Q_{nsca}}(D) = \sum_{\lambda=n}^{i} \mathrm{Q_{sca,np}}(\mathrm{D}, \lambda) \cdot \frac{S(\lambda) \cdot \mathrm{C_{QE}}(\lambda)}{N} \qquad \textbf{5.10}$$

where, Q_{nsca} is the quantum scattering efficiency normalized over the illuminating spectrum, S(λ) is the relative spectral intensity of the light source (**Figure 5.18**), n&i are the spectral range (300 and 800 nm respectively in the present case), N is a normalization constant, and $C_{QE}(\lambda)$ is the detector's wavelength dependent quantum efficiency. N was obtained by integrating across the entire illuminating spectrum such that,

$$\mathrm{N} = \int_{\mathrm{n}}^{\mathrm{i}} S(\lambda) \cdot \mathrm{C_{QE}}(\lambda)\ d\lambda \qquad \textbf{5.11}$$

Detector quantum efficiencies, $C_{QE}(\lambda)$, for the Hamamatsu ORCA-R2 C10600-10B digital CCD camera are available online on Hamamatsu's website and are obtainable upon request.

5.4.4 Systematic Error Correction

On average, the predicted diameter values tended to under-predict the TEM measured values, a result of the low optical intensity of smaller diameter wires. As we would expect the predicted values to be evenly distributed about unity, this suggests that this error is systematic, rather than a result of imprecise measurement, or random error. To account for this systematic error a correction factor was introduced, shifting the predicted values by a constant, with the predicted value P given by $P = P_0 + E_s$, where P_0 is the original predicted value, and E_s is the correction for systematic error. To determine the systemic error constant, Es, a linear least squares fit was used, comparing the optically predicted NW diameters to the TEM determined values. This was experimentally measured to be ~9.0 nm which is in good agreement with the shift in NW diameter expected from Mie theory.

5.5 References

1. Street, R. a, Wong, W. S. & Paulson, C. Analytic Model for Diffuse Reflectivity of Silicon Nanowire Mats. *Nano Lett.* **9,** 3494–3497 (2009).

2. Tsakalakos, L. Strong broadband optical absorption in silicon nanowire films. *J. Nanophotonics* **1,** 013552 (2007).

3. Muskens, O. L. *et al.* Epitaxial Growth of Aligned Semiconductor Nanowire Metamaterials for Photonic Applications. *Adv. Funct. Mater.* **18,** 1039–1046 (2008).

4. Brönstrup, G. *et al.* Optical Properties of Individual Silicon Nanowires for Photonic Devices. *ACS Nano* **4,** 7113–7122 (2010).

5. Priolo, F., Gregorkiewicz, T., Galli, M. & Krauss, T. F. Silicon nanostructures for photonics and photovoltaics. *Nat. Nanotechnol.* **9,** 19–32 (2014).

6. Kelzenberg, M. D. *et al.* Photovoltaic Measurements in Single-Nanowire Silicon Solar Cells. *Nano Lett.* **8,** 710–714 (2008).

7. Zhang, X. *et al.* Horizontal Silicon Nanowires with Radial p–n Junctions: A Platform for Unconventional Solar Cells. *J. Phys. Chem. Lett.* **4,** 2002–2009 (2013).

8. Cao, L. *et al.* Semiconductor Nanowire Optical Antenna Solar Absorbers. *Nano Lett.* **10,** 439–445 (2010).

9. Tian, B. *et al.* Coaxial silicon nanowires as solar cells and nanoelectronic power sources. *Nature* **449,** 885–889 (2007).

10. YAMADA, H., CHU, T., ISHIDA, S. & ARAKAWA, Y. Si Photonic Wire Waveguide Devices. *IEICE Trans. Electron.* **E90-C,** 59–64 (2007).

11. Wang, H. *et al.* Hydrogen-Terminated Si Nanowires as Label-Free Colorimetric Sensors in the Ultrasensitive and Highly Selective Detection of Fluoride Anions in Pure Water Phase. *Adv. Funct. Mater.* **25,** 1506–1510 (2015).

12. Zhang, A. *et al.* Silicon nanowire detectors showing phototransistive gain. *Appl. Phys. Lett.* **93,** 121110 (2008).

13. Yang, C., Barrelet, C. J., Capasso, F. & Lieber, C. M. Single p-Type/Intrinsic/n-Type Silicon Nanowires as Nanoscale Avalanche Photodetectors. *Nano Lett.* **6,** 2929–2934 (2006).

14. Lee, S.-H. *et al.* Characterization of Channel-Diameter-Dependent Low-Frequency Noise in Silicon Nanowire Field-Effect Transistors. *IEEE Electron Device Lett.* **33,** 1348–1350 (2012).

15. Singh, N. *et al.* Ultra-Narrow Silicon Nanowire Gate-All-Around CMOS Devices: Impact of Diameter, Channel-Orientation and Low Temperature on Device Performance. in *2006 International Electron Devices Meeting* 1–4 (IEEE, 2006). doi:10.1109/IEDM.2006.346840

16. Kempa, T. J. *et al.* Coaxial multishell nanowires with high-quality electronic interfaces and tunable optical cavities for ultrathin photovoltaics. *Proc. Natl. Acad. Sci.* **109,** 1407–1412 (2012).

17. Brönstrup, G. *et al.* A precise optical determination of nanoscale diameters of semiconductor nanowires. *Nanotechnology* **22,** 385201 (2011).

18. Cao, L., Fan, P., Barnard, E. S., Brown, A. M. & Brongersma, M. L. Tuning the Color of Silicon Nanostructures. *Nano Lett.* **10,** 2649–2654 (2010).

19. Heurlin, M., Anttu, N., Camus, C., Samuelson, L. & Borgström, M. T. In Situ Characterization of Nanowire Dimensions and Growth Dynamics by Optical Reflectance. *Nano Lett.* **15,** 3597–3602 (2015).

20. Jacques, S. L. Optical properties of biological tissues: a review. *Phys. Med. Biol.*

58, R37–R61 (2013).

21. Zhang, W., Tong, L. & Yang, C. Cellular Binding and Internalization of Functionalized Silicon Nanowires. *Nano Lett.* **12,** 1002–1006 (2012).

22. Zimmerman, J., Parameswaran, R. & Tian, B. Nanoscale semiconductor devices as new biomaterials. *Biomater. Sci.* **2,** 619 (2014).

23. Tian, B. *et al.* Three-dimensional, flexible nanoscale field-effect transistors as localized bioprobes. *Science* **329,** 830–4 (2010).

24. Chiappini, C. *et al.* Biodegradable silicon nanoneedles delivering nucleic acids intracellularly induce localized in vivo neovascularization. *Nat. Mater.* **14,** 532–539 (2015).

25. Zimmerman, J. F. *et al.* Free-Standing Kinked Silicon Nanowires for Probing Inter- and Intracellular Force Dynamics. *Nano Lett.* **15,** 5492–5498 (2015).

26. Razi, M. & Tooze, S. a. in *Methods in enzymology* **452,** 261–275 (Elsevier Inc., 2009).

27. Venkatapathi, M. & Kumar Tiwari, A. Radiative and non-radiative effects of a substrate on localized plasmon resonance of particles. *J. Appl. Phys.* **112,** 013529 (2012).

28. Cao, L. *et al.* Engineering light absorption in semiconductor nanowire devices. *Nat. Mater.* **8,** 643–647 (2009).

29. Phillips, K. G., Jacques, S. L. & McCarty, O. J. T. Measurement of Single Cell Refractive Index, Dry Mass, Volume, and Density Using a Transillumination Microscope. *Phys. Rev. Lett.* **109,** 118105 (2012).

30. Knight, M. W., Fan, J., Capasso, F. & Halas, N. J. Influence of excitation and collection geometry on the dark field spectra of individual plasmonic nanostructures. *Opt. Express* **18,** 2579 (2010).

31. Bohren, C. F. & Huffman, D. R. *Absorption and Scattering of Light by Small Particles*. *Absorption and Scattering of Light by Small Particles* (Wiley-VCH Verlag GmbH, 1998). doi:10.1002/9783527618156

32. Palik, E. D. *Handbook of Optical Constants of Solids*. **3,** (Academic Press, 1989).

33. Ma, D. D. D. Small-Diameter Silicon Nanowire Surfaces. *Science (80-.).* **299,** 1874–1877 (2003).

34. Myroshnychenko, V. *et al.* Modelling the optical response of gold nanoparticles. *Chem. Soc. Rev.* **37,** 1792 (2008).

35. Gallinet, B., Butet, J. & Martin, O. J. F. Numerical methods for nanophotonics: standard problems and future challenges. *Laser Photon. Rev.* **27,** n/a–n/a (2015).

36. Wang, N., Butler, J. P. & Ingber, D. E. Mechanotransduction across the cell surface and through the cytoskeleton. *Science* **260,** 1124–1127 (1993).

37. Fletcher, D. a & Mullins, R. D. Cell mechanics and the cytoskeleton. *Nature* **463,** 485–492 (2010).

38. Oddershede, L. B. Force probing of individual molecules inside the living cell is now a reality. *Nat. Chem. Biol.* **8,** 879–86 (2012).

39. Grashoff, C. *et al.* Measuring mechanical tension across vinculin reveals regulation of focal adhesion dynamics. *Nature* **466,** 263–266 (2010).

40. Wang, X. & Ha, T. Defining single molecular forces required to activate integrin and notch signaling. *Science* **340,** 991–4 (2013).

41. Marawske, S. *et al.* Fluorophores as optical sensors for local forces. *ChemPhysChem* **10,** 2041–2048 (2009).

42. Neuman, K. C., Chadd, E. H., Liou, G. F., Bergman, K. & Block, S. M. Characterization of photodamage to Escherichia coli in optical traps. *Biophys. J.* **77,** 2856–2863 (1999).

43. te Velthuis, A. J. W., Kerssemakers, J. W. J., Lipfert, J. & Dekker, N. H. Quantitative Guidelines for Force Calibration through Spectral Analysis of Magnetic Tweezers Data. *Biophys. J.* **99,** 1292–1302 (2010).

44. Tian, B., Xie, P., Kempa, T. J., Bell, D. C. & Lieber, C. M. Single-crystalline kinked semiconductor nanowire superstructures. *Nat. Nanotechnol.* **4,** 824–9 (2009).

Chapter 6. Conclusions and Future Outlook

In this report we have shown that substrate free silicon nanowires (SiNWs) can be used as a platform for designing and implementing novel nanoscale intracellular devices. To do this, we have demonstrated a new optical microscopy technique, Scatter Enhanced Phase Contrast (SEPC), which allowed for the visualization of SiNW internalization dynamics. Additionally, we have explored the mechanism of nanowire uptake, showing that SiNWs are primarily internalized through a phagocytosis process. Using cystoketal interactions, we were able to turn these devices into intracellular force probes, calibrating these devices using an optical to electron microscopy (EM) mapping function process. Collectively, this work represents one of the first dynamic studies of semiconductor nanowire internalization and offers valuable insight into designing devices for bio-molecule delivery, intracellular sensing and photoresponsive therapies.

Despite these advances, several important questions still remain. Notably, nanowire biocompatibility has not been fully address, and is of great interest to future endeavors. One potential approach is using proteomic and gene expression assays to examine the impact of nanowire internalization. Additionally, the effects of nanowire length, and diameter should be critically assessed during this process, as they appear to play a key role in determining biocompatibility and cell health. It also not clear how nanowires impact the generation of reactive oxygen species, and whether or not they place an increased metabolic burden on the cell.

In this vein, it would also be interesting to see how cells accustomed to dealing with molecular silicon species respond to the presence of artificial silicon nanomaterials.

Namely, diatoms are a unicellular organisms capable of producing a frustule, or a silica shell, as an outer coating[1]. While no atomically pure silicon, the shell of nanowires can also be oxidized to form a silica coating. As a result, diatoms may be able to respond to presence of silicon nanowires, possibly by demonstrating an increased ability to decompose nanowires or by incorporating them into pre-existing structures. Additionally, it is also possible that the presence of silicon nanowires might act as a morphogenic stimulator, alter the morphology of the outer silica shell. While it is known that Diatoms deposit their shell through silicon deposition vesicles (SDV)[1], it is not clear how they would respond to an external artificial scaffold.

There are also several interesting fundamental biophysical studies that remain. For instance, while here we used the individual nanowire tracking algorithm to understand the internalization process in more detail, nanowires could also potentially be used a biological probe. Namely, the effects of nanowire length and diameter could be used to study cellular response to variable load weights, or if there is a maximal weight and dimension that cells are able to transport. Such studies could be used to provide force information about intracellular motors, and how intracellular transport processes deals with large artificial materials. Similarly, the force probes that we have demonstrated in this text could be used for a wide variety of studies. For example, by combining kinked force probes with traction force microscopy techniques, one could imagine study force transduction dynamics between intra and extracellular spaces, examining how these forces propagate within a single cell and across cellular networks.

The nonspecific binding of proteins to the nanowire surface should also be examined in more detail. While this is a complicated and dynamic process, it also has

the potential of being a useful metric for studying cell health and viability. One can imagine using SiNWs as a form of 'dipstick' where nanowires are incorporated into cells, allowed to bind intracellular proteins and then removed, assessing the concentration and makeup of proteins adsbored to the nanowire surface. Such a method could serve as a interesting probe for single cell protein expression levels, and has the potential to provide multiplexed detection. Alternatively, it could also be possible with surface modification to create a nanoscale immunofluorescence assay, where intracellular proteins bind to reactive fluorescence sites on the nanowire surface, providing real time information about the health of individual cells. While these are just a few potential applications, the non-specific surface binding of proteins to nanowires creates an interesting space for designing novel devices.

Overall however, the main thrust of this report has been the ability of nanowires to be used as novel intracellular devices. Our hope in studying this behavior, has been that that this research can serve as a basis for understanding future device configurations. The advances reported here suggest that we are just at the beginning of using semiconductors as nanoscale biomaterials for novel cellular applications, and that there are many more exciting applications to look forward to in the future.

6.5 References

1. Hildebrand, M. Diatoms, biomineralization processes, and genomics. *Chem. Rev.* **108,** 4855–4874 (2008).

Appendix: Supplemental Figures and Algorithms

A. Supplemental Video Figure Captions

Video S.1 HUVEC membrane extending along a kSiNW
The cell's membrane is able to sense the NW's topology, pausing briefly at the kink before extending along the rest of the wire. Upon grabbing the kSiNW, the cell exerts force on the wire causing it to bend. 20 µm scale bar. 200x speed, (pixel size: 0.1 µm x by 0.1 µm y)

Video S.2 Single Cell SiNW Active Transport
(**a**) SEPC micrograph of a SiNW during internalization (Scale bar 15µm). (**b**) MSD 'diffusivity exponent', α, indicating mode of active vs restricted-diffusive transport. Diffusivity exponent, α. was obtained over a rolling 30 frame period. (**c**) Instantaneous velocity of the SiNW's time (15 frame average). All values given for tip 1 (red). (**d**) Path of travel for both tips of the SiNW as a function of time (red=upper tip, blue=lower top).

Video S.3 Macrophage Internalization of SiNWs
SEPC micrograph of a mouse derived J774A.1 macrophage internalizing a SiNW during co-culture (60x play speed, Scale bar 15 µm).

Video S.4 SiNW Membrane Engulfment
SEPC micrograph of a membrane protrusion extending along a single long SiNW during internalization (160x play speed, Scale bar 20 µm).

Video S.5 Intracellular Force Sensing
A HASMC undergoing ANGII induced contraction with an internalized kSiNW force sensor in the lamella(left), with corresponding force readout (right). 50 µm scale bar. 400x speed, (pixel size: 0.3 µm x by 0.3 µm y)

Video S.6 Calibrated Intracellular Force Sensing
Scatter Enhanced Phase Contrast video of a HASMC undergoing induced muscle contraction using the hormone angiotension II (administered 3 minutes prior to video), with an internalized kSiNW force sensor (left). Corresponding force fitting measurements are given (upper-right), and time-lapse force measurements (10 frame moving average) (lower-right). Scale bar, 20 µm. 10 seconds per frame.

B. Important Algorithms

SiNW Video Coordinates:

Notes: Returns the coordinates of white pixels on a thresholded ImageJ stack. Can be used to track inidividual SiNWs for force probes and internalization studies. Saved to a text file to be loaded into python for later use.

Programming language: ImageJ Macro Language
Version: ImageJ 1.49n, Java 1.6.0_20 (64 bit)

```
getDimensions(w,h,ch,Slices,frames);
//path = getDirectory("Choose a Directory");
i = 1
j = 0;
value = 0;
for (i=1; i<=nSlices; i++) {
	setSlice(i);
	for (x=0; x<w; x++) {
	 for (y=0; y<h; y++) {
		value = getPixel(x,y);
			if (value == 255) {
				// Gives each white pixel an individual ID
				setResult("Num",j,j);
				// Records the value of that pixel, could be used with a mask
				setResult("Value",j,value);
				//Returns which slice the pixel is in
				setResult("Slide",j,i);
				//Returns pixel's X coordinate
				setResult("X",j,x);
				//Returns pixel's Y coordinate
				setResult("Y",j,y);
				j=j+1;
			}
	 }
	}
	showProgress(i/nSlices);
}
updateResults();

//Saving the results as a text file for later use in other analysis software such as python
```

Individual Nanowire Tip Tracking:

Notes: Returns the tip positions of nanowires from raw pixel coordinate data. Works on files generated with **SiNW Video Coordinates:** algorithm. This identifies the tips as Top and bottom tips. When a rotation occurs, than the coordinates get switched between the two,

and will need to be manually rotated. Tip coordinates are fit using a linear least square fit of the whole wire to provide more accurate coordinates than an individual pixel.

Programming language: Python
Version: Python 2.7.6 |Anaconda 2.0.0 (64-bit)| (default, May 27 2014, 15:00:33) [MSC v.1500 64 bit (AMD64)]

```
import numpy as np
import math
import scipy.interpolate
from scipy import stats
from scipy.ndimage import filters
from scipy import optimize
from matplotlib.pyplot import *
%matplotlib inline

#Physical Constants. Dimensions of the original video (in pixels)
Xdim = 1200
Ydim = 500
AcqTime = 500 #acquisition time or time between frames in milliseconds

#Define our Fitting Parameter
def LineFit(q,x):
  return ((q[0]*x)+q[1])
def errfunc(q,x,y):
  return y-LineFit(q,x)

xy = np.loadtxt('Path/Coordinates_file.txt')
#puts into x,y arrays

SlideNum = np.array(xy[:,3])
xGlob = np.array(xy[:,4])
yGlob = np.array(xy[:,5])
if Ydim%2 == 1:
  RefLine=(Ydim+1)/2
else:
  RefLine=Ydim/2

#Reflects image to match that seen on imageJ, which counts up in Y, not down

#Get Number of Points per Frame
SlideCnter = np.array([])
i = int(0)
for j in range (1,int(SlideNum.max())):
    count = int(0)
    while SlideNum[i] == j:
      count = count +1
      i = i +1
    SlideCnter = np.append(SlideCnter,count)
SlideCountCum = np.concatenate(([0],np.cumsum(SlideCnter)))
SlideCountCum = np.append(SlideCountCum,SlideNum.size)

#Setup arrays
M = np.array([])
```

```
TypeArray = np.array([])
InitFit = np.array([])
Tip1x = np.array([])
Tip1y = np.array([])
Tip2x = np.array([])
Tip2y = np.array([])
Rsqrs = np.array([])

#Main fitting algorithm
for k in range (1,SlideCountCum.size):
  x = np.array([])
  y = np.array([])
  for v in range (int(SlideCountCum[k-1]),int(SlideCountCum[k])):
    x = np.append(x,xGlob[v])
    y = np.append(y,yGlob[v])

  #Take 90 degree Fit First
  Ytilt = x
  Xtilt = -y
  # initial estimate of parameters
  m = (Ytilt[Ytilt.size-1]-Ytilt[0])/(Xtilt[Xtilt.size-1]-Xtilt[0])
  b = Ytilt[0]-m*Xtilt[0]
  if math.isinf(m):
    m = 0
    b = Ytilt[0]
  q0 =[[m],[b]]
  # 90 degree fit
  tfit = optimize.leastsq(errfunc,q0,args=(Xtilt.astype(np.float64),Ytilt.astype(np.float64)))
  FitArray = np.array(tfit[0])
  #tracking Fits
  #Rotates the fit if the linear fit is above 45 deg, to provide a better fit for wires that are perpindicular
  InitFit = np.append(InitFit,FitArray[0])
  if abs(FitArray[0])<1:
    if FitArray[0]>0:
      TypeArray = np.append(TypeArray,int(1))
      xtemp1 = int(Xtilt.min())
      ytemp1 = LineFit(tfit[0],int(Xtilt.min()))
      xtemp2 = int(Xtilt.max())
      ytemp2 = LineFit(tfit[0],int(Xtilt.max()))
      #Track Alogrithim
    else:
      #Track Alogrithim
      TypeArray = np.append(TypeArray,int(2))
      #Assign Values
      xtemp1 = int(Xtilt.min())
      ytemp1 = LineFit(tfit[0],int(Xtilt.min()))
      xtemp2 = int(Xtilt.max())
      ytemp2 = LineFit(tfit[0],int(Xtilt.max()))

    Tip1x = np.append(Tip1x,ytemp1)
    Tip1y = np.append(Tip1y, -xtemp1)
    Tip2x = np.append(Tip2x,ytemp2)
    Tip2y = np.append(Tip2y, -xtemp2)
  else:
    # initial estimate of parameters
    m = (y[y.size-1]-y[0])/(x[x.size-1]-x[0])
```

```
    b = y[0]-m*x[0]
    q0 =[[m],[b]]
    fit = optimize.leastsq(errfunc,q0,args=(x,y))
    FitArray = np.array(fit[0])
    if FitArray[0]>0:
      Tip1x = np.append(Tip1x,x[x.size-1])
      Tip1y = np.append(Tip1y,LineFit(fit[0],x[x.size-1]))
      Tip2x = np.append(Tip2x,x[0])
      Tip2y = np.append(Tip2y,LineFit(fit[0],x[0]))
      #Track Alogrithim
      TypeArray = np.append(TypeArray,int(3))
    else:
      Tip2x = np.append(Tip2x,x[x.size-1])
      Tip2y = np.append(Tip2y,LineFit(fit[0],x[x.size-1]))
      Tip1x = np.append(Tip1x,x[0])
      Tip1y = np.append(Tip1y,LineFit(fit[0],x[0]))
      #Track Alogrithim
      TypeArray = np.append(TypeArray,int(4))

#Array of timepoints
timeline = np.linspace(0,(Tip1x.size-1)*AcqTime,Tip1x.size)

#Save the tip position
np.savetxt('Path\filename.txt',np.transpose([timeline,Tip1x,Tip1y,Tip2x,Tip2y]))
```

Nanowire Tip Tracking Analysis:

Notes: Computes the velocity and rolling mean squared displacement of single tips from the data produced by the tracking algorithim.

Programming language: Python
Version: Python 2.7.6 |Anaconda 2.0.0 (64-bit)| (default, May 27 2014, 15:00:33) [MSC v.1500 64 bit (AMD64)]

```
import numpy as np
import math as math
import scipy.interpolate
from scipy import stats
from matplotlib.pyplot import *
%matplotlib inline
from scipy import optimize


from mpl_toolkits.mplot3d.axes3d import Axes3D

def compute_MSD(x,y):
  totalsize=len(x)
  msd=[]
  for i in range(totalsize-1):
  #for i in range(0,11):
    j=i+1
```

```
    msd.append(np.sum((((x[0:-j]-x[j::])**2)+(y[0:-j]-y[j::])**2))/float(totalsize-j))

  msd=np.array(msd)
  return msd

def compute_SD(x,y,interval):
  sd = []

  for i in range(x.size/4):
    j=i+1
    sd.append((((x[0:-j]-x[j::])**2)+(y[0:-j]-y[j::])**2))
  SD=np.array(sd)
  AVG = np.ones((SD.shape[0],SD.shape[1]-(interval-1)))
  #print(AVG.shape)
  #print(SD.shape[0])
  for i in range(0,SD.shape[0]-1):
      #print(i)
      AVG[i,:] = movingaverage(SD[i],interval)
  return AVG

def compute_V(x,y,interval):
  global Conv
  totalsize=len(x)
  v=[]
  j = interval
  v = np.sqrt((x[0:-j]-x[j::])**2+(y[0:-j]-y[j::])**2)*Conv/(2.5*(j))

  Vel=np.array(v)
  return Vel

def compute_Angl(x,y):
  #Ref Angle
  Cellmag = 1
  CellXv = [0]
  CellYv = [1]
  Cellv = np.array([CellXv,CellYv])

  dx = np.array([])
  dy = np.array([])
  ResultArray = np.array([])
  dx = np.array((X1[:]-X2[:]))
  dy = np.array((Y1[:]-Y2[:]))

  ResultArray = np.array([])
  for i in range(1,(dx.size-1)):
    Result = np.arccos(((dx[i]*CellXv[0])+(dy[i]*CellYv[0]))/(np.sqrt(dx[i]**2+dy[i]**2)*Cellmag))
    ResultArray = np.append(ResultArray,Result)

def rollingMSD(x,y,t,interval):
  totalsize=len(x)
  msd=[]
  tlong = []
  RollA = np.array([])
  for i in range(int(interval/2),totalsize-(int(interval/2)+2)):
    x_short = np.array([])
    y_short = np.array([])
```

```
    t_short = np.array([])
    for j in range(i-int(interval/2),i+int(interval/2)):
      x_short = np.append(x_short,x[j])
      y_short = np.append(y_short,y[j])
      t_short = np.append(t_short,t[j])
    t_short = t_short - t_short[0]
    t_short = np.delete(t_short,0,0)
    msd_short = compute_MSD(x_short,y_short)
    logMSD = np.log(msd_short)
    #print(logMSD.size)
    logT = np.log(t_short)
    tlong.append(t[i])


    if (np.trapz(logMSD,logT)<0):
      slope = 0
    else:

      slope, intercept, r_value, p_value, std_err = stats.linregress(logT,logMSD)
      if (np.isnan(slope)==True):
        print(i)
    RollA = np.append(RollA,slope)
    #print(i)

  return (RollA , np.array(tlong))

def movingaverage(values,window):
  weigths = np.repeat(1.0, window)/window
  #including valid will REQUIRE there to be enough datapoints.
  #for example, if you take out valid, it will start @ point one,
  #not having any prior points, so itll be 1+0+0 = 1 /3 = .3333
  smas = np.convolve(values, weigths, 'valid')
  return smas # as a numpy array

#Lens Conversion (um/pixel)
Conv = (float(50)/156)

#Load File
filename = 'Path\Tiptrace_filename.txt'
rawdata = np.loadtxt(filename)

#Position data for a stationary particle collected at the same time to correct for stage drift
bkgfilename = 'Path/stationary_particle_position_filename.txt'
bkgrawdata = np.loadtxt(bkgfilename)

interval = 2
#Parse Data
T = movingaverage(rawdata[:,0],interval)
X1 = movingaverage(rawdata[:,1]-(bkgrawdata[:,1]-bkgrawdata[0,1]),interval)
Y1 = movingaverage(rawdata[:,2]-(bkgrawdata[:,2]-bkgrawdata[0,2]),interval)
X2 = movingaverage(rawdata[:,3]-(bkgrawdata[:,1]-bkgrawdata[0,1]),interval)
Y2 = movingaverage(rawdata[:,4]-(bkgrawdata[:,2]-bkgrawdata[0,2]),interval)

#Calculate Your Data
#Number of frames considered in the rolling mean sqaured displacement
RollMSD_Int = 30
```

```
#Interval over which the velocity is considered; longer = less noisy, but less temporally precise
Vel_Int = 15
rollMSD,tframe = rollingMSD(X1,Y1,T,RollMSD_Int)
vel = compute_V(X1,Y1,Vel_Int)

#Plot the resulting data
fig = figure(figsize=(15,8))
ax = fig.add_subplot(2, 2, 1)
ax.plot(tframe/60,rollMSD,label='Rolling MSD')
#ax.legend()
ax.plot([0, T[:vel.size].max()], [1,1 ], 'k--', lw=1)
ax.set_ylabel('Diffusivity Coef',size=18)
ax.set_xlim(0,T[:vel.size].max()/60)
ax.set_ylim(-0.2,2.2)

ax2 = fig.add_subplot(2, 2, 3)
ax2.plot(T[:vel.size]/60,vel)
ax2.set_xlabel('Time(min)',size=18)
ax2.set_ylabel('Velocity $\mu$m/s',size=18)
ax2.set_xlim(0,T[:vel.size].max()/60)

#Bounding box for the 3D plot
xmin = -35
xmax = 0
ymin = 24
ymax = 44
tmin = 0
tmax = T[:vel.size].max()/60

ax3 = fig.add_subplot(1, 2, 2, projection='3d')
#ax3 = fig.gca(projection='3d')
ax3.plot([xmin,xmax],[ymax,ymax],[tmin,tmin],'k-')
ax3.plot([xmin,xmin],[ymin,ymax],[tmin,tmin],'k-')
ax3.plot([xmin,xmin],[ymax,ymax],[tmin,tmax],'k-')
ax3.set_xlim(xmin,xmax)
ax3.set_ylim(ymin,ymax)
ax3.plot(-X1*Conv, Y1*Conv,T/60,linewidth=2)
ax3.plot(-X2*Conv, Y2*Conv, T/60,'r-',linewidth=2)

#Save your data
#savefig('Path\ \Graphic.png',dpi=450)

np.savetxt('Path//velocity_filename.txt, vel)
np.savetxt('Path//rollingMSD_filename.txt, rollMSD)
np.savetxt('Path//MSD_time_axis_filename.txt, tframe)
```

Ensemble Nanowire Cell Overlap:

Notes: This is intended to be used on binary thresholded phase contrast and darkfield images of the same region, to analyze the overlap of cells with silicon nanowires (**Figure 3.1**). This method works by creating an "AND" image which contains the overlapping pixels shared by both the nanowire and cell images. Before performing this

analysis, the user should make sure that the thresholded images contain only SiNW and cell pixels, and that optical artifacts have been removed from the analysis. It is suggested that a minimum of eight pairs of images is used for each time point, as the ensemble overlap can vary significantly by region.

Programming language: ImageJ Macro Language
Version: ImageJ 1.49n, Java 1.6.0_20 (64 bit)

```
//Choose the path to Darkfield and Phase contrast Images
//Files should be saved as image sequence with "DF" and "PC" as the names
dfpath = getDirectory("Choose Nanowire Path");
pcpath = getDirectory("Choose Cell Path");
//Change this variable to be equal to the number of images you have of each
numIMG = 32;
for(i=0;i<numIMG;i++) {
	//Set Path name
	if(i >= 10){
	 if(i >= 100){
		PC = pcpath + "PC0" + i + ".tif" ;
		DF = dfpath + "DF0" + i + ".tif" ;
	 }
	 else{
		PC = pcpath + "PC00" + i + ".tif" ;
		DF = dfpath + "DF00" + i + ".tif" ;
	 }
	}
	else{
	 PC = pcpath + "PC000" + i + ".tif" ;
	 DF = dfpath + "DF000" + i + ".tif" ;
	}

	// Analyze Nanowire image
	open(DF);
	run("Select All");
	getHistogram(values, DF_CNT, 256);

	//Get total Image Pixel Size
	DFtotal = 0;
	for (p=0;p<256;p++) DFtotal = DFtotal + DF_CNT[p];

	// Analyze Cell image
	open(PC);
	run("Select All");
	getHistogram(values, PC_CNT, 256);

	//Create Composite nanowire + cell image
	imageCalculator("AND create", 1, 2);
	getHistogram(values, And_Cnt, 256);
	j = nResults;

	close();
	close();
	close();
```

```
        //Reports Slide
        setResult("Track", j,i);
        //Reports Total Image Size
        setResult("Total_Count",j,DFtotal);
        //Reports Nanowire Pixel Count
        setResult("NW_Cnt",j,DF_CNT[255]);
        //Reports Cell Pixel Count
        setResult("PC_Cnt",j,PC_CNT[255]);
        //Reports Overlap of Cells with nanowires
        setResult("And_Cnt",j,And_Cnt[255]);
}

//Save the measurement as a text file for later analysis in the program of choice
```

Nanowire Force Probe Measurement:

Notes: Uses the thresholded coordinates extracted from the ImageJ Macro, **SiNW Video Coordinates:**, to determine the force load on a SiNW. Assumes a simply supported euler-bernouli beam model for each image. Also needs knowledge of the lens magnification for the unit conversion, and the young's modulus of the material. An input file, with the distribution of optical-EM predicted nanowires diameters is also used. A hexagonal beam has been assumed for the cross section moment of inertia. Returns force load information, as well as the position of the force load over time.

Programming language: Python
Version: Python 2.7.6 |Anaconda 2.0.0 (64-bit)| (default, May 27 2014, 15:00:33) [MSC v.1500 64 bit (AMD64)]

```
import numpy as np
import scipy.interpolate
from scipy import stats
from scipy.stats import norm
from matplotlib.pyplot import *
%matplotlib inline
from scipy import optimize
try:
  from IPython.core.display import clear_output
  have_ipython = True
except ImportError:
  have_ipython = False

#Minimizing Function
def MinFit(q,c,x,L):
  global E,I
  ytemp = np.array([])
  a = abs(L - c)
  for n in range (0,x.size):
    if x[n] < a:
      ytemp = np.append(ytemp,(((q*c*x[n])*((L**2)-(c**2)-(x[n]**2)))/(6*L*E*I)))
```

```
    else:
      ytemp = np.append(ytemp,((((q*c*x[n])*((L**2)-(c**2)-(x[n]**2)))/(6*L*E*I))+((q*((x[n]-a)**3))/(6*E*I))))
  return ytemp

def lstsq (q,b,x,yz,L):
  return (yz-MinFit(q,b,x,L))

def lstsb (b,q,x,yz,L):
  return (yz-MinFit(q,b,x,L))

def movingaverage(values,window):
  weigths = np.repeat(1.0, window)/window
  #including valid will REQUIRE there to be enough datapoints.
  #for example, if you take out valid, it will start @ point one,
  #not having any prior points, so itll be 1+0+0 = 1 /3 = .3333
  smas = np.convolve(values, weigths, 'valid')
  return smas # as a numpy array

def Parse(k):
  global xGlob,yGlob,SlideCountCum,conv
  dists = np.array([])
  x = np.array([])
  y = np.array([])
  xsmt = np.array([])
  ysmt = np.array([])
  Xnew = np.array([])
  Ynew = np.array([])
  for v in range (int(SlideCountCum[k-1]),int(SlideCountCum[k])):
    x = np.append(x,xGlob[v])
    y = np.append(y,yGlob[v])
  ysmt = movingaverage(y,10)
  xsmt = movingaverage(x,10)
  x = (x[:]-xsmt[0])/conv
  y = (y[:]-ysmt[0])/conv

  #Rotation 1
  Dist = np.sqrt((xsmt[xsmt.size-1]-xsmt[0])**2 + (ysmt[ysmt.size-1]-ysmt[0])**2)
  if ((ysmt[ysmt.size-1]-ysmt[0])/(xsmt[xsmt.size-1]-xsmt[0]))>0 :
    theta = -np.arccos((xsmt[xsmt.size-1]-xsmt[0])/Dist)
    #print('Mode1')
  else:
    theta = np.arccos((xsmt[xsmt.size-1]-xsmt[0])/Dist)
    #print('Mode2')
  Xnew = (np.cos(theta)*x)-(np.sin(theta)*y)
  Ynew = (np.sin(theta)*x)+(np.cos(theta)*y)
  x = Xnew
  y = Ynew

  ysmt = movingaverage(y,10)
  xsmt = movingaverage(x,10)


  L = xsmt[xsmt.size-1]-xsmt[0]
  #y = y - y[0]
  #xuni = np.linspace(0,L,xuni.size)
  return xsmt, ysmt , L , x , y
```

```
#Parsing Data if Kink is still extent
def ParseK3(k):
  global xGlob,yGlob,SlideCountCum,conv
  x = np.array([])
  y = np.array([])
  xuni = np.array([])
  yavg = np.array([])
  Xnew = np.array([])
  Ynew = np.array([])
  for v in range (int(SlideCountCum[k-1]),int(SlideCountCum[k])):
    x = np.append(x,xGlob[v])
    y = np.append(y,yGlob[v])
  #ysmt = movingaverage(y,10)
  #xsmt = movingaverage(x,10)
  x = (x[:]-x[0])/conv
  y = (y[:]-y[0])/conv


  #Rotation 1
  ymax = np.where(y==y.max())[0][0]
  xmax = np.where(x==x.max())[0][0]
  Dist = np.sqrt((x[ymax]-x[xmax])**2 + (y[ymax]-y[xmax])**2)
  theta = -np.arccos((x[ymax]-x[xmax])/Dist)
  Xnew = np.cos(theta)*x[:]-np.sin(theta)*y[:]
  Ynew = np.sin(theta)*x[:]+np.cos(theta)*y[:]
  x = Xnew = Xnew - Xnew.min()
  y = Ynew = Ynew - Ynew.min()



  #Construct Bending Portion
  Xtemp,Ytemp = centavg(x,y)
  Xtemp = movingaverage(Xtemp,10)
  Ytemp = movingaverage(Ytemp,10)

  dists = np.diff(Xtemp,axis=0)**2 + np.diff(Ytemp,axis=0)**2
  dists = np.sqrt(dists)


  Xnew = np.array([])
  Ynew = np.array([])

  for k in range(0,Xtemp.size-1):
    if dists[k] < float(0.35):
      #print(dists[k])
      Xnew = np.append(Xnew,Xtemp[k])
      Ynew = np.append(Ynew,Ytemp[k])
      #print('X : ' + str(Xnew[k]))
      #print('Y : ' + str(Ynew[k]))
    else:
      break


  #Rotation 2
  xmin = np.where(x == x.min())[0][0]
```

```
  Dist = np.sqrt((x[0]-x[xmin])**2 + (y[0]-y[xmin])**2)
  theta = -np.arccos(x[0]/Dist)
  Xtemp = np.cos(theta)*x[:]-np.sin(theta)*y[:]
  Ytemp = np.sin(theta)*x[:]+np.cos(theta)*y[:]
  x = Xtemp
  y =Ytemp

  Xtemp = np.cos(theta)*Xnew[:]-np.sin(theta)*Ynew[:]
  Ytemp = np.sin(theta)*Xnew[:]+np.cos(theta)*Ynew[:]
  Xnew = Xtemp
  Ynew =Ytemp

  L = Xnew[Xnew.size-1]-Xnew[0]

  return Xnew, Ynew, L, x , y

def LoadFitTest(x,b,q,):
  global L
  if b > L:
    b = L
  if b < 0:
    b = 0

  a = abs(L - b)
  if x < a:
     return(((q*b*x)*((L**2)-(b**2)-(x**2)))/(6*L*E*I))
  else:
    return((((q*b*x)*((L**2)-(b**2)-(x**2)))/(6*L*E*I))+((q*((x-a)**3))/(6*E*I)))


def vLoadFit(x,b,q):
 y = np.zeros(x.shape)
 for i in range(len(y)):
  y[i]=LoadFitTest(x[i],b,q,)
 return y

#Find Center Average
def centavg(x,y):
  delMe = np.array([])
  xuni = np.array([])
  yavg = np.array([])
  for k in range(0,x.size):
    if x[k] not in xuni:
      xuni = np.append(xuni,x[k])
  xuni = np.sort(xuni)
  for k in range(0,xuni.size):
    x_temp = np.array(np.where(x==xuni[k])[0][:])
    if x_temp.size == 1:
      delMe = np.append(delMe,k)

    y1 = np.average(y[x_temp])
    yavg = np.append(yavg,y1)
  #print(delMe)
  #xuni = np.delete(xuni,delMe)
  #yavg = np.delete(yavg,delMe)
  return xuni,yavg
```

```
def Find_Curve2(xsmt,ysmt,L,b_prev,xraw,yraw):
  global E,I
  ytemp = movingaverage(ysmt,10)
  xtemp = movingaverage(xsmt,10)
  if ysmt.sum()>0:
    #cord_max = np.array(np.nonzero(ysmt==ysmt.max())[0][0])
    cord_max = np.array(np.nonzero(ytemp==ytemp.max())[0][0])
  else:
    #cord_max = np.nonzero(ysmt==ysmt.min())[0][0]
    cord_max = np.nonzero(ytemp==ytemp.min())[0][0]

  print('xmax= ' + str(xsmt[cord_max]))
  b_guess = np.sqrt(np.absolute(np.array((L**2)-(3*(xtemp[cord_max])**2))))
  #b_guess = L/2
  print('b_guess= ' + str(b_guess))
  if b_guess > L:
    b_guess = b_prev
    print('Adjusted b_guess')
  #b_guess = L - xsmt[cord_max]
  Q_guess = (ysmt[ysmt.size/2]*27*L*E*I)/(np.sqrt(3)*b_guess*np.sqrt(((L)**2-b_guess**2)**(3)))

  fit,cov,infodict,mesg,ier = optimize.leastsq(lstsq,Q_guess,args=(b_guess,xraw,yraw,L),full_output=True)
  Q_guess = fit[0]
  fit,cov,infodict,mesg,ier = optimize.leastsq(lstsb,b_guess,args=(Q_guess,xraw,yraw,L),full_output=True)
  b_guess = fit[0]
  fit,cov,infodict,mesg,ier = optimize.leastsq(lstsq,Q_guess,args=(b_guess,xraw,yraw,L),full_output=True)

  return b_guess,fit[0],infodict

#Load file with a distribution of predicted SiNW diameters from EM-Transform (in nm)
#Diam file is a simple float list of nanowire diameters
diam_filename = 'Path\Diam_filename.txt'
d = np.loadtxt(diam_filename)

#Get the mode of the distribution
x = np.linspace(0,d.max()+1,20000)
fit = scipy.stats.gaussian_kde(d)

D = x[np.where(fit(x)==fit(x).max())[0][0]]*(1E-9)
D_err = d.std()*(1E-9)

#Load Physical Constants
#Young's Modulus (tera pascals)
E = 0.169
#Second Moment of Inertia
I = ((5*np.sqrt(3))/144)*(D**4)*(1000000**4)
#Pixel to um Conversion based on lens(pixels/um)
conv = 156/(50)

#Text file including the pixel coordinates of the force probe,
# retrieved from the SiNW Video Coordinates ImageJ Macro
data_file = 'Path/filename.txt'

#Load XY data
xy = np.loadtxt(data_file)
```

```
#put into x,y arrays
SlideNum = np.array(xy[:,1])
xGlob = np.array(xy[:,2])
yGlob = np.array(xy[:,3])

#Get Number of Points per Frame- Parse slide nmbers
SlideCnter = np.array([])
i = int(0)
for j in range (1,int(SlideNum.max())):
    count = int(0)
    while SlideNum[i] == j:
      count = count +1
      i = i +1
    SlideCnter = np.append(SlideCnter,count)
SlideCountCum = np.concatenate(([0],np.cumsum(SlideCnter)))
SlideCountCum = np.append(SlideCountCum,SlideNum.size)

#Record Video
Force = np.array([])
bMat = np.array([])
LMat = np.array([])
SSq = np.array([])
Rsqrs = np.array([])
#break

for k in range(1,SlideCountCum.size-1):
  xsmt = np.array([])
  ysmt = np.array([])
  print('#:'+ str(k))

  #Parse Data - Returns NW Value of bending + Kink
  #Change to ParseK3 if you still have the kink in your original coordinates data
  xsmt,ysmt,L,rawx,rawy = Parse(k)
  if k == 1:
    bprev = L/2
  #If you need additional Smoothing, use here
  #xsmt = movingaverage(xsmt,5)
  #ysmt = movingaverage(ysmt,5)

  #Fit Function
  b_guess,q_guess,infodict =Find_Curve2(xsmt,ysmt,L,bprev,xsmt,ysmt)
  #print('L= ' + str(L))

  bprev = (b_guess)

  #Record Data
  LMat = np.append(LMat,L)
  Force = np.append(Force,q_guess)
  bMat = np.append(bMat,b_guess)
  ssErr = ((ysmt-MinFit(q_guess,b_guess,xsmt,L))**2).sum()
  ssTot = ((ysmt-ysmt.mean())**2).sum()
  rsquared = (1-(ssErr/ssTot ))**2
  Rsqrs = np.append(Rsqrs,rsquared)
  s_sq = (infodict['fvec']**2).sum()/ (xsmt.size-2)
  SSq = np.append(SSq,s_sq)
```

```
  #Save Figure To make video

  plot(rawx,-rawy,'r+')
  plot(xsmt,-ysmt,'g.')
  plot(xsmt,-MinFit(q_guess,b_guess,xsmt,L),'b-')
  plot([0, L], [0,0 ], 'k--', lw=1)
  xlabel('X ($\mu$m)', style='italic', fontsize= 24)
  ylabel('dY ($\mu$m)', style='italic', fontsize= 24)
  xlim(0,40)
  ylim(-5,12)
  Str = 'P = ' + "%.3g" % -q_guess + ' N'
  text(2,-2,Str,fontsize= 17)
  text(L-b_guess,0,"|", color="blue" )
  savefig('Path/File_basename'+str(k)+'.png',bbox_inches='tight', pad_inches=.1)
  clf()

#Review Data Analysis

#Plot Force Over time
z = 10
linespace = (np.linspace(0,Force.size+5,Force.size)/6)+3
linespace = movingaverage(linespace,z)
plot(linespace ,-movingaverage(Force,z),'r-')
print(np.absolute(-movingaverage(Force,z)).max())

ylabel('Force (N) ', fontsize= 18)
xlabel('Time(min)', fontsize= 18)
#Save Figure
#savefig('Path/filename.png',dpi=900)

#Smooth Data
Force_avg = -movingaverage(Force,z)
print(Force_avg[np.nonzero(Force_avg == Force_avg.max())[0][0]])

#Position of Load Over Time
z = 10
linespace = (np.linspace(0,Force.size,Force.size)/6)+3
linespace = movingaverage(linespace,z)
#plot(L-bMat)
plot(linespace,L-movingaverage(bMat,z),'r-')
plot([0, Force.size], [0,0 ], 'k--', lw=1)
plot([0, Force.size], [LMat.max(),LMat.max() ], 'k--', lw=1)
ylim(-5,40)
xlim(0,100)
ylabel('Load Position', fontsize= 18)
xlabel('Frame', fontsize= 18)

#Plot An individual Frame
xsmt = np.array([])
ysmt = np.array([])


#Parse Data - Returns NW Value of bending + Kink
xsmt,ysmt,L,rawx,rawy = Parse(222)

b_guess,q_guess,infodict =Find_Curve2(xsmt,ysmt,L,bprev,xsmt,ysmt)
```

```
print('L= ' + str(L))
print('q= ' + str(q_guess))


#Get Dem Stats
ssErr = ((ysmt-MinFit(q_guess,b_guess,xsmt,L))**2).sum()
ssTot = ((ysmt-ysmt.mean())**2).sum()
rsquared = (1-(ssErr/ssTot ))**2
s_sq = (infodict['fvec']**2).sum()/ (xsmt.size-2)

#Save Figiure
plot(rawx,-rawy,'r+')
plot(xsmt,-ysmt,'g.')
plot(xsmt,-MinFit(q_guess,b_guess,xsmt,L),'b-')
plot([0, 40], [0,0 ], 'k--', lw=1)
xlabel('X (um)', fontsize= 18)
ylabel('dY (um)', fontsize= 18)
Str = 'q = ' + "%.3g" % q_guess + ' N/um  R^2=' + "%.2g" %rsquared
text(5,-1.5,Str)
text(L-b_guess,0,"|", color="blue" )
savefig('Path\filename.png',dpi=900)

#Test Error Based on Diameter
def_E = E
def_I = I
#Pick a frame of force fitting data that is near you max Force and is well fit
frame_num = 222
xsmt,ysmt,L,rawx,rawy = Parse(frame_num)
ForceErr = np.array([])

#Cycles through diameter file to get a distribution of force data based on diameter
for i in range(0,d.size-1):
  bprev = 0
  print('#: ' + str(i))
  D = d[i]*(1E-9)
  I = ((5*np.sqrt(3))/144)*(D**4)*(1000000**4)
  b_guess,q_guess,infodict =Find_Curve2(xsmt,ysmt,L,bprev,xsmt,ysmt)
  ForceErr = np.append(ForceErr,q_guess)
  print('D: ' + str(D))
  print('q_guess: ' + str(q_guess))
n, bins, patches = hist(r, 5,normed=1,  histtype='stepfilled')

E = def_E
I = def_I

x = np.linspace(0,ForceErr.min()*1.1,20000)
fit = scipy.stats.gaussian_kde(ForceErr)

mode = x[np.where(fit(x)==fit(x).max())[0][0]]
print(mode)

#Get Info out about your uncertainty in the force
n, bins, patches = hist(-ForceErr*1E12, 40,normed=1,  histtype='stepfilled')
xlim(0,600)
#plot(-x,fit(x))
xlabel('Force (N)',fontsize=18)
```

```
ylabel('PDF',fontsize=18)
#plot([ForceErr.mean(), ForceErr.mean()], [0,60], 'k--', lw=1)

print('Mode: ' + str(x[np.where(fit(x)==fit(x).max())[0][0]]))
print('Mean: ' + str(ForceErr.mean()))
print('Median: ' + str(np.median(ForceErr)))
print('STD: ' + str(ForceErr.std()))
print('SEM: ' + str(ForceErr.std()/np.sqrt(d.size-1)))
print(' ')
print('%Er ' + str(ForceErr.std()/ForceErr.mean()))
print('Nonparametric skew=' + str((ForceErr.mean()-np.median(ForceErr))/ForceErr.std()))

savefig('Path\Force_Unc_filename.png',dpi=900)

#Save your data
np.savetxt('Path\Force_overtime_filename.txt', Force)
np.savetxt('Path\Force_position_filename.txt', bMat)
np.savetxt('Path\Force_error_filename.txt', ForceErr)
```

Lorentz-Mie Theory:

Notes: Used to predict the optical scattering of SiNWs inside a variety of different mediums and with different light sources. Need a source file containing the complex refractive index of your material, the wavelength dependent intensity of the imaging light source as well as the quantum efficiency of the recording camera as a function of wavelength. As all of these values are not likely to be reported for the same exact wavelengths, values are interpolated over the wavelength range to match the reported refractive index measurements.

Programming language: Python
Version: Python 2.7.6 |Anaconda 2.0.0 (64-bit)| (default, May 27 2014, 15:00:33) [MSC v.1500 64 bit (AMD64)]

```
import numpy as np
from scipy import stats
import scipy.special as spc
import scipy.signal as signal
from scipy.stats import norm
from matplotlib.pyplot import *
from math import pi
%matplotlib inline
from scipy import optimize
from matplotlib.mlab import griddata
import scipy.interpolate as interp
import math

#Scattering for transversal magnetic field
def Qsa_TM (n,x,i):
  Sum_est = np.array([])
```

```
  for j in range(1,i):
    Sum_est = np.append(Sum_est,abs(Bi(n,x,j))**2)
  q = 2*((abs(Bi(n,x,0))**2) + 2*Sum_est.sum())/x
  return q

#Scattering for transversal electric field
def Qsa_TE (n,x,i):
  Sum_est = np.array([])
  for j in range(1,i):
    Sum_est = np.append(Sum_est,abs(Ai(n,x,j))**2)
  q = 2*(abs(Ai(n,x,0))**2 + 2*Sum_est.sum())/x
  return q

def Ai(n,x,i):
  A = n*spc.jn(i,n*x)*spc.jvp(i,x)
  B = spc.jvp(i,n*x)*spc.jn(i,x)
  C = n*spc.jn(i,n*x)*spc.h1vp(i,x)
  D = spc.jvp(i,n*x)*spc.hankel1(i,x)
  An = (A-B)/(C-D)
  return An

def Bi(n,x,i):
  A = spc.jn(i,n*x)*spc.jvp(i,x)
  B = n*spc.jvp(i,n*x)*spc.jn(i,x)
  C = spc.jn(i,n*x)*spc.h1vp(i,x)
  D = n*spc.jvp(i,n*x)*spc.hankel1(i,x)
  An = (A-B)/(C-D)
  return An

#Path to the text files containing information on:

#The material's refractive index as a list (Wavelength, Real Part, Complex Part)
Ref_Infex_Path = '\\Refractive_Index.txt'

#The Light source intensity (Wavelength, intensity)
LED_path ='\\SEPC_LED_Spectrum.Scope'

#The black body light source intensity (Wavelength, intensity)
Black_Body_path = '\\Black_Body_3000k.txt'

#The black body light source intensity (Wavelength, intensity)
Black_Body2500_path = '\\Black_Body_2500k.txt'

#Camera Quantum Efficiency by wavelength (Wavelength, intensity)
Camera_QE_Path= ' \\Camera_QE_Manual.txt'

Ref_Index = np.loadtxt(Ref_Infex_Path)
Black_Body = np.loadtxt(Black_Body_path)
Black_Body2500 = np.loadtxt(Black_Body2500_path)
LED = np.loadtxt(LED_path)
Camera_QE = np.loadtxt(Camera_QE_Path)

#Silicon Refractive Indexes, Realpart = REFFRE, Imaginary Part = REFFIM
WAVEL= Ref_Index[:,0]*1000
REFRE = Ref_Index[:,1]
REFIM = Ref_Index[:,2]
```

```
#Refractive Index of Medium
#Air
REFMED= 1.0

#Water
#REFMED= 1.3330

#Cell
#REFMED = 1.402

#IPA
#REFMED= 1.3776

#Getting N (n+ik)
REF_complex = np.array([])
for i in range(0,REFRE.size):
  REF_complex = np.append(REF_complex,complex(REFRE[i],REFIM[i])/REFMED)

#SEPC DARKFIELD Spectrum
LED_WAVE = LED[:,0]
LED_SPEC = LED[:,1]

#Camera Spectrum
Camera_Wave = Camera_QE[:,0]
Camera_Eff = Camera_QE[:,1]

#Normalizing Light Spectrum
LED_SPEC = LED_SPEC[:]/LED_SPEC.max()

#Match LED Spectrum to refractive index points
Short_WAVEL = np.array([])
Short_REF_complex = np.array([])
for i in range(0,WAVEL.size):
  if WAVEL[i]>300:
    if WAVEL[i]<800:
      Short_REF_complex = np.append(Short_REF_complex,REF_complex[i])
      Short_WAVEL = np.append(Short_WAVEL,WAVEL[i])

#Fit Camera QE For continuous Function
wave_ptile = np.linspace(np.amin(Camera_Wave),np.amax(Camera_Wave),len(Camera_Wave))
QE_spline = interp.UnivariateSpline(wave_ptile,Camera_Eff,s=2)

cont_QE = lambda opt: QE_spline(opt)

#Run the Mie theory calc. with the chosen refractive index
# inc = included range = maximum diameter of SiNW calculated
inc = 300
spec_array = np.zeros((inc,Short_WAVEL.size))

for z in range(0,inc):
  #Set the Diameter of the calculation
  d = 1+z
  Ind_spec_array = np.array([])

  for j in range (0,Short_WAVEL.size):
```

```
    #Define refractive index (n) and prefactor(x)
    x = 2*pi*d/(2*Short_WAVEL[j])
    n = Short_REF_complex[j]
    TE = Qsa_TE(n,x,10)
    TM = Qsa_TM(n,x,10)
    #Compute Scatter
    Ind_spec_array = np.append(Ind_spec_array,((1/2.0)*(TE+TM)))
  spec_array[z,:] = Ind_spec_array[:]

#Make Sexy Qsca graphs
x, y = np.meshgrid(Short_WAVEL,np.linspace(0,300,300))
z = np.array(spec_array).reshape(x.shape)

fig, ax = subplots(figsize=(10,9))

heatmap = ax.pcolor(x,y,z, cmap=cm.Blues, vmin=0, vmax=8)
#ax.set_xticklabels(row_labels, minor=False)
#ax.set_yticklabels(column_labels, minor=False)
cb = colorbar(heatmap)
ax.set_xlabel('Wavelength (nm)',fontsize=18)
ax.set_ylabel('Diameter (nm)',fontsize=18)
xlim(300,Short_WAVEL.max())
show()

#Need to normalize data by wavelength of input light
LED_ptile = np.linspace(0,1,len(LED_SPEC))
LED_SPEC_spline = interp.UnivariateSpline(LED_ptile,LED_SPEC,s=.01)

WAVE_ptile = np.linspace(0,1,len(LED_WAVE))
LED_WAVE_spline = interp.UnivariateSpline(LED_WAVE,WAVE_ptile,s=.01)

transform = lambda opt: LED_SPEC_spline(LED_WAVE_spline(opt))


#Construct Normalization Data
Short_LED_Spec = transform(Short_WAVEL[:])
#Divide by 100 if data is in percentile, otherwise ignore
Short_Camera_QE = cont_QE(Short_WAVEL)/100

Short_Norm = Short_LED_Spec*Short_Camera_QE
Short_Norm = Short_Norm/np.trapz(Short_Norm,dx=1)


#Black body radiator spectrum normalized
Black_Spec_norm = Black_Body/np.trapz(Black_Body,dx=1)

#Black body radiator at 2500k spectrum normalized
Black_Spec2500_norm = Black_Body2500/np.trapz(Black_Body2500,dx=1)


Intsum = np.array([])
blacksum = np.array([])

#Normalize Qsca Data for Light, and Camera
for j in range(0,spec_array.shape[0]):
  #Intsum = np.append(Intsum,np.sum(spec_array[j,:]*Short_LED_Spec*Short_Camera_QE))
```

```
  Intsum = np.append(Intsum,np.sum(spec_array[j,:]*Short_Norm))

  blacksum = np.append(blacksum,np.sum(spec_array[j,:]*Black_Spec_norm))
  #blacksum = np.append(blacksum,np.sum(spec_array[j,:]*Short_Norm))

#Save the resulting normalized scattering data
np.savetxt('Path\\filename.txt',Intsum)
```

Optical-EM Transform:

Notes: Used to predict the sub-diffraction limited diameter of a individual SiNW. This depends on a large library of text files, which contain linescans of nanowires collected in DF (**Figure 5.3.a**), typically on the order of several hundred. These can be collected using the linescan function in imageJ. Additionally, this also depends on ensemble measurements of nanowire diameters using electron microscopy.

Programming language: Python
Version: Python 2.7.6 |Anaconda 2.0.0 (64-bit)| (default, May 27 2014, 15:00:33) [MSC v.1500 64 bit (AMD64)]

```
import numpy as np
import scipy.interpolate
from scipy import stats
from scipy.stats import norm
from matplotlib.pyplot import *
%matplotlib inline
from scipy import optimize
from functools import partial
import matplotlib.pyplot as plt

def LoadPlot2 (k,data_file_basename):
  data_file = data_file_basename+str(k)+'.txt'
  LinePlot = np.loadtxt(data_file)
  LinePlot = LinePlot[:,1]

  #Basic linear deconvolution of background scattering
  m = (LinePlot[LinePlot.size-1]-LinePlot[0])/LinePlot.size
  b = LinePlot[0]
  for i in range(0,LinePlot.size):
    LinePlot[i] = LinePlot[i]-(m*i+b)

  maxNum = LinePlot.max()

  #LinePlot = LinePlot/np.trapz(LinePlot,dx=1)
  return LinePlot,maxNum

def ScanPlots2 (j,k,data_file_basename):
  global LinePlot
  max_ar = np.array([])
```

```
  #Get Point Spread Function for Wire In question
  for i in range(j,k):
    LinePlot,LinePlot_max = LoadPlot2(i,data_file_basename)
    max_ar = np.append(max_ar,LinePlot_max)

    #print(data_file_basename+'plot_' + str(i))

  return max_ar

#Load EM ensemble Diameter Data (int list) in nanometers
data_file = data_file = 'path\NW_Diameter_filename.txt'
Diam = np.loadtxt(data_file)

#Define Base Path to Ensemble Optical Measurements
optical_path = 'Path\basefilename'

#Setup Arrays
optical_Max = np.array([])

#Load Arrays
# Number of line scans you have for DF nanowires
numWires = 300
 #Scans line plots of nanowire linescans. txt file have an array of (distance, intensity)
optical_Max = ScanPlots2(1,numWires,optical_path)
#Optical-EM Mapping Function
Diam_ptile = np.linspace(0,1,len(Diam))
Diam_spline = scipy.interpolate.UnivariateSpline(Diam_ptile,sorted(Diam))

optical_ptile = np.linspace(0,1,len(optical_Max))
optical_spline = scipy.interpolate.UnivariateSpline(sorted(optical_Max),optical_ptile,s=.003)

transform = lambda opt: Diam_spline(optical_spline(opt))

#Use this transform function to move from an optical intensity data set to a diameter data set
#Only uses within the same sample, and with optical intensities collected under same conditions
```
